Optically addressable, integrative composite polymer microcapsules

Bédard, Matthieu

Optically Addressable, Integrative Composite Polymer Microcapsules

A THESIS SUBMITTED TO THE UNIVERSITY OF LONDON FOR THE DEGREE OF DOCTOR OF PHILOSOPHY

By

Matthieu Bédard

School of Engineering and Materials Science

Queen Mary University of London

United Kingdom

July 2009

Declaration

I certify that the present work is prepared solely by me during the course of my studies at Queen Mary University of London. It has not been submitted for a degree at this or any other University. Any words and/or figures from the work of other people are fully acknowledged according to standard referencing.

This thesis fully complies with the regulations set by the University of London and the Queen Mary, University of London.

Matthieu Bédard

July 2009

ABSTRACT

The development of remotely addressable tools to encapsulate, store and deliver active materials to living cells is a particularly challenging topic of material science. As drug delivery agents, microcontainers not only require high mechanical stability or to be delivered at target cells, but they should also possess efficient remotely addressable release mechanisms. Light responsive polyelectrolyte capsules are well suited for such purposes. Capsules are constructed using the Layer-by-Layer technique where oppositely charged polymers are alternatively deposited on a sacrificial template. The interest for such microcapsules lays in their versatile composition and stimuli-responsive properties, which can be altered to suit specific needs.

The primary aim of this work was to develop polymeric capsules with efficient optically addressable release mechanisms. Previous work on this topic revealed severe flaws in biological environments, especially with regards to the high energy requirements necessary for laser-induced release and in the very limited knowledge of the fate of microcapsules in living cells. These issues were addressed by developing alternative types of light-responsive capsules and gaining better understanding of existing ones. Three types of materials were used to sensitize microcapsules to the near-UV, visible and near-IR spectral regions: (1) azobenzene-substituted polymers, (2) gold nanoparticles and (3) photocatalytic porphyrinoid dyes. Various methods were used for the characterization of microcapsules, including laser scanning confocal microscopy, colloidal probe and standard atomic force microscopy, electron microscopy, fluorescence spectrophotometry, UV-visible spectroscopy and differential scanning calorimetry. Shells were probed for their mechanical stability as well as encapsulation and release behavior based on parameters such as: assembly strategies, shell deformability, permeability, thermal response and response to laser irradiation.

This thesis begins with a brief introduction followed by an extensive literature review summarizing the various topics relevant to the work. The materials and methods used in the investigations are catalogued in *Chapter 3* . *Chapter 4* presents the destructive effects of pulsed UV lasing on polymeric microcapsules and introduces azobenzene-functionalized capsules with the ability to encapsulate macromolecules by exposure to continuous wave UV light. *Chapter 5* looks at the mechanical properties of capsules functionalized with gold nanoparticles as well as their remote release capabilities under near-IR irradiation. While most of these studies were conducted *ex vivo*, *Chapter 5* concludes with a summary of studies performed *in vitro*, which demonstrates that it is not only possible to release substances in living cells by light but that the latter also survive in the process. Finally, in *Chapter 6*, the assembly and light induced destabilization of microcapsules containing porphyrinoid dyes is presented.

TABLE OF CONTENTS

ACKNOWLEDGMENTS

First and foremost, I would like to express my gratitude to my mentor, Prof. Gleb Sukhorukov who took me under his wing and always provided me with challenges, time and opportunities while encouraging me to develop my own ideas. I am indebted to my friends and colleagues at the Max-Planck Institute of Colloids and Interfaces (Potsdam, Germany) and particularly to Prof. Dr. Helmuth Möhwald for providing me with all the time, equipment and financial help necessary but also for integrating me in a great scientific environment in his department. I would like to thank Dr. Andre Skirtach for acting as my co-supervisor, advising me and bearing with my questions and criticisms, but also for his constant good mood and positive attitude towards problems. I would like to thank Dr. Dmitry Shchukin for his useful advices and Prof. Dr. Markus Antonietti as well as Dr. Laura Hartmann for our successful collaborations. I would like to acknowledge the help of Dr. Christophe Déjugnat, Dr. Oliver Kreft and Dr. Karen Köhler who provided me with invaluable insights on some scientific issues at the beginning of my thesis. For conducting experiments and providing instrumental support I wish to thank Anneliese Heilig (AFM), Dr. Renate Müller (CP-SFM), Heidemarie Zastrow (DLS), Rona Pietschke (EM), Silvia Pirok (EM) and Annegret Praast for general technicalities.

Some aspects of this work would not have been possible without the collaboration of other institutions. At Philipps Universität Marburg (Marburg, Germany) would like to acknowledge Prof. Dr. Wolfgang Parak, Dr. Almudena Muñoz Javier and Dr. Pablo del Pino for their untiring efforts towards the work involving intracellular delivery. On the same topic, I would like to thank Raghavendra Palankar (Jacobs University Bremen, Germany) for his hard work on cellular delivery, which despite not being included here provided us with crucial information on cell-microcapsule behavior. I wish to acknowledge Dr. Dmitry Gorin and his group (Saratov State University, Russia) for their warm hospitality and devotion. Finally, thanks to Dr. Bruno De Geest (Ghent University, Belgium) for his help on various projects.

At QMUL, I express my gratitude to Dr. Mike Reece, Jonathon Hills and the team at Nanoforce Technology Inc. as well as my group members for all these small things that facilitated my transition to London.

I am grateful to my friends Vladimir, Éric and my fiancée Veneta for providing me with guidance and support throughout my education. And last but none the least, to all my Professors over the years whose influence have led me where I am today.

I dedicate this thesis to my parents Jean and Nicole, for always supporting my choices, as counter-intuitive as they have been and for teaching me the true value of hard work.

LIST OF FIGURES

List of Figures

LIST OF TABLES

LIST OF SYMBOLS AND ABBREVIATIONS

GREEK LETTERS

α	Degree of dissociation
δ	Resolution
δ_c	Deformation
ε	Molar absorptivity
ε_0	Absolute dielectric constant
ε_R	Relative dielectric constant
Ψ	Potential
Ψ_0	Surface potential
Ψ_S	Stern potential
κ^{-1}	Debye length
λ	Wavelength
η	Viscosity
χ	Stiffness
ρ	Density
μ	Shear modulus
ζ	Zeta potential

LATIN LETTERS

a	Monomer size (polymers)
A	Area
A_0	Heating rate
c	Concentration
c_i	Concentration of ion *i*
C_p	Heat capacity
d	Average distance between nanoparticles
D	Diffusion constant
d_A	Average capsule diameter
dT	Temperature change
e	Elementary charge
E	Electric field
E_{kin}	Kinetic energy
E_m	Young's modulus
F_1	Fundamental frequency
F_{def}	Force of deformation
F_S	Filling factor
F_v	Odd harmonic frequency
h	Film thickness,
$\hbar$	Planck's constant
I	Ionic strength
I_0	Light intensity
I_λ	Attenuated light intensity

k	Thermal conductivity
K	Thermal conductivity of the medium
k_B	Boltzmann constant
l	Path length
l_B	Bjerrum length
l_{eff}	Effective electrostatic distance
m	Mass of absorbed material
m_e	Electron mass
N	Number of monomer unit (polymers)
N_A	Avogadro's number
NA	Numerical aperture
pK_a	Acid dissociation constant
$pK_{a(app)}$	Apparent acid dissociation constant
Q	Absorption coefficient
q_0	Persistence length of uncharged polymer
q_e	Electrostatic persistence length
q_p	Persistence length
r	Radius
r_0	Diameter of a nanoparticle
R_0	Diameter of a capsule
r_i	Distance *i* from a nanoparticle
R_{ee}	End-to-end radius
R_H	Hydrodynamic radius
S_c	Surface area of a capsule
S_i	Cross-sectional area of a nanoparticle
T	Temperature
T_g	Glass transition
u	Electrophoretic mobility
U	Voltage
v	Velocity
v_p	Poisson ratio
z_i	Charge valency of ion *i*

ABBREVIATIONS

Agg.	Aggregated gold nanoparticles
Agg-Au4	$(PDDA/Au/PSS)_4$
AFM	Atomic force microscopy
CCD	Charged coupled device (optics)
CW	Continuous wave
DLS	Dynamic light scattering
DSC	Differential scanning calorimetry
Eq	Equation
EM	Electron microscopy
ESA	Electrostatic self-assembly
F	Fluorescence
Fig.	Figure

Homo.	Homodispersed gold nanoparticles
Homo-Au2	PDDA/PSS/PDDA(Au/PSS/PDDA)$_2$PSS
Homo-Au4	(PDDA/Au/PSS)$_4$
HOMO	Highest occupied molecular orbital
IR	Infrared
LbL	Layer-by-Layer
LSCM	Laser scanning confocal microscopy
LUMO	Lowest unoccupied molecular orbital
M	Molar
NA	Numerical aperture
Nd:YAG	Neodinium: yttrium aluminium garnet
NMR	Nuclear magnetic resonance
P	Phosphorescence
PDI	Polydispersity index
PDT	Photodynamic therapy
QCM	Quartz crystal microbalance
SEM	Scanning electron microscopy
SPR	Surface plasmon resonance
TEM	Transmission electron microscopy
UV	Ultraviolet

MATERIALS

AF	Alexa Fluor
AF 488	Alexa Fluor dextran, λ_{ex} 494 nm, λ_{em} 519 nm
AF 555	Alexa Fluor dextran, λ_{ex} 555 nm, λ_{em} 565 nm
AF 594	Alexa Fluor dextran, λ_{ex} 590 nm, λ_{em} 617 nm
AlPcS	Al (III) phthalocyanine chloride tetasulfonic acid
Azo1	Phenylazobenzoic acid
Azo2	2-(4-hydroxyphenylazo)benzoic acid
Azo3	Methyl red (dye)
Azo-PAH	Azo-substituted PAH
BY	Brilliant Yellow (dye)
CaGreen™	Calcium Green dextran
CB	Cascade Blue dextran, λ_{ex} 400 nm, λ_{em} 420 nm
CuPcS	Cu (I) phthalocyanine tetasulfonic acid
DAR	Diazo-10, 4-diazodiphenylamine/formaldehyde condensate hydrogensulfate-zinc chloride salt
Dex-HEMA	Dextran-hydroxyethylmethacrylate
DMAEMA	Dimethylaminoethyl methacrylate
DMF	Dimethylformamide
DNA	Deoxyribonucleic acid
DZR	Diazoresin
EDC	1-(3-dimethylaminopropyl)-3-ethylcarbodiimide hydrochloride
FePcS	Fe (III) phthalocyanine chloride tetasulfonic acid
FITC	Fluorescein isothiocyanate
HB	Hypocrellin B

H-PDDA	High MW poly(diallyldimethylammonium chloride)
L-PDDA	Low MW poly(diallyldimethylammonium chloride)
MF	Melamine formaldehyde
MW	Molecular weight
NHS	N-hydroxysulfosuccinimide sodium salt
PAA	Poly(acrylic acid)
PAH	Poly(allylamine hydrochloride)
PAzo	Poly(1-4(4-(3-carboxy-4-hydroxyphenylazo)benzene-sulfonamido)-1,2-ethanediyl)
Pc	Porphyrinoid dye
PcS	Phthalocyanine tetasulfonic acid
PDDA	Poly(diallyldimethylammonium chloride)
PEI	Poly(ethylene imine)
PLA	Poly(lactic acid)
PEG	Poly(ethylene glycol)
PS	Poly(styrene)
PSS	Poly(styrene sulfonate sodium salt)
PVS	Poly(vinylsulphonate sodium salt)
THF	Tetrahydrofuran
TPPS	Meso-tetrakis (4-sulfonatophenyl) porphine
TRITC	Tetramethylrhodamine isothiocyanate
VL-PDDA	Very low MW poly(diallyldimethylammonium chloride)

1 INTRODUCTION

The development of novel remotely addressable materials is a challenging and promising facet of materials science which attracts much interest from other fields such as chemistry, aeronautics and health sciences where, for reasons dictated by nature's laws, certain events must be triggered without disturbing the medium between the addressed material and the source of the trigger. Living cells, for example, possess complex biochemical mechanisms involved in the recognition, internalization and processing of elements in their environment. Tricking cells into interacting with materials they have not evolved to deal with is an extremely difficult task; even if an alien substance is uptaken be a cell, it will most probably be degraded or excreted immediately after entering it. Yet, it is an endeavor worth investing efforts into since a great deal of indispensable knowledge can be obtained by working with cells and tissues such as the molecular requirement for the development of new drugs, sensors and actuators. To obtain the most from cell and tissue experimentation, one should be able to deliver a substance in the cell in a remote way, using means intended to minimize the stress inferred that might cause cell death or behavioral changes. Microencapsulation systems in which substances can be loaded and later released in response to a given stimulus are an ideal tool for intracellular studies since the capsules' shell can be modified to incite cellular internalization while smuggling a cargo cells would not normally accept.

Polymeric microcapsules are constructed using the Layer-by-Layer (LbL) method, [1] which consists of alternatively depositing oppositely charged polyions on a substrate to produce multilayered films held together primarily by electrostatic interactions. The LbL coating technology is an important technique that comes with a range of opportunities for the fields in need of stimuli-responsive materials. Originally meant as an alternative to conventional methods of producing multilayer coatings on flat substrates, the LbL technique was rapidly adapted to coat colloid particulate, which could be subsequently decomposed to produce hollow polymer shells. [2-4] For the past decade, polyelectrolyte nano- and micro-capsules have attracted much interest due to the vast number of materials that can be used as template and shell constituents as well as for the ease with which such shells can be functionalized. Furthermore, the majority of polyions possess intrinsic stimuli-responsive properties that are then transferred to microcapsules. These properties are currently largely based on the polyelectrolytes' sensitivity to solution properties such as pH, temperature and ionic strength.

Amongst the various physical properties of microcapsules, shell permeability is perhaps the most interesting and complex. [5-8] Polyelectrolyte capsules are essentially semi-permeable membranes with selective permeability to certain molecules. [9] The permeability of polymer-based thin films can be affected by various stimuli, direct and indirect in nature. Encapsulation of a substance that initially permeates the LbL microshells can be accomplished by increasing the wall density, either chemically (*i.e.* forming cross-links in the shell) or by physical means. The latter involves decreasing permeability using one of various strategies which include solvent exchange, [10,11] high temperature [12-15] and pH. [16-18] Control over thin film permeability is an area of intense research that is directly connected to applications involving encapsulation and release of materials. Methods of permeability control for microcapsules include various proximal factors that require direct interaction with microcapsules, such as inducing mechanical damage to the shells or altering the solution conditions. However, it is preferable to avoid such *proximal* factors for encapsulation and release when investigating biomedical applications as they tend to be detrimental to cells and tissues. [19] Consequently, microdelivery systems with intelligent designs that can be addressed with *external* factors that need not to be mediated through the solution would be useful. For example, non-destructive remote release of encapsulated materials could be performed using microcapsules with a built in sensitivity to triggers such as magnetism, ultrasound, microwaves and light. The latter is particularly interesting because a large variety of materials interact with light, giving rise to a broad range of potential optical responses to functionalize microshells with.

Light-responsive microcapsules were first introduced in 2004 by the group of Sukhorukov (Max Planck Institute of Colloids and Interfaces, Germany) and similar work by the group of Caruso (Melbourne University, Australia) followed. [20,21] Since then, most work on this topic has involved functionalizing microcapsules with nanoparticles of noble metals to render the microshells sensitive to light. The interest in nanoparticles such as gold and silver for light addressability lays in their ability to convert a photon's energy to thermal energy due to a property known as surface plasmon resonance (SPR). Providing sufficient energy in the form of light, it is possible to transform such nanoparticles into heating centers that can disrupt the microcapsule wall freeing the encapsulated content. [22] Sukhorukov *et al.* showed that it is possible to implement metal-polymer composite microcapsules for use in the presence of living cells, introducing remotely addressable microcapsules to the biomedical field. [23] This discovery was followed by less than a dozen studies, which all suffered from various technical difficulties and unsolved questions with regards to both capsules and cells.

The most important limitations to further progress with regards to optically addressable microcapsules are: (1) the nanoparticles used have a **poor absorption** at near-infrared wavelengths where living cells are least affected, because of this (2) a **large nanoparticle concentration** has to be inserted in the shell to maximize the laser-induced opening capability, (3) the capsules typically **explode** due to the uncontrolled heat release resulting from the large nanoparticle content requirements, and (4) **no alternative** light responsive material to metal nanoparticles has been investigated. Issues which concern primarily cells are: (5) the capsules **localization** inside the cell after internalization is unknown, (6) it is unclear whether cells can **survive or divide** after internalizing capsules and/or releasing their cargo inside the cells, and finally (7) the parameters to improve the **mechanical stability** of capsules and prevent them from deforming upon cellular uptake have not been studied. Despite the fact that previous work has shown the feasibility of constructing light addressable polyelectrolyte microcapsules there is surprisingly very little known about the mechanical properties, physical characteristics and ideal conditions for using such systems in the context of micro-encapsulation and delivery vehicles.

The aim of this thesis consists in investigating the optically addressable composite shells with regards to the issues mentioned above and to explore new light-responsive materials that could be used to sensitize polymer microcapsules to light. The three key types of microcontainers that are the subject of the present work are summarized in Figure 1.1 where the oppositely charged polyions constituting the capsule wall are represented as orange and blue and metal nanoparticles are depicted as red circles. The first approach depicted in the left column (**A1**) illustrates a polymer-based microcontainer whose shell permeability to a molecule is decreased by exposure to light. The middle column (**A2**) shows the light-induced release of an encapsulated substance from a microcapsule using shells that are not functionalized with nanoparticles. Finally, on the right (**B**), a development that is particularly important consists in finding a way to release materials from metal-polyion composite microcapsule without bursting the shell, preferably at low laser intensity of using infrared irradiation as opposed to visible light. Furthermore, the mechanical properties of nanoparticles-functionalized microcapsules need to be investigated in order to determine the role of nanoparticles on shell stability. Because of the enormous number of existing light sensitive materials, the amount of work necessary to develop the new microcapsules was reduced by focusing on the use of the well characterized PDDA/PSS and PAH/PSS polyelectrolyte shell structures.

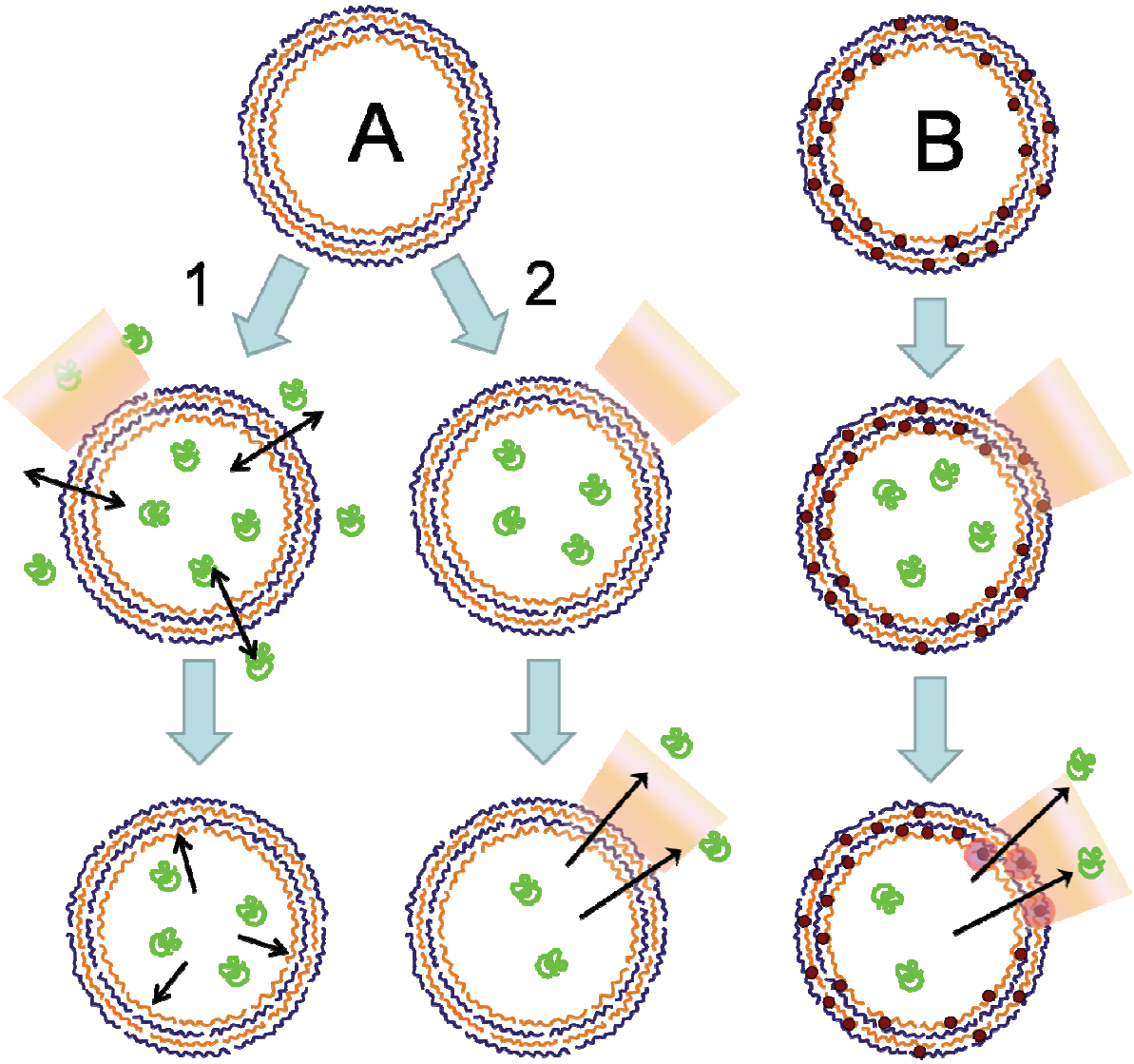

Fig. 1.1 Scheme of the light addressable microcapsules sought for this thesis: the development of light-induced encapsulation (A1) and release (A2) microshell systems lacking metal nanoparticles and investigate approaches to release material from metal-containing shells in a non-destructive manner(B).

2 LITERATURE REVIEW

This chapter provides the scientific basics for the reader to better understand the nature and properties of the system investigated.

2.1 POLYELECTROLYTES

The term polyelectrolyte refers to molecules constituted of charged or ionizable monomer units and low molecular weight counterions that maintain electrical neutrality. Charged polymers are omnipresent in nature and their special structures are at the very foundation of biological processes in the form of polypeptides and DNA. They can be separated as polycations and polyanions depending on their charge as well as polyampholytes if the polymers contain both negative and positive functional groups. Zwitterionic polymers can alternate between cationic and anionic forms. [24]

Addition of polyelectrolytes to a polar solvent generally leads to the dissociation of the ions from the charged groups. Solubilization occurs even if the polymer main chain is hydrophobic and the extent of solubility depends largely on the charge density and dissociation constant of the ion pair concerned. Polyelectrolytes can be classified as strong when they are charged at most pH values, and as weak when they are partially dissociated over a large pH range. In dilute solution, an ionizable molecule obeys acid-base equilibrium such that the ion pair *HA* may reversibly dissociate into cationic and anionic constituents.

Eq. 2.1 $$HA \leftrightarrow H^+ + A^-$$

In the case of weak polyelectrolytes, however, the dissociation behavior at each ionizable unit is influenced by that of their neighbors. [25] In addition, the conditions to which different portions of the polymer are exposed typically vary since different conformations are possible and units at the ends of middle may further influence dissociation. Therefore, unlike a simple acid or base, weak polyelectrolytes display a broad equivalence point defined by an apparent pK_a that can span several pH units. [26] For a weak polyelectrolyte an apparent equilibrium constant of acidity ($K_{a(app)}$) can be described,

Eq. 2.2 $$K_{a(app)} = \frac{[H^+]+[A^-]}{[HA]}$$

where brackets denote the concentration of each species. The degree of dissociation (α) corresponds to,

Eq. 2.3 $$\alpha = \frac{[A^-]}{[A^-]+[HA]}$$

Equation 2.2 and 2.3 can be combined to describe $K_{a(app)}$ as a function of pH using a modified version of the Henderson-Hasselbalch equation taking into account the charge density along the polymer chain with the empirical parameter *n*:

Eq. 2.4 $$pK_{a(app)} = pH - n \cdot \log\left(\frac{\alpha}{\alpha - 1}\right)$$

The conformation of a polyelectrolyte in solution depends on its concentration, molecular weight and on the solvent used just as for any other polymer, in addition to its linear charge density, counterions, and the dissociation constant of its ion pairs. Polyelectrolytes are expected to adopt an elongated conformation as a result of the strong repulsive forces between same-charge groups along the main chain, which act by forcing the polymer's constituent units apart.

Long polymers can adopt a large number of conformations that can only be described statistically. Hence, it is difficult to predict the average polyelectrolyte conformation in aqueous media using theoretical models. Two models that are often used to describe the average conformation of flexible neutral polymers in dilute solution are the Freely-jointed-chain model and the Gaussian model. While they differ in their assumptions with regards to bond length and joint angles, the two models state that the mean-squared end-to-end radius (R_{ee}) is proportional to the number of monomer units (N) in the polymer chain multiplied by the monomer size (a): [27]

Eq. 2.5 $$\left\langle R_{ee}^2 \right\rangle = Na^2$$

Equation 2.5 appropriately describes uncharged polymers because R_{ee} is typically much smaller than the length of the extended polymer. However, this simplistic relationship does not

take into account steric effects from adjacent side chains and excluded volume effects from non-adjacent monomers. Polyelectrolytes are therefore best described in terms of persistence length (q_p), which is a measure of the stiffness or relative length of a charged polymer in solution. The persistence length of a polyelectrolyte depends on the electrostatic interactions between monomer and on the counterions present around it. The stiffness is given by the sum of the steric length (q_0), which corresponds to the persistence length of an equal length uncharged polymer, and the electrostatic contribution (q_e):

Eq. 2.6 $$q_p = q_0 + q_e$$

The electrostatic contribution is described as,

Eq. 2.7 $$q_e = \frac{l_B}{4}\left(\frac{\kappa^{-1}}{l_{eff}}\right)^2$$

where l_B is the Bjerrum length, κ^{-1} is the Debye length and l_{eff} is the effective distance between charges. [28] The Debye length describes the spherical volume around a charge where an effective charge screening occurs. The Bjerrum length is the distance at which the columbic interaction between two unscreened elementary charges e in a dielectric medium is equal to the thermal energy K_BT as per,

Eq. 2.8 $$l_B = \frac{e^2}{4\pi\varepsilon_0\varepsilon_R k_B T}$$

where ε_0 and ε_R are the absolute and relative dielectric constants. As an example, for two singly charged ions in water (ε_R = 80) at 300 K, $4\pi\varepsilon_0$ is equal to 1 and l_B = 0.7 nm. In presence of polyelectrolytes, it may be energically favorable for a counterions cloud to form due to competing forces between gaining enthalpy by combining with the polymer and losing entropy by being removed from water. In fact, counterions can condense on the polyelectrolyte if the distance between charges is smaller than the Bjerrum length decreasing its effective charge density.

The impact of ionic strength (I) on the electrostatic persistence length (Eq. 2.7) of a polyelectrolyte in solution is found by measuring the Debye length:

Eq. 2.9 $$\kappa^{-1} = \sqrt{\frac{\varepsilon_0 \varepsilon_R k_B T}{2 N_A e^2 I}}$$

where N_A is Avogadro's number.

The ionic strength of the solution in turn is defined as,

Eq. 2.10 $$I = \frac{1}{2} \sum_i z_i^2 c_i$$

with z_i corresponding to the charge valency, c_i to the concentration of ion species *i*. Therefore, as the concentration of screening ion increases (Eq. 2.10), the Debye length decreases (Eq. 2.9) and the persistence length decreases (Eq. 2.5). In other words, while the conformation of polyelectrolytes tends to be elongated in solution at relatively low ionic strength, the addition of electrolytes makes a coiled conformation more favorable.

2.2 POLYELECTROLYTE COMPLEXES

Oppositely charged polyelectrolytes form complexes when mixed in solution following relationship:

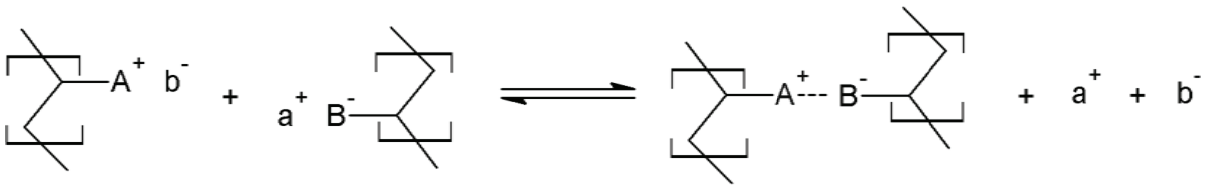

While Coulombic and hydrophobic interactions may be involved in the aggregation process, the driving force for polyelectrolytes' complexation is the entropy gained from the release of counterions a^+ and b^- in solution. The 1:1 stoichiometric ratio between cations and anions is usually found in complexation between two strong polyelectrolytes. This ratio varies for weak polyelectrolytes in accordance to the relative charge densities and solution conditions. Both polyelectrolyte types are affected by moderate to high salt concentration, however, since charge screening by counterions decreases persistence length resulting in fewer exposed charges. Hence, the structure of the complex also depends on the polyelectrolyte's conformation prior complexation.

Two models have been proposed to describe the structure of polyelectrolyte complexes in solution (Figure 2.1). The *stretched* conformation where oppositely charged polyelectrolytes stack parallel to each other is favored at low ionic strength when the polyelectrolytes have a longer persistence length. Otherwise, the *entangled* conformation is favored leading to a high degree of interdigitation between the polyelectrolytes and a large proportion of charges left uncompensated for. In reality, one should expect a statistical distribution of both types of complexes to co-exist in solution that can be shifted either way by adjusting the solution parameters.

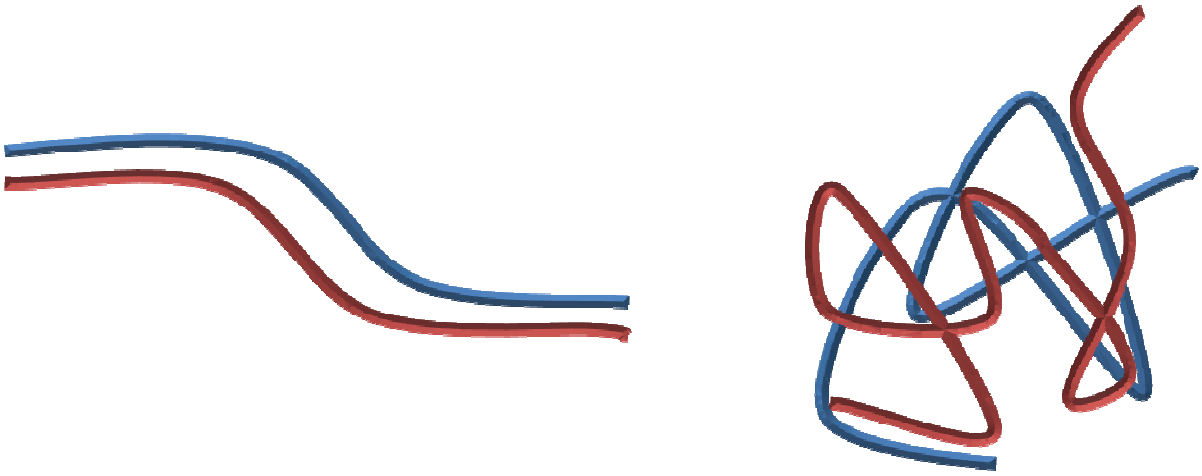

Fig. 2.1 Scheme illustrating the idealized conformations of polyelectrolytes in solution, a *stretched*-type (left) and *entangled*-type (right) polyelectrolyte complexes.

At the macroscopic scale, polyelectrolyte aggregation can result in the formation of soluble or insoluble complexes (the latter of which leads to precipitation), or in an in-between where complexes remain soluble but are large enough to scatter light making the solution appear turbid. Soluble complexes are found mostly in non-stoichiometric mixtures of polyelectrolytes with very different molecular weights where the smaller polymer is in excess and acts by completely screening the larger one. Flocculation occurs mostly for polymers of similar lengths where complete screening of any charged species is not kinetically favored, leaving complexes with differently charged areas that can further aggregate with one-another. The rate-limiting step for complex formation is defined by polymer diffusion. Once complexed, the polycation-polyanion pairs are in a non-equilibrium state and it was shown that exchanges of polymers between complexes occur. [29] Addition of salt or modification of the pH can lead to a secondary

form of aggregation due to charge screening or, at high salt concentration, to the complete disassembly of aggregates. [30]

2.3 POLYELECTROLYTE MULTILAYERS

The absorption of polyelectrolytes at surfaces depends on a variety of parameters including charge density, molecular weight and conformation of the polymers as well as the properties of the surface such as charge sign, charge density and topology. In addition, the solvent's pH and ionic strength play important roles in the absorption of polyelectrolytes at interfaces.

2.3.1 POLYELECTROLYTE ABSORPTION ON A SOLID SURFACE

Just as in the case of polyelectrolyte complex formation, polymer diffusion in solution is the rate limiting step for the absorption of polyelectrolytes at interfaces. On the other hand, the structure of the film created during absorption depends largely on the conformation of the polyelectrolytes in solution, and thus on the ionic strength of the solution. Using a polyelectrolyte solution containing a very low ion concentration favors the deposition of a thin film since the polymers absorb on the oppositely charge surface in a stretched form. Under such circumstances, most charges along the polyelectrolyte pair up with an opposite charge partner at the surface. In contrast, a polymer absorbing in coiled conformation is unlikely to fully deposit on the surface and will instead show non-absorbed chain sections called "loops" and "tails" (Figure 2.2). A tail is found when the polymer's end section dangles in solution while loops are mid-chain sections that are not in contact with the surface. These features exist primarily because absorption is faster than rearrangements can occur in the entangled coiled polymer. Electrostatic repulsion and steric effects are likely contributing to the absorption of only certain sections of the polyelectrolyte. Since thin films are the product of a large number of polymers, the formation of tails might also happen because the surface adjacent to the end of a polymer is already occupied by another polyelectrolyte. The presence of loops and tails in a polyelectrolyte coated surface results in a polymer film with the charge sign opposite to that of the substrate. This effect known as "charge overcompensation" is the key requirement for the creation of multilayer systems using the Layer-by-Layer technique.

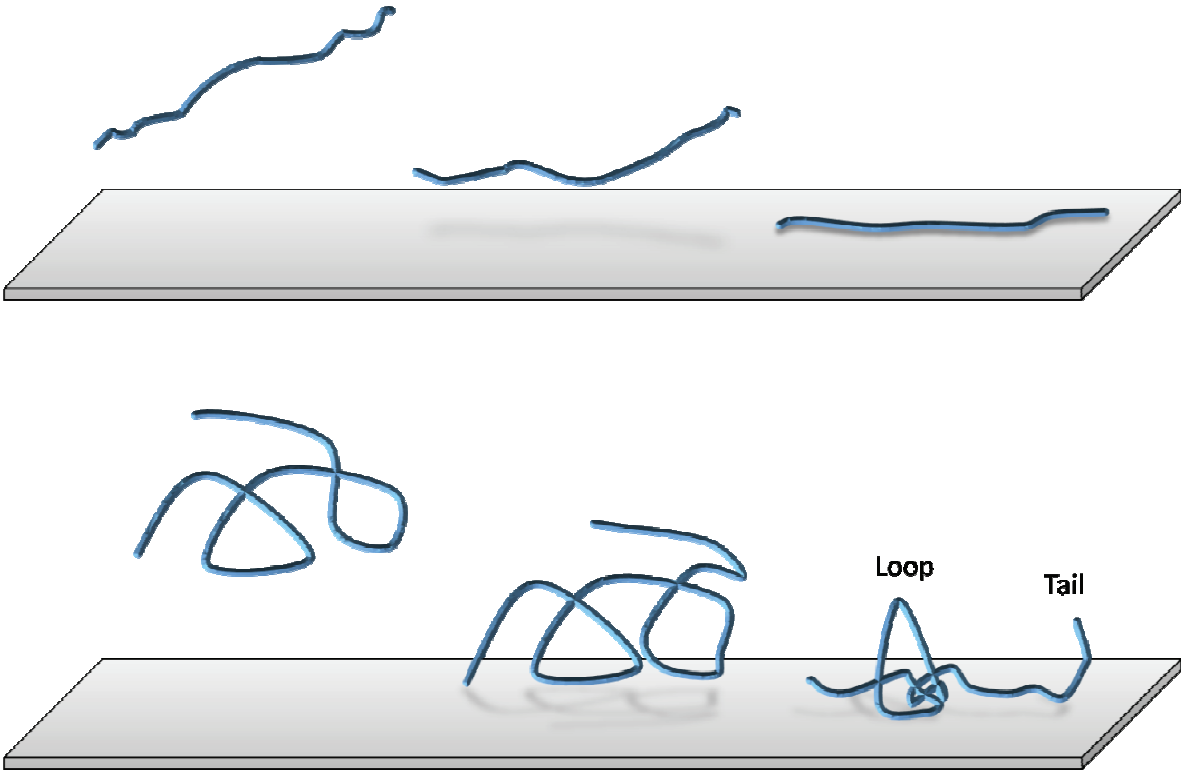

Fig. 2.2 Schematic of a polyelectrolyte's absorption at a charged surface, (top) in a rod-like formation and (below) in a coiled conformation as they deposit onto an oppositely charged substrate. When absorption is complete, polymer sections that are incapable to bind the substrate termed "loops" and "tails" form resulting in charge overcompensation.

2.3.2 LAYER-BY-LAYER POLYELECTROLYTE ASSEMBLY

The LbL assembly technique is based on depositing oppositely charged polyelectrolytes onto a charged substrate in a sequential manner, taking care to alternate the charge of the absorbed polyion at each layer. [31] For example, in a typical LbL procedure a negatively charged surface would be dipped in a solution containing salt and a polycation. After some minutes the substrate is removed from the solution and rinsed with distilled water to remove any polyelectrolyte that has not properly absorbed at the interface. The substrate, now coated with a film exhibiting an excess positive charge is transferred to a solution containing salt and a polyanion. After a few minutes, the substrate is once again washed and finds itself now coated with of a thermodynamically stable polyelectrolyte bilayer. The treatment of a template with

the *polycation/wash/polyanion/wash* sequence of events may be repeated as many times as necessary to produce a film of desired thickness. Films constituted of up to 1000 layers have been constructed. [32] Polyelectrolyte multilayers are deposited at larger scales using the spaying [33] and spin coating [34,35] techniques.

To assure uniform coverage, the polymer concentration necessary for the LbL assembly typically needs to be in excess relative to the area of the coated surface. The gradual removal of polyelectrolytes from the dipping solution should also be taken into account when multilayers are constructed and might necessitate the preparation of fresh solutions or the use of higher concentrations to insure that a sufficient amount of polyelectrolyte is present to uniformly coat the substrate at later deposition stages. The thickness of each layer can be tuned from a few angstroms to some nanometers depending on the solution conditions and the materials used in the assembly. The classical LbL polyelectrolytes are synthetic in origin but "natural" polyelectrolytes have also been used in the construction of polyelectrolyte multilayers such as DNA, polypeptides and polysaccharides.[36,37] Also, various materials were successfully inserted in LbL films to create composite multilayer films often with special properties. Such functionalizing agents include quantum dots, [38] metal nanoparticles, [39-42] dyes [21,43,44] and carbon nanotubes. [45]

2.3.3 STABILIZING INTERACTIONS WITHIN MULTILAYERS

Despite the enthalpy contributions from the electrostatic interactions arising during the complexation of oppositely charged polyions, the driving force for each layer deposition is entropy and the thickness of each layer is limited by electrostatic repulsions between like-charge polyelectrolytes. Nonetheless, it has been proposed that a minimum charge density must exist for some polyelectrolytes to absorb to a charged surface. [46] A special case where absorption of a polyion occurred below the minimum charge density [47] suggests that the strength of the electrostatic interaction is of greater importance than the earlier proposal of a charge density threshold. It was previously mentioned that the presence of ions in the polyelectrolyte solution is necessary to obtain proper charge overcompensation and allow the next layer to absorb. The washing step between layer absorptions not only removes free polyelectrolytes but also takes ions that were associated with the polyion in solution out of the film. This results in a more compact layer with a greater ratio of electrostatic interactions than in presence of salts which screen some of the interactions, swelling the multilayers. [48]

However, as long as a sufficient number of polyion pairs are present, the film remains stable. Adding salt in high concentration inevitably results in excessive screening within the film, potentially leading to its disassembly. The effect of ionic strength on the ratio of polyelectrolyte ion pairs in the multilayer film is expressed by the following relationship, where the left side illustrates the polyion pair held by an electrostatic bond and a^+ and b^- represent ions added to the solution. [49]

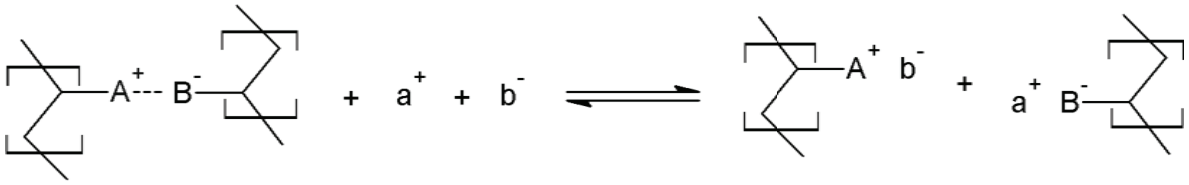

High salt concentration decreases the electrostatic interactions forcing the polyions to adopt the thermodynamically favored conformation and returning to the bulk solution. In other words, while the polyions adopt a compact, thin structure when sandwiched between oppositely charged polyelectrolytes, the addition of ions relaxes their conformation by loosening the electrostatic interactions up to a point where the latter are too few to keep the polyions from desorbing. The electrostatic contribution is therefore more important in terms of layer stability than in its formation.

Additional energy may be gained from the contribution of weak interactions such as hydrogen-bonding and hydrophobic interactions between polyelectrolytes. [50] Kotov *et al.* suggested that polyelectrolyte complexation could not occur without the contribution of short range Van der Waals interactions. [50] The contribution of hydrophobic interactions was also shown to play role in film stability. [51] The assembly of LbL multilayers using only hydrogen bonding interactions was shown for several polyion pairs. [52,53] The assembly of same charge polyelectrolyte multilayers held together only by hydrogen bonding was also shown to be possible. [52,54]

2.3.4 FILM GROWTH

The thickness increment after each polyelectrolyte addition was shown to vary differently according to the polymer used. The film growth of multilayers consisting of most polyelectrolytes, especially in the case of strong polyelectrolytes tends to increase linearly, meaning that the absorbed mass of a given polyelectrolyte is nearly constant at each layer. [55,56]

On the other hand, the film growth of some weak polyelectrolyte such as biopolymers was shown increase exponentially as layering progresses. Exponential growth occurs due to the ability of at least one of the constituent polymer to diffuse through the LbL film increasing the mass of previously absorbed layers. [57]

According to the *zone model* the multilayer film structure consists in three distinct regions named *Zone 1* to *Zone 3* each having a well-defined set of properties. [58] *Zone 1* is the first layer, in contact with the substrate, which thickness is typically lesser than subsequent layers. *Zone 3* is the last layer, exposed to the bulk solution, which is defined by an excess charge and a penetration depth that can be understood as irregularities in the film through which polyelectrolytes can penetrate beyond *Zone 3* and diffuse to layers in *Zone 1* or *Zone 2*. As previously mentioned, this form of diffusion leads to exponential film growth but it may become saturated as layers grow thicker changing the film growth profile to linear. [59,60] *Zone 2* is therefore the intermediate region where no net charge should exist. *Zone 2* determines largely the relative permeability and mechanical stability of LbL films.

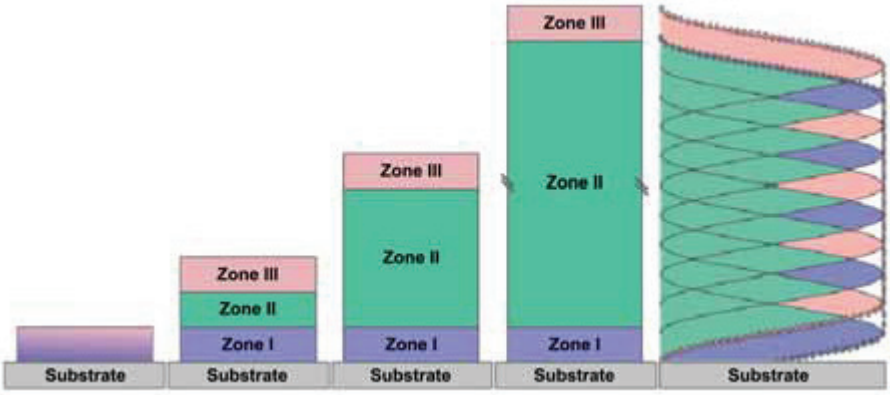

Fig. 2.3 Zone model illustrating the growth of polyelectrolyte multilayers. From left to right, this model shows the progressive evolution of the three different zones in a 10 layer film. Reprinted from [61].

2.4 POLYELECTROLYTE MICROCAPSULES

In the 1990's Decher and the group led by Möhwald (MPI-KG, Germany) developed the electrostatic self-assembly (ESA) procedure, by which thin films could be repetitively deposited onto a surface to produce multilayered films. [1] This method was first proposed by Iler *et al.* in 1967. [62] Unlike multilayer films obtained by other well-established deposition technique, ESA is completely indifferent to the type of substrate used, so long as it is charged. The driving force of ESA resides in creating a surface charge excess, or overcompensation, at the interface of a material of interest. ESA could additionally be used on non-planar surfaces and eventually became known as the Layer-by-Layer technique. [4] Microparticulate templates with various porosity and compositions can thus be LbL-coated. Providing that multilayer film is stable enough, the template can then be dissolved to yield a free-standing membrane, which in the case of a particle gives a capsule with a distinct hollow inner cavity. [2,3] LbL-based polymeric microcapsules possess significant advantages over other types of microcontainers (*e.g.* micelles, liposomes, inorganic hollow shells) notably in their mechanical behavior and for the ease with which a large number of shell parameters can be controlled to various degrees, including: shell composition, thickness, stiffness, roughness, density, hydration, diameter and permeability. Early literature on the preparation of synthetic polymer microcapsules and encapsulation of substances within microcapsules was demonstrated as early as the 1960s, with the publication of a method to stabilize droplets of organic solvents in aqueous media using polyelectrolytes. [63]

2.4.1 PREPARATION

In the late 1990s, the basics of LbL assembly were transferred to non-planar surfaces by Sukhorukov *et al.* in the form of colloidal particles. [3,4] The obvious advantage of polyelectrolyte multilayer assembly is that any charged surface may be used as a substrate, independently of its dimensions, morphology or composition. Multilayer films of various polyelectrolyte combinations can be obtained in the same way as for flat substrates with the exception that the stability of the colloidal particle suspension used requires alternative means to exchange solvents. The solution parameters are also optimized to provide the proper pH, ionic strength and polyion concentration to prevent aggregation and ensure homogeneous coating. Once the desired number of layers has been assembled, the template particle is decomposed to form hollow polyelectrolyte microcapsules. A scheme summarizing the steps for microcapsule assembly is presented in Figure 2.4.

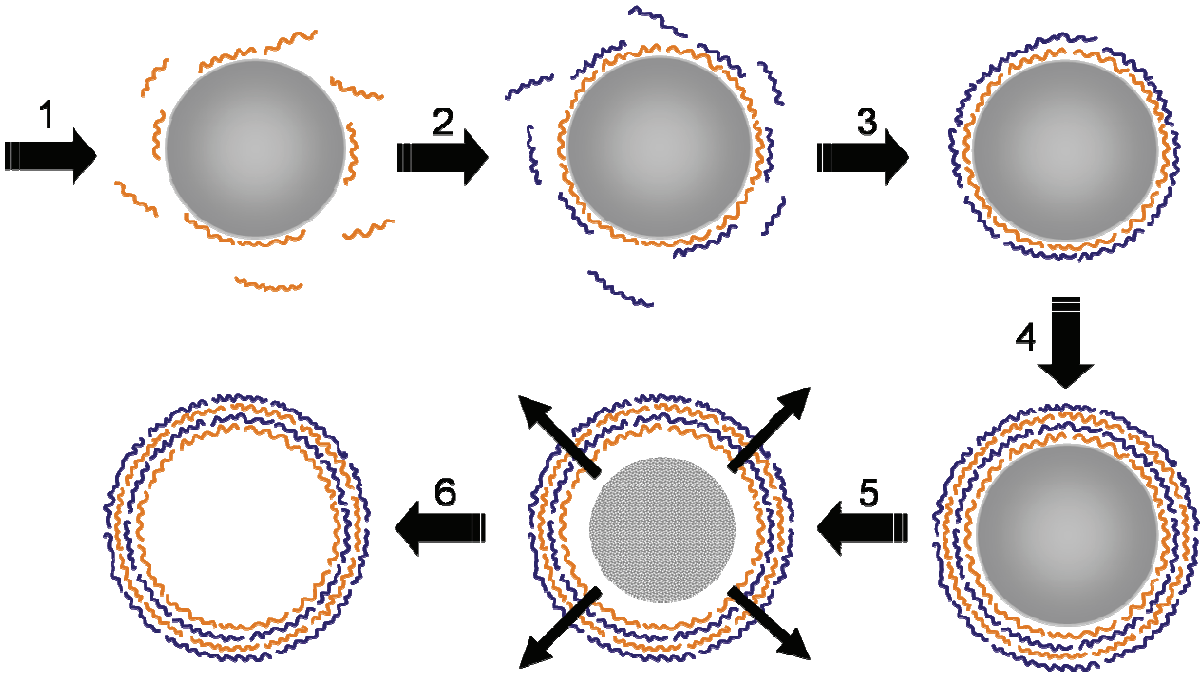

Fig. 2.4 Schematic of the general LbL assembly of polymeric microcapsules. The procedure begins by coating a charged colloid with a polyelectrolyte (1). After washing the particles, the procedure is repeated with a second polyelectrolyte of opposite charge (2) resulting in a bilayer (3). Steps 1-2 are repeated until the desired number of layers are obtained (4). The template is then decomposed (5) leaving a hollow polyelectrolyte capsule (6).

Microcapsules are constructed in solution using one of two self-assembly procedures; (1) sequential additions of polymer solution, followed by centrifugation to separate the coated colloids from the supernatant, [4] or (2) using a micro-filtration setup [64] allowing supernatant removal without the extra steps of centrifugation. Sufficient washing is necessary to remove loosely bound and non-absorbed excess polyelectrolyte in order to prevent polyelectrolyte complexes to form in solution upon the addition of subsequent layers as this would result in the formation of impurities. It is theoretically possible to add the exact amount of polyelectrolyte necessary to coat flat surfaces but this not practically feasible for microcapsules due to the fact that it is virtually impossible to precisely calculate the total surface area of the colloid particles in the suspension. [2,65]

Typical shell constituent materials to assemble polyelectrolyte microcapsules include at least one polyion, which can be any charged polymer with a sufficiently large charge density from synthetic polyelectrolytes to biomolecules such as polysaccharides and DNA. The assembly of LbL films composed of one or more layer of small or low charge density molecules can be difficult since all the charges on low molecular weight objects can easily find a countercharge, neutralizing the surface charge instead of reversing it, preventing the next layer to absorb. However, with a little help from chemistry, single component microcapsules were reported where the authors took advantage of chemical cross-linking [66-68] and "click chemistry". [69,70] These methods make it possible to fix small molecules or same charge materials into multilayer complexes, or can otherwise by used to strengthen the LbL film. Diblock copolymers were also used to produce single component microcontainers. [71] Recently, Wang *et al.* constructed thick-walled microcapsules using a mesoporous substrate [72] treated with a single layer of polyelectrolyte and chemically cross-linking the polymers before dissolving the template. [68]

2.4.2 TEMPLATE DISSOLUTION

Many different templates have been used in the preparation of polymeric microcapsules. LbL microshells can be constructed on solid particles, liquid droplets and more recently microbubbles. [73-75] The latter two template types are kinetically unstable and therefore challenging to manipulate, but may be used to stabilize multiphase systems. Solid sacrificial templates can be organic material (latexes, [2,16,76] gel beads [77,78]), inorganic micro- and nanometer sized particles (silica, [79-84] $CaCO_3$ [37,85-89]), and even living cells. [90,91] The diameter range of microcapsules constructed following this approach varies 15 nm [92] to over 1 mm. [73] The lower diameter limit is set by the stability reduction associated with coating small particles whereas the upper diameter limit is related to the osmotic pressure resulting from the decomposition of a large particle embedded into a thin polymeric wall. Osmotic effects were reduced in microshells that were cross-linked on hydrogel beads before dissolving the template. [69]

Monodisperse, weakly cross-linked melamine formaldehyde (MF) microparticles are often cited as a capsule template in the literature. [9,91] MF particles are rapidly decomposed by acidic hydrolysis with HCl (pH ≤ 1.6) or polar solvents such as dimethyl sulfoxide (DMSO) and N,N-dimethylformamide (DMF) to oligomers whose molecular weight depends a lot on the age of

the MF solution. However, it was found that the 4-14 kDa oligomers resulting from the decomposition of MF particles cannot diffuse out of the shells as rapidly as they are formed which can damage or even rupture the capsules.[93] In addition, a significant amount of residual decomposition product may remain inside the shells and in the capsule wall resulting in altered shell properties and reproducibility complications. [93,94] Other common organic particle materials are polystyrene (PS) and poly(lactic acid) (PLA) can also be dissolved in organic solvents. The latter were shown to affect the structure of multilayers and induce a swelling of the shell upon core dissolution. [16] PLA particles are also known to leave residues inside the microcapsules during dissolution. Because the films resulting from LbL assembly are typically in the glassy state, the morphology of capsules is identical to the template used. Microcapsules assembled on cells conserved their shape after the cells were dissolved for instance.

In contrast with organic materials, inorganic microparticles such as manganese and calcium carbonate ($MnCO_3$, $CaCO_3$) as well as silicon oxide (SiO_2) microparticles can be completely removed from the capsule construct during dissolution. [81,95] This is because, under the appropriate conditions these structures are turned into ions and carbon dioxide which are allowed to permeate LbL microshells with ease. While the dissolution of carbonates is accomplished in mildly acidic conditions or by treatment with ethylenediaminetetraacetic acid (EDTA), [37] these particles tend to be highly porous, polydispersed and have irregular shapes which lead to the production of heterogeneous capsule samples. By contrast SiO_2 particles are very smooth and homodispersed but their dissolution is accomplished in hazardous ammonium fluoride (NH_4F) or hydrogen fluoride (HF) solution, which can cause aggregation in the case of capsules containing weak polyelectrolytes. [13,96] Yet, due to the fact that their removal is complete and that they have little or no effect on the multilayer structure, inorganic particles are the preferred templates to prepare microcapsules meant for biomedical applications.

2.5 STIMULUS-FREE ENCAPSULATION AND RELEASE METHODS

Encapsulation methods can be categorized in two distinct groups where; (1) the desired material is incorporated in the template prior LbL assembly, and (2) by using a stimuli-responsive method to decrease the permeability of the microcapsules to a material that can initially diffuse through the shell.

Materials can be encapsulated by directly coating materials with poor solubility that can be released under certain conditions but would otherwise aggregate or phase separate. On the other hand, this approach is limited to materials with certain sizes and shapes such as crystals, nanoparticles and aggregates of particles. [79,97] Carbonated template particles offer other encapsulation strategies where materials can be (1) co-precipitated in the particles when these are formed, [37,86] or (2) by impregnating the particles with the material to be encapsulated by simple diffusion into the porous carbonate structure. [88] The LbL treatment of $CaCO_3$ particles prepared by either of these options, followed by the dissolution of the template resulted in polyelectrolyte microshells with an encapsulated substance in the cavity. Co-precipitation is most convenient to encapsulate materials that are too big to diffuse through the shell or sensitive to the conditions of standard approaches. [98] This approach was recently adapted to produce multicompartment microcapsules where a $CaCO_3$ particles co-precipitated with a substance "A" was coated with a multilayer shell, and co-precipitated in larger $CaCO_3$ particles in the presence of a substance "B", which was itself LbL coated. [99,100] By dissolving both $CaCO_3$ particles with EDTA, a shell-in-shell microcontainer resulted with an inner capsule loaded with "A" itself encapsulated within a larger capsule containing its own load "B". An SEM image depicting the general aspect of 3-5 μm $CaCO_3$ particles is illustrated in Figure 2.5A and their porous nature is shown magnified in 2.5B. Another encapsulation strategy consists in using emulsion-emulsion synthesized microgels as a template for microcapsule construction, which yields particles typically larger than other templates. [77,101] A SEM picture of a 100 μm dextran-based hydrogel bead (Dex-HEMA) is shown Figure 2.5C along with a magnified area in inset showing a smooth surface. While these approaches are sometimes favored for the ease with which they can be manipulated, they suffer from the polydispersity of the particles size and morphology.

When co-encapsulation methods are not an option, encapsulation and release of substances in microcapsules are performed using stimuli-responsive properties of the shells, which will be presented in the following sections. Such strategies are regularly used for manipulations involving microcapsules constructed on commercial microparticles such as SiO_2, PS and MF.

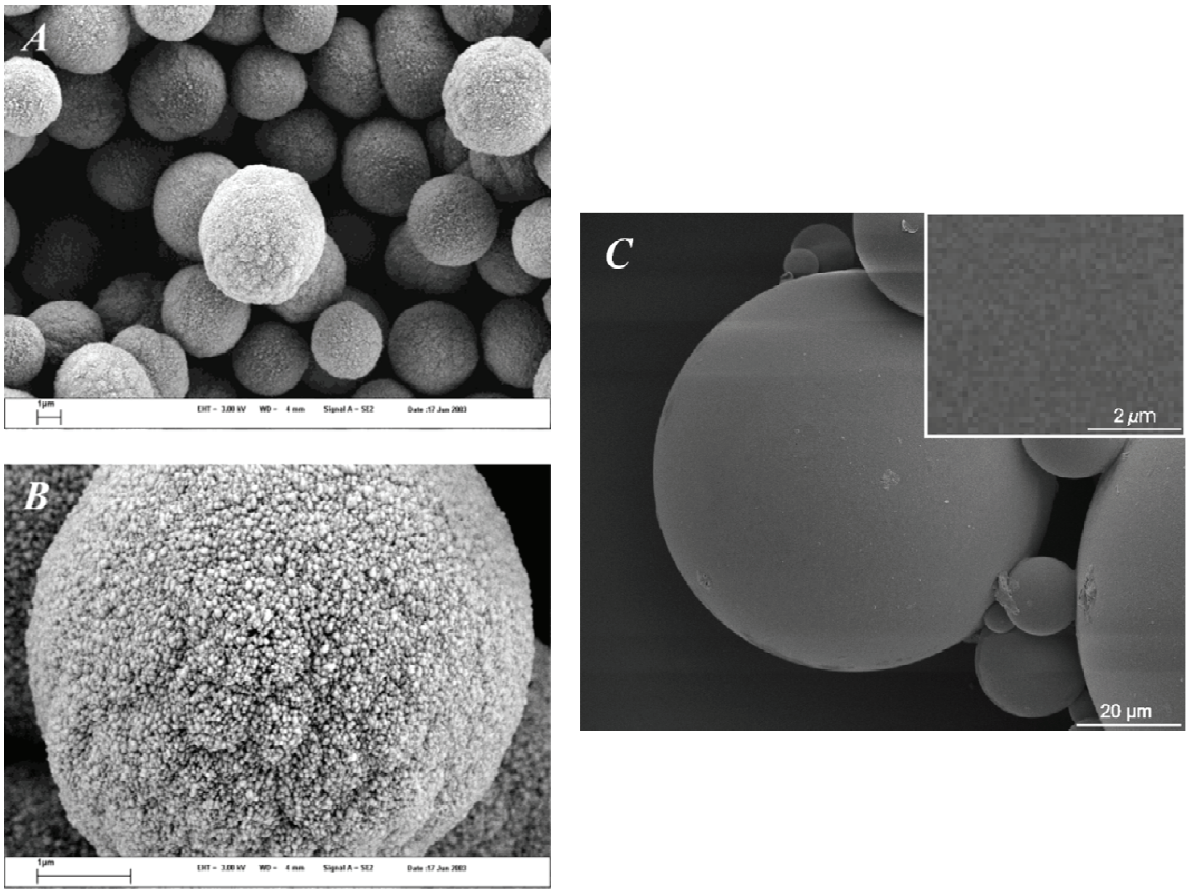

Fig. 2.5 SEM images of $CaCO_3$ and Dex-HEMA hydrogel template particles. The magnified $CaCO_3$ particle in panel B depicts the highly porous nature of such particles. Panels *A* and *B* are reprinted from [89].

Physically pressing on capsules to deform them may constitute a trivial, yet limited method to release encapsulated material, but deformability studies also revealed much information on the mechanical properties of polymeric microcapsules. [15,102] Shear stress experiments and compressing the shells with the tip of an atomic force microscope are among the tests conducted to study the mechanical behavior of polymer based microcapsules. [84,102-105] Alternatively, the permeability of microshells built from biological polyelectrolytes can be altered to release encapsulated substances by the addition (or presence) of appropriate enzymes in solution. [37,100] Small molecules were also found to accumulate inside microcapsules by preferentially binding to other materials inside the capsules, such as leftover core materials. [76,88,106]

2.6 STIMULI-RESPONSIVE ENCAPSULATION AND RELEASE

While most small ions [107] and water molecules tend diffuse freely through the semi-permeable wall of polyelectrolyte microshells, larger molecules tend to be subject to certain size restrictions. [108] Just like LbL multilayers on flat substrates, the permitted size range for diffusing molecules depends on the polyelectrolyte used, the solution conditions during assembly, the film thickness as well as the core used to prepare the capsules. [6] The various triggers that can be used to release substances from the microcapsule cavity [109] can be separated in two groups: (1) proximal triggers that need to be mediated through the solvent or require a physical interaction with the capsule, and (2) external triggers, which act directly on the microcontainer, with negligible or no effect on the solvent. Proximal stimuli are non-destructive (at the molecular level) solution parameters which include pH, temperature and ionic strength. On the other hand, external stimuli are mostly destructive radiation-based triggers used principally to destroy the capsule shell and induce release. These include light, ultrasound and microwaves. However, mild, non-destructive approaches to alter shell permeability are preferred for most applications.

This section summarizes standard encapsulation and release strategies which depend on proximal and non-optical external triggers. External triggers involving light form a distinct group of stimuli-responsive strategies particularly relevant to this thesis and will be presented in the remaining of this chapter beginning from *Section 2.7*.

2.6.1 PROXIMAL TRIGGERS

Stimuli-responsive encapsulation and release strategies are available for a broad spectrum of polyion covering weak and strong polyelectrolytes or combinations of the two. The most important proximal triggers studied to this date require softening the LbL interactions by changing the pH or ionic strength of the capsule solution, or by resuspending the shells in a different solvent. [14,16,17,110,111]

Capsules constituted of one or two weak polyelectrolytes are stable only within a certain range of pH. [16,112] PAH/PSS capsules for example were made permeable to high molecular weight poly(acrylic acid) (PAA) by adjusting the pH to 11.2 and encapsulation of an amount of PAA in the order of a few picograms was accomplished by re-adjusting the pH to acidic conditions, inciting the microcapsules to shrink and the permeability to decrease accordingly. [113] When the solution pH of such capsules is adjusted at the outer limit of the pH range for a given polyion,

the charge density decreases such that the electrostatic interaction contribution between layers decreases swelling the capsules. [114] In addition, capsules that originally formed from a fine balance of charges across the wall find themselves with an excess of one charge creating a net repulsion between the more densely charged layers. [17,115,116] The combination of both these effects induces the capsules' diameter to increase and their permeability to increase as the shell density is reduced. If left uncontrolled, microshells stored at an inappropriate solution pH can undergo irreversible structural changes or even completely disappear as the multilayers are disassembled.

Salt is also routinely used to soften the microshells and allow large molecular weight materials to diffuse into the capsule's cavity (*e.g.* to encapsulate a molecule that does not permeate the microshell). A drawback of salt addition is that capsules become quite fragile. Adding excessive salt (*i.e.* decimolar-molar range) may even result in the complete dissolution of the multilayer complex. Consequently, just as it was the case for pH variations, the influence of salt on permeability goes both ways. At low ionic strength the electrostatic interactions are weakened increasing the permeability while maintaining the capsule's integrity and structural organization. [117] At high ionic strength, shell restructuration is possible as the polyions are less dependent on their pairing partner and capsules tend to shrink as the hydrophobic part of the polymer main chain becomes a significant force that acts by reducing capsule's surface area exposed to water. [14,110,118]

Resuspending microcapsules in a polar organic solvent was also shown to significantly affect permeability. Shells treated with THF and then resuspended in water were notably thinner than prior THF treatment while their diameter appeared unaffected. [10,16] Decreasing the dielectric constant of the solvent increases the magnitude of the electrostatic interactions between the interacting polyelectrolytes, making the polymers contract. There is opposing opinions in the literature with regards to the reversibility of changing the shell permeability by solvent exchange. [10,119] Solvent exchange was used for PAH/PSS films, impermeable to the protein urease in water, but permeable in ethanol/water mixtures. [119] Once urease had diffused through shell, the capsules were simply resuspended in water, thus rendering the shell impermeable again and keeping the proteins that had diffused in the capsules encapsulated.

The impact of high temperature on LbL multilayer on flat surfaces was investigated by several groups. [59,120,121] It was shown that the rate of film growth for various polyion pairs largely

increases at high temperature and decreases back close to the initial regime when the temperature is decreased to 25°C. [59] This is analogous to the work of Garza *et al.* who demonstrated that "compartments" of specific permeability can be produced in multilayer films by changing the solution pH during LbL assembly. [122] This relationship between the effects of temperature and ionic strength increments suggests that temperature influences the polyion conformation in solution by changing its ionic activity. However, the deposition temperature was found to have a significant effect for both weak[123] and strong[124] polyelectrolytes, suggesting instead that temperature might significantly affect secondary interactions rather than electrostatic interactions alone.

Until the impact of heat on polymer microcapsules was thoroughly investigated by Köhler *et al.*, [13,15,125-129] the general understanding of this subject was quite limited and little had been done despite the large changes observed with minor temperature variations. At elevated temperature, capsules can either shrink or swell depending on their constitution. Capsules can respond to temperature treatment by shrinking providing that they contain an even number of layers and the appropriate solution conditions are present. [128] Shrinking also results in a decrease in shell permeability due to the capsules' wall becoming thicker and denser (Figure 2.6), [120,126,127,129-131] and occurs for capsules containing weak and/or strong polyelectrolytes. In the absence of salt, neither process occurs at room temperature because the polyions are in a glassy state where it is not possible for them to change conformation. Above the glass transition temperature (T_g), the polyelectrolyte main chain is more flexible and structural reorganization is possible. Through well-supported empirical studies, Köhler *et al.* demonstrated that temperature-induced swelling and shrinking is in fact due to the balance between two forces in the LbL capsules upon annealing: (1) the hydrophobic force arising from the polyelectrolyte main chain and (2) the electrostatic force which is driven by the repulsion between like-charge polymers within the shell. [127,128] If the net charge within the wall is close to neutral, the electrostatic force is assumed to be negligible since most charges are paired with another charge. Heating microcapsules in these conditions results in the shells shrinking to minimize the surface area exposed to the solvent. If the number of charges within the shell is uneven, by having a capsule built with an odd number of layers for example, the hydrophobic force is negligible and electrostatic repulsions throughout the wall incite the polyions to stretch and move away from each other. The result is swelling which may induce the capsules to rupture.

An important advantage of the heat treatment encapsulation approach is that the mechanical properties of the LbL multilayers are greatly improved in terms of stiffness, making the thermally shrunk capsules more resistant to deformation. [15,132] Capsules may become thermo-sensitive by loading them or functionalizing them with thermo-responsive materials. For example, poly(N-isopropylacrylamide) (PNIPAM) was encapsulated in PAH/PSS microshells in an effort to study the effect of heat on a thermally sensitive molecule in a confined space. [133] The effect of high temperature on the morphology and mechanical properties of composite polyelectrolyte shells, however, were unknown prior the present work.

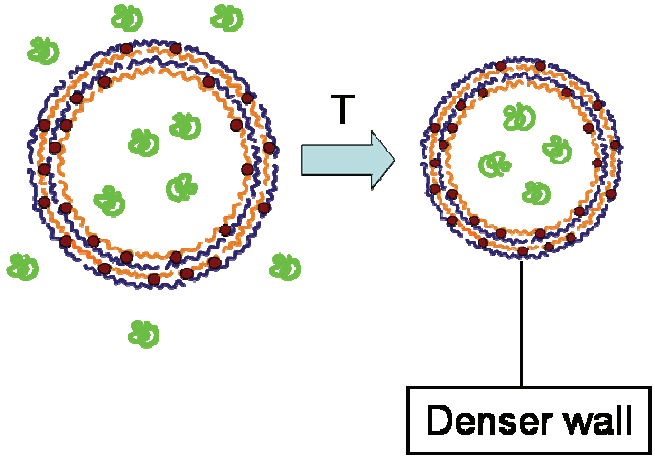

Fig. 2.6 Schematic of the thermal encapsulation process in microshells containing nanoparticles Incubating microcapsules with a molecule (green) that permeates the shell results in the shrinking and densification of the shell, correspondingly decreases its relative permeability.

2.6.2 NON-OPTICAL EXTERNAL TRIGGERS FOR RELEASE

External triggers with the ability to affect microstructures come in the form of magnetism as well as in three flavors of electromagnetic waves; ultrasound, microwaves and light (Figure 2.7). The development of microcontainers highly sensitive to any of these triggers has important implications, especially in the fields of health and surface sciences, where oftentimes microdelivery systems cannot be addressed with proximal triggers. In general, the magnetic force is used primarily to localize and visualize materials that contain magnetic or

paramagnetic constituents. [100,134] Lu *et al.* were able to use an alternating magnetic field to change the permeability of microcapsules impregnated with Co-Au core shell nanoparticles. [135] The magnetic force in this case, made the nanoparticles to rotate damaging the shell, irreversibly increasing the wall permeability by creating holes in it. A similar example of release of encapsulated material using magnetism as a remote trigger was demonstrated very recently by Hu *et al.* [136] Magnetic microcapsules with an anti-cancer drug could allow the medical practitioner to position and localize the microcontainers around a target area of sick tissue, minimizing the dose necessary and the corresponding side effects of the treatment. [137]

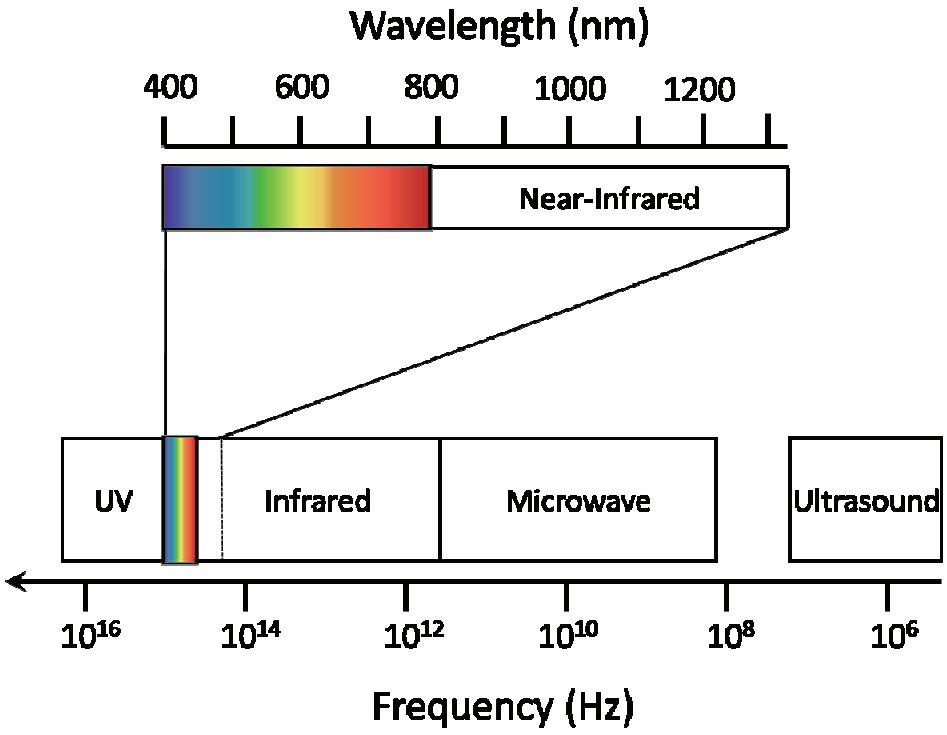

Fig. 2.7 Electromagnetic wavelengths used for wave-sensitive microcapsules. The enlarged region is the portion investigated in the present work.

Ultrasound radiation with frequencies in the order of kilo and mega Hertz (20 kHz- 10 MHz) are extensively used for the synthesis of nanomaterials [75,138] as well as for imaging and diagnostic purposes in medicine. [139] Ultrasound can lead to the cavitation and collapse of microbubbles from dissolved gases, a highly energetic process with the capability of breaking molecular bonds. [140] Taking advantage of this effect, ultrasound was recently introduced as an

alternative approach to release encapsulated materials from polymeric microcapsules. [141] Microwaves on the other hand, possess shorter waves than ultrasound spanning electromagnetic frequencies between 0.3 GHz and 300 GHz.

Microwaves have more subtle interactions with matter than ultrasound although they are not energetic enough to ionize matter. It was recently shown that microwaves can be used to control the aggregation of proteins. [142] Gorin and coworkers demonstrated that low intensity microwaves (2-8 GHz) can lead to the destruction of LbL microcontainers. [143] The destructive effect of microwave exposure was especially strong in shells that contained silver nanoparticles. This nanoparticle-microwave interaction could be another promising approach to remotely affect the properties of capsules.

2.7 OPTICAL EXTERNAL TRIGGERS FOR RELEASE

Light radiation with wavelength in the range 200-1200 nm is the most studied type of remote trigger used with polymeric capsules. One of the prominent applications of microcapsules is intracellular delivery and release. [40] In this regard, the optical, or more specifically near-IR spectral range (~ 750-1200 nm) is one of the most biologically friendly regions of the electromagnetic spectrum. One of the emerging priorities of recent research on polymeric microcontainers has been to control their permeability using mild external triggers such as light. The few investigations on this topic have been largely limited to the study of polymer-nanoparticle composite shells designed to release encapsulated substances.

2.7.1 ULTRAVIOLET-RESPONSE

The main constituents of LbL microcapsules are polymers consisting primarily of atoms of oxygen, carbon, nitrogen and hydrogen held together by covalent bonds. Far-UV irradiation ($\lambda < 200$ nm) is energetic enough to ionize covalent bonds of such polymers (and most molecules around them) and, therefore, polymeric microcapsules absorb irradiation at far-UV wavelengths. Laser ablation, the thermodynamic process by which bonds within molecules are broken upon absorption of photons, is common when exposing organic material to ionizing energy. [144,145] But the underlying mechanisms of polymer ablation under far-UV irradiation are highly unspecific and destructive towards organic materials, [146] so that far-UV is not a particularly attractive source of irradiation to control the encapsulation and release of fragile

structures such as polyelectrolyte microcapsules. At longer wavelengths (> 200 nm), specific absorption may occur in polyelectrolytes but in this case the absorption process is due to other materials or chromophores present in the capsules, such as nanoparticles or unsaturated side chains attached to the polymers. Few polyelectrolytes such as PSS and DNA, which are used in the construction of LbL capsules absorb in the near-UV region (~200-400 nm).

Materials with various functionalities were used to sensitize polymeric microcapsules to near-UV light. An interesting group of molecules that responds to both near-UV and visible light are azobenzenes. An azobenzene molecule contains two phenyl groups joined by a azo (N=N) bond. [147] Azobenzene groups typically respond to UV absorption by undergoing an internal rearrangement from the *trans* to *cis* (E→Z) geometrical isomer, as illustrated in Figure 2.8, top panel, but can occur also in the opposite direction. On the other hand, thermal isomerization typically occurs from the least stable *cis* to the most stable *trans* moiety (Z→E). At the molecular level, these *cis-trans* isomerizations come with significant changes in terms of molecular geometry and polarity, but they are rather weak when incorporated in macrosystems. The largest of absorbance region of azobenzene molecules is situated in the near-UV between 300-400 nm (Figure 2.8, Π→Π*) but can extend to the visible range depending on the phenyl substitution, solvent and other factors. [148] This absorption region is due to Π→Π* transitions from the benzene ring. A second less intense absorption region (Figure 2.8, n→Π*) is located at longer wavelengths. Figure 2.8 illustrates that the intensity of the two peaks varies oppositely depending on the equilibrium between the two isomers. *Cis-trans* isomerization is often reversible and it was shown very recently that lipid vesicles containing azo moieties could be made to bud into multiple vesicles upon UV light exposure and fuse with one another when exposed to green light. [149]

Diazoresins (DZR) were shown to form covalent bonds with PAA or PSS in LbL films upon UV irradiation. [150] Similarly, composite shells of DZR and PSS could be polymerized by exposure to ultraviolet light. [67] The resulting cross-linked DZR/PSS microcapsules displayed superior mechanical stability over capsules that were not exposed to light. [151,152] The incorporation of the azobenzene molecule Brilliant Yellow (BY) in LbL films of the type BY/PAH showed slow isomerization kinetics in comparison to pure azo films. [153]Additionally, isomerization in such films was irreversible whereas photodegradation was detected at low levels. The potential use of azobenzene molecules to control the permeability of microcapsules was briefly investigated. [43] Reversible isomerization of azobenzene groups in LbL films was

shown to occur in various films [154,155]including some containing the polyanion poly(1-4(4-(3-carboxy-4-hydroxyphenylazo)benzene-sulfonamido)-1,2-ethanediyl) (PAzo). [35,156] PAzo is a polyelectrolyte with carbonated azobenzene side chains and a Π→Π* absorption centered at 366 nm. This polyelectrolyte was used in the design of capsules that shrink upon UV exposure in the study of the optical properties of gold nanoparticles attached to the shell. [157,158]

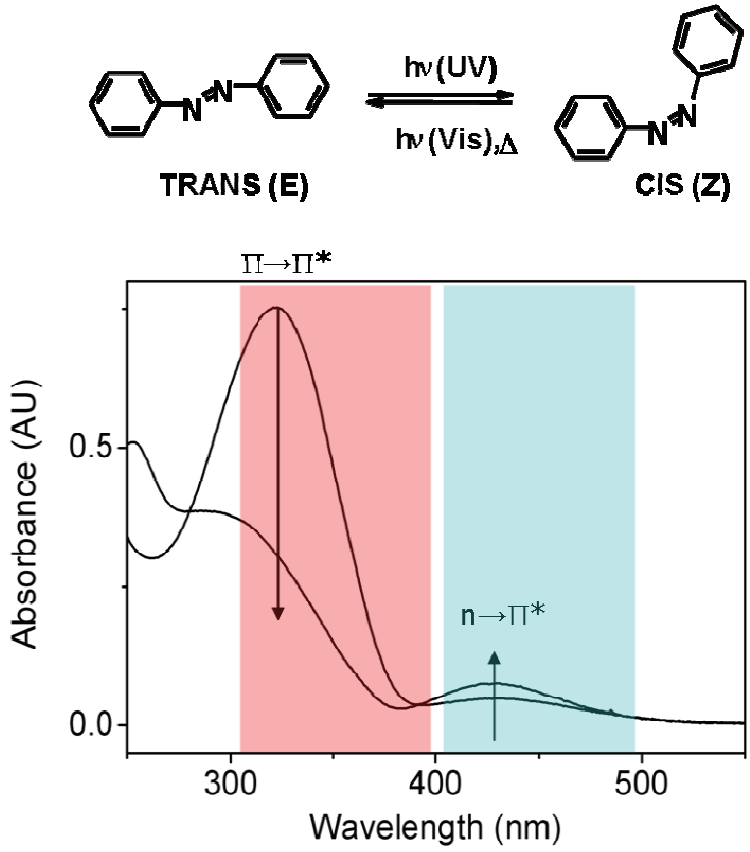

Fig. 2.8 *Trans-cis* isomerization of the parent azobenbenzene molecule. Upon irradiation, a geometrical rearrangement of the azobenzene molecule (top panel) is typically accompanied by change in its absorption spectrum.

A far more versatile approach to sensitize microshells to near-UV irradiation, however, involves impregnating polymer capsule constructs with metal oxide photocatalytic nanoparticles (*e.g.* TiO_2) to form polymer/nanoparticle composite films. Several reports have been already published on the incorporation of TiO_2 nanoparticles into microcapsules, via in-situ synthesis of the nanoparticles within films, [159,160] doping [161,162], as a component layer in LbL films [163] and as an encapsulated substance. [164]

2.7.2 VISIBLE- AND INFRARED-RESPONSE

2.7.2.1 FLUORESCENT DYES AND PHOTODYNAMIC AGENTS

Dyes are colored compounds that absorb or emit light in the visible range. Those which emit do so in various manners including phosphorescence (P) and fluorescence (F). Functional dyes are those molecules that display properties beyond color [165]. Photochromic dyes, such as reversacol for instance, reorganize and become colored or change color only when exposed to light. Photocatalysts such as chlorophyll-type molecules or materials found in photovoltaic cells lower the activation barrier of certain reactions when irradiated at the proper wavelength. These optically addressable functionalities and many others could be harvested to introduce new properties to thin films. Many functional dyes are designed to possess a high optical stability (*i.e.* fastness) making them all the more suitable for light addressable applications. Taking the inherent stability of such dyes in addition to their small size and functional versatility as a whole, it is hoped that composite films of functional dyes and polyelectrolytes offer a more precise approach to optically control the properties of thin films.

Fluorescent dyes are regularly used to visualize polymeric microcapsules. Because of the difficulties related with the permanent incorporation of small molecules in LbL films, fluorescent labels are typically inserted in the polymeric shells in their monomeric form after capsule preparation, [21,84] or covalently bound onto a polymer constituent of the shells. [166] Another consequence of incorporating small dyes in the wall of microcapsules (at any stage of sample preparation) is that they may affect the shell's mechanical and structural properties by specifically binding to sites inside the polyelectrolyte mesh. Common alternatives to organic dyes for visualization of microcapsules are inorganic fluorophores such as quantum dots. [167,168]

Although light addressable microcapsules have proved to be effective for shells doped with metal nanoparticles, the success rate of this approach depends largely on the size, shape and distribution of the nanoparticles in the shell wall. [7,40,83,169] Hence the intensity of the laser irradiation has to be varied accordingly to open the capsules. Also, the release of the encapsulated material occurs very quickly, limiting the uses for metal-containing microshells in applications where sustained release of encapsulated material is required.

The effects of photobleaching light sensitive molecules within LbL microcapsules have been briefly investigated. [21] A fluorescent near-IR dye (IR 806) was absorbed on the surface of in PAH/PSS based microcapsules. The shells were found to become severely damaged or

deformed when irradiated with CW IR at moderate intensity (830 nm, 60 mW) while capsules containing no IR 806 remained unaffected by the laser. Although these results are encouraging and useful as a proof of concept, the use of a simple fluorescent dye to damage microcapsules comes at the cost of photobleaching the dye, which is both irreversible and constitutes a source of reactive degradation products such as radicals, which are undesirable in biological applications.

Porphyrin and phthalocyanine dyes are members of the larger group of porphyrinoid (Pc) conjugated cyclic systems of methine groups, which contain 4 and 8 aza (-N=) groups within the ring system, respectively. [147] Some structures are illustrated in Figure 3.3. Porphyrins are part of the largest group of naturally occurring dyes (chlorophyll) and have strong absorbance regions between 400-500 nm. Porphyrin-type molecules are used in photodynamic therapy (PDT) and are known to induce and enhance oxidation reactions upon irradiation with light. [170,171] Due to the extensive conjugation between their four pyrrole groups (for aza[18]annulene structures), phthalocyanines display strong absorption bands in at around 670 nm (Q bands) and are essentially transparent to wavelengths between 400-600 nm. The penetration depth of red light makes compounds that absorb in this range useful for therapeutic purposes. [172] The presence of a metal ion at the center of the structure increases the stability of PDT dyes but also affects their photocatalytic properties.

The optical activity of most porphyrins and phthalocyanines are highly concentration dependent as they tend to aggregate in solution. [173-175] However, the aggregation state of porphyrins can also be controlled in solution via light [175] and within LbL films by adjusting the pH. [176] The preparation, optical properties and applications of films containing porphyrin and phthalocyanine dyes has been reviewed. [177]

Illumination and absorption of photons by Pc molecules results in the production of an excited singlet state complex (^{1}Pc*), which may then be transformed in to a triplet state by way of inter-system crossing (^{3}Pc*). From there the activated complex may release its energy to drive various reactions such as the production of radicals (Type I reaction) or of singlet oxygen (Type II reaction). Figure 2.9 illustrates the possible reactions between PDT agents and hydrogen containing molecules and oxygen in a modified Jablonsky diagram. [178] Type I mechanisms involve hydrogen removal or electron transfer between a donor and the excited molecule resulting in free radicals. The type II mechanism involves energy transfer during a collision between triplet oxygen and the activated molecule.

The incorporation of paramagnetic metal ions or ions with open *d* shells such as Co^{2+}, Fe^{2+}, Ni^{2+}, V^{2+}, Cr^{2+}, Pd^{2+} or Cu^{2+} significantly decreases the triplet state lifetime of the excited molecule favoring a return to ground state via inter-system crossing, rendering such molecules useless for PDT applications. [179] Porphyrinoid dyes coordinated with diamagnetic metal ions such as Zn^{2+}, Al^{3+} and Ga^{3+} have long triplet lifetime in the order of micro- to milli-second range. [180]

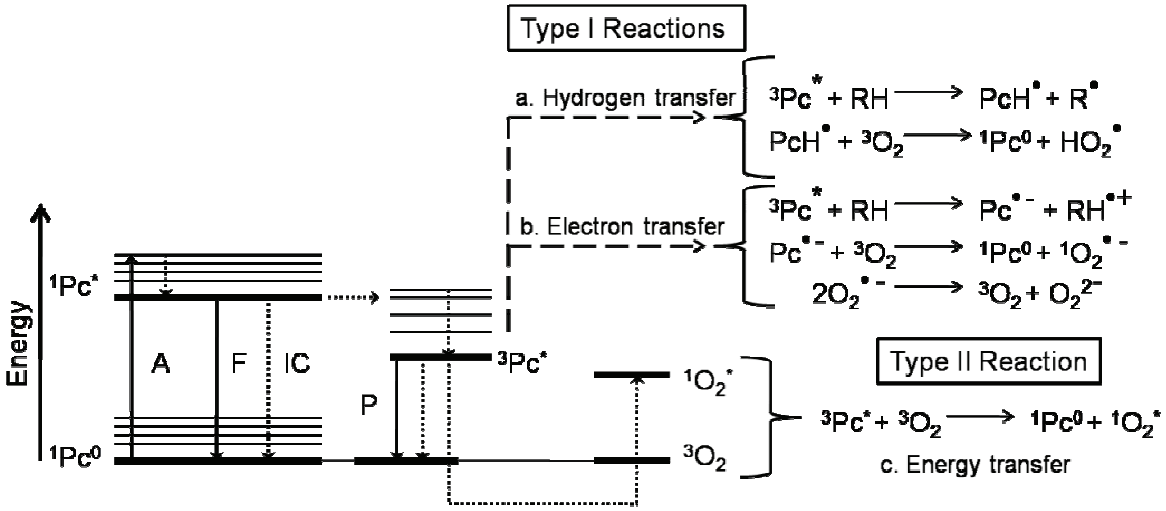

Fig. 2.9 Jablonsky diagram showing the reactions between porphyrinoids and oxygen.

Singlet oxygen is particularly important because it is extremely reactive and possesses a relatively long half-life, making it an ideal oxidizing molecule. Singlet oxygen thus has various applications in synthetic chemistry as well as in some key biochemical reactions. [181] Triplet states with energies higher than 1.14 eV (110 kJ/Mol) are sufficient to generate singlet oxygen.[182] The length of time the excited molecule remains in triplet state is not only important because it increases likelihood of Type I or Type II reactions to occur but also because each of the various reaction types is rapidly quenched in solution. The presence of impurities in polymers or photosensitizers can catalyze the formation of singlet oxygen, which is deteriorating many industrial products but taken to an advantage in PDT; the numerous side-effects associated with common chemotherapy are avoided by substituting systemic chemicals with sensitizing agents that are only active in when the targeted tissue is exposed to laser irradiation. [170] Therefore, the medical practitioner may use laser light only on the sick tissue without affecting other cells or organs. The drawback of this practice, however, is that current second generation PDT agents are still highly unspecific and very stable molecules, which

means that the patient's skin and eyes are significantly more sensitive to light following treatment. [183] It may be possible to prevent the uncontrolled spread of PDT agents using microencapsulation techniques. In addition, PDT molecules could be useful to alter the permeability of polyelectrolyte microshells.

The use of fluorescent Pc molecules could be helpful in tracking a microcontainers' movement in living systems. Such porphyrin containing capsules can have potential applications as light harvesting systems, microdelivery and cosmetic products for skin care. The microshell in this case, acting solely as a container for the molecule of interest. Some porphyrin dyes such as meso-tetrakis (4-sulfonatophenyl) porphine (TPPS) have the ability to form ordered structures like helicoidal particles. [184,185] It was previously shown that TPPS can self-assemble to form rigid nanotubes on polyelectrolyte capsule wall. [186] Few reports have shown that water soluble dyes can be incorporated in the polyelectrolyte capsule wall using the layer-by-layer approach but their use as photocatalysts to damage microshells and release encapsulated materials using light has not been shown. [21,43,187] The broad spectroscopic, catalytic and self-assembly properties of porphyrinoid-type functional dyes makes them an interesting substance to functionalize LbL capsules and perhaps, induce optical responses to control microcapsule permeability.

2.7.2.2 METAL NANOPARTICLES

Metal and metal oxide nanoparticles lend themselves to a variety of applications from the formation of inorganic thin films with well defined pore size [188] and catalytic synthesis of other nanoparticles, [42,161] to the formation of polymer/nanoparticles composite films. [189] However, it is the surface plasmon resonance absorption of metallic nanoparticles, with an absorption cross-section drastically more intense (> 10^6) than typical dyes, which gathers most interest in recent years. In the case of silver and gold, these oscillations, often referred to as *plasmons*, have frequencies of approximately 425 nm and 525 nm, respectively. Surface plasmons can be excited optically, releasing the absorbed photon energy as heat. Being held together by electrostatic interactions, microcapsules are sensitive to high temperature and their functionalization with such nanoparticles constitute a promising approach to trigger an optical response in microcontainers. However, for bio-medical applications it is desirable to obtain structures possessing near-infrared (near-IR) absorption, which penetrate deeper in living tissues than visible or UV light and may alleviate potential side-effects of irradiation to biological tissue, such as burns and damages to genetic material. [16]

Certain geometries of nano-gold such as nanorods have been used as efficient absorption centers in the near-IR and their wavelength dependant absorption was studied recently. [190] Yet, the large concentration of stabilizers necessary for their synthesis and storage can affect their adhesion with other materials making them challenging to introduce in polyelectrolyte microshells. An alternative approach with near-IR absorption is possible by aggregating gold nanoparticles in a controlled manner. [191,192] When in close proximity, the surface plasmons of adjacent colloidal gold particles are coupled introducing an absorption region in the near-IR region. It is also known that changing the surface properties, shape, size, synthetic approach and the distance between neighboring gold particles can affect the absorption spectra of gold nanoparticles. In general, these effects come with a red-shift in the main plasmon absorption region of the nanoparticles or in the apparition of a second absorption region at longer wavelengths. The possibility of tuning the main absorption region of gold nanoparticles significantly increases the versatility of the laser/nanoparticle interaction and consequently makes it possible to get the most out of the gold nanoparticles as a visible light and near-IR sensitizer for microcontainers.

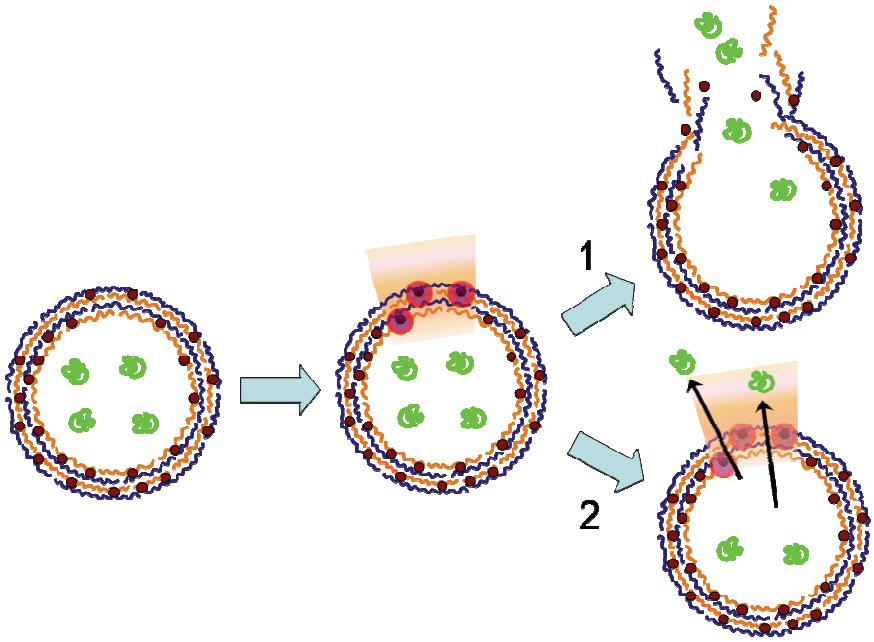

Fig. 2.10 Destructive and non-destructive release using the laser-nanoparticle interaction. (1) Upon illumination, the nanoparticles produce a large amount of heat that breaks the capsule wall open. (2) During illumination, the nanoparticles produce a small amount of heat sufficient to exceed the glass transition of the polymer complex of the capsule, decreasing the shell's permeability until illumination is stopped.

Independently from the wavelength used to excite nanoparticles, the absorption of photons by gold nanoparticles during irradiation can be harvested to release encapsulated substances from microcapsules destructively (1) or non-destructively (2) as illustrated in Figure 2.10. The first studies to remotely release encapsulated materials from microcapsules involved the use of pulsed (modulated) laser sources and microcontainers functionalized with very large amounts of metal nanoparticles, both resulting in the destruction of the microcontainer. [20,21] While it was demonstrated that many capsules could be damaged by continuous irradiation, this remote release approach has rather large energy requirements despite the high surface coverage of nanoparticles. The effects of modulated near-IR pulses were investigated using an average intensity of 30-700 mJ cm^{-2} per pulse to damage various polymeric microcapsules containing one or more layer of densely packed gold nanoparticles. [20,193] Much lower input energy of 10μJ/pulse was needed in another study were the laser beam was focused onto single capsules using an 840 nm near-IR pulsed laser. [99] De Geest *et al.* made light responsive hybrid capsules that could be destroyed by laser irradiation using $CaCO_3$ as a sacrificial template. [41] Wu *et al.* used gold nanoshells to remotely release the content from liposomes using pulsed IR. [194] The incorporation of metal nanoparticles in hydrogel matrixes was also shown to provide the latter with new light responsive capabilities that could be useful in drug delivery technology. [195] However, the effects of pulsed lasers on microcapsules are not well understood and might involve undesirable ablation effects. Concerns with regards to the explosive destruction of microcontainers in various applications and the potential toxicity [167] of metal nanoparticles in cells led to focus the research on significantly reducing the radiation energy requirements for capsule activation and minimizing the concentration of light sensitizing agents in microshells.

Unlike UV laser ablation which is a photochemical process in which energetic photons disrupt molecular bonds, the effects of IR ablation are due to thermal processes. [144] Pola and coworkers have conducted several investigations on the decomposition of bulk polymers by IR laser ablation. [196] However, laser irradiation conducted in liquids also involves molecular collisions of the irradiated material with the solvent which can deactivate the excited molecule. The shell of multilayered polymeric capsules containing metallic nanoparticles is partially hydrated and contains molecular interactions absent in bulk polymer making IR ablation events more complex but less likely to occur. [130,197] With regards to the presence of gold nanoparticles in the capsule wall, Volkov *et al.* recently investigated the theoretical energy transfer of gold nanoparticles in water when irradiated with laser pulses. [198] The results show

that irradiating gold nanoparticles in water with sufficient fluence can result in exceeding the critical temperature of water (T_c = 647 K) with the explosive formation of vapor bubbles. This effect is accompanied by significant pressure and temperature increment that exponentially decays with distance from the nanoparticle surface. These results also support observations where a cell can be killed by IR laser pulses after internalizing gold nanoparticles. The effects of IR ablation on living tissues have been thoroughly reviewed by Vogel and Venugopalan. [144]

Photo-chemical events associated with laser ablation are likely contributing to the observations made by various groups who explained that release of material by pulsed IR irradiation from gold functionalized capsules is presumably only due to the laser/nanoparticle interaction. [20,99,100] Still, there are no reports on the mechanico-chemical effects of pulsed lasers on polymeric microcapsules. Therefore, it cannot be excluded that the observed release may be also partially due to laser ablation, independently from the gold nanoparticles within the shell. Impregnating microcapsules with a low surface coverage of gold nanorods [169] or aggregates of gold nanoparticles, both of which have strong intrinsic absorption in near-IR, instead of a densely packed shell of gold nanoparticles could be advantageous in order to significantly reduce the activation energy necessary to optically release substances by near-IR. [193] In this sense, one would expect that the presence of a single gold nanorod or nanoassembly per capsule should be sufficient to open the capsules.

A step in this direction has been made by Skirtach and coworkers who recently began incorporating relatively low concentrations of homodispersed nanoparticles and release the encapsulated content using a CW visible laser whose typical average intensity is higher than that of pulsed lasers but much lower than the mean intensity of laser pulses used in other studies. [21,22,40] CW lasers are preferable for remote release applications that require greater control over permeability in a non-destructive manner. The recent literature covering this topic has numerous examples of laser-induced release of encapsulated materials using gold nanoparticles-incorporated microcontainers but offers no alternative approach.

2.8 LIGHT INDUCED PROCESSES

2.8.1 ORGANIC DYES AND FLUOROPHORES

Molecules that absorb light in the visible range are called chromophores but the ability of materials to absorb photons extends far beyond this range from far-UV radiation to the significantly less energetic far-IR spectral region. In biology, the near-IR window is most desirable as few or no biological component absorb in that region. While not being completely transparent, near-IR radiation penetrates deep in living tissues allowing greater energy to be transmitted since heating effects are diffuse. On the other hand, far-UV is typically considered far too energetic for biological applications. Near-UV and visible light do also present advantages and constitute important spectral regions for numerous applications such as polymer synthesis where ultraviolet light is commonly used, or in the treatment of certain skin ailments by photodynamic therapy where visible light is necessary.

Light responsive materials can be encapsulated in the cavity of polymeric microcapsules or inserted in the capsules' wall to give them some functionality. While fluorescent dyes are routinely used to visualize microshells, nanoparticles of noble metals were recently shown to induce permeability changes in the capsule wall upon laser irradiation allowing encapsulated material to be released. [21] This topic was covered in to some extent in section 2.7.2.1.

2.8.2 HEAT PRODUCTION FROM THE LASER-NANOPARTICLE INTERACTION

The use to gold nanoparticles to sensitize the microcapsules to light is the result of their ability to convert photons into thermal energy, which if sufficient can affect the permeability of the polymer shell. To explain the mechanism of laser-induced changes of nanoparticle functionalized microcapsules, Skirtach *et al.* recently introduced a model [22] that accounts for the influence of the size, absorption and concentration of the nanoparticles. Based on this one, the temperature change (dT) at a distance r_i from a nanoparticle of a diameter r_0 can be described as follows:

Eq. 2.11
$$\frac{dT(r_i)}{dE} = \frac{r_0^3}{r_i}$$

where $E = A_0/3K$. A_0 is defined as the heating rate of the nanoparticles per volume per time unit and K the thermal conductivity of the medium. Equation 2.11 shows that the temperature around the nanoparticle is reciprocal to the distance from the nanoparticle and that it changes by the cube of its radius. As a result, the temperature change around an irradiated nanoparticle is greatest near its surface and for large nanoparticle. Assuming a homodispersed distribution of nanoparticles in the microcapsules, the density of nanoparticles can be expressed in terms of surface filling factor (F_S). F_S is defined as the ratio of the sum of the cross sections of n nanoparticle per capsule S_i, to the surface area of that capsule S_C. Using TEM to count the number of nanoparticles n per capsules and LSCM to determine the average diameter of the capsules R_0, F_S can be simplified with the following relationship:

Eq. 2.12
$$F_S = \frac{\sum_i^n S_i}{S_C} = \frac{n r_0^2}{4R_0^2}$$

As a result the hypothetical case where $F_S = 1$ would describe a microcapsule that is completely covered with nanoparticles whereas $F_S = 0$ would be a capsules that does not contain nanoparticles.

Equation 2.11 showed that the temperature increase resulting from irradiation is lower far from the nanoparticle surface, but thermal contributions from one or more neighboring nanoparticles also affect the general change the heat distribution around any given nanoparticles. The average distance d between nanoparticles within the polyelectrolyte capsule is related to the diameter and density of the nanoparticles as described by the following equation:

Eq. 2.13
$$d = r_0 \frac{2}{\sqrt{F_S}}$$

Substituting the variable r_i in Equation 2.11 with Equation 2.13 can produce the following approximation:

Eq. 2.14
$$\frac{dT}{dE} \cong r_0^2 \sqrt{F_S}$$

Therefore, Equation 2.14 demonstrates that the change of temperature in a microcapsule functionalized with light absorbing metal nanoparticles is highest for larger nanoparticles and microcapsules with a dense nanoparticle distribution. However, this relationship assumes a homodispersed distribution of nanoparticle within the capsule wall and cannot be used to analyze the thermal changes associated with the optical excitation of aggregates of metal nanoparticles.

2.9 MICROCAPSULE FOR DRUG DELIVERY

2.9.1 REMOTE RELEASE IN LIVING CELLS AND TISSUES

Polymeric shells that can be remotely opened by optical means to release encapsulated substances are interesting materials for *in vitro* and *in vivo* studies. Such systems offer a protective environment to the encapsulated material allowing for the storage of substances inside a living organism until the proper conditions are met to release the substance in question. [82,199] This is advantageous *in vitro* because the cell or tissue can be given the necessary time to restore an equilibrium state after being put in presence of capsules. *In vivo*, however, serious concerns arise as very little is known on the fate of such complex systems. In other words, should microencapsulation system perform well the task of recognizing a cell, being internalized and releasing its content in the appropriate cellular compartment, the question as to what happens precisely to the capsule construct remains ill understood. Even less is known about the fate of such capsules in higher organisms in which microcapsules are exposed to metabolic processing. [200] The best studied system for intracellular studies are gold containing polymer microcapsules.

Sukhorukov *et al.* were the first to report on the uptake of polymeric capsules by cells. [5,22] Parak *et al.* pushed their research further in this direction and studied the cellular uptake, [201,202] optical release of encapsulated cargo [203] and toxicity [167] of microcapsules to living cells. It was shown for instance that shells of capsules based on PAH/PSS or PDDA/PSS induced no cytotoxic response in tumor cells. [167] The interest in cancerous cells and tissues lays primarily in the unselective manner with which such cells internalize materials in their environment, making them an ideal model to study polymeric capsules as microdelivery agents. However, certain nanoparticles used to sensitize the capsules to light remain a potential toxicity concern.

[204] Gold nanoparticles were reported to be toxic due to (1) aggregation, [82] (2) surface chemistry, [205] and (3) size. [200,205] However, Hauck *et al.* recently reported that PDDA/PSS coated gold nanorods have little or no effect on cell viability [206].

The capsules studied by the joint efforts of the Sukhorukov and Parak groups were constructed from non-degradable polyelectrolytes. [40,98,201] For drug delivery purposes degradability is often required. This aspect of biodegradability was assessed by the group of De Geest *in vitro* [19,207] and *in vivo*. [85] Capsules consisting of biopolymers such as polysaccharides and polypeptides showed to be prone to enzymatic digestion upon internalization by cultured cells. De Koker *et al.* injected such microcapsules subcutaneously in mice and tissue sections taken at different time intervals allowed to investigate the fate of the injected capsules as a function of time. [85] Initially the capsules behaved as a porous implant which becomes gradually infiltrated by inflammatory cells, emerging from the border of the injection spot. Two weeks post injection, the injection volume was completely infiltrated by inflammatory cells and the capsules were found largely deformed inside cells. Thirty days post injection, no intact capsules could be observed anymore and only debris of broken capsules was visible. [19]

Besides release from capsules governed by enzymatic digestion of the polyelectrolyte shell, another remote release strategy of interest is to release active species only at specific sites and/or upon a specific trigger.

2.9.2 FATE OF MICROCAPSULES INTERNALIZED BY LIVING CELLS

This ability of polymeric microcapsules to release their payload into the cellular cytosol points out an important property of laser activated capsules. In general, phagocytosed species end up in endo/lysosomal compartments where they are broken down by enzymes and, if necessary, exocytosed by the cell. [98] However, for several classes of drug molecules, which cannot readily permeate through the cell membrane, the aim is not only to reach the endo/lysosomes but the cytosomal space and/or other compartments within the cell as well (*e.g.* nucleus). This is the case in gene therapy where polynucleotides such as siRNA, mRNA and DNA should be delivered into the cellular cytosol and should even be transported to the cell's nucleus in the case of DNA. Yet, conquering the endo/lysosomal membrane is not that straightforward. Several strategies have been developed in order to improve the release of encapsulated material from the endo/lysosomes into the cellular cytosol. Common methods involve using membrane-disruptive peptides, lipids or polymers, or use the buffering capacities of polymers

such as poly(ethylene imine) (PEI) to cause osmotic bursting of the endo/lysosome. Recently, other means involving light irradiation such as the use of photosensitizers have been explored. The latter can accumulate in the endo/lysosomal membrane and form oxygen radicals upon light irradiation causing the endo/lysosomal membrane to rupture. Although highly efficient these photosensitizers are often toxic and should be administered separately from the drug. This could cause difficulties in an *in vivo* setting where the minimal dose of photosensitizing dye necessary to open the endo/lysosomal membrane without affecting other cellular activities is a very challenging task. Also these small molecular weight compounds will drain easily from the administration spot while microparticulate drug formulation will have a much long residence time in the tissue where they are administered.

Taking these considerations into account allows defining some potential solutions using remotely activated polymeric microcapsules. Firstly, these capsules allow the simultaneous delivery of photoactive species and drug molecules. Moreover, due to their size an efficient targeting to phagocyting cells can be obtained and surface functionalization of the capsule wall with specific ligands (*e.g.* antibodies) is easily performed, which allows to enhance their uptake by specific tissues or cells. Wang *et al.* recently introduced capsules loaded with hypocrellin B (HB), a photosensitizer used in so-called photodynamic therapy to treat diseases such as some forms of cancer and viral infections. [82] Upon exposure to light, HB generates singlet oxygen ($^1O_2$), which is cytotoxic and induces cell death. However, HB displays no cytotoxicity in the absence of light irradiation. To allow the not water-soluble HB to enter living cells, it was loaded in polymeric microcapsules by non-specific interactions applying a solvent exchange step using ethanol as a solvent for HB. Upon incubation with living cells, the HB loaded capsules were efficiently taken up and neither capsules nor HB loaded capsules appeared to be cytotoxic for the cells. However, upon irradiation with 488 nm light, cell viability dropped by 70 %. In this in vitro setting, light addressable microcapsules showed promising candidates for the specific delivery of drugs molecules that need a protective container on the way to their target cells or tissue.

3 MATERIALS AND METHODS

3.1 MATERIALS

3.1.1 POLYMERS

FITC-dextran (20 kDa), poly(allylamine hydrochloride) (PAH, 70 kDa), very low molecular weight poly(diallyldimethylammonium chloride) (VL-PDDA, 20 wt. %, < 100 kDa), low molecular weight poly(diallyldimethylammonium chloride) (L-PDDA, 35 wt. %, 100-200 kDa), medium molecular weight poly(diallyldimethylammonium chloride) (PDDA, 35 wt. %, 200-350 kDa), high molecular weight poly(diallyldimethylammonium chloride) (H-PDDA, 35 wt. %, 500 kDa), poly(ethylene glycol) (PEG, 20 kDa), poly(vinylsulphonate sodium salt) (PVS, 70 kDa), poly(styrenesulfonate, sodium salt) (PSS, 70 kDa), poly{1-[4-(carboxy-4-hydroxyphenylazo) benzenesulfoamido]-1,2-ethanediyl, sodium salt) (PAzo, 100 kDa) were purchased from Sigma-Aldrich (Taufkirchen, Germany). Poly(ethyleneimine) (PEI, branched, 30 % solution) was purchased from Polyscience Europe (Eppelheim, Germany).

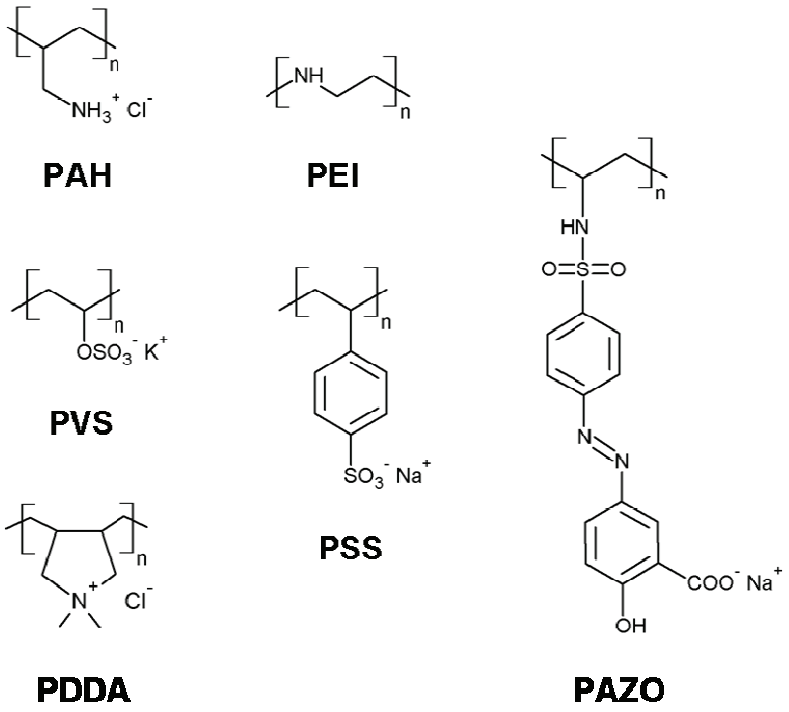

Fig. 3.1 Structural formulas of polyelectrolytes used in capsule preparation.

Diazoresin (DAR, diazo-10, 4-diazodiphenylamine/formaldehyde condensate hydrogensulfate-zinc chloride salt) was purchased from PC Associates (Livingston N.J.).

Dextran-hydroxyethyl methacrylate (dex-HEMA, 19 kDa) was kindly provided by Dr. Bruno De Geest. The degree of substitution (*i.e.* amount of HEMA groups per dextran chain) was 2.5 as determined by H-NMR.

Alexa Fluor® 488 dextran (AF 488, 3 kDa), Alexa Fluor® 488 dextran (AF 488, 10 kDa), Alexa Fluor® 555 dextran (AF 555, 10 kDa), Alexa Fluor® 594 dextran (AF 594, 10 kDa), CaGreen™-1 dextran (CG, 3kDa), Cascade Blue® dextran (CB, 10 kDa), TRITC dextran (4.4 kDa), TRITC dextran (65-76 kDa) were purchased from Invitrogen (Karlsruhe, Germany).

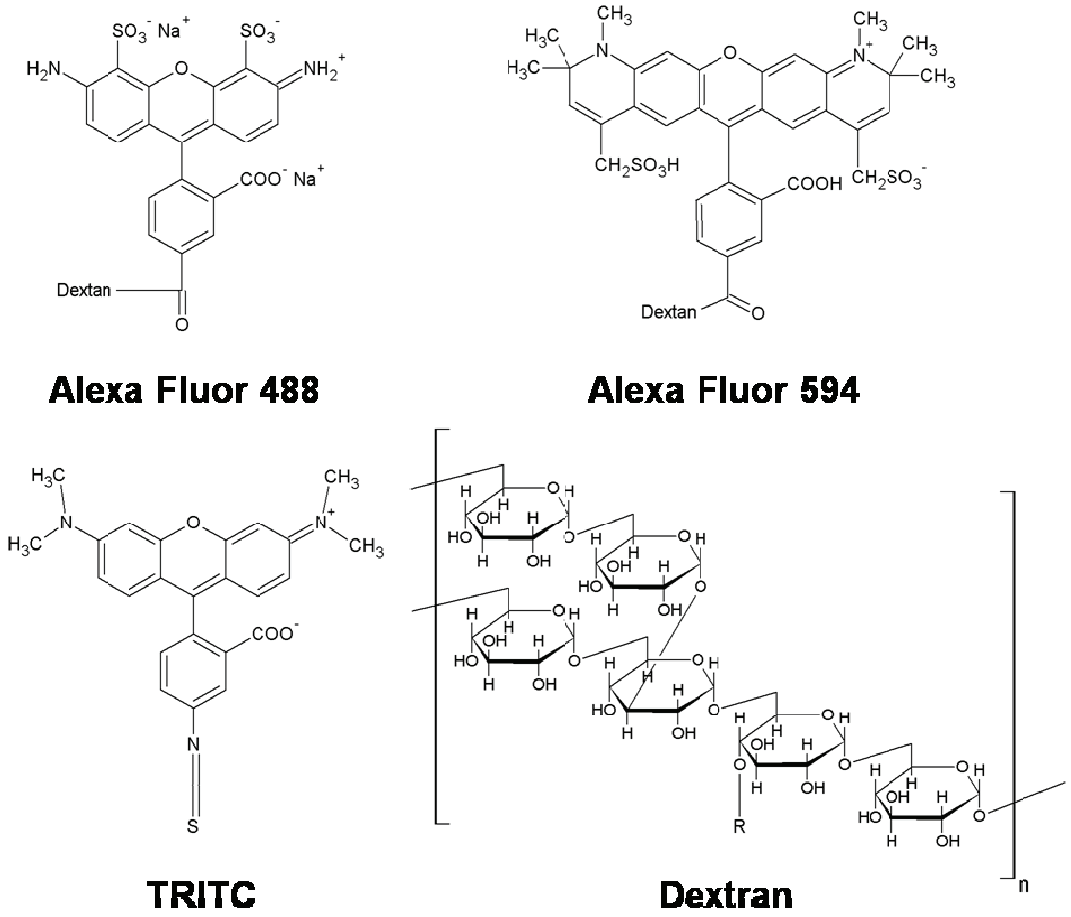

Fig. 3.2 Structural formulas of some fluorophores and dextran. The structures of AF 555, CG and CB are not shown.

3.1.2 PARTICLES

Monodisperse silica particles (SiO_2) with a diameter of 1.93 µm, 3 µm 4.55 µm and 4.78 µm, as well as anionic polystyrene particles suspensions (PS, 10 wt. %,) with a diameter of 4.62 µm and 10.25 µm were purchased from Microparticles GmbH (Berlin, Germany). Colloid gold solutions with mean a particle diameter of 5, 10 and 20 nm were purchased from Sigma-Aldrich (Taufkirchen, Germany).

3.1.3 OTHER CHEMICALS

1-(3-dimethylaminopropyl)-3-ethylcarbodiimide hydrochloride (EDC), 2-(4-hydroxyphenyl azo)benzoic acid (**Azo2**), 4-(2-hydroxyethyl)piperazine-1-ethanesulphonic acid (HEPES), ammonium fluoride (NH_4F), ammonium hydroxide (NH_4OH, 25 %), deuterium oxide (D_2O, 99.9 % deuterium), dimethylaminoethyl methacrylate (DMAEMA), ethanol, ethylenediaminetetraacetic acid disodium salt (EDTA), hydrofluoric acid (HF, 50 w/v), hydrogen peroxide (H_2O_2, 30%), hydroxyquinone (HQ), isopropanol, L-ascorbic acid (99.0%), lithium chloride (LiCl), methanol, methyl acrylate, methyl red (**Azo3**), N-hydroxysulfosuccinimide sodium salt (NHS), N,N,N',N'-tetramethylenediamine (TEMED), phenylazobenzoic acid (**Azo1**), potassium chloride (KCl), potassium persulfate (KPS), rhodamine 6G, rhodamine B, sodium borate, sodium borohydride ($NaBH_4$, 99.0%) tetrahydrofuran (THF) and thymine were purchased from Sigma-Aldrich (Taufkirchen, Germany).

Calcium chloride ($CaCl_2$), hydrochloric acid (HCl), sodium carbonate (Na_2CO_3), sodium chloride (NaCl), sodium hydroxide (NaOH) were purchased from Merck (Darmstadt, Germany).

Meso-tetrakis (4-sulfonatophenyl) porphine (TPPS), phthalocyanine tetasulfonic acid (PcS), Al (III) phthalocyanine chloride tetasulfonic acid (AlPcS), Cu (I) phthalocyanine tetasulfonic acid (CuPcS) and Fe (III) phthalocyanine chloride tetasulfonic acid (FePcS) were purchased from Frontier Scientific (Carnforth, United Kingdom).

All chemicals were used without further purification. All solutions were prepared with water from a three stage Millipore Milli-Q plus 185 water purification system (Millipore, United States of America) with a resistivity higher than 18.2 Ω·cm.

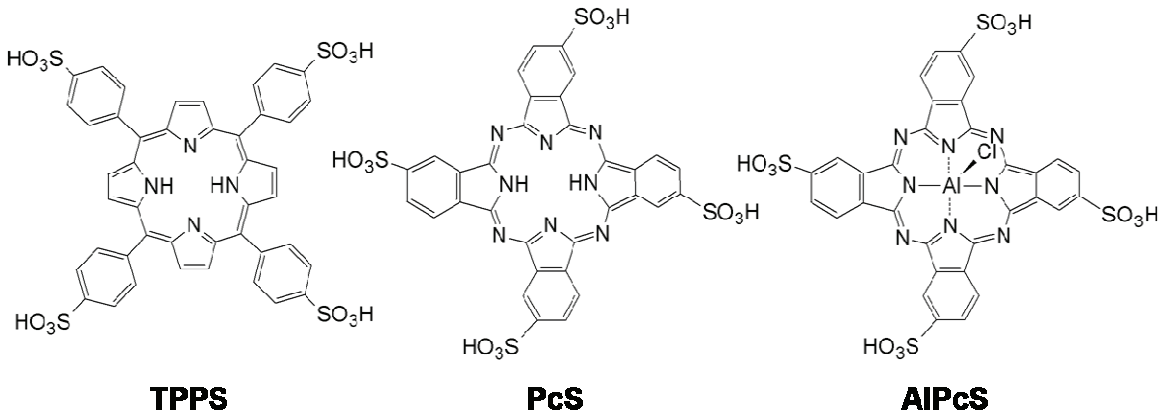

Fig. 3.3 Structural formulas of some porphyrinoid dyes used in capsules preparation. The copper and iron variations have the PcS structure with an Cu(I) and an FeO_2 atom at the center.

3.2 SYNTHESES

3.2.1 COUPLING OF AZOBENZENE DERIVATIVES TO PAH

In a beaker mounted on a magnetic stirrer, 1 mmole of PAH was dissolved in 20 ml of HEPES (0.1 M, pH = 7) or borate buffer (0.1 M, pH = 7). Upon complete dissolution, the desired mole percent of azobenzene derivative (Azo1, Azo2 or Azo3, see 3.5 for structures) was added to the solution. The targeted percent substitution had to be multiplied by 5 as the yield of this reaction was determined to be about 20 %. 0.1 mole % of NHS was then dissolved in 0.5 ml of buffer and added to the solution. 1.5 mole % EDC, a carboxylic acid group activator, was dissolved in 1 ml of cold water before being added to the reaction beaker. The beaker was immediately put in the dark and left to swirl overnight at room temperature. The products obtained were filtered for impurities, dialyzed against water for 7 days and freeze-dried. UV/Vis absorbance spectroscopy was used to calculate the substitution ratio. The chemical structure of Azo1-PAH is illustrated in Figure 3.5.

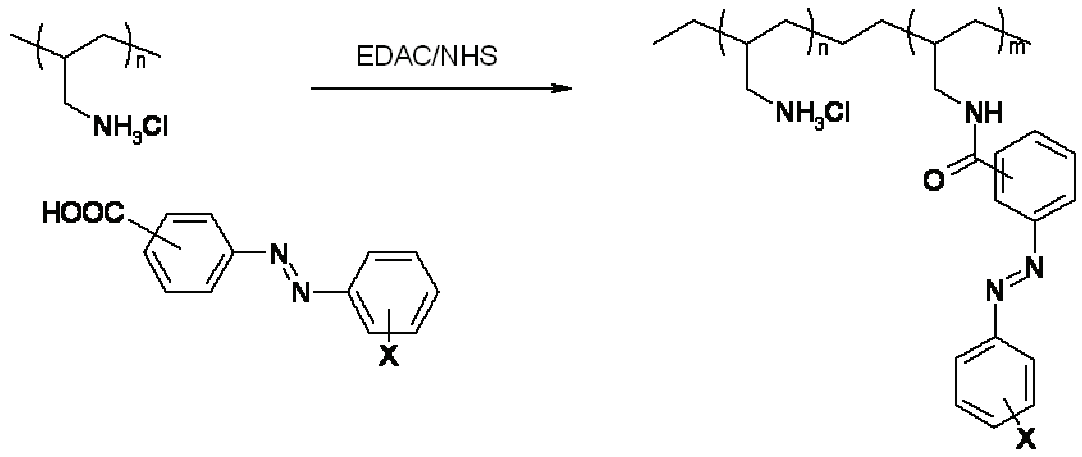

Fig. 3.4 General substitution reaction of azobenzene derivatives onto PAH.

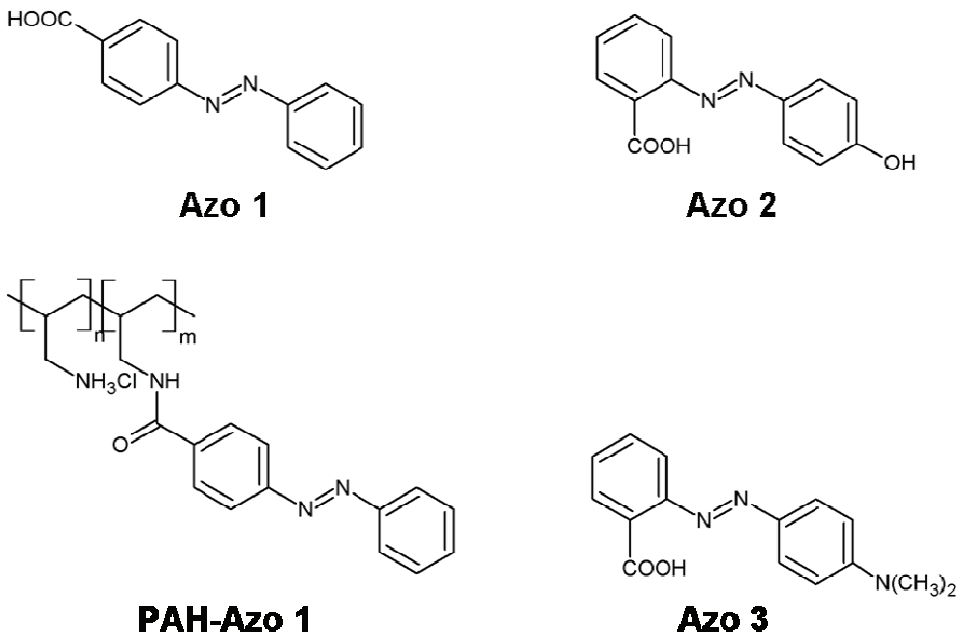

Fig. 3.5 Chemical structures of Azo1, Azo2, Azo3 and Azo1-PAH.

3.2.2 PREPARATION OF $CACO_3$ MICROPARTICLES

Calcium carbonate ($CaCO_3$) microparticles were prepared by colloidal crystallization. [87,89] In a clean beaker mounted on a magnetic stirrer, a solution of 0.33 M of $CaCl_2$ was added at once to an equal volume of 0.33 M of Na_2CO_3 while stirring at room temperature. The mixture rapidly turned milky and stirring was maintained for 30 seconds before putting aside for 5 minutes. The resulting white suspension was centrifuged and washed several times. For long term dry storage, the microparticles were rinsed with ethanol and dried. For short term storage, the suspension was kept at 4°C.

3.2.3 SYNTHESIS OF DEX-HEMA MICROGELS

In a glass vial dex-HEMA (400 µL, 15 % (w/w)) is slowly introduced with a pipette into a PEG solution (4.577 mL, 30 % (w/w)) under slow continuous stirring by a Teflon coated magnetic stirring bar. When a homogeneous dispersion is obtained, 35 µL DMAEMA is added and the mixture is slowly stirred for 1 minute. Subsequently radical polymerization is initiated by addition of TEMED (100 µL, pH neutralized by 4 M NaCl) and KPS (180 µL, 50 mg/mL). The mixture is further stirred for 15 minutes and is then allowed to stand for 30 minutes. Afterwards the microgels are twice centrifuged/washed with 20 mL water and finally stored in 5 mL water at -20°C until use.

3.3 SAMPLE PREPARATION

3.3.1 RCA CLEANING OF SUBSTRATES FOR LAYER DEPOSITION

Silicon wafers, glass, quartz and silica microparticles were cleaned from potential organic contaminants using the RCA-1 cleaning procedure. The substrates were first immersed in a 1:1 isorpopanol/water solution and sonicated for 5 minutes in a sonication bath. The substrates were then thoroughly rinsed with distilled water and transferred to a 5:1:1 solution of water/NH_4OH/H_2O_2. The solution was heated in a water bath, uncovered, at 75°C for 15 minutes. The RCA solution degrades any organic materials during this time. The solution was then allowed to cool down to room temperature and the substrates was thoroughly rinsed with water and dried under nitrogen gas. Silica particles were sedimented by centrifugation after each wash and resuspended in water without any drying.

3.3.2 LBL ASSEMBLY ON FLAT SUBSTRATES

The assembly of multilayer films on flat substrates was done on quartz and silicon wafers. The substrate was first cleaned from organic impurities using the RCA-1 cleaning procedures described above (section 3.3.1). Layering was then done manually or using a homemade *dipper* (robotic arm connected to a computer controlled x-y-z axis) by dipping the substrate in solutions, rinsing with water and drying under nitrogen after each deposition, or automatically in the cases for which the *dipper* was used. The coated substrates were stored in a dry container. Solid quartz crystal slides were used to study the absorption behavior of phthalocyanine-polyelectrolyte multilayers by monitoring the UV-visible spectra of the deposited films after each layer addition.

3.3.3 PREPARATION OF MICROCAPSULES

Polyelectrolyte microcapsules with different shell constituents were constructed following different strategies. Core pretreatment with RCA-1 was only necessary in the case where silica particles were coated with the weak polyelectrolyte PAH in order to improve the adherence of this weak polyelectrolyte to the silica surface.

Construction of microcapsules on silica particles was done by sequentially resuspending the particles in two oppositely charged polyelectrolyte solutions, alternating between the solutions after each layer. Following, each layer addition, polymers that were not absorbed by the particles were removed by 2 or 3 water wash sedimented each time by centrifugation at 1500 g. The concentration of polyelectrolyte in solution was typically 2 mg/mL, contained 0.5 M NaCl and the solution pH was situated between 5 and 7. Aggregation of the silica particles was more likely to occur after a certain number of polyelectrolyte layers were added, depending on the size of the particles. 10 seconds of sonication during each washing step helped to prevent aggregation of the particles. Gold nanoparticles were incorporated in the multilayer shell by re-suspending the particles in a mixture of water and colloid gold solution while gently stirring. Aggregates of gold nanoparticles were incorporated into the capsules by first adding the gold colloid solution in a solution of NaCl for a desired time before re-suspending PDDA-coated silica with the gold nanoparticle solution. The layer on which colloid gold nanoparticles was added was always PDDA because colloid gold is negatively charged and could only be deposited onto positively charge polyelectrolytes. The silica particles were ultimately dissolved by adding the coated-particle suspension, dropwise, to a 0.3 M HF solution while

gently stirring for 20 minutes. The sample was then washed with water until the pH of the solution reaches above 5.5 and all fluoride ions were washed away yielding hollow polyelectrolyte capsules.

The coating of $CaCO_3$ particles with PDDA/PSS multilayers was done following the same procedure as described for silica particles. The dissolution of the template, however, was accomplished by resuspending the coated $CaCO_3$ particles with a solution of 0.2 M EDTA at pH 7 for 30 minutes, followed by 3 washes in water.

The coating of PS particles with polyelectrolytes multilayers was preceded by thorough rinsing of the particle with water to remove stabilizers present in the particle stock solution that can affect the adhesion of the polymers at the surface of the particles. In general, the multilayers were assembled following the same procedure as described for silica particles. However, in the case of PAH/PAzo complex, the PAzo solution contained 0.1 M NaCl and its pH was adjusted to 9.5 as higher salt concentration or lower pH led to the flocculation of the polymer. The pH of PAH solution was adjusted to 4, which insured that at least 90 % of amine groups were charged for the LbL assembly. Removal of the PS template was accomplished by treating the coated particles thrice with THF for 2 hours, followed by five washes with water to remove all THF and dissolution products.

3.3.4 HEAT TREATMENT AND ENCAPSULATION

Microcapsules were heated to monitor their shrinking behavior as a function of temperature and to encapsulate substances in PDDA/PSS type capsules templated on SiO_2 particles. A typical heating experiment was performed by adding 100 µL of a capsule solution to a 0.5 mL Eppendorf tube and incubating it in a water bath at the desired temperature in the range of 30°C to 90°C for 20 minutes.

For encapsulation of polymers, an aliquot of microcapsules was mixed with a solution of the substance to encapsulate. The substance to encapsulate present in the bulk was allowed to permeate the microshell by gently shaking the mixture on a vortex for 30 minutes. When fluorescent materials were used, the sample was monitored by laser scanning confocal microscopy (LSCM) to confirm that the fluorescence was similar inside and outside the microcapsules. The mixture was then heated for 20 minutes to shrink the capsules, rendering their wall denser less permeable. The temperature used for the incubation was selected based on the capsules construction and the concentration to the substance to encapsulate.

3.3.5 PREPARATION OF SAMPLE CHAMBERS FOR OPTICAL EXPERIMENTS

Sample chambers (or sample cells) were used in experiments involving laser irradiation to prevent the microcapsules from moving, drying or being damaged during manipulations. Typically, a 1.3 mm X 23 mm X 46 mm glass wafer (Roth, Germany) was first cleaned with the RCA-1 protocol (section 3.3.1). The wafer was then immersed in a salt-free solution of PDDA or PEI to obtain a positively charged surface that could hold microcapsules with a negatively charged outer layer. The wafer was then thoroughly rinsed and dried under nitrogen gas. 20 µL of capsule suspension was pipetted to the center of the polyelectrolyte-coated wafer and a 23 mm X 23 mm cover slide was adjusted on top. The uncovered area around the top cover slide was then sealed off with a fast drying nitrocellulose-based lacquer (*i.e.* nail polish). Sample cells could be kept for months 4°C without noticeable changes in the capsules morphology or response to stimuli.

3.4 METHODS

3.4.1 LASER SCANNING CONFOCAL MICROSCOPY

Laser scanning confocal microscopy (LSCM) is a non-destructive imaging technique frequently used in the visualization and high resolution 3D reconstruction of biological samples. LSCM offers several advantages over traditional wide-field microscopy, including controllable depth of field visualization and the elimination of out-of-focus scattering and emission. Depending on the constructor, confocal microscopes operating in transmission, reflection and fluorescence modes are available. However, most LSCM operate in fluorescence.

The principles of confocal microscopy were first introduced by Minsky in the 1960s as an alternative to traditional microscopy techniques, which suffered from a poor resolution capability. In a common light microscope, every object in a sample is irradiated simultaneously. As a result, reflections or fluorescence emissions from the sample come from every plane of focus contributing to out-of-focus blur and reducing image sharpness and contrast. Thus, a typical wide-field microscope operating in transmission mode can be used to visualize a sample with a thickness in the order of 10 µm.

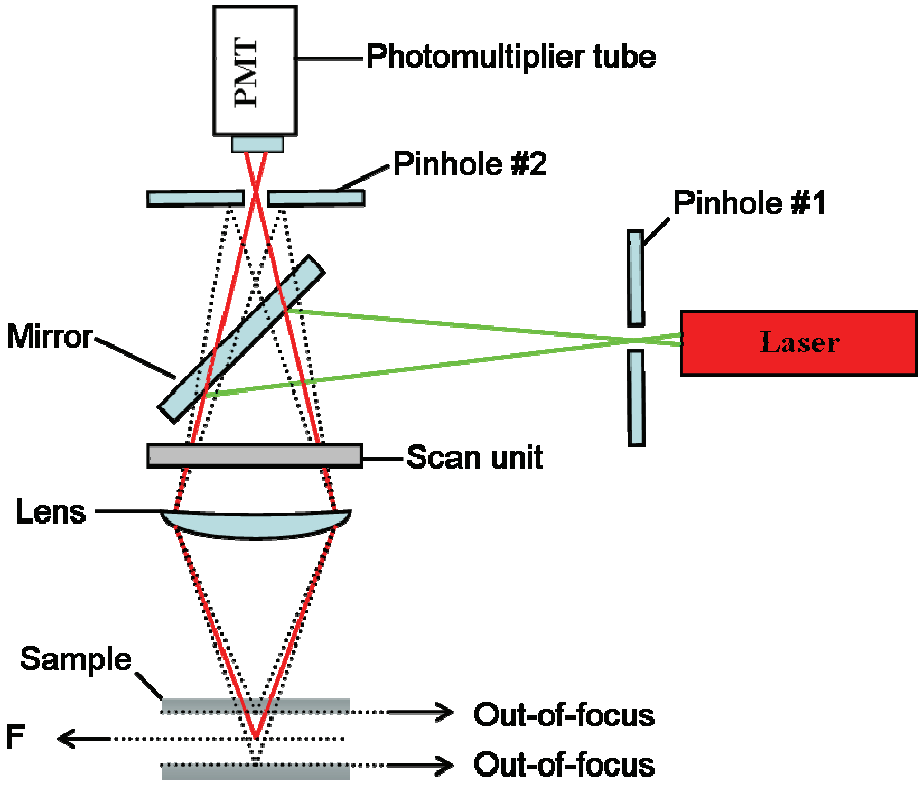

Fig. 3.6 Schematic of LSCM setup illustrating how light emitted from the focal point region (F) passes through the second pinhole while only a fraction of out-of-focus emissions pass the second pinhole.

A schematic of a typical LSCM is shown in Figure 3.6. In LSCM, coherent light emitted from a laser source passes through a pinhole positioned to eliminate laser reflections intrinsic to laser sources. The laser is then reflected on a dichroic mirror and expanded to fit the aperture of a microscope objective. The light is then focused onto the sample through the objective illuminating in plane and out-of plane region of the sample. The light reflected or emitted by the sample, which reaches the objective's aperture is focused through the dichroic mirror to a second pinhole. A photomultiplier tube located after the second pinhole collects the photons, which are transformed into data points by a computer. The light originating from the focal point has inevitably the highest, unimpeded intensity because light originating from out-of focus planes of the sample reach the aperture of the second pinhole also unfocussed. Assuming that the beam profile of the light reaching the second pinhole is circular and that the intensity throughout the beam is homogeneous, the intensity of any light reaching the detector

is therefore related to the difference between the maximum intensity of the light passing through the pinhole and the light that is stopped by the pinhole piece. Consequently, most of the light coming from out-of-focus areas reaches the pinhole as an expanded beam, with only a fraction of it passing through the pinhole contributing virtually nothing to the data acquisition.

In order to generate digital images by LSCM, the focused laser scans through an area of the investigated sample in a raster pattern using two rapidly oscillating mirrors. One mirror scans in the horizontal direction, while the second mirror deflects the beam reflected on the first mirror in the lateral direction. Once the selected area has been scanned in the x direction, the beam is sent back to its first position and slightly displaced in the y direction to scan a new horizontal section. The scanning mirrors, moved by galvanometer motors, can translate 450 lines per second. The photons detected by the photomultiplier at each point are converted from an electrical signal to pixels by an analog-to-digital converter. The relative intensity of the light detected is also contained in the corresponding pixel and is translated on a color coded scale by a computer program.

The focal plane can be adjusted manually as in a standard light microscope or by a computer controlled fine-step motor. The diameter of the pinhole can be adjusted to reduce the thickness of the sample investigated. Optical imaging of sample sections with thicknesses in the order of 100 nm is achieved with LSCM. Typical LSCM functioning in fluorescence mode are equipped with several excitation laser sources as well as prisms and diffraction gratings positioned before the detector to allow multiple emission lines to be detected simultaneously.

Optical images of polyelectrolyte microshells in solution were obtained on a Leica TCS SP confocal scanning system (Leica, Germany) equipped with a 100x/1.4-0.7 oil immersion objective. Sample imaging was done by depositing a small volume of sample solution onto a glass wafer.

3.4.2 UV LAMP IRRADIATION

Lamp irradiation experiments were carried out in a quartz cuvette. The sample cuvette was immersed in a cooled water bath mounted on a magnetic stirrer. For experiments involving azobenzene derivatives, a 150 W super-quiet xenon lamp (Hamamatsu, Japan) placed in a E7536 lamp housing with an automatic cooling fan (Hamamatsu) was used as light source. A

silver mirror was positioned at an angle of 45° in front of the exit window on the side of the lamp housing reflecting the beam down. The power used to irradiate the sample was measured to by approximately 3 watts. Encapsulation by light was accomplished by first mixing an appropriate fluorescently labeled dextran with capsules sample for at least 30 minutes to allow the dye to permeate capsules completely. A high-pressure mercury lamp (Müller Elektronik LAX1450) combined to a Schott color filter was used to get a 5 mW broad UV (300-390nm) irradiation source was used for long exposure experiments involving microcapsules containing no specific chromophores.

3.4.3 ND:YAG PULSED UV LASER

An active/passive mode-locked Neodynium: yttrium-aluminium-garnet (Nd:YAG) laser (B.M. Industries, YAG 502 DPS 7910DP) has been utilized to produce the 355 nm frequency-tripled light, with 35 ps pulses and a repetition rate of 10 Hz. The intensity of the incoming beam read at the oscillator was always stable, having a value between 0.047 J and 0.09 J. The intensity of the 355 nm outcoming beam has been varied between 0.005 J and 0.200 J for our experimental purposes. The experimental setup is presented in Figure 3.7. In consists in a pinhole positioned at the exit of the laser box, set in a way that the light goes through the system with a diameter of 5-6 mm. The beam is directed to a Ag-mirror (Schott), which reflects the beam to a UV-lens (Linos Photonics, f = 100 mm) adjusted so that the beam is focused to the sample after passing through a visible cutoff filter UG-11 (Schott). The exposition time and beam intensity have been varied during the experiments. The intensity values reported were determined using a powermeter.

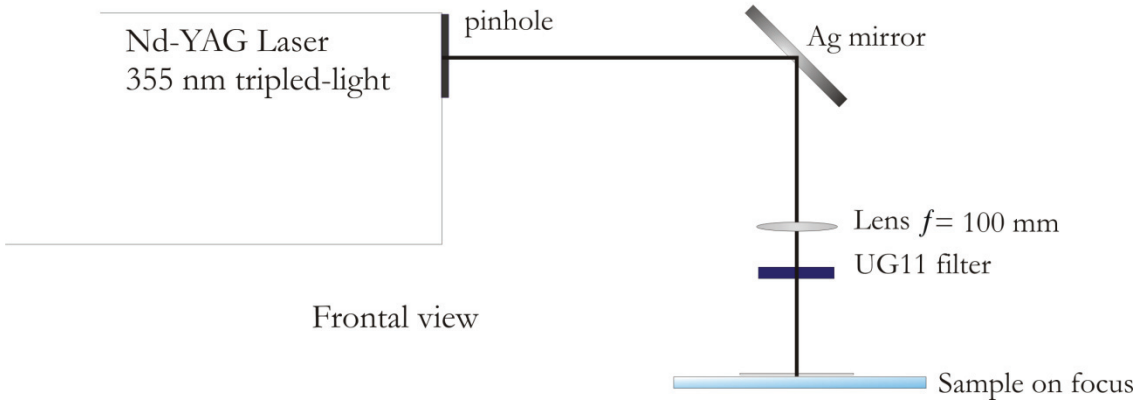

Fig. 3.7 Scheme Nd:YAG pulsed UV laser setup.

3.4.4 PULSED IR LASER

A Midi-Nitrogen-Laser (MNL 200, LTB, Berlin) equipped with a dye cell emitting at a wavelength of 830 nm with a pulse halfwidth of about 1 ns and intensity of 0.3 J was used in a home made setup described in *Section 3.4.4*. An aliquot of capsules was transferred on a RCA clean microscope cover slide treated 5 minutes in a solution of polyethylenimine (5mg/mL) to make it positively charged so that capsules can adhere to the surface. The first cover slide was then covered with a second slide and sealed to prevent the sample to dry out. Images of capsules were first recorded by LSCM. The sample was then transferred to the laser setup and the capsules of which images were recorded identified using a CCD camera connected to a monitor. The laser pulses are visible on the monitor and can be precisely positioned on a desired area of a capsule. In a typical experiment, after 5-10 seconds of irradiation, the laser was switched off and the sample was immediately transferred back to the LSCM (taking approximately 15 seconds) to record any changes.

3.4.5 CONTINUOUS WAVE LASER DIODES

The schematic diagram of the setup used for most experiments involving laser diodes is shown in Figure 3.8. The near-IR laser was obtained from a 1.4 V continuous wave laser diode with a mean wavelength centered at 830 nm with optical power up to 100 mW. The collimated laser beam was aligned in the Z direction and focused onto the sample cell (Section 3.3.5) through a 40X or 100X microscope objectives (N.A. 1.25) (Edmund Scientific, Commercial Grade). The sample was positioned by a micrometer resolution XYZ stage. Illumination was made in transmission mode using a 150 W white light source, and the images were recorded by a charge coupled device (CCD) camera connected to a computer. The sample cell containing the capsules was deposited onto a microscope slide under the microscope objective. Laser intensity was measured incident upon the microscope objective by a Newport-1830C powermeter.

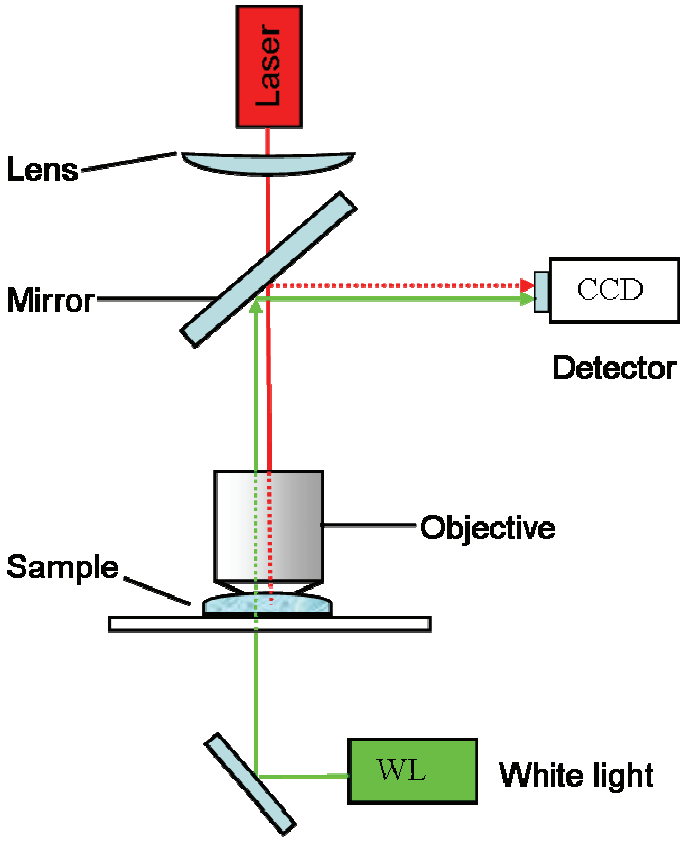

Fig. 3.8 Schematic of the laser diode setup. The emission laser beam is focused onto the sample with a microscope objective. A weak reflection from the laser beam is transmitted to a CCD camera allowing positioning the laser. A white light source allows visualizing the sample.

3.4.6 UV-VISIBLE SPECTROSCOPY

Most organic materials are transparent in the ultraviolet and visible regions of the electromagnetic spectrum, which spans from approximately 200 to 800 nm. For those materials that absorb in this range, UV-visible spectroscopy consists in a simple, non-destructive technique, which provides useful information about absorbing solutes, such as concentration and molecular structural information. The method can also be useful for complex tasks as monitoring the evolution of chemical reactions.

Absorption occurs when light passes through a transparent material with intensity I_0 and exits from this material with a reduced intensity I_λ. In dilute solutions, absorbance (A) at a given wavelength is defined as log function of the ratio of incident light (I_0) over the reduced

intensity (I_λ). In turn, this relationship is also equal to the multiplication of the molar concentration of solute (c) by the molar absorptivity of the solute (ε) by the distance the light has to travel through the material (l_λ). This second relationship, known as the Beer-Lambert Law is rigorously obeyed when a single molecular species of is responsible for the absorbance observed. Due to the linear relationship between absorbance and concentration, it is possible to determine the concentration of a known solute providing that molar absorptivity is known for this solute.

Eq. 3.1 $$A_\lambda = Log\left(\frac{I_{o,\lambda}}{I_\lambda}\right) = \varepsilon_\lambda cl$$

At the molecular level, light absorption is a mechanism by which the excitation energy corresponds to the energy gap between the electronic ground state and excited state. The most likely electronic transitions of this type occurs from the highest occupied molecular orbital (HOMO) to the lowest unoccupied molecular orbital (LUMO) The relationship between the different energy levels is illustrated in Figure 3.9. In other words, HOMO and LUMO are the lowest energy molecular orbitals, which contain excitable electrons and can accept excited electrons, respectively. The typical energy difference between these electronic levels is in the order of 100-650 kJ/mol. The order of electronic energy levels increases in the order σ, π, n, π*, σ*. Molecules that absorb UV-visible light possess diffuse spectra with relatively broad absorbance peaks as opposed to sharp ones. This is because each electronic state usually contains several vibrational and rotational energy levels that are overlapping the electronic levels. The energy between these sub-energy levels is rather small in comparison to the energy separating electronic levels so that several types of vibrational and rotational electronic transitions are possible from the same excitation source. As a consequence, a large population of molecules will display a peak that accounts for all these transitions as well as other processes (*e.g.* quenching from the solvent molecules) giving the greatest absorbance value at a point that corresponds to where the electronic transitions are most frequent.

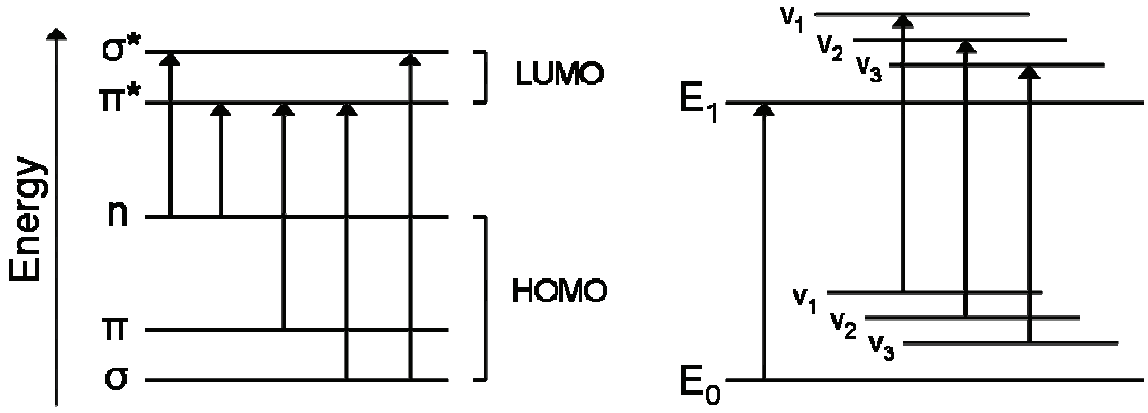

Fig. 3.9 Energy diagram illustrating the possible electronic transitions from the HOMO to the LUMO molecular orbitals (left). The electronic ground and excited states contain distinct rotational and vibrational states (right).

UV-visible spectroscopy was used for quantification purposes in the synthesis of PAH derivatives as well as for qualitative purposes for photochromic substances and gold nanoparticles. UV-vis spectra were measured in quartz or plastic cuvettes using a CARY 50 conc. (Varian, Germany) UV-Vis spectrophotometer. Spectra were always recorded against an appropriate blank sample.

3.4.7 FLUORESCENCE SPECTROSCOPY

Fluorescent spectroscopy was used to monitor the emission spectra of TPPS in solution and as a complex in the shell of microcapsules. There are various mechanisms by which the energy of a photon absorbed by a molecule can be release. If the relaxing electron emits a photon, the process is termed luminescence and can be divided in two groups named fluorescence and phosphorescence. In phosphoresce the excited electron undergoes a forbidden energy state transition to an energy level of higher spin multiplicity (usually a triplet state). In fluorescence, the energy state transition occurs between levels of same spin multiplicity (singlet state). Unlike phosphorescence, the excited electron remains in this state for a relatively short time of the order of 10^{-8} seconds. In luminescence the excited electron loses energy in this state due to vibrational and rotational motions and collisions, which results in an energy difference between the exciting photon and the emitted photon. The emitted photons consequently have a lower energy than the absorbed ones and thus, the photons emitted have a longer

wavelength then the excitation source. The energy gap between the absorbance curve and emission curve maxima is called Stokes shift.

The Fluorescence spectra were recorded on Spex Fluorolog-2 (model Fl-2T2) spectrofluorometer (ISA, Olching, Germany) at room temperature. The excitation wavelength used throughout the experiments was 420 nm.

3.4.8 ATOMIC FORCE MICROSCOPY

Atomic force microscopy (AFM) is an ideal technique to probe surfaces at higher magnifications than possible with radiation-based microscope. This is because AFM relies on the atomic interactions between the surface probed and a tip attached to a flexible cantilever. The cantilever is itself connected to piezoelectric actuators and moved in a 2 dimensional raster pattern. A laser is reflected off the end of the cantilever to a photodiode array detector. As the tip encounters attractive or repulsive forces, the cantilever is moved in the z directions according to Hooke's law resulting changes of the angle of the laser. A computer interface recreates an image of the signal received from the detector as color-coded pixels.

A scheme of a typical AFM setup is illustrated in Figure 3.10. AFM is typically operated in one of two modes. In contact mode the position of the tip relative to the surface is fixed. Due to the close interaction of the tip with the substrate and the shear forces involved, contact mode is primarily designed to probe for smooth, hard materials. Soft material are preferably investigated in tapping mode, the cantilever is excited to vibrate in the vertical direction close to its resonance frequency by an additional piezo. As a result the tip-surface interactions are damped as frequency is decreased. This method largely reduces the specific interactions between the tip and the substrate, preventing the latter to be damaged during scanning.

AFM measurements were performed in air at room temperature using a Nanoscope III Multimode AFM (Digital Instruments, USA) operating in tapping mode. The samples were prepared by placing a drop of the sample solution onto a freshly cleaved mica substrate and drying at room temperature. The wall thickness and roughness of capsules were calculated by averaging the corresponding values from flat regions (areas of dried capsules wall that did not display folds) of 30 capsules using a software.

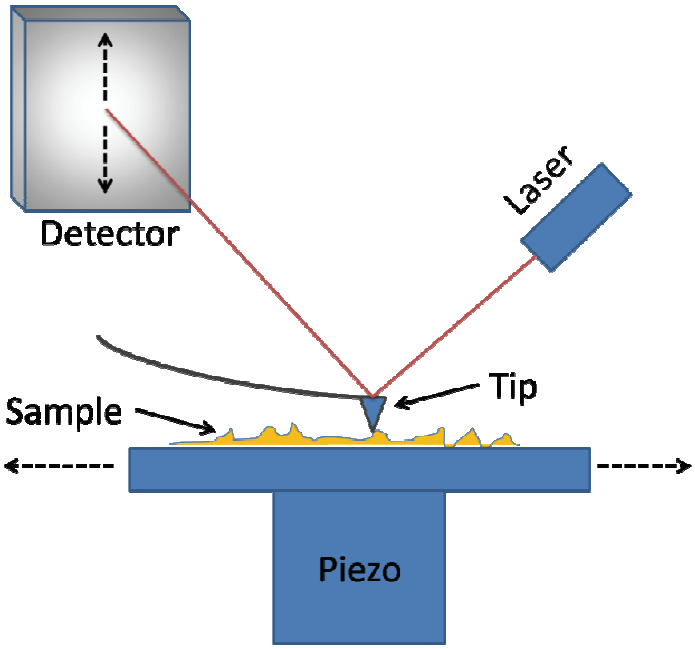

Fig. 3.10 Schematic of AFM technique. As the piezo moves the sample relative to the tip, the latter follows the surface morphology, deflecting a laser beam reflected towards a detector.

3.4.9 COLLOIDAL PROBE ATOMIC FORCE MICROSCOPY

Besides its imaging capability, AFM can be employed in force spectroscopy. As such, the AFM can be used to measure forces 10^{-11} and 10^{-6} N and deformations up to 1 mm. [208] The colloidal probe technique was used for the force deformation measurements to measure the elastic constants of the capsule wall material in shells containing different amounts of gold nanoparticles. Ignoring permeability changes, polymeric microcapsules respond to a small deforming force with a proportional restoring force. [209] In this linear range, the Reissner relation of shell deformation can be used to measure the stiffness χ, which is defined as the ration of the deformation force F_{def} and the deformation δ_c, with the wall thickness h, radius r, Poisson ration v_p and Young's modulus E_m: [15]

Eq. 3.2
$$\chi = \frac{F_{def}}{\delta_c} = \frac{4}{\sqrt{3\left(1-v_p^2\right)}} \bullet \frac{E_m h^2}{r}$$

Knowing the capsule properties, one can determine E_m using the force distance curves from colloidal probe AFM.

A MFP1d (Asylum Research, USA) AFM instrument was used for measurements of shells in water, at room temperature. The AFM was placed atop of an inverted optical microscope (Olympus IX71, Japan) so that fluorescence microscopy could be used to locate and monitor the capsules during the experiment. Colloidal particles (glass beads, diameter ≈ 30-50 μm, Polyscience Inc., USA) were attached to tipless cantilevers (MicroMash, Spain) with a two component epoxy glue (UHU Plus endfest 300, UHU GmbH & Co.KG, Germany) using a micromanipulator (Suttner Instrument Co., USA). The spring constants of the cantilevers were determined using the thermal noise method [210] and the Sader method. [211] Both methods agreed within 10 % and values of the spring constants were in the range reported by the manufacturer. A droplet of the solution containing the capsules was placed onto a coverslip which was previously coated with PEI such that the capsule adhered to it. During the experiment, individual capsules were compressed and both the force and the deformation of the capsule were measured. [15,212] Only deformations on the order of the wall thickness of the capsules were measured, in order to avoid plasticity and effects due to the permeation of the solvent through the capsule membrane. [213] For each data point, 5 – 45 capsules were measured.

3.4.10 ELECTRON MICROSCOPY

Electron microscopy is a powerful method to image materials in terms of morphology, topology and composition. In this group of techniques, an electron beam is accelerated in an electric field towards a surface.

Like other microscopy techniques, the resolution δ of electron microscopes follows the Abbe equation where λ is the wavelength used and NA corresponds to the numerical aperture of the magnifying objective.

Eq. 3.3 $$\delta = \frac{0.61\lambda}{NA}$$

A much higher resolution can be obtained from electron microscopy because electrons have energies nearly four orders of magnitude greater than light and correspondingly shorter wavelengths.

3.4.10.1 SCANNING ELECTRON MICROSCOPY

In scanning electron microscopy (SEM), an electron beam focused to 5 nm scans across a sample. Electrons are being back-scattered along with secondary electrons emitted from the sample towards a detector which results in high resolution image reconstructions of the sample. This technique was primarily used to obtain visual information about the quality and roughness of the microcapsules samples. SEM measurements were conducted with a Gemini Leo 1550 instrument at an operation voltage of 3 keV. For the measurements, a drop of a dilute capsule solution was placed on a glass wafer, left to dry under nitrogen and sputtered with gold.

3.4.10.2 TRANSMISSION ELECTRON MICROSCOPY

In transmission electron microscopy (TEM), electrons pass through a thin sample before being directed to a detector, providing information about the composition of the sample investigated. TEM was used to monitor the distribution of gold nanoparticles in microcapsules due to the large contrast differences that TEM yield between metal nanoparticles and polyelectrolytes. TEM measurements were conducted using a Zeiss Omega EM 912 at an operating voltage of 120 kV.

3.4.11 DIFFERENTIAL SCANNING CALORIMETRY

Differential scanning calorimetry (DSC) provides information about transition temperatures and enthalpies of a material by monitoring the heat capacity (C_p) of the probe at constant pressure. The instrument consists of a reference and a sample chamber each coupled to a heating and a cooling device in an insulated jacket. The chamber contains equal volumes of a reference liquid and a probe solution and the chambers' temperature is controlled by a program to be always equal. During the experiment, the program calculates the power difference needed to maintain the temperature of the sample equal to that of the reference. Enthalpy changes in the probe result in the program telling the sample chamber to heat or cool down to match the reference cell. These differences in C_p appear as spikes. For first order transitions, taking the first derivative of the curve typically yields a step at the glass transition point.

DSC measurements of capsules were performed in water using a MicroCal-VP DSC (MicroCal Inc. United States of America). Prior each measurement, the capsule suspension was degassed under vacuum for 15 minutes. Temperature scans were performed at a rate of 0.5°C

min^{-1} after 10 minutes of equilibration at 10°C. The thermogram of the reference water chamber was subtracted from thermogram of the sample. To determine the temperature range at which a glass transition occurred, thermograms were used as such without further mathematical treatment and the approximate glass transition value was determined as the temperature with the highest C_p within the transition region.

3.4.12 DYNAMIC LIGHT SCATTERING

Dynamic light scattering (DLS) is a technique used to determine the size distribution of small particles in solution. The electric component of light can create an oscillating dipole in the electron cloud of an irradiated atom. This light is irradiated back at various, scattered angles from the normal (Raleigh scattering) as the dipole fluctuates. Scattering of light occurs in all directions when sufficiently small particles (1 mm or less) are illuminated. When the incident beam is laser light, the scatterers create a time-dependant fluctuation in intensity. This is due to the constantly changing distance between the scattering particles in solution (Brownian motion) and results in constructive and destructive interference patterns which contains information about the motion, size and concentration of the particles. This method is very sensitive to particle size since thermal motions are greater for smaller objects. Motions are determined using a correlation function that quantifies the non-randomness of the measured signal. This is done by comparing the signal's intensity with subsequent intensities which should come from the same particle. If the motions are too fast, the scattering from particles cannot be correlated with the original particles' positions and diffusion cannot be calculated. A typical DLS gives an autocorrelation curve as an exponentially decaying function. Particle size or hydrodynamic radius R_H is extracted from this function using the Stokes-Einstein-Sutherland relationship:

Eq. 3.4
$$R_H = \frac{k_B T}{6\pi\eta \cdot D}$$

Where k_B is Boltzmann's constant, T the temperature, η the viscosity of the medium and r the radius of the particles and D the diffusion constant.

DLS was used to determine the growth of gold nanoparticle aggregates in solution. For measurements a small volume of gold nanoparticle solution (10^{11} nanoparticles/mL) was transferred to a transparent capillary cell and placed in a thermostated cavity. When a 23°C

temperature was attained, a He/Ne 488 nm laser beam was directed through the sample and scattered light was recorded at a 5-10° angle on a photomultiplier connected to a multichannel analyzer. A beam blocker assured that the primary beam from the incoming source did not reach the detector, which would have saturated the measured signal. Measurements were made on a High Performance Particle Sizer, Malvern Instruments (USA).

3.4.13 ZETA POTENTIAL

The ionic environment at solid-liquid interfaces is organized in a way that insures electroneutrality is preserved despite the fact that the solid surface may itself possess a net charge. As a result, ions with a charge similar to the surface are repelled and ions with a charge opposite tend to remain close to it due to Coulomb interactions. The ions, however, have thermal energy and are allowed to move on the surface resulting in what can be described as an electrical cloud rather than a fixed layer of ions. The electrical potential thus decreases as away from the surface. Figure 3.11 illustrates this phenomenon known as the electrical double layer for a charged colloidal particle.

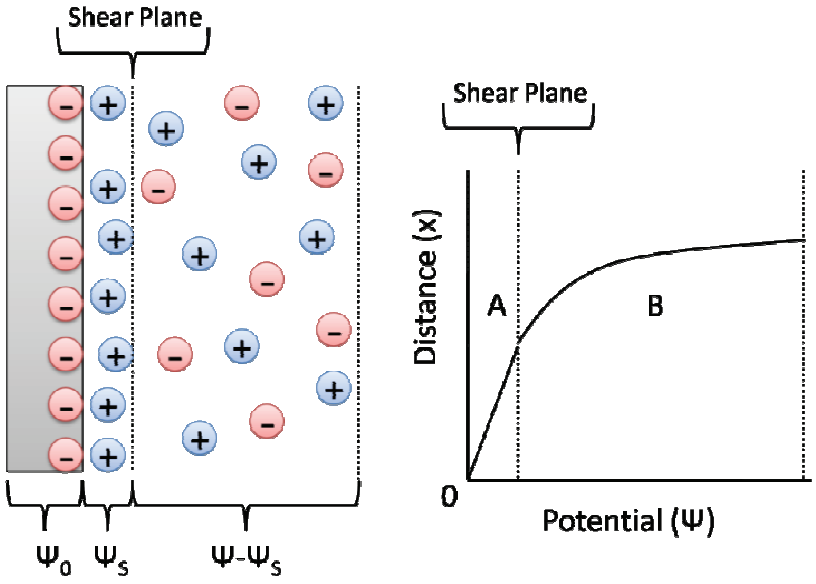

Fig. 3.11 The electrical double layer describes the change in electrical potential of a charged substrate with surface potential Ψ_0 in solution. It is best described by the Stern Model which consists of the Stern Layer (A) where ions are tightly bound to the surface and a potential Ψ_S, as well as the diffuse layer (B).

Two models are commonly used to describe the variation in electrical potential as a function of distance from a charged substrate in solution. The Gouy-Chapman model describes differences between ions near charged substrates against those in the bulk. It states that in the diffuse ion layer, the distribution of ions depends on electrostatic interactions and thermal motions. The Gouy-Chapman model describes the potential Ψ at a distance x from the surface and a Debye length κ^{-1} can be described by the Debye-Hückel approximation:[214]

Eq. 3.5 $$\psi = \psi_0 \exp(-\kappa x)$$

Equation 3.5 shows that the potential exponentially decays from the surface potential Ψ_0 and that this decay depends on the ion concentration and valency (due to the dependency on the Debye length, see Equation 2.9). The main outcome of this model is that the thickness of the electrical double layer decreases with increasing ionic strength (> $1/\kappa$). However, the Gouy-Chapman model makes several important assumptions which are not valid for ions at the surface, the most important of which is that the model requires ions to be treated as point charges, neglecting the ions' radii. Equally important is that by assuming ions are point charges one would expect that oppositely charged ions can be infinitely close to one another in the electrical double layer. That is clearly not the case.

The Stern model takes specific ion adsorption into account by introducing an area termed the Stern Layer to electrical double layer to define the ions that are bond strongly enough to the surface that they are relatively unaffected by thermal motion. The Stern potential Ψ_S describes the linearly changing potential within the Stern Layer from the theoretical surface potential Ψ_0 up to the Gouy-Chapman Layer (or diffuse layer) where ions are mobile and the potential decreases exponentially.

Colloidal particles have a charged surface without which they would immediately precipitate out of solution. Particles and their electrical double layers can move relative to the surrounding liquid under the influence of an applied field. The surface charge of a particle in solution can thus be determined by measuring its electrophoretic mobility in an electrical field. The ζ potential is a number that describes ion mobility at the *shear plane* where the diffuse layer potential is highest. The ζ potential cannot be used to evaluate surface potential within the Stern Layer because ions there cannot readily move. Although the microelectrophoretic technique used is often doubtful, it is useful in to measure assure that charge reversal is obtained upon LbL addition. Failure to completely absorb a layer would result in a ζ potential

with the same sign as the previous layer and could partially explain why certain microcapsule construction do not keep their integrity upon core dissolution. The electrophoretic mobility u of a colloid particle in a given electric field E is related to the ζ potential, the solvent viscosity η and the dielectric constant according to the Smoluchowski equation:

Eq. 3.6 $$\zeta = \frac{u\eta}{\varepsilon E}$$

ζ potential measurements were performed in water using a Zetasizer Nano (Malvern Instruments, Germany). The values measured were averaged from 3 cycles of 10 measurements.

3.4.14 QUARTZ CRYSTAL MICROBALANCE

Quartz crystal microbalance (QCM) was used to evaluate the amount of absorbed materials during the LbL process. QCM is used to determine the mass per unit area by measuring the change in quartz crystal fundamental frequency. Although this technique cannot be used to determine the amount of material adsorbing onto particulate matter, it enjoys a measurement accuracy to the nanogram range and provides information that may be extrapolated to microcapsule assemblies. The technique of QCM is based on the principle that a piezoelectric quartz crystal has a fundamental frequency that changes linearly with mass as materials are deposited on it. A QCM crystal is a thin glass wafer coated on both sides with layers of gold which act as electrodes. Applying an alternating current across the electrodes induces the crystal oscillate as a standing wave is generated. The QCM technique usually measures the change in fundamental quartz plate frequency F_1 and its odd harmonics F_v, where v is a positive odd integer. The Sauerbrey equation can be used to relate the mass of absorbed material m on the quartz surfaces to the frequency change ΔF_v, where the shear modulus of quartz μ_q is 2.95 x 10^{11} g/(cm·s^2), the density of quartz ρ_q is 2.65 g/cm^3 and the electrode area is A: [215]

Eq. 3.7 $$\frac{\Delta F_v}{v} = \frac{2F_1^2}{A\sqrt{\mu_q \rho_q}} m$$

This equation is valid to calculate the mass of absorbed material in vacuum and error will arise in a humid atmosphere or if the quartz is measured in liquid because density and viscosity of the medium are bound to affect the quartz's frequency. [216]

The multilayers were deposited on AT-cut 8.86 MHz quartz crystal electrode was coated with the desired multilayer structure using a Polyion 1M dip-coating robot (Saratov State University, Russia).[217] The system built in-house consists in a sample holder held by a robotic arm fitted with a z-axis motor for dipping the substrate and a short-range x-axis motor for shaking the sample. The solutions (polyion and wash) are set in a circle about a plate which rotates and positions each solution beneath the sample. The dipping plate used was fitted with 8 solution wells, 2 polyions and 3 wash solutions for each polyions, allowing the multilayer coating to proceed cyclically without exchanging solutions. The system is controlled through a series of ports by a custom made computer interface via a Win32 platform. The interface allows for z-axis distance, dipping time, mixing and the number of dipping cycles to be controlled for each solution.

For the multilayer assembly, a base layer of PEI (2 mg/mL, 0.5 M NaCl) was first deposited. Solutions of PAH, PDDA and PSS were used at 2 mg/mL and 0.5 M NaCl. The dye solutions contained 0.1 M dye in 0.5 M NaCl. The crystal was dried under nitrogen for 10 minutes before resonance was measured. With the setup described here, Equation 3.7 becomes:

Eq. 3.8 $$\Delta F_v = 2.3\times10^6 \frac{F_1^2 \times m}{A}$$

where A is 0.25 cm^2. The quartz fundamental frequency was compared against the manufactors' specifications during calibration before any polyelectrolyte layer was deposited. A graph of layer number against ΔF or m was plotted to follow LbL progression

3.4.15 NUCLEAR MAGNETIC RESONANCE

Nuclear magnetic resonance measurements were made in an attempt to characterize the substitution ratio of azobenzene-substituted PAH. ^{1}H NMR spectra could be used to calculate the substitution ratio by rationalizing and comparing the integration values of single protons from the polymer backbone against the single protons of azobenzene side chains. Unfortunately, signals of the azobenzene molecule were too weak for quantification, within the error associated with the background noise. The phenylic signals for instance, appeared between 7 ppm and 8 ppm but were too low for quantification purposes. ^{1}H NMR measurements were recorded using a Bruker spectrophotometer (600MHz).

4 EFFECT OF ULTRAVIOLET LIGHT ON POLYELECTROLYTE MICROCAPSULES

In this chapter, the behavior of various microcapsules upon near-UV irradiation is investigated. To improve the sensitivity of the microshells to near-UV, four azobenzene-substituted polyion derivatives were incorporated in the shell construct. Such microcapsules allow for the encapsulation of materials by simple exposure to continuous wave UV irradiation.

4.1 EFFECT OF NEAR-ULTRAVIOLET IRRADIATION ON MICROCAPSULES

4.1.1 PULSED UV IRRADIATION OF MICROCAPSULES WITH NO INTRINSIC UV ABSORBANCE

The first logical step in order to develop new UV responsive polymeric microcapsules was to study how this otherwise well characterized material behaves under exposure to UV irradiation. Thus, the effects of high intensity pulsed-UV laser on polymeric microcapsules were first investigated. Irradiation experiments were conducted using a pulsed Nd:YAG laser operating at 355 nm and providing fluencies up to 1 J/cm^2. Parameters such as the duration of laser exposure and power density were studied in order to estimate the minimum irradiation requirements necessary to damage capsules containing no specific UV chromophores.

The model system studied consisted of eight bilayers of PAH/PSS or PAH/PVS assembled using the LbL self-assembly protocol (see *Section 3.3.3*) onto 10.25 μm PS sacrificial particles. The PAH/PSS polycation/polyanion combination was chosen because it has been extensively investigated in previous work and is known to form stable multilayer films. [113,218] PVS was also chosen as an alternate polyanion due to its structural similarity with PSS (both are poly(sulfonates)) but also because unlike PSS it possesses no UV chromophores. Yet, none of these polymers absorb significantly at 355 nm. This is shown in Figure 4.1 for 1 mg/mL solutions of each polyelectrolyte. While PVS and PAH display cutoff absorption regions, it should be noted that the polyion PSS possesses an absorption maximum at around 225 nm, which is not shown in Figure 4.1 to emphasize that its absorption at 355 nm is negligible (see Figure 6.6 for an example of the full absorption spectrum of PSS). Microscopic images taken using LSCM in transmission mode revealed that the capsule samples were homodispersed, spherical as illustrated in Figure 4.2.

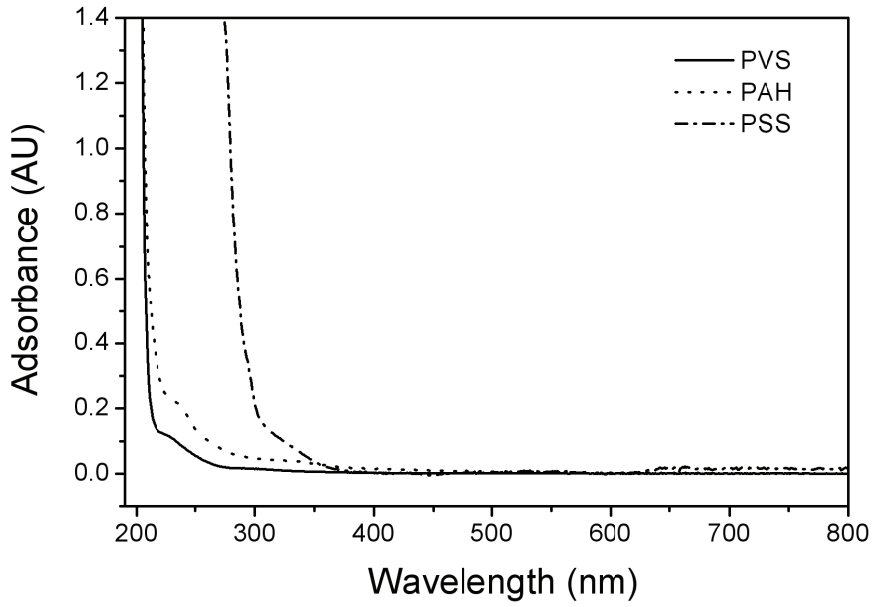

Fig. 4.1 Absorbance spectra of PVS, PAH and PSS.

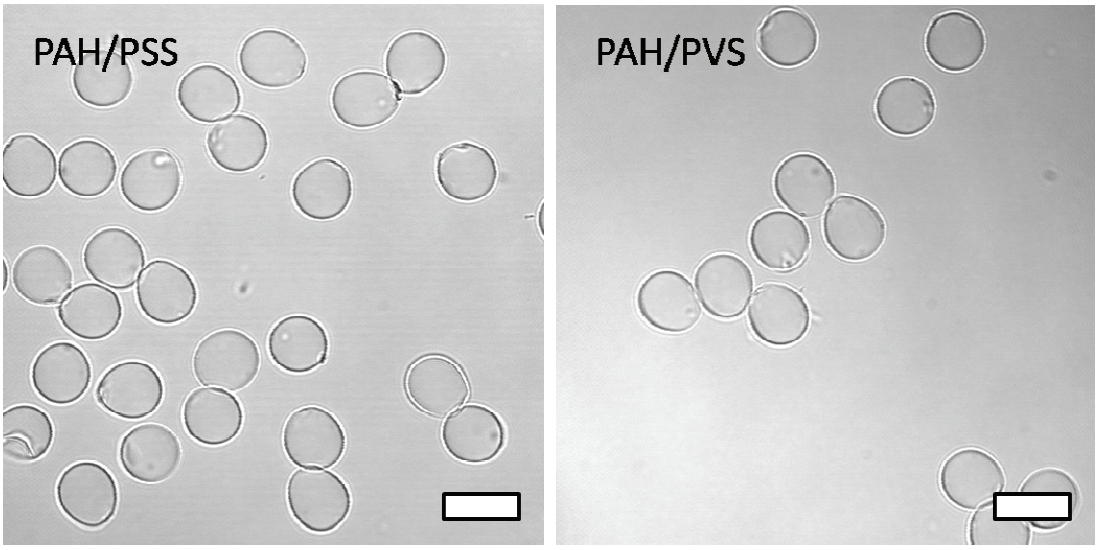

Fig. 4.2 Microscopic images of PAH/PSS and PAH/PVS microshells. Scale bar measure 15 μm.

To irradiate the microcapsules solutions with pulsed UV, sample chambers were prepared and loaded with 20 µL of capsule suspension. The glass surfaces were first cleaned and treated with PEI (10 mg/mL) solution to prevent the microcapsules from moving according to the protocol described in Section *3.3.5* (capsules with PSS as the outermost layer bind to PEI-coated substrates). Microscopic images were then taken from a marked area of the sample chamber and again after pulsed UV irradiation. Representative images of the results are presented in Figure 4.3.

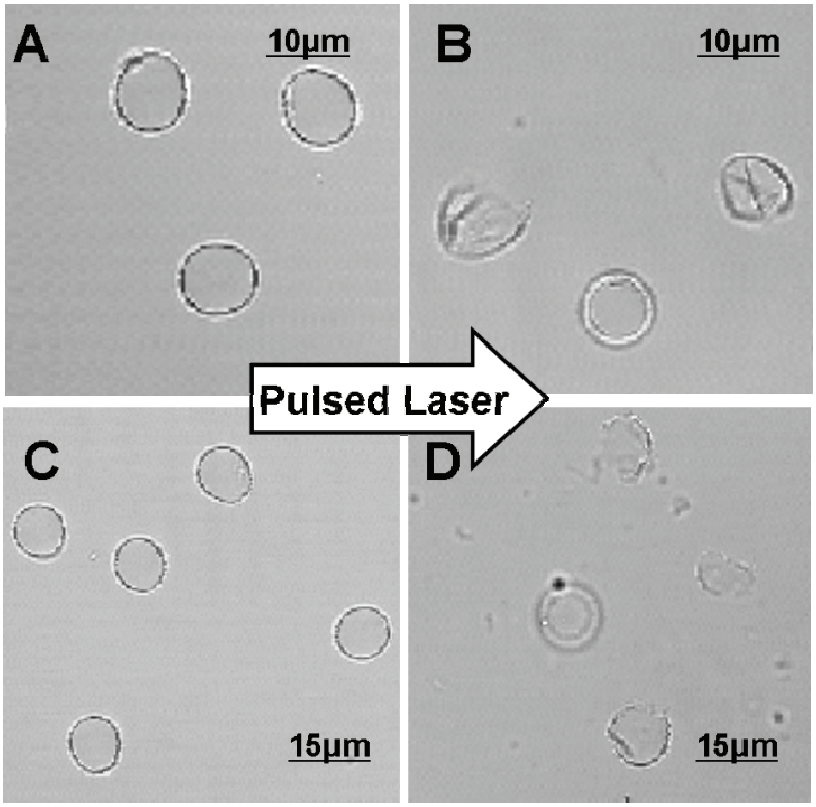

Fig. 4.3 UV-laser ablation effects on $(PAH/PSS)_4$ microcapsules in water after exposure to pulsed UV irradiation at 355 nm. Top: sample area containing three capsules before (A) and after (B) laser irradiation with 20 laser pulses (70mJ/cm^2). Bottom: five capsules before (C) and after (D) exposure to 10 laser pulses (200 mJ/cm^2).

Pulsed near-UV irradiation at 355 nm was found to leave the capsules undamaged when using relatively low laser fluencies (<40 mJ/cm^2) after an exposure time of up to one hour (35 ps per pulse, repetition rate of 10 Hz). Above fluencies of 40 mJ/cm^2 capsules became

gradually more deformed and/damaged with increasing power density (*i.e.* fluence) and duration. This is illustrated in Figure 4.3 before (A) and after (B) exposure to the UV laser beam for $(PAH/PSS)_8$ microcapsules at 70 mJ/cm^2. At laser fluencies greater than 100 mJ/cm^2, the microcontainers became severely damaged after only a few pulses. The $(PAH/PSS)_8$ shells in Figure 4.3 C were irradiated with 10 pulses at 200 mJ/cm^2 resulting in some shells appearing as if cut to pieces (D). There was no difference in the general response to irradiation between $(PAH/PSS)_8$ and $(PAH/PVS)_8$ capsules. Because the investigated capsules lacked significant UV absorption at the wavelength used, the damages observed could be attributed to a combination of the effects of the pressure created by the incoming pulse [219] acting on relatively weak capsules [84,103] and plasma generation [144] (which depends on factors such as molar absorptivity, penetration depth of the laser beam and wavelength).

These results are in agreement with similar work published at the time these experiments were being conducted, where the authors who used continuous wave (CW) near-UV concluded that the microcapsules containing near-UV absorbing chromophores (*i.e.* PSS/PDDA, DNA/PAH, PSS/PAH) were degraded to various oligomers, ions, radicals and oxides upon UV exposure and that this effect is dependent on the duration and intensity of irradiation. [157] It was suggested that the decomposition products originate from the destruction of capsule materials that absorb significantly in the near-UV such as the aromatic styrene groups of the polymer PSS with an absorption maximum at ~225 nm. The capsules remained seemingly unaffected by UV when constructed from only non-aromatic polymers. While capsules damaged by this approach could also be effectively opened to release encapsulated substances, UV ablation is a very energetic process which could equally damage the encapsulated substance.

Köhler and coworkers recently reported that certain capsules undergo an important shrinking when heated in water at high temperature (see *Section 2.6.1*). [129] Capsules in the experiments reported here were never found to shrink in the center of irradiation or its periphery in any samples. From these observations, it was concluded that the destruction of a capsule is probably due to absorption of UV by its materials and not by a temperature increase of the solution. Another consequence of irradiation is that capsules tend to detach from the substrate as they interact with the laser. Adhesions of PAH/PSS capsules onto charged substrates due to electrostatic interactions has been shown to be strong but non-specific. [220] As a result, it was found that that the momentum carried by laser pulses was sufficient to displace some capsules

away from the irradiation center, [221] which made the experiments difficult to reproduce and unsuitable for quantification.

4.1.2 PREPARATION AND IRRADIATION OF AZO1-PAH/PSS MICROSHELLS

To improve UV sensitivity of the microcapsules and attempt to lower the energy requirements to induce changes in the microshells, the polyelectrolyte PAH was modified by replacing a portion of its amino groups by the functional UV responsive molecule phenylazobenzoic acid (Azo1, see structure in Figure 3.5). Azo1 is a low solubility yellow compound with a maximum absorption peak at 325 nm (Figure 4.4). The strategy employed involved grafting the azobenzene molecule possessing a carboxylic acid functional group onto an amine group of PAH using a carbodiimide (EDC) reagent catalyzed by NHS (see Figure 3.4). The reaction goes as follows: once activated with NHS, the carbodiimide bridge of EDC is attacked by the carboxylic acid group of the azo molecule. The primary amine of PAH then attacks the EDC-bound carboxylic group in a sp_3 type reaction yielding an azo-substituted amine group as well as a proton and a urea complex. An amide bond is formed in the grafted polymer. The principal advantages of this reaction are that it is performed as a one-pot synthesis and results in no additional atom between the substitute and the host molecules. However, the reaction reagents are quite sensitive to light so the reaction was conducted in darkness. Room temperature must be used for the reaction due to the poor solubility of the azobenzene substituent at low temperature. Another disadvantage is the low yield of the reaction, estimated to reside between 10 % and 20 % depending on the reaction conditions. The reaction was conducted in buffer to help maintain the solution pH throughout the reaction.

Several failed attempts to synthesize Azo1-grafted PAH with a high Azo1/amine grafting ratio were attributed to the high viscosity of the synthetic soup required for the reaction and/or to the decreasing solubility of the modified PAH as its amino functions are replaced by the far less soluble Azo1 group. It was determined that a 5 % target substitution ratio insured both the presence of Azo1 and that a sufficient proportion of charges along PAH remained for complexation with a polyanion to occur once microshells would be built. [155] After dializing the new polymer for seven days against water, the presence of Azo1 on PAH was confirmed by UV-visible spectroscopy (Figure 4.4). The new polymer was named Azo1-PAH.

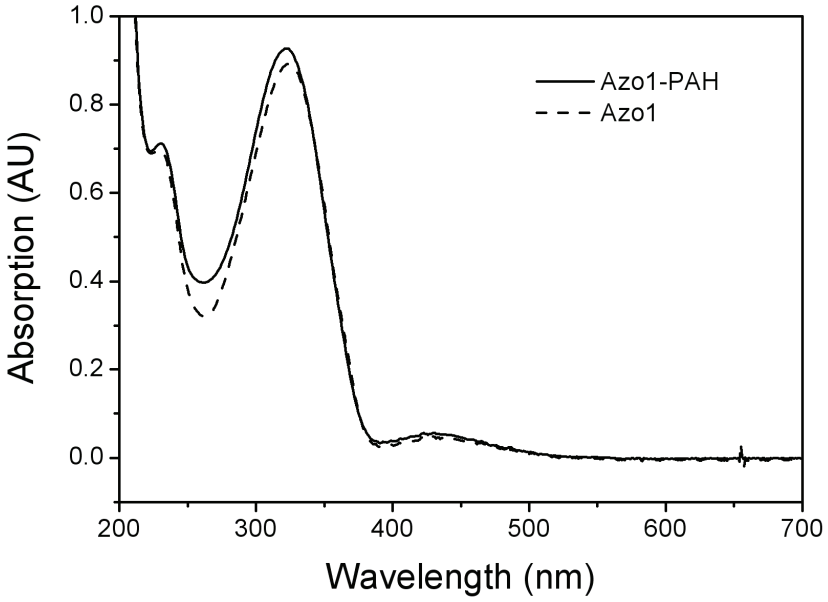

Fig. 4.4 Normalized UV-visible spectra of Azo1 monomer and Azo1-PAH in water.

Azo1-PAH was used to construct microcapsules with $(Azo1\text{-}PAH/PSS)_8$ shells which appeared identical to $(PAH/PSS)_8$ microcapsules when observed in a bright field microscope. There was no significant difference in the diameter of the two types of capsules which were measured by LSCM to be 10.15 μm and 10.07 μm for Azo1-PAH/PSS and PAH/PSS shells, respectively. $(Azo1\text{-}PAH/PSS)_8$ capsules however, possessed much thicker shells than that of typical $(PAH/PSS)_8$. Figure 4.5 shows SEM images of a $(PAH/PSS)_8$ shell (A) and a $(Azo1\text{-}PAH/PSS)_8$ shell (B). This apparent change in thickness was supported by AFM measurements which revealed that the average bilayer thickness of $(Azo1\text{-}PAH/PSS)_8$ capsules is 6.5 nm, thicker than capsules built from the PAH/PSS pair which was reported to be 3.9 nm ±0.2. [16] This change in wall properties along with the assumption that Azo 1 gives capsules an increased capability to absorb UV light led us to hypothesize that the requirements to damage Azo1/PSS particles could be different than those needed to observe damage in PAH/PSS capsules.

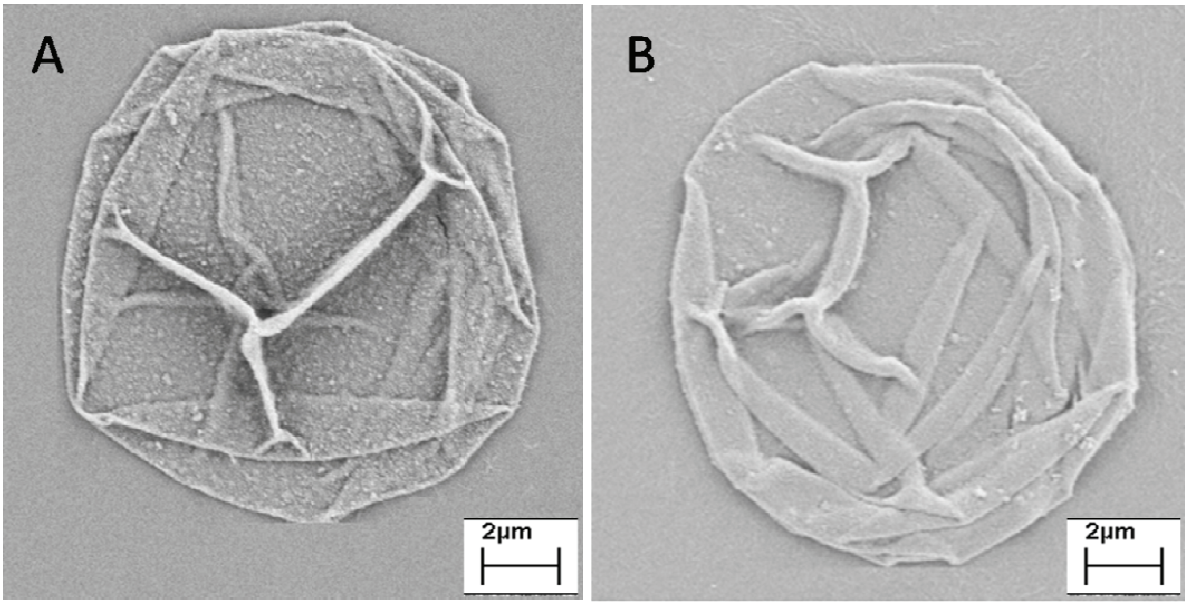

Fig. 4.5 SEM images of a $(PAH/PSS)_8$ capsule and $(Azo1\text{-}PAH/PSS)_8$ capsule, A and B respectively.

Capsules were successfully destroyed using a coherent high intensity 355 nm laser source. The results were surprisingly similar to those obtained for $(PAH/PSS)_8$ and $(PAH/PVS)_8$ capsules. At a fluence of 30 mJ/cm^2, no significant change in capsules morphology was observed after up to 300 seconds of irradiation. At higher fluencies the capsules were found to become damaged.

A much more efficient method was demonstrated by Katagari *et al.* recently who showed that organic-inorganic microcontainers impregnated with TiO_2 rupture upon exposure to CW near-UV light at relatively low intensity (5-20 mW/cm^2). [160] The current model to explain the destruction of certain types of metal-containing microcapsules by irradiation that the nanoparticles act as absorbing centers that mediate an accumulation of thermal energy within the multilayered shell which in turn leads to the destruction of this one. [21,222] Similarly, UV light is absorbed by the polymers used in our experiments and this energy is released as heat in the surroundings. The densely packed structure of absorbing polymer in the multilayers acts as an insulator rendering heat dissipation away from the capsules difficult. When a sufficient amount of heat is stored in this process, accumulation results in a local melting of portions of the wall from a glassy to a viscoelastic state. [15] Since the melting behavior of polymers depends on a variety of factors and that it differs significantly from one polymer structure to another, [223]

such state transitions are expected to be rather unevenly distributed within the capsules wall producing a large mechanical stress within the multilayers. At reasonably low energy, this state transition would lead to the deformation of the shell while larger amounts of absorbed energy induce a stress sufficient to buckle the capsule wall. This is also consistent with previous report for other IR-absorbing organic dyes. [21] Based on this model, another explanation for the behavioral similarities between Azo1-PAH/PSS and PAH/PSS or PAH/PVS capsules upon UV exposure was put forward. While Azo1 was shown to absorb more light and could be expected to produce more heat, the nearly-doubled wall thickness of Azo1-PAH/PSS capsules grants them with an increased heat storage capacity. As a result, it appears as though both types of capsules have similar time of exposure and beam intensity requirements for damage to occur, but it can be hypothesized that the increased volume of Azo1-PAH/PSS capsules compensates its increased heat production capacity.

4.2 UV-TRIGGERED ENCAPSULATION IN AZOBENZENE CONTAINING MICROCAPSULES

An interesting group of molecules called azobenzene that responds to both near-UV and visible light were introduced in the previous section as a mean to introduce a UV sensitive molecule into the construct of microcapsules. Azobenzenes are molecules that contain two phenyl groups joined by a N=N bond. [147] Azobenzene groups respond to UV absorption by undergoing reversible internal rearrangements termed *cis-trans* (Z-E) isomerizations (see Figure 2.8). Thermal isomerization typically occurs from the least stable *cis* to the most stable *trans* form (Z→E), while optical isomerization can occur either way. At the molecular level, these *cis-trans* isomerizations come with significant changes in terms of molecular geometry and polarity, but they are rather weak when incorporated in large systems. Although we observed no difference between PAH/PSS or PAH/PVS microshells and shells functionalized with an azobenzene upon pulsed UV irradiation it was of interest to verify the effect of this isomerization in microcapsules using CW light.

4.2.1 SYNTHESIS OF AZO-PAH DERIVATIVES

Commercially available azobenzene-substituted polyelectrolyte derivatives are scarce but azo dyes are common. Various azobenzene molecules absorb light predominantly in the near-UV

region but also in different spectral ranges and have widely varying stability in the least favored conformation, usually the *cis* form. Therefore, to add to the versatility of this study, a series of azobenzene-PAH derivatives were prepared. The substitution of Azo1 (discussed in the previous section), 2-(4-hydroxyphenylazo)benzoic acid (Azo2) and methyl red (Azo3) to PAH was accomplished using a carbodiimide linker to bind the amino group of PAH to a carboxylic acid of the Azo moiety. The structures of Azo 1, Azo 2 and Azo 3 as well as an example of Azo-PAH are shown in Figure 3.5. It should be noted that the presence of a carboxylic acid group on the monomers is required in order for this reaction to proceed, whereas the presence (or absence) of other functional groups on the monomers gave us different λ_{max} to work with.

In a typical reaction, a mass of PAH was dissolved in buffer followed by the addition of the desired mole percent of azobenzene molecule. The molar quantity of azobenzene corresponding to a target grafting ratio was multiplied by five to account for the low reaction yields observed in the synthesis of Azo1-PAH. Using a tenfold multiple of the azobenzene target molar ratio led to a viscous reaction mixture that appeared to produce an emulsion during the reaction and yielded very poor grafting ratios. The catalyst NHS was weighed and added to the reaction flask and left to completely dissolve. Finally, the linking reagent EDC was added to a separate aliquot of water, which once completely dissolved was transferred to the reaction vessel. The yellow or orange mixtures were left to stir in darkness overnight.

The azobenzene monomers used for the synthesis were all poorly soluble, in the order of milligrams per liter of solution. The solubility of the monomers was largely lowered outside the pH range from 4 to 10, and their solubility steadily decreased as ionic strength was increased from 0 to 0.5 M NaCl. Maximal solubility varying between 1.0 to 5.0 mg ml^{-1} under optimized conditions of pH and salt were observed. While Azo2 was the most soluble of all three azobenzenes, Azo3 was the least soluble and had to be heated in water to 50°C to help solubilization prior being added to the reaction vessel. Azo2 was therefore expected to produce a higher substitution ratio on PAH. Several attempts of each substitution reaction were made to obtain compounds of different grafting ratio (Table 1). The products were collected and dialyzed against water and freeze dried for storage.

4.2.2 CHARACTERIZATION OF AZO MONOMERS

The UV-visible spectra of Azo1, Azo2 and Azo3 revealed a broad absorbance peak centered at 325 nm, 399 nm and 432 nm, respectively. Using Beer's Law (Eq. 4.1) it was possible to calculate the extinction coefficient ε of each dye at the absorption maxima. The absorbance A of the solute at a selected wavelength was plotted against various dye concentration c keeping the path length l constant. The coefficient ε was extracted as a function of mass from the equation of the resulting slope.

Eq. 4.1 $$A = \varepsilon \cdot c \cdot l$$

A solution of 10 µg/mL of azobenzene was prepared in water and the pH adjusted at 12. In basic condition the solutions were clear and orange-red in color. Titration was done against 0.1 M HCl using a burette mounted above the stirring solution. Aliquots of solution were taken at each 0.2 pH unit change and the UV-visible spectra recorded. The calculated extinction coefficient expressed in units of grams were multiplied by the molecular weight of the molecule yielding a standard value of molar absorptivity ε_M for each monomer. The values are tabulated in Table 1.

The change in absorbance at a given wavelength λ obeys Equation 4.2. This equation can be modified to get rid of the concentration parameter A^- by taking a two-wavelength absorbance ratio. Equation 4.2 for wavelength λ_1 is divided by itself at a wavelength λ_2 to obtain Equation 4.3. Assuming that all other parameters are known, the latter can then be solved for pK_a by taking the negative logarithm of K_a. The molar extinction coefficients values for each wavelength were chosen to have a maximum difference to reduce the error. The pK_a of Azo1 was found to be 5.8, 8.3 for Azo2 and 5.3 for Azo3.

Eq. 4.2 $$A_\lambda = \left[A^-\right] \cdot \left(\varepsilon_{AH(\lambda)} \frac{10^{-pH}}{K_a} + \varepsilon_{A-} \right)$$

Eq. 4.3 $$\frac{A_{\lambda 1}}{A_{\lambda 2}} = \frac{10^{-pH}\varepsilon_{AH(\lambda 1)} + \varepsilon_{A-(\lambda 1)}K_a}{10^{-pH}\varepsilon_{AH(\lambda 2)} + \varepsilon_{A-(\lambda 2)}K_a}$$

4.2.3 DETERMINATION OF GRAFTING RATIO FOR AZO-PAH DERIVATIVES

One way to determine the substitution ratio of Azo-substituted PAH is to compare the number of protons of PAH monomers to those of Azo-PAH. This can be achieved by ^{1}H NMR by rationalizing the signals obtained from each type of protons. Unfortunately, the new polymers were insufficiently soluble to produce strong signals from the grafted azobenzene molecules and determining the substitution ratio in this manner was deemed unreliable. Therefore, in order to determine the actual proportion of Azo monomer grafted to PAH (χ), an alternative UV-visible-based mathematical relationship that is valid for any Azo-substituted PAH via the carbodiimide reaction described earlier was derived. We begin with the assumption that the molar absorptivity of the monomer and that of the monomer grafted to PAH are identical. Taking the molecular weight of a single PAH unit as 93.5g mol^{-1}, the molecular weight of the Azo-substituted PAH (M_P) can be expressed by:

Eq. 4.4
$$M_P = 93.5g \cdot mol^{-1} \times (1-\chi) + \chi\left(M_M + 39.0g \cdot mol^{-1}\right)$$

where M_M is the molecular weight of the monomer substituted onto PAH. The first term of Equation 4.4 corresponds to the molecular weight contribution of PAH monomer to the total molecular weight of the substituted polyion, while the second term corresponds to the contribution of the Azo-substituted PAH units. After simplification Equation 4.4 becomes:

Eq. 4.5
$$M_P = 93.5g \cdot mol^{-1} + \chi\left(M_M - 54.5g \cdot mol^{-1}\right)$$

However, Equation 4.5 still contains two unknown since M_P is unknown making it impossible to solve for χ without substituting M_P by a known relationship. The Beer-Lambert law states that the extinction coefficient, concentration and absorption of a material vary linearly at a any given wavelength. Since it is assume that the extinction coefficients of the Azoic dyes and their corresponding Azo-substituted polymer are equivalent, χ can be described as the ratio of the molar extinction coefficient ratio of the polymer ε_P divided by that of the monomer ε_M at the least transmitted quantifiable wavelength (λ_{max}) (Eq. 4.6).

Eq. 4.6
$$\chi = \frac{\varepsilon_p}{\varepsilon_m}$$

As a result, a substitution ratio of 0 would mean that no absorption of the Azo-PAH derivative is detectable at the chosen λ and that this polymer contains no Azo group. A substitution ratio

of 1, however, would mean that every available amine group of PAH has been substituted with an Azo group. Because M_P is unknown, ε_P cannot be determined directly and its mass equivalent ε_P^* was extracted from absorption/concentration curves of each substituted polymer, as previously described for solutions of Azo dyes alone. The arbitrarily named parameter "mass extinction coefficients" are denoted as ε^* with ε_P^* and ε_M^* corresponding to that of the polymers and monomers, respectively. Therefore, molar absorptivity ε is the product of ε^* and the molecular weight, allowing Equation 4.6 to become:

Eq. 4.7
$$\chi = \frac{\varepsilon_P^* \times M_P}{\varepsilon_M^* \times M_M}$$

Isolating M_P from Equation 4.7 and substituting the relationship into Equation 4.5 allows us to get rid of the unknown and develop a suitable relationship for χ shown in Equation 4.8. The mass extinction coefficients were obtained for the monomers and polymers using UV-visible spectroscopy and put in the Equation 4.8. The results for various polymer syntheses are tabulated below (Table1).

Eq. 4.8
$$\chi = \frac{93.5 g \cdot mol^{-1} \times \varepsilon_P^*}{\varepsilon_M^* \times M_M - \varepsilon_P^* \left(M_M - 54.5 g \cdot mol^{-1} \right)}$$

TABLE 1 PERCENT SUBSTITUTION OF AZO-PAH.

	ε^*_m	M_M	ε^*_p	χ (%)	Target	Yield
Azo1a	57.5	226.24	2.6	1.9	10	19
Azo1b			1.28	0.9	5	19
Azo1c			7.85	6.3	50	13
Azo2a	101.6	242.24	2.66	1.0	5	21
Azo2b			7.00	2.8	15	19
Azo2c			9.85	4.0	50	8
Azo3a	77.5	269.3	13.85	7.2	25	29
Azo3b			10.1	5.1	25	20
Azo3c			7.36	3.6	20	18

4.2.4 SOLUTION PROPERTIES OF PAH-AZO DERIVATIVES

The effects of salt and pH on Azo-PAH were also investigated. Dissolving Azo1-PAH and Azo2-PAH produced clear solutions and displayed a good solubility at a concentration of 2 mg/mL and high pH, at the exception Azo1c and Azo2c which appeared turbid at these conditions and were completely clear only below 1 mg/mL concentration. The effect of salt on the spectroscopic properties of Azo-substituted PAH was measured by dissolving the different polymers and monomers in 0.2 M, 0.35 M and 0.5 M NaCl solution. The spectra were compared to those of the PEs dissolved in salt-free solution. These observations are summarized in Table 2 along with the commercial azo-substituted polyelectrolyte PAzo. The results showed a red-shift of the absorption maximum following the addition of salt in the case of Azo2b, Azo3c and PAzo, which all possess an ionizable group. The spectrum Azo1a was unaffected by the presence of salt or change in pH. This is because the only ionizable functional group on the structure of Azo1, a carboxylic acid, was consumed during the coupling reaction with PAH. Azo2b underwent an important red-shift of 74 nm from pH 7.6 to 8.5, which matches the 8.3 pKa value found for the hydroxyl group of Azo2. The maximum absorbance of Azo3c blue-shifted by 94 units from pH 4.1 to 5.4, also related to the 5.3 pKa value of Azo3 for the dimethylamine group. Finally, the absorbance maximum of PAzo was red-shifted by 78 nm between pH 10 and 11. It should be noted that PAzo is introduced here as it will also be later used as a polyanion in the assembly of microshells. The respective spectra of PAzo in water at pH 10 and 11 are illustrated in Figure 4.6.

TABLE 2 EFFECTS OF SALT AND PH ON THE ABSORBANCE OF AZO-POLYMERS

	pH Effect on Absorbance curves				Salt Effect
	pH range		λ_{max}		$0 \rightarrow 0.5$M NaCl
Azo1a	3	12	325nm	325nm	0nm
Azo2a	7.6	8.5	341nm	415nm	+2nm
Azo3c	4.1	5.4	526nm	430nm	+5nm
PAzo	10	11	362nm	440nm	+10nm

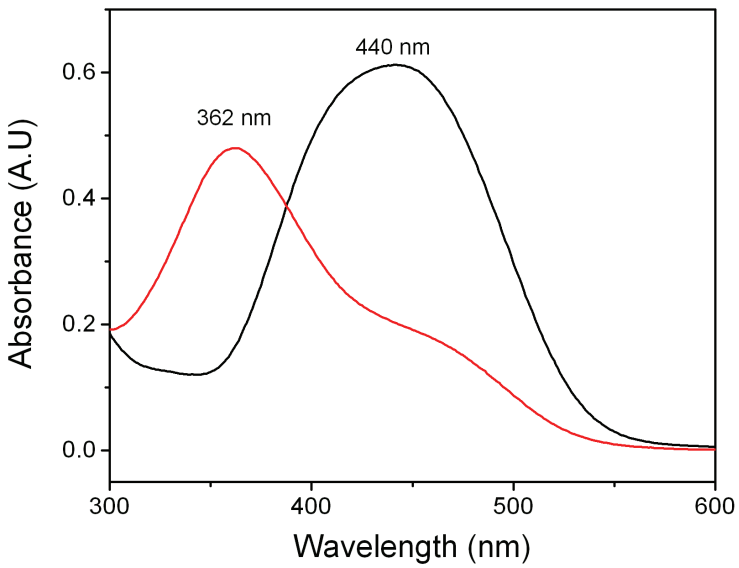

Fig. 4.6 UV-visible absorbance spectra of PAzo in water at pH = 10 and 11, left and right respectively.

The low solubility of Azo molecules was expected to affect the solubility of the Azo-substituted PAH. Azo molecules exist largely in their non-polar *trans* configuration. Substituting primary amine groups along the PAH main chain with large uncharged, slightly or non-polar molecules reduce the polymer's solubility. Since the conformation of PAH in solution and its subsequent deposition during the LbL assembly process to produce microcapsules is highly dependent on salt concentration, dynamic light scattering (DLS) experiments were performed in order to determine whether polymer complexes of Azo-PAH molecules formed in the presence of salt. These experiments were carried out with fresh and old solutions of each polymer with or without added salt (0.5 M NaCl). The results suggest that aggregates of various sizes are present in all solutions, but also that those aggregates become larger and more numerous as the solution ages or when salt is added. The polydispersity index (PDI) of 1 % Azo1a and Azo2a in 0.5 M salt was about 40 % greater than in water. The high PDI values for all solutions indicate that aggregates of various sizes are present in solution. For this reason, a precise hydrodynamic radius could not be determined from the DLS correlation curve. Due to the poor solubility of Azo3-PAH polymers, it was decided to not continue using this polyion in further experiments.

4.2.5 TRANS-CIS ISOMERIZATION OF AZO POLYIONS

The *trans-cis* isomerization of the azobenzene moieties of Azo-PAH polyions was induced using a 150 W super-quiet xenon lamp. Experiments were first performed in 0.1 mg/mL polymer solutions and any spectral change monitored by UV-visible spectroscopy. Of the three polymers tested, only Azo1-PAH (a) showed a *trans-cis* isomerization upon UV irradiation. This is shown in Figure 4.7. A complete *cis-trans* thermal recovery of the spectrum occurred by keeping the sample solution in darkness overnight. Azo2-PAH and PAzo were not found to undergo this transition.

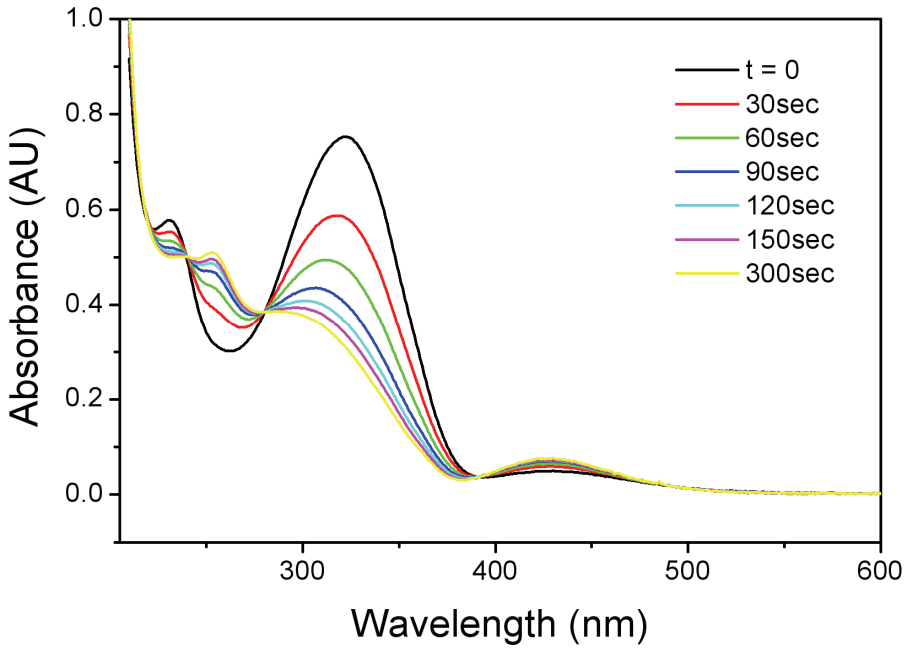

Fig. 4.7 Trans-cis isomerization of Azo1-PAH upon UV irradiation.

4.2.6 MICROCAPSULES ASSEMBLY USING AZO POLYIONS

Three Azo-functionalized microcapsule types were constructed on 4.6 μm PS particles following the LbL procedure: $(Azo1\text{-}PAH/PSS)_4$, $(Azo2\text{-}PAH/PSS)_4$ and $(PAH/PAzo)_3PAH/PVS$. Solutions containing 0.5 M NaCl and 2 mg/mL were used for all polyelectrolytes except PAzo. Azo-PAH solutions were orange after core dissolution and the capsules were found similar to previously reported $(Azo1\text{-}PAH/PSS)_8$ shells assembled also on PS (10.25 μm). The shells were made fluorescent with an aliquot of rhodamine dye (10^{-7} M) and their diameters averaged by LSCM, giving 4.43 μm and 4.48 μm based on averaging 20 capsules per sample for (Azo1-

$PAH/PSS)_4$ and $(Azo2\text{-}PAH/PSS)_4$, respectively. PAzo had to be handled differently because it becomes fairly insoluble at pH values below 9.5 and in ionic solutions. In order to provide sufficient material for LbL assembly, a 0.2 M NaCl stock solution of PAzo (1 mg/mL) with a pH adjusted to 12 was kept aside. Immediately before the addition of a PAzo layer, an aliquot of PAzo solution was taken and its pH value decreased to 9.5 using a titration burette and 0.1 M HCl. This method was chosen because it had been observed that PAzo rapidly flocculates below pH 9 and above 0.3 M NaCl. Attempts to prepare capsules using a turbid solution of PAzo were not successful as they resulted in large scale aggregation of the samples. Using pH exceeding 12 was also found to jeopardize the capsules' integrity due to the largely deprotonated state of PAH at this pH. In fact, the preferable solution pH for LbL assembly involving PAH is in the range 4-7, where most amine groups are protonated. As a result it was better to use the lowest possible solution pH in order to encourage the formation of a PAzo layer. The $(PAH/PAzo)_4$ shells however, tended to aggregates after core dissolution in DMF or THF. The construct was then modified to add a layer of the polyanion PVS as the outermost layer, instead of PAzo which led to some aggregation of the capsule samples.

4.2.7 OPTICAL SHRINKAGE OF PAH/PAZO MICROSHELLS

The stability of $(Azo1\text{-}PAH/PSS)_8$, $(Azo1\text{-}PAH/PSS)_4$ and $(Azo2\text{-}PAH/PSS)_4$ capsules under low intensity UV irradiation was tested for extended periods of time up to fifteen hours in duration. The effect of irradiation on capsules was investigated using a 150 W xenon lamp equipped with a broad-band UV filter (300-390nm). The irradiation intensity of this apparatus was determined to be in the range of 2-5 mW/cm^2. For the experiments, an aliquot of capsule solution was transferred to a quartz cuvette, mounted on a magnetic stirrer in a cooling bath. The cooling bath was maintained at 20°C to prevent heating the solution during prolonged UV irradiation. The samples were carefully scrutinized by LSCM for changes in appearance but no change was observed after up to 15 hours of UV exposure.

On the other hand, exposure of a solution of $(PAH/PAzo)_3PAH/PVS$ microshells to UV light led to a significant decrease in the size of the microcapsules. Throughout the irradiation experiments, aliquots of the samples solutions were taken after up to 10 hrs and the resulting shrinkage was monitored by LSCM. The diameter of capsules was measured in transmission mode without staining the shells. Figure 4.8 illustrates the reduction in size as well as the changes in morphology of capsule shrinkage of $(PAH/PAzo)_3PAH/PVS$ capsules as a function of time. Before irradiation, the capsules are round with an average diameter of 4.74μm (±0.1) and

possess a smooth wall. Immediately after being exposed to the light source, the hollow shells began to shrink. A reduction in the average diameter of the shells from 4.8 µm to 4.1 µm is observed after 30 minutes of irradiation, which translates to a loss of over 27 % in surface area per capsule. Additionally, the roughness of the shells roughness significantly increase and they generally appear thicker than prior shrinking. The capsules then continue to decrease in size at a slower but constant rate if irradiation is maintained to reach an average diameter of about 2.6 µm or 45 % of their original size after 10 hours of exposure to light. However, it is noteworthy that a substantial number of capsules were found to have a diameter even below this range, measuring as little as 1.3 µm. The observations that light not only shrinks $(PAH/PAzo)_3PAH/PVS$ capsules, but also results in apparent changes in the wall morphology led us to test whether their permeability to dyes is affected as well.

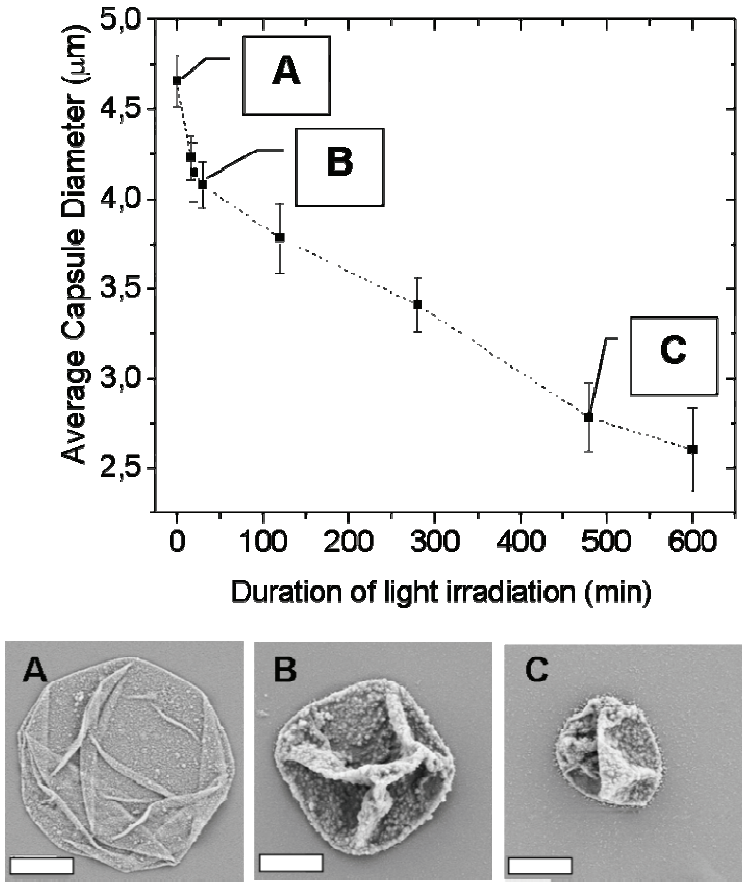

Fig. 4.8 Light-induced shrinkage of $(PAH/PAzo)_3PAH/PVS$ microshells upon UV exposure. Lower panel: SEM images of capsules (A) before irradiation, (B) after 60 minutes and (C) after 8 hours of light irradiation. The scale bars measure 2 µm.

Köhler and coworkers demonstrated that heating PDDA/PSS and PAH/PSS microshells makes them shrink as a result of changes in the arrangement of the polymers constituting the shell. [127,129] To prevent this, all reported UV shrinking experiments discussed so far were conducted in a thermostated environment maintained at 20°C. [224] However, local heating effects due to absorbing azobenzene moieties within polyelectrolyte microcapsules have also been shown to have the capability to bring about important changes to the wall. [40] The azobenzene group present in PAzo has an adsorption maximum of 362 nm in water at neutral pH. As previously stated, the energy absorbed by azobenzene molecules is released in a conformational change and possibly heat to a lesser extent.

To test whether the accumulation of heat in the irradiated capsules could be at the origin of the observed shrinkage in $(PAH/PAzo)_3PAH/PVS$ capsules, we immersed a solution of these capsules along with $(PAH/PSS)_4$ and $(PDDA/PSS)_4$ shells for 20 minutes in a water bath heated to temperatures up to 95°C. The results are summarized in Figure 4.9. The average diameter measured for the heated samples showed that $(PAH/PSS)_4$ shells lost their integrity between 50°C and 60°C and that the diameter of $(PDDA/PSS)_4$ sharply decreased from 40°C to 60°C. However, $(PAH/PAzo)_3PAH/PVS$ microshells underwent no significant size reduction in that range. These results illustrate the high thermal stability of $(PAH/PAzo)_3PAH/PVS$ and support the assumption that the effect of local heat increments within the shells as a result of the UV-absorbing polyelectrolyte PAzo may only play a minor role, if any, in the shrinking and encapsulation of dye of the capsules.

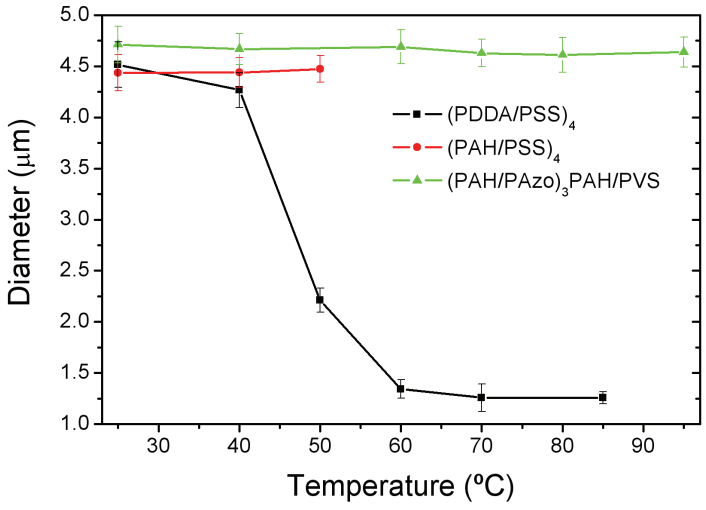

Fig. 4.9 Effect of heat on $(PAH/PAzo)_3PAH/PVS$ microshells in comparison to PDDA/PSS and PAH/PSS capsules.

4.2.8 ENCAPSULATION OF DEXTRAN BY UV LIGHT

The encapsulation of macromolecules was studied using AF488-dextran (10 kDa) and CaGreen™-1 dextran (3kDa) as model substances. These fluorescently labeled polysaccharides were chosen due to their strong fluorescence and their resistance to photobleaching, essential prerequisites that allowed us to monitor the shrinkage and changes in permeability of microshells during long periods of irradiation. Capsules were incubated in a solution of labeled polymer for 1 hour and subsequently exposed to light. Figures 4.10A and 4.10B illustrate that only incubating the $(PAH/PAzo)_3PAH/PVS$ capsules with the 10 kDa labeled dextran (A) followed by the removal of the supernatant by washing the capsules against water leaves unfilled capsules (B), whereas capsules exposed to UV light for some time retain the encapsulated polymers as shown in panel *C*. The percentage of filled capsules changed with time of illumination and remained unchanged afterward (15-20 % of the capsules retained labeled dextran in a sample irradiated for 20 minutes as compared to ~ 50 % after 120 minutes of irradiation). Despite all capsules shrinking upon irradiation, it was not possible to obtain ratio of capsules with encapsulated dextran grater and 50 %.

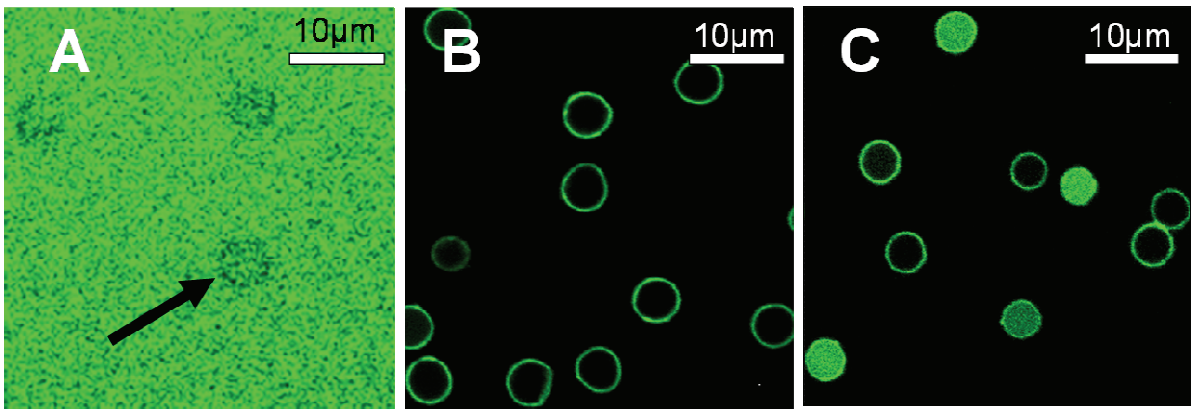

Fig. 4.10 Encapsulation of AF 488-dextran by UV irradiation in $(PAH/PAzo)_3PAH/PVS$ microshells. The capsules are permeable to the fluorescent polymer prior irradiation (A) but cannot retain the dye if washed (B) unless it is irradiated first (C). Encapsulation is observed after only a few minutes of irradiation.

Observations of microcapsules becoming damaged upon UV irradiation was reported for various types of microcapsules in a study by Katagiri *et al.*, where the authors demonstrated that microshells containing polymers that absorb near-UV became damaged with sufficient CW

irradiation. [157] The damages were attributed to breaking the absorbing bonds within the microcapsules shells thus changing the chemical and mechanical structure of the shells. One curious outcome of this work is that while undergoing destructive interactions with light, capsules gradually shrunk, probably due to the corresponding reduction in steric effects of degraded polymers. The authors, however, made no suggestion of using this effect for encapsulation purposes, a clear and important follow up of this work. An explanation for this discontinuity is that it was not possible to encapsulate materials in microcapsules that were being optically degraded, which unlike common encapsulation methods, most likely leads to an increase in shell permeability.

It was hypothesized that the mechanism for the shrinking and encapsulation behaviors observed was not due to thermal rearrangements but was instead driven by the cis-trans isomerization. There are two main components to this hypothesis. (1) The azo group goes from relatively apolar to polar from the E→Z conversion (Figure 2.8) which might affect the water content of the microshells. The significance of the trans-cis isomerization of a simple azobenzene molecule is reflected in a length reduction of this group from 9.0 to 5.5 Å following exposure to a UV source. [155] Isomerization of this class of dye is usually accompanied by molecular changes in physical properties such as polarity, viscosity and absorbance. As part of a polymer backbone or grafted onto it, this light-induced isomerization were shown to lead to important changes in films such as variations in thickness and wettability. [155,225] As a result, it is possible that the irradiated microcapsule walls swell during UV irradiation due to an increase in polarity in its azobenzene content. (2) The functional groups that contribute to multilayer formation on PAzo are a hydroxyl and a carboxyl attached to the second phenyl group from the main polymer chain. By inducing a E→Z conformational change, some functional groups which has no amine partner (from PAH) may find themselves in the proximity of one, leaving an empty space behind. Figure 4.11 illustrates this hypothesis. Therefore, shrinkage may be due to unpaired Z isomers creating closer interactions with PAH. The polyelectrolyte multilayer system is not absorbed in well defined layers but rather as an interpenetrated meshwork with high water content.

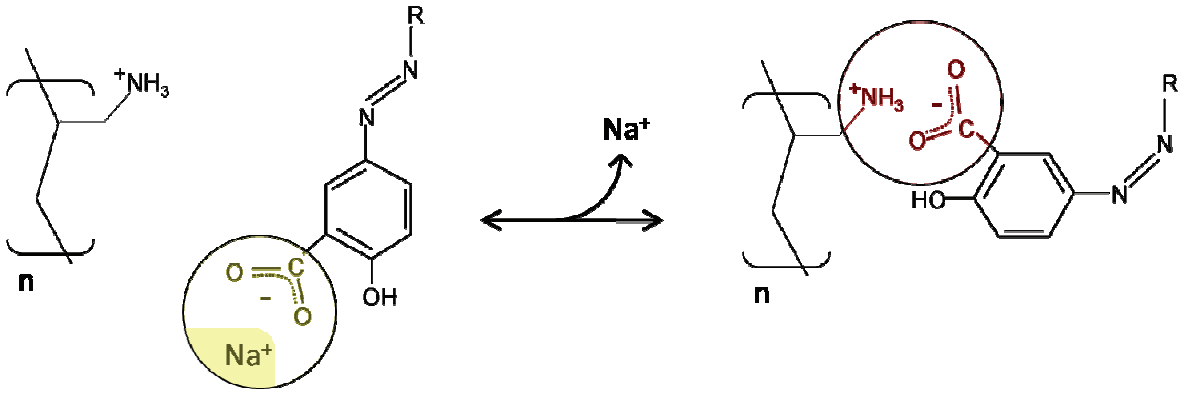

Fig. 4.11 UV-induced repositioning of an Azo group on PAzo to an new position.

The polyelectrolytes within the multilayers are maintained in a frozen state from kinetic entrapment and the extensive bonding they are stabilized by. [226] Self-diffusion constants within PAH/PSS films were found to be in the order of 10^{-15} cm^2/s, similar to glassy polymers. [227] This process is largely speeded up in polyelectrolyte multilayers by introducing ions, temperature or changing the pH in the case of weak polyelectrolytes, where the effect weakens the electrostatic interactions. The example discussed here could be thought of as catalyzed by light as new bonds are formed but driven by the release of counterions.

4.3 CONCLUSIONS

In this chapter, it was shown that microcapsules tend to be damaged upon irradiation with an intense near-UV pulsed laser source despite the absence of any strongly absorbing near-UV chromophores in the microshells. When using a 355 nm pulsed UV laser source of irradiation, no damages were found at a power density less than 40 mJ/cm^2. However, significant damages were found in capsule samples exposed to power densities between 40-200 mJ/cm^2, with the extent of damage increasing with higher fluence suggesting that laser ablation could be responsible for the damages found at higher energy input. These observations are in agreement with work by Skirtach *et al.* who showed that microcapsules could be damaged by photobleaching dye molecules embedded within the microshells. [21] Capsules were never found to shrink upon pulsed UV exposure, even when relatively low intensities were used for periods

extending to hours. This is in contrast with a study by Katagiri *et al.*, who systematically demonstrated that microcapsules shrunk in the presence of near-UV irradiation when microshells contained appropriate chromophores. [157] The assembly of microcapsules containing the azobenzene-substituted polycation Azo1-PAH, which strongly absorbs light at 355 nm, did not appear to behave differently than irradiated microcapsules constructed from PAH, PVS and PSS. One explanation for this is that the chromophores content in Azo1-PSS was in fact rather low, occupying less than 5 % of the available amino groups along the PAH backbone and was therefore unlikely to significantly increase the microcapsule sensitivity to near-UV irradiation.

Less energetic CW near-UV irradiation was then used to study the response of microcapsules containing azobenzene molecules under non-ionizing conditions. In addition to Azo1-PAH, two other types of azobenzene molecules were grafted on PAH to create Azo2-PAH and Azo3-PAH. All three variant of PAH suffered from low substitution ratios and despite the fact that photoisomerization was indeed observed for Azo1-PAH, no capsule containing these molecules underwent changes in permeability or morphology after prolonged exposure to UV light. The lack of response in LbL films can be explained due to the low degree of substitution achieved for the Azo-PAH variants. PAzo, however, possesses a sulphonated azo group at each unit along its main chain.

Microcapsules constructed with PAzo with the structure $(PAH/PAzo)_3PAH/PVS$ yielded the best quality samples. The strong polyelectrolyte PVS was used as the outermost layer of the capsules due to its lack of absorption in the near-UV as well as its ability to prevent aggregation between microshells. The samples appeared red in color and remained stable over two years of storage in darkness. $(PAH/PAzo)_3PAH/PVS$ microcapsules (only PAzo absorbs light in the range 300-400 nm), where found to shrink when exposed to UV. In addition, shrinking was shown to decrease the permeability of the shells permitting the encapsulation of dextran. Encapsulation, however, was never possible throughout the entire capsule sample and remained limited to approximately 50 % of the $(PAH/PAzo)_3PAH/PVS$ shells. This was attributed to the inhomogeneous distribution of material throughout the shell possibly due to the limited solubility of PAzo in presence of salt which was the main limitation to the assembly procedure.

With regards to the effect of heating the bulk solution, the diameter of PAH/PAzo capsules was shown to remain unaffected at 95°C whereas PAH/PSS capsules dissolved and

PDDA/PSS capsules shrunk. This suggest that the PAH/PAzo polyelectrolyte pair has a high glass transition which cannot be reached in thermostated conditions, solely due to UV absorption. Therefore, based on the knowledge that azobenzene molecules possess a high resistance to photobleaching and that capsules that did not contain PAzo were unaffected by CW near-UV, a possible explanation for the optical shrinking and encapsulation of dextran in $(PAH/PAzo)_nPAH/PVS$ microshells is that slow rearrangements due to cycling cis-trans/trans-cis isomerizations allows for the LbL wall structure to become denser as more favorable interactions are created between layers.

5 ENCAPSULATION AND RELEASE OF MATERIALS USING GOLD NANOPARTICLES AS A LIGHT SENSITIZER

The investigations reported in this chapter are divided into three sections. First, *Section 5.1* will look into the effect of incorporated nanoparticles on shell mechanics. Then *Section 5.2* will present the effect of particle distribution on encapsulation and release behavior. Finally, *Section 5.3* presents an overview of experiments conducted with microcapsules in cells, which consisted in the primary motivation for this work.

5.1 FABRICATION AND CHARACTERIZATION OF GOLD NANOPARTICLES-CONTAINING MICROCAPSULES

5.1.1 PREPARATION OF GOLD-FUNCTIONALIZED MICROCAPSULES

The thermal shrinking behavior of polymer microshells functionalized with different concentration of gold nanoparticles was investigated. Unless otherwise stated, citrate stabilized gold nanoparticles with an average diameter of 20 nm were selected for this study due to their high affinity for the polycation PDDA used in capsule construction, making it easier to control the amount of nanoparticles incorporated in the shells. 20 nm gold nanoparticles additionally possess a more efficient heat generation response when irradiated with light than smaller gold particles as well as a good size relative to the thickness of the capsule wall (20-40 nm). Larger particles were found to reduce the efficiency of thermal encapsulation by increasing the likeliness of defects in the shell.

Polymeric microcapsules doped with gold nanoparticles were constructed from polyelectrolytes solutions of PDDA and PSS onto sacrificial silica template using the LbL method. PDDA/PSS microcapsules were chosen as a model system for this study due to their tendency to be very stable and yield highly homogeneous samples, a particularly important aspect since extensive statistics are required. In a typical capsule preparation, 200 µL of a silica particles suspension (10 % w/v) and a colloidal gold solution containing 4.1 x 10^{11} nanoparticles/mL were used. A homodispersed nanoparticle distribution was inserted in the capsule wall by resuspending PDDA-coated particles with a desired volume of colloidal gold solution. Gold was added to the two middle PDDA layers. The addition step was repeated to obtain shells with a heavier gold content. Homogeneous gold nanoparticle coverage throughout the capsule sample was assured by first resuspending the silica precipitate in a

small volume of water followed by a rapid addition of the colloid gold solution. Gold nanoparticles adhere to the polyelectrolyte layer due to the attractive electrostatic interactions between the negatively-charged citrate molecules coating the nanoparticle and the positively changed PDDA. The absorption of gold could be followed by eye as the typically white color of the polyelectrolyte-coated silica particles turned red. Complete absorption of gold nanoparticles was confirmed spectroscopically by measuring the absorbance of the supernatant after each sequence of gold addition/sedimentation. An appropriate volume of HF was added to remove the sacrificial silica template leaving behind a solution of capsules with the following composition: PDDA/PSS/PDDA/(Au/PSS/PDDA)$_2$PSS. To lighten the text, the capsules construct will be referred to as Homo-Au2 shells (which stands for *homodispersed gold, 2 layers*). Note that "Au/" in the previous annotation does not indicate the presence of a distinct layer of gold nanoparticles but instead is written in this manner to indicate the point of insertion of gold nanoparticles.

The capsules samples contained virtually no aggregation and showed a good contrast under visible microscopy. Figure 5.1 illustrates this along with a LSCM image of the capsules after being stained with a small amount of rhodamine for confocal visualization. The microcapsules were found to have an average diameter of 4.61µm.

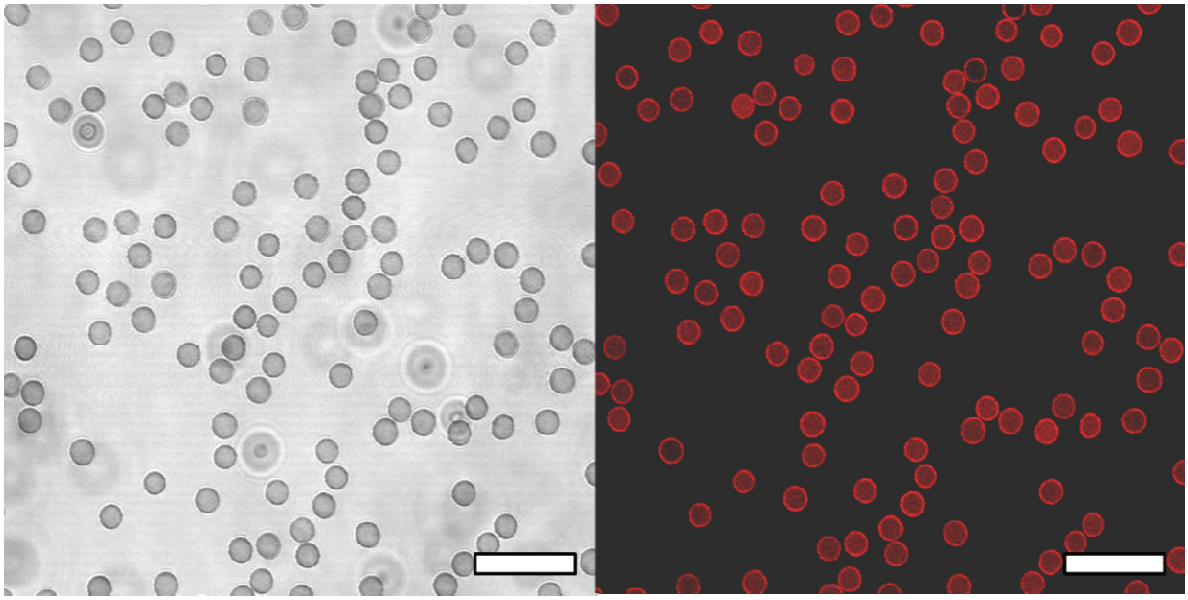

Fig. 5.1 LSCM images of PDDA/PSS/PDDA/(Au/PSS/PDDA)$_2$PSS shells, (*i.e.* Homo-Au2) in transmission and confocal modes. Scale bar is 20 µm.

5.1.2 THERMAL SHRINKAGE AS A FUNCTION OF NANOPARTICLE DENSITY

Thermal or heat shrinking curves are a simple first-hand way to determine whether structural differences exists between microcapsules samples because the shells' response to high temperature is highly dependent on the physical properties of its constituents. The presence of low amounts of gold nanoparticles in the shell structure was expected to have no significant impact on the thermal curves since the temperatures used were known to affect only the polymers within microshells. Consequently, the general properties of polyelectrolyte microcapsules functionalized with gold nanoparticles had not been previously investigated.

The heat shrinking behavior of $(PDDA/PSS)_4$ capsules as well as the shrinking curves of similar shells containing 5 nm and 20 nm citrate-stabilized gold nanoparticles (~2000 particles/capsule) was measured. Heat shrinking was done by incubating a small aliquot of microcapsule suspension in a thermostated water bath for 20 minutes. The aliquot was then allowed to cool down to room temperature. To visualize the microshells by LSCM and measure their diameter, the capsules were made fluorescent by the addition of a drop of 10^{-7} M solution of rhodamine 6G. It is essential to treat the microcapsules with dye ***after*** thermal treatment since charged dye molecules bind electrostatically to the capsule shell and may influence their response to heat. The average capsule diameter for each sample was determined for at least 20 capsules per sample per incubation temperature. Thermal curves were obtained by plotting the diameter of the capsules as a function of incubation temperature.

Fig. 5.2 shows the thermal curves obtained for $(PDDA/PSS)_4$ capsules in comparison to Homo-Au2 shells containing 5 nm and 20 nm gold nanoparticles. The curves consist of two plateaus surrounding a steep region. The onset temperature where capsules begin to shrink is related to the glass transition (T_g) of the PDDA/PSS complex and is approximately 37-40°C. [13] At temperatures above T_g, changes in capsules diameter are driven by the hydrophobic nature of the shells' polyelectrolyte backbone forcing the microcapsules minimize the surface area exposed to water. [127,128] At the second plateau, the microcapsules are completely shrunk and typically have no hollow interior anymore. The results depicted in Figure 5.2 revealed that the average diameter of shells doped with gold nanoparticles is higher at most temperature in comparison to shells containing no metal particles. Secondly, it appears that the minimum diameter to which the shells can be shrunk increases in samples containing nanoparticles. At identical nanoparticle density, similar results were obtained for capsules containing a mixture of 5 nm and 20 nm nanoparticles as well as for shells containing 30 nm nanoparticles

supporting that nanoparticle density is a more important factor in the variations between the different thermal curves. These observations are reminiscent of the changes in thermal shrinking behavior of polymeric capsules upon increasing the layer number. [126]

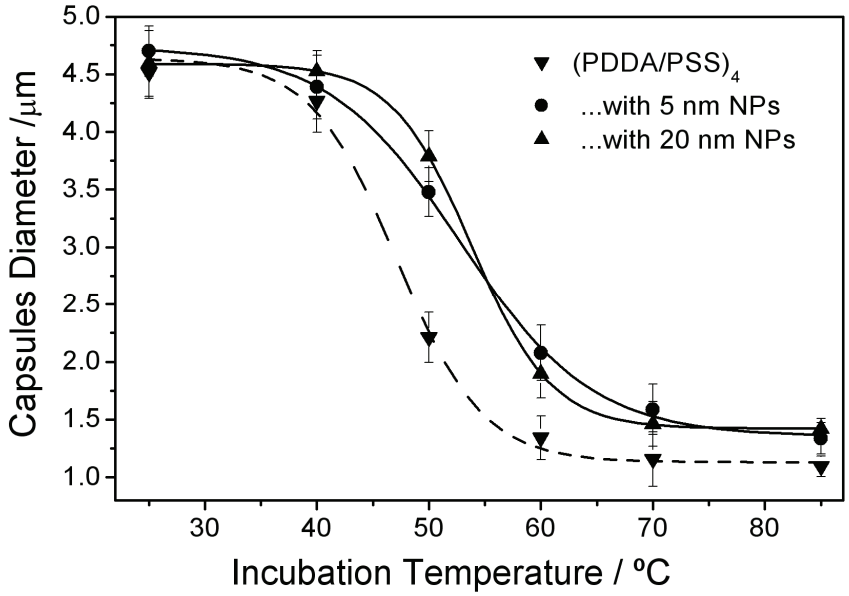

Fig. 5.2 General heat shrinking behavior of $(PDDA/PSS)_4$ shells containing nanoparticles or not.

In order to better understand the effect of nanoparticles on the thermal shrinking behavior of microcapsules, microshells containing different concentration of 20 nm gold nanoparticles were assembled and subjected to thermal shrinking. TEM images for three different samples of microcapsules were taken and the nanoparticles counted for 10 capsules per sample. This information along with the diameter obtained from LSCM was used to calculate the approximate gold nanoparticles concentration in the composite microshells in terms of surface filling factors (F_S). The computation of F_S requires the assumption that nanoparticle are homodispersed.

The TEM images of capsules were recorded in the dried state for shells that were not thermally shrunk. F_S for three samples were found to be 0.07, 0.15, and 0.28 corresponding to microcapsules containing low, medium and high gold concentration, respectively (Figure 5.3). However, it appeared that small clusters of gold nanoparticles formed when we attempted to deposit high concentration of gold nanoparticles. The first clusters of gold nanoparticles appeared in the capsules with $F_S \sim$ 0.1-0.15. These apparent clusters, visible in Figure 5.3,

could originate from the fact that the gold nanoparticles were spread over more than one layer during capsules assembly, therefore what appears as clusters may simply be the combination of nanoparticles that happen to be on top of one another. In addition, what is seen by imaging a capsule by TEM is the superposition of two walls overlapping as a result of the drying process.

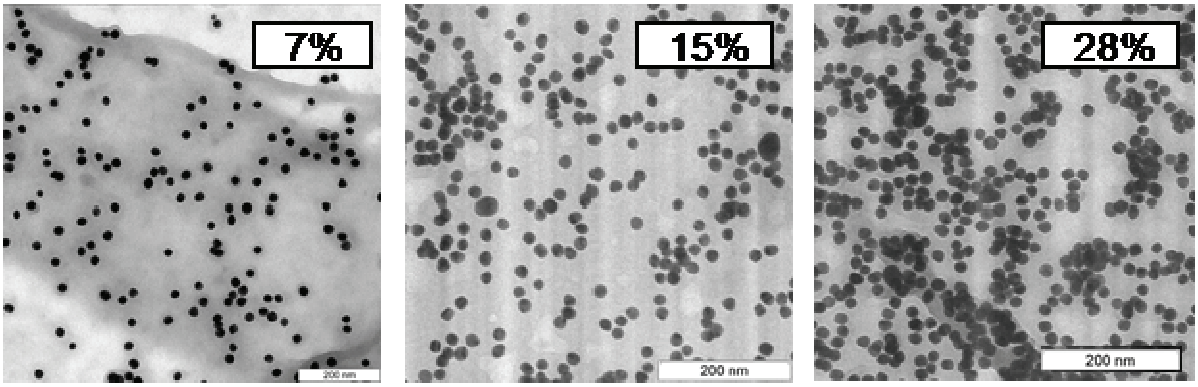

Fig. 5.3 TEM images of the distribution of 20 nm gold nanoparticles of a 1 μm² area of polymeric shell before thermal shrinking. Scale bars measure 200 μm.

Aliquots of capsule solutions doped with the three concentrations of gold nanoparticles found in Figure 5.3 were heated at various temperatures from ambient to 80°C. After thermal treatment, the capsules solutions were left to cool down and the shells stained with fluorescent dye to determine the samples' average diameter by LSCM. The shell diameters values given were averaged from at least 30 capsules using LSCM. Figure 5.4 illustrates the thermal shrinking curves obtained. It was found to be increasingly difficult to thermally shrink polymeric shells as the gold content within the wall is increased. In addition, it was found that higher gold content limits the minimum diameter the capsules may be shrunk to. This minimal shell diameter as a function of gold concentration is particularly important to consider for thermal encapsulation purposes, because this relationship comes with a contrariety: constructing shells with a high gold content is expected to provide a more efficient optical release, but also a lower encapsulation efficiency since shells containing greater amounts of nanoparticles become significantly heavy and more likely to become damaged during the centrifugation steps of sample preparation.

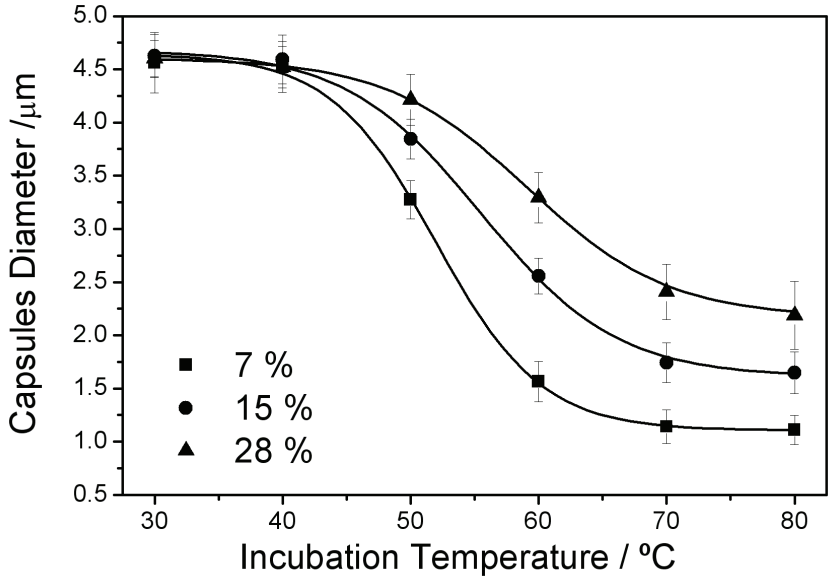

Fig. 5.4 Thermal shrinking behavior at various gold filling factors for Homo-Au2 capsules (filling factor 7 %, 15 %, 28 %). The percentages shown represent the calculated surface area coverage of nanoparticles throughout the polymeric shell. Each data point is calculated from the diameter of at least 30 capsules, error bars correspond to standard deviation.

SEM was used to obtain information about shells morphology as a function of diameter. Figure 5.5 shows representative SEM images of Homo-Au2 shells with F_S = 0.07 and F_S = 0.28 after thermal shrinkage at selected temperatures. The average diameter d_A corresponding to the sample from which each picture was taken can be found underneath. One can clearly see from these images that the high gold content capsules are larger at every temperature compared to shells containing low amounts of gold. Shells that are larger than half their original diameter have low density walls and collapse upon drying as seen for both samples (7 % and 28 %) that were treated at lower incubation temperatures. At 60°C, the wall of capsules containing 7 % gold is dense enough that some shells are able to support themselves in the dried state, whereas shells carrying a high gold load need further heating before this could be partially achieved. This wall density difference is experimental evidence that shells with different gold content possess different mechanical properties. Interestingly, it was also found that shells containing high concentration of gold nanoparticles in their walls were fusing more frequently and at lower temperature in capsules containing no gold. Various phenomena, such as capsule fusion [228] or rupture, were observed after thermal treatment in presence of other substances.

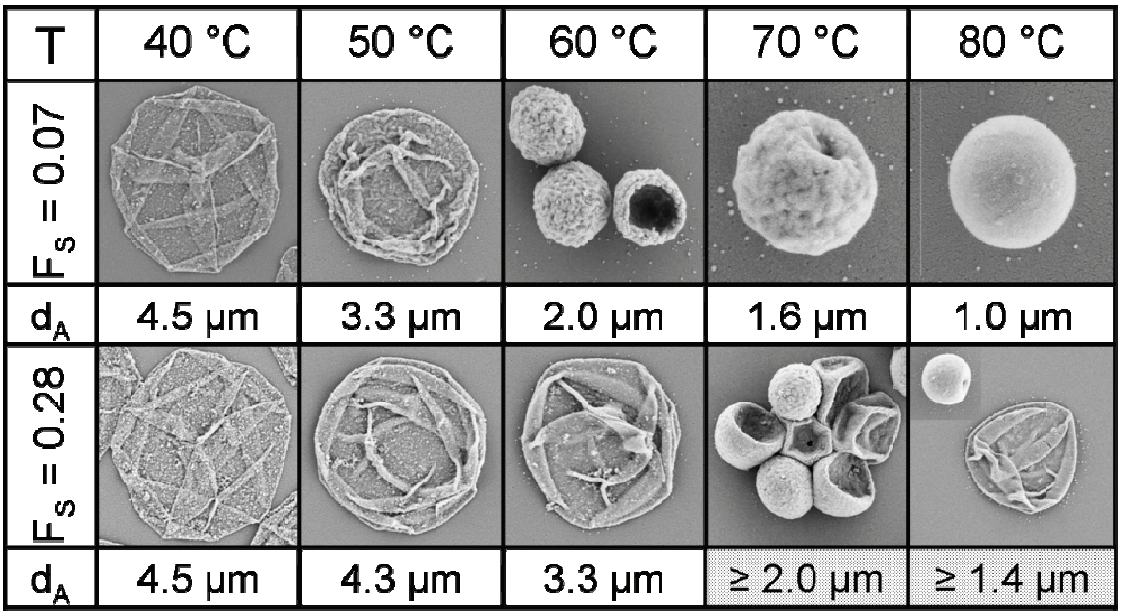

Fig. 5.5 SEM images of Homo-Au2 capsules at various temperatures having a gold nanoparticles surface coverage of 7 % and 28 %, top and bottom row, respectively. Each column shows an image of each type of capsule shrunk under the same conditions with their average diameter (d_A). The two d_A values that are shaded had a broad size distribution with a significant number of fused or damaged capsules.

5.1.3 THERMAL SHRINKAGE AS A FUNCTION DEXTRAN CONCENTRATION

Thermal shrinking of polymeric capsules induces a restructuration of the shells to a thicker and denser state that tends to be significantly less permeable then prior shrinking. This side effect of thermal shrinking is conveniently used to encapsulate substances in microcapsules by incubating and heating shells with macromolecules that can originally permeate the capsule wall. However, the effect of the concentration of encapsulated material on the thermal curves of microcapsules was not reported.

The thermal curves of Homo-Au2 shells doped with 7 % (F_S = 0.07) gold nanoparticles were investigated as a function of the concentration of dextran before thermal treatment. Aliquots of capsules solution were resuspended in 0.5, 1.0, or 2.0 mg/ml of fluorescently labeled AF 555 dextran for 30 minutes. Samples were then heated at various temperatures from 25°C to 80°C, at 5°C intervals. After thermal shrinking, capsules samples were allowed to cool down and washed with water twice after mild centrifugation and removal of the supernatant to discard

any dextran that had not been encapsulated. The average diameter of capsules was measured by LSCM.

Figure 5.6 shows an LSCM compound caption of Homo-Au2 microshells with encapsulated AF 555 dextran (0.5 mg/mL) after being shrunk at 55°C for 20 minutes. The image was obtained by overlaying the confocal fluorescence channel (λ_{ex} = 534 nm) with the transmission image recorded at the same time. This approach allows easily distinguishing between shells that contain encapsulated fluorescent material against empty shells.

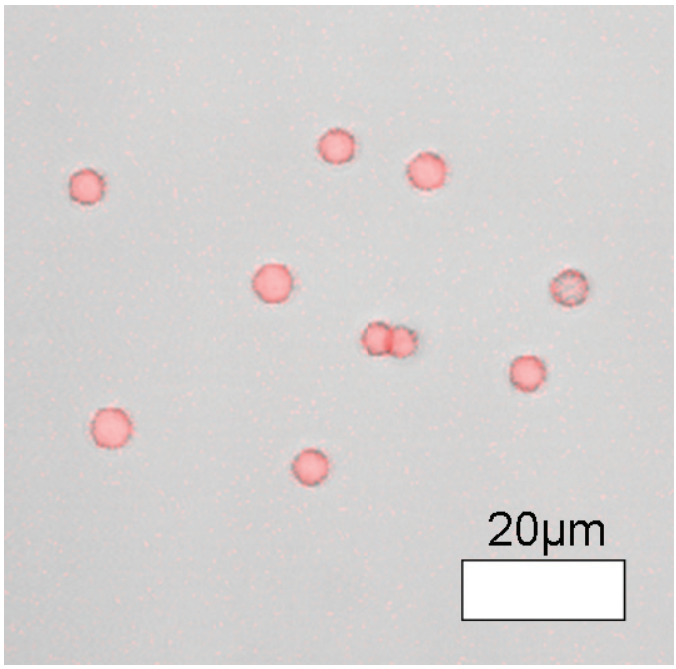

Fig. 5.6 LSCM image of Homo-Au2 capsules with a 7 % gold nanoparticle surface density and encapsulated dye in the cavity. The shells were thermally shrunk in presence of 0.5 mg/mL fluorescently labeled dextran in order to encapsulate the dye.

The results obtained for the thermal encapsulation of 3 kDa dextran at different concentrations are illustrated in Figure 5.7. The thermal curves obtained were compared to capsules shrunk in the absence of dextran. It was found that as the dextran concentration is increased the microshells are more difficult to shrink. In addition, the minimum diameter that capsules with encapsulated material can be shrunk also increased significantly with increased dextran concentration. This can be attributed to the diffusive force caused by the concentration difference in dextran across the wall of the shrunken capsules. The shell permeability may vary

significantly depending on its thickness and constituents, but also on the temperature of incubation and encapsulated substance used. This is because, the permeability of any semi-permeable membrane is a function of the rate of diffusion specific to a particular compound and depends on the interactions of a molecule with the membrane and the density of this one. The shrunk capsule shell with a denser wall is less permeable to any given material than in its unshrunk state. The final concentration of an encapsulated substance by thermal treatment of microcapsules can be approximated by the expression:

Eq. 5.1 $$C_F = C_i\left(r_i^3 - r_F^3\right)$$

where C_i is the initial encapsulate concentration and r_i, r_F are the initial and final capsule diameters, respectively. For example, if we neglect the changes in wall thickness, shrinking capsules of 4.6 μm to 2.3 μm corresponds to a tenfold decrease of the inner capsule volume. Meanwhile, the capsule wall becomes thicker and rapidly impermeable to molecules as shell shrinking progresses. As a result of the heat treatment, molecules that could previously diffuse across the capsules wall become sequestered inside a shrinking shell, leading to the creation of a diffusive force which opposes the hydrophobic force that drives shrinking.

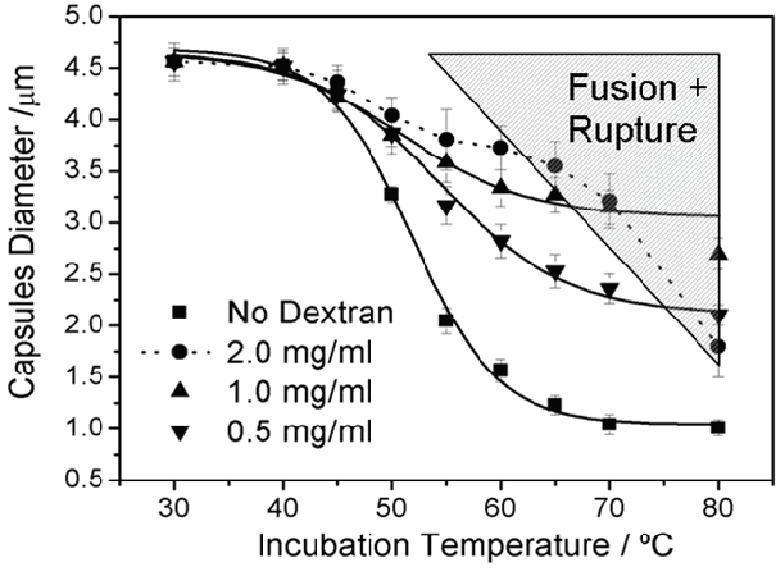

Fig. 5.7 Effect of dextran concentration on the heat shrinking curves and encapsulation efficiency of Homo-Au2 microshells with a gold surface coverage of 7 %.

Figure 5.7 also reveals that under conditions of high incubation temperature and high dextran concentration a proportion of capsules were found damaged. Capsules that were considered damaged were typically deformed and contained no fluorescent material in the cavity after being exposed to heat. Ruptured capsules appeared at around 60°C, 65°C and 75°C for samples that were thermally treated in presence of dextran concentrations of 2.0 mg/ml, 1.0 mg/ml and 0.5 mg/ml, respectively. Since the onset for damaged microcontainers decreases as dextran concentration is increased, rupture is thought to be the result of accumulating an excessive diffusive pressure across the wall during shrinkage. These observations indicate that a poor quality sample resulting from thermal encapsulation could be due to an attempt to encapsulate too much material and of doing so at high temperature.

To determine whether increasing the molecular weight of the encapsulated substance affected the behavior previously observed, fluorescently labeled dextran with a molecular weight of 10 kDa was encapsulated at concentrations of 0.5 mg/mL and 1.0 mg/mL. The resulting thermal shrinking curves are shown as black curves in Figure 5.8, where the hard curve was plotted from the average diameter of capsules shrunk in the presence of 0.5 mg/mL dextran and the dashed curve is the result of measurements done in presence of 1.0 mg/mL dextran. The two curves are plotted against the thermal curves taken at the same concentrations using 3 kDa dextran from Figure 5.7. The comparison of the two dashed and two hard curves supports that there is a shift of the thermal curves to the right when using 10 kDa dextran suggesting that higher molecular weight dextran requires more higher temperature to be encapsulated in a capsule shrunk down to the same diameter as one shrunk in the presence of lower molecular weight dextran.

In view of these results, it can be postulated that the useful range of encapsulate concentration for moderate size polymers using the thermal encapsulation method, should ideally be in the order of 0.5 mg/ml or less. Thermally shrinking capsules in presence of a higher concentration of material to encapsulate may bring about undesired side effects such as fusion and rupture of the microshells as well as imposing a limit to the diameter capsules can be shrunk to. The useful range of temperatures at which optimal number of capsules with encapsulated material was between 50 and 60°C.

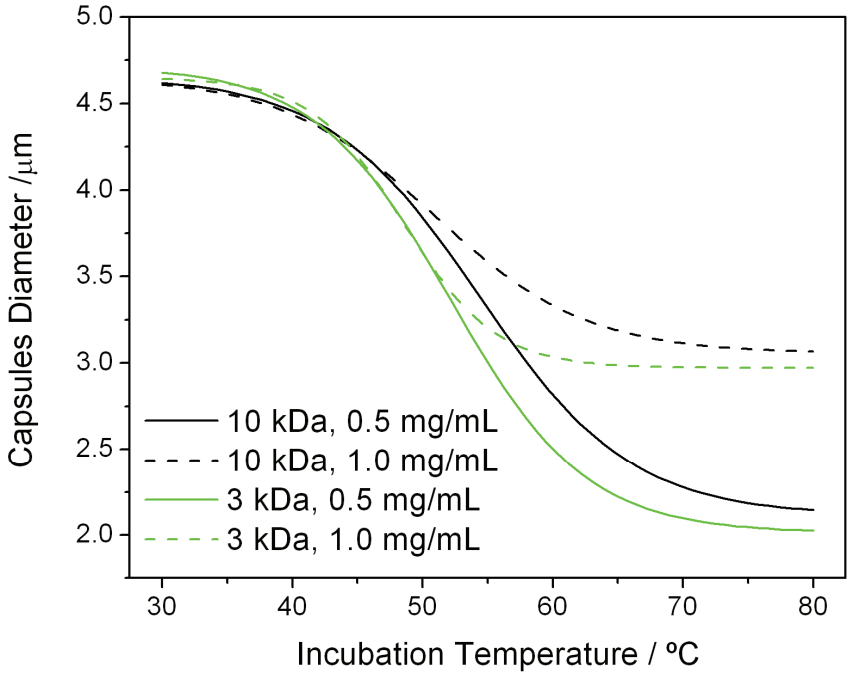

Fig. 5.8 Effect of the molecular weight of dextran on heat shrinking and encapsulation efficiency of Homo-Au2 microshells with a gold surface coverage of 7 %. The green curves illustrate that capsules incubated with 0.5 mg/mL (hard line) and 1.0 mg/mL (dashed line) 3 kDa dextran were generally easier to thermally shrink than in the presence of 10 kDa dextran.

5.1.4 MECHANICAL DEFORMATION AS A FUNCTION OF NANOPARTICLE CONCENTRATION

The influence of gold content on the mechanics of polymeric microcapsules was investigated. An accurate method to determine mechanical properties of polyelectrolyte capsules in solution is AFM force spectroscopy with the colloidal probe technique. In this method, a glass bead is glued to a tipless cantilever providing a well-defined contact area between the capsule and the bead. The glass bead is then centered on the microcapsule which is fixed by electrostatic interactions to a substrate immersed in water and pressed on the microcapsule by bringing the tip towards the capsules. Once the glass bead gets in contact with a microcapsule, the latter displays a “resistance” to the applied force until it is eventually deformed when sufficient force is applied. This effect can be thought of as if one was pressing down on a ping-pong ball, continuously increasing the load until the ball bumps inward. This situation can be described

within the theoretical model of Reissner. [15] It relates the samples' spring constant *c* to the Young's Modulus of the material *E*, the wall thickness of the shell *h* and the radius of the shell *R*:

Eq. 5.2 $$c \propto \frac{E \cdot h^2}{R}$$

The spring constant is derived from the slope of the force-deformation curve and is a measure of mechanical stability for the microcapsule shell. For this study, Homo-Au2 shells doped with nanoparticles at percent filling factors of 1 %, 7 % and 28 % were selected. Representative force-deformation curves for individual capsules of each type are shown in Figure 5.9. A clear trend can be seen: increasing gold concentration in the wall of the Homo-Au2 capsules of the same size increases the resistance of microshells to deformation. The increase in the capsules spring constant due to the gold content seems to be non-linear. For F_S values of 0.01 and 0.07 there is a relatively small difference in the spring constant of shells of the same size, the mechanical properties are similar to non-doped capsules. When compared to the high gold concentration, there is an increase in the stability of the capsules by a factor of approximately five. This result is in line with the work of Dubreuil *et al.* who found a considerable increase in the spring constant due to the incorporation of nanoparticles into the shells. [228]

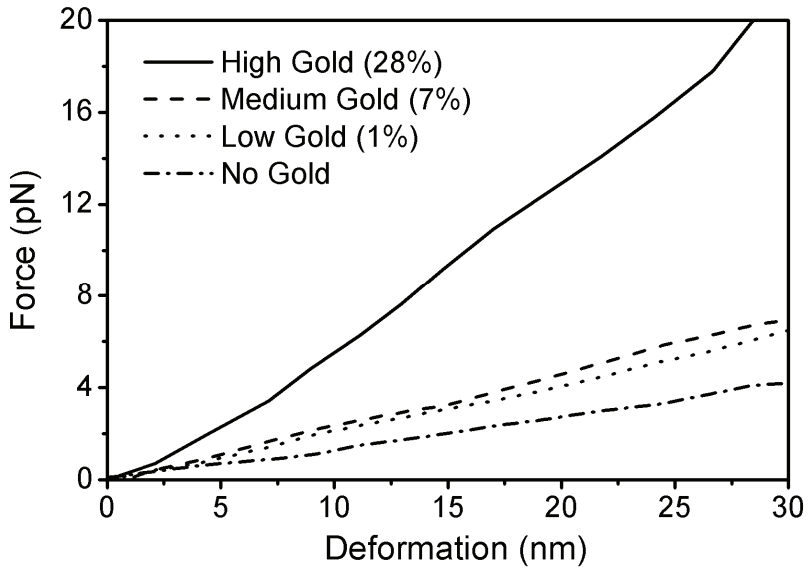

Fig. 5.9 Force-deformation curves of representative Homo-Au2 capsules with different gold content and different sizes. A small stiffness increase is found in shells with surface filling ratio of 0.01 or 0.07, whereas a large increase is found in shells with the highest load of gold nanoparticles.

This is also reflected by the average values of the spring constants of up to 45 individually tested shells which are presented in Table 3. A possible explanation for the non-linear change observed in the spring constant values is percolation. Percolation between nanoparticles should be infrequent at the beginning of thermal shrinking resulting in the wall properties around nanoparticles being independent of their presence. Therefore, below a certain critical percolation frequency the mechanical properties of microcapsules are governed by the polyelectrolyte matrix. However, as shrinking progresses the capsule wall provides a decreasing volume to accommodate the nanoparticles. At a critical concentration, percolation takes place and the nanoparticles begin to interact with each other, dominating the shell mechanics. The standard error associated with the stiffness values presented in Table 3 originates from differences in the geometry of capsules. For most types of measurements, all capsules within a given sample can be assumed to be ideal spheres with identical radii and wall thicknesses as well as possessing a defect free wall. However, these assumptions are not applicable in mechanical studies which are closely dependant on structural properties and the presence of defects within the wall structure. The error associated with these assumptions in addition to the error resulting from the optical setup used to align the colloid probe above the microcapsules (0.2 μm) results in an error of 75-250 pN/nm in shell stiffness. [15] As well, there might be slight changes in the wall thickness that affect mechanical constants of the capsules. It was previously demonstrated that increasing the number of layers of micro-shells of comparable diameter also increases their mechanical stability. [15,229]

TABLE 3 DIAMETER, GOLD CONTENT AND STIFFNESS OF HOMO-AU2 CAPSULES.

Capsule	**Diameter [μm]**	**S_F [%]**	**Stiffness [pN/nm]**
No Gold	4.57 ± 0.2	0	183.1 ± 74
Low Gold	4.52 ± 0.3	1	259.2 ± 140
Medium Gold	4.58 ± 0.2	7	293.3 ± 90
High Gold	4.48 ± 0.3	28	1447.6 ± 352
Medium Gold	~ 2.5	7	1460.6 ± 588

Comparing the values found in Table 3, it is found that the stability of capsules with a diameter of about 4.5 μm and a high gold content (F_S = 0.28) is comparable to capsules with a diameter of 2.5 μm with a medium gold content (F_S = 0.07). Thus, by annealing the capsules large effects in shell stability can be obtained without changing the gold content in the microcapsule wall. For biomedical application a higher shell gold nanoparticle density is not desirable because such capsules possess a more heterogeneous shell construct and a greater potential to display defects. Therefore, shrinking capsules with a lower gold concentration in the shell is favorable to produce microcontainers with a tailored gold content, as well as a tailored stability.

5.1.5 SURFACE ROUGHNESS

Incorporating charged colloids between polyelectrolyte layers affects the adhesion of subsequent polymeric layers. The adhesion of gold nanoparticles onto a polyelectrolyte coated surface offers a different structure to which subsequent layers of polyelectrolyte may absorb. The spherical nature and intrinsic repulsion of like-charge colloids make it impossible to obtain full nanoparticle coverage (F_s = 1) for a polyelectrolyte-coated surface by simply adding nanoparticles during LbL assembly. Consequentially, the gold nanoparticles used in this work offer inflexible, yet partial charge overcompensation to the next layer. The PSS layer that is added after gold nanoparticles during the LbL assembly completes the overcompensation of the surface, by absorbing in all areas where gold nanoparticles have not bound. The following PDDA layer finds two types of surfaces possessing different charge densities to absorb onto. Gold nanoparticles with an average diameter of 20 nm were expected to affect the surface and roughness of the capsule surface.

Figure 5.10 shows the roughness profiles of 1 μm^2 area of $(PDDA/PSS)_4$ microcapsule (left) and of a Homo-Au2 shell doped with 7 % of gold nanoparticles (right) as measured by AFM. It should be noted that neither sample had been previously treated with heat and AFM measurements were conducted on dried microcapsule samples. As a result of the drying process, microshells typically collapse and display numerous folds and creases. To minimize the incorporation of error in the measurements due to folds and creases, only areas of the capsules' surface lacking such features were considered. The average roughness values were found to be 1.5 nm and 2.1 nm for the reference and the gold-containing samples, respectively. This corresponds to a surface roughness increase of about 30 %. More polymeric material was expected to precipitate onto the colloid particles during the layer additions that followed the

absorption of nanoparticles. Therefore, alongside roughness the surface area available for the next layer to adhere was expected to rise significantly.

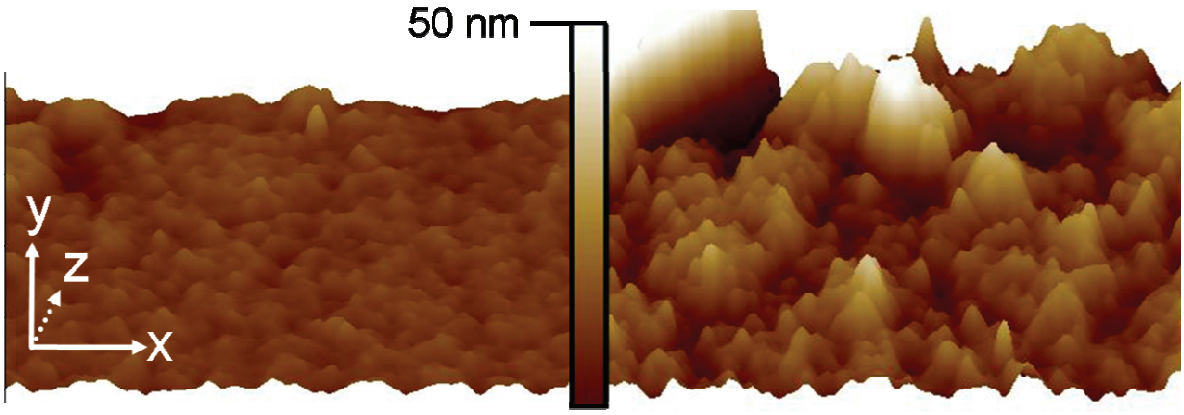

Fig. 5.10 Topographic AFM image of $(PDDA/PSS)_4$ and Homo-Au2 shells illustrating the surface roughness of a 1 μm^2 area. The x and z axes measure 200 nm. The range of height (y axis) of the surfaces is ca. 50 nm, as depicted by the scale in the center.

Roughness measurements represent the average values obtained from measuring 1 μm^2 flat areas of 10 capsules for each type of shell. The average wall thickness of 30 capsules of the two aforementioned samples was measured using AFM by subtracting the background (substrate) height from the height of microcapsules. These measurements revealed that control microcapsules lacking nanoparticles had an average thickness of 18.4 nm (± 1.5 nm) and an average thickness of 20.4 nm (± 1.8 nm) for Homo-Au2 (7 %) capsules. The large thickness variations due to the presence of gold particles were accounted for by specifically taking thickness values at the lowest point of each measured capsule. The measured wall thicknesses suggest that the wall of a capsule containing gold nanoparticles is approximately 10 % thicker than a shell lacking nanoparticles. However, it is difficult to completely eliminate the possible contribution of nanoparticles embedded in the polyelectrolyte wall as a source of error in thickness measurements. Yet, any increment in wall thickness may further contribute to the shell stability of microcapsules containing nanoparticles as a direct consequence of an increased shell roughness.

5.1.6 CONCLUSIONS

Using PDDA/PSS-based microcapsules as a model system doped with citrate stabilized gold nanoparticle, it was shown that there are large differences in sample properties based on the concentration of nanoparticles in the shell. Varying the surface coverage of gold nanoparticles decreases the ability of microshells to thermally shrink and can largely limit the lower size they may be shrunk to. Increasing the concentration of material to be encapsulated is found to decrease the ability of microcapsules to thermally shrink, while limiting the lowest capsule diameter obtainable. Separately, increasing both gold content and encapsulate concentration led to an increase in the probability of finding broken or fused microshells at lower incubation temperatures. Breakage and fusion has for consequence to reduce sample quality and appears to be related to the microshells higher surface roughness for samples of increasing gold content, and weakened electrostatic interaction when using higher concentration of encapsulation material. Force-deformation measurements show that in their unshrunk state, there are slight differences in shell stiffness for shells with percent filling factors equal to 1 % and 7 %, but resistance to deformation was increased by a factor of five in unshrunk capsules microshells functionalized gold at a percent filling factor of 28 %. Shrinking Homo-Au2 shells containing 7 % gold to half their diameter had a similar effect on capsule stiffness. The improvement in shell stiffness due to gold content is non-linear, for low nanoparticle concentrations the mechanical properties are dominated by the polymeric matrix and above a critical concentration the capsules stability stems from nanoparticles.

5.2 THE EFFECT OF NANOPARTICLE DISTRIBUTION ON ENCAPSULATION AND RELEASE

Colloid gold nanoparticles appear red and display a strong absorbance at around 520 nm due to the presence of surface plasmons at the nanoparticle surface. Aggregation of gold nanoparticles in solution by ionic species results in a change in color to blue and the apparition of an absorption region between 600 nm and 900 nm. [230] The position of and broadness of the aggregation peak is generally understood as a function of the morphology of the aggregates, which in turn depends on factors such as nanoparticle size, charge and the aggregation conditions. Chemical cross-linking of nanoparticles can also induce optical changes and is well documented. [231] Attempts to control the assembly of gold nanoparticles by electrostatic means have been done on the ionic portion of the stabilizing ligands, such as the carboxylic acid group of citrate-stabilized gold particles, for example by changing the solution pH or adding cationic polyelectrolytes. [232,233] At low pH, carboxyl groups become protonated decreasing the electrostatic repulsive forces between nanoparticles. Alternatively, polyelectrolytes and their counter ions can bind several nanoparticles, forcing flocculation.

There are two distinct aggregation processes for gold nanoparticles when using electrostatic means; (1) multiply charged ligands seem to be able to take multiple gold nanoparticles and force them in cluster-type structures, (2) singly-charged ligands are believed to induce a slower assembly process by which nanoparticles form string-type structures. [230,234] Both mechanisms typically result in color change due to interparticle plasmon coupling but differ in their relative response time to the addition of ions. An exception to this requirement was recently discovered when gold nanoparticles were found to change between red and blue in the presence of ozone suggesting that the color change is not dependant on aggregation but rather a physical property of the gold surface. [235]

Although there have been some investigations on the nature of the aggregation process of gold nanoparticles, application of such assemblies in complex systems has been limited largely due to the hurdles related to controlling it. [236] The incorporation of one or several close-packed layers of gold nanoparticles within the shells of microcapsule proved efficient for near-IR induced release [20,193] but also resulted in composite shells that responded to light violently, which could be detrimental to the encapsulated cargo. Clusters of nanoparticles on the other hand allow preserving most of the native properties of polymeric microcapsules because they cover only certain areas of the shell, but inevitably introduce heterogeneities that might

interfere with sample quality. [233] The drawbacks related to both nanoparticle organizations in composite shells infer limitations to their use as microdelivery systems. Colloidal nanoparticles could potentially solve these issues if it were not for their low absorption in the near-IR region. Gold nanorods are another potential alternative due to their large molar absorptivity in the near-IR, [190] however, the ionic stabilizers necessary to prevent them from aggregating affects their interaction with other materials. No thorough investigation has been done on comparing the effect of nanoparticle distribution on the laser-induced release of composite polymer shells. This section present our investigation of the general influence and benefits of using different distributions of gold nanoparticles as light sensitizing agents on capsule properties such as thermal stability, permeability, as well as encapsulation and release. [237]

5.2.1 SPECTROSCOPIC PROPERTIES OF GOLD NANOPARTICLES

The influence of salts on the aggregation of colloid gold was briefly investigated. Solutions of lithium chloride (LiCl), sodium chloride (NaCl) and potassium chloride (KCl) with concentrations of 0.1 M were prepared. An aliquot of colloid gold nanoparticles (20 nm) was added dropwise to the volume of salt solution while stirring at room temperature. Stirring was found to have little influence on the aggregation behavior. No significant change in the absorbance spectra of gold nanoparticles of diameters of 5 nm or 10 nm was observed when salt was added as shown in the lower panel of Figure 5.11. LiCl still provided no aggregation even at a concentration of 1 M in addition of being a harmful chemical and was therefore not considered for other studies. After mixing a solution of NaCl (0.1 M) with a solution of citrate-stabilized gold nanoparticles (20 nm), the latter became unstable and the solution rapidly changed color. The absorption spectra solutions of citrate-stabilized gold nanoparticles measured before and 1 minute after addition to 0.1 M NaCl is shown in Figure 5.11 left and right, respectively. It is seen that the original plasmon peak is still present after aggregation although red-shifted by about 4 nm from 520 nm to 524 nm. The absorption spectrum also displays a novel broad absorption region between 700 nm and 900 nm with a maximum centered at 740 nm. A similar absorption peak, red-shifted by 20-30 nm, appears upon mixing a solution of KCl (0.1 M) with an equivalent volume of gold nanoparticles solution. The new aggregation peak originates from the coupling of plasmon absorbance and shifts to the right as aggregates of nanoparticles grow larger.

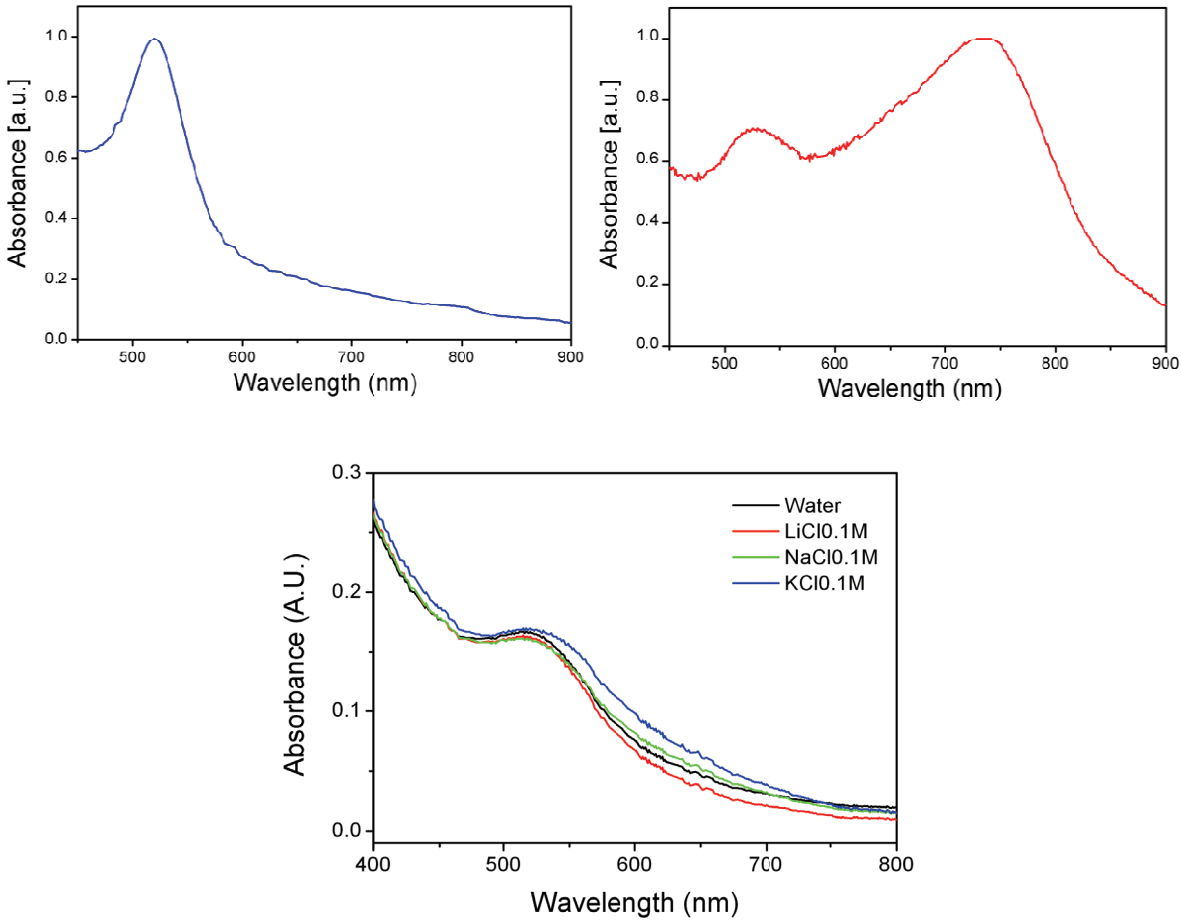

Fig. 5.11 Absorbance spectra showing the effect of NaCl on 20 and 5 nm colloidal gold. Top panel: 20 nm nanoparticles aggregate in solution upon addition to salt resulting in a change in the absorbance spectra, which typically displays a single strong absorbance peak at 520 nm (left), yielding a second intense absorption peak at 740 nm. Lower panel: the absorbance of 5 nm gold solution upon addition to various salt solutions.

Figure 5.12 illustrates the effect of salt concentration on the absorption spectra of a solution of 20 nm gold nanoparticles 1 minute after the nanoparticles were added to the salt solution. The aggregation peak is shown to grow more intense and farther to the right while the plasmon absorbance decreases in intensity around what appears to be an isosbestic point. This indicates that the molar absorptivity of homodispersed and aggregated nanoparticles are linearly related providing evidence that the surface plasmon resonance absorption is related to the aggregation absorbance. Using a NaCl concentration below 40 mM for 10^{11} nanoparticles

could not induce aggregation even after several hours. This is in agreement with previous reports that suggested that aggregation kinetics of gold nanoparticles requires a minimum solution activity which depends on the nature and valence the destabilizing ion. [238,239]

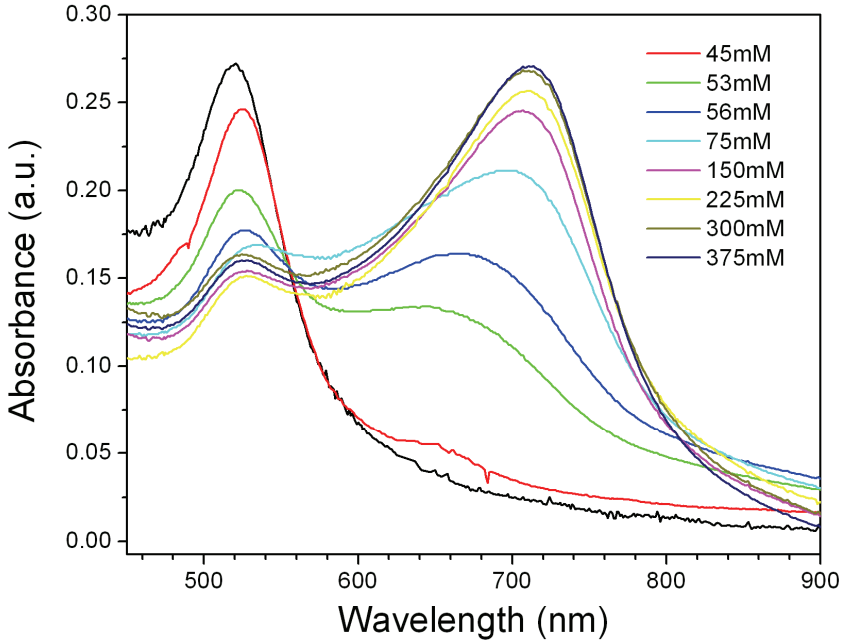

Fig. 5.12 Absorbance spectra of gold solution as a function of salt concentration 1 minute after addition to a NaCl solution. The salt concentrations shown in the legend are the calculated final concentration in the aggregated nanoparticle solution.

UV-visible spectroscopy supports color change typically occurs within 5 seconds after adding gold to salt. Measuring the absorbance of the same solution at 5 and 20 minutes after mixing suggested that the aggregation slows but continuous as the aggregation peak undergoes a bathochromic shift. Inverting the order of addition by adding a solution salt to colloid gold was found to induce aggregation to a much lesser degree. The spectrum on the right of Figure 5.13 illustrates that an absorbance change occurred rapidly within the first minute after adding gold to the NaCl solution but rapidly slowed down, red-shifting and losing intensity as aggregation proceeds. The solution remained red for several hours but aggregates had precipitated at the bottom of the test tube overnight, suggesting that aggregations still takes place when salt is added to gold but with very different kinetics.

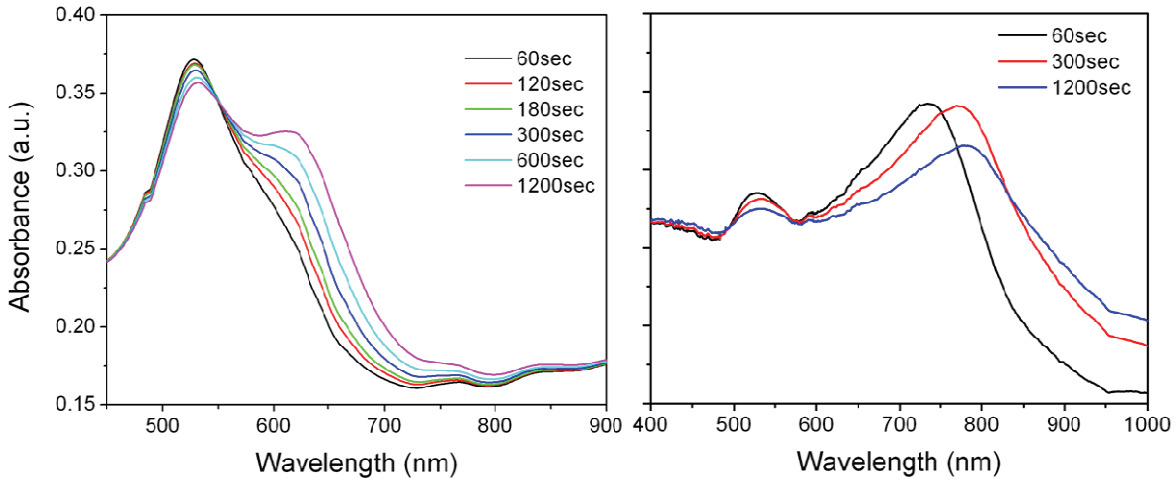

Fig. 5.13 Absorbance spectra colloidal gold as a function of time after gold is added to the salt solution (left) and salt is added to the gold (right).

Dynamic light scattering (DLS) measurements were taken before and after mixing NaCl and gold solutions. Figure 5.14 shows the DLS results taken in *radii by mass*, which reveal that the aggregation proceeds very rapidly during the first 2 minutes and levels off afterward. A curve showing the average tendency of the data was extracted but with a poor fit. At first, it appears that the aggregate growth exponentially decays as nanoparticles are consumed by assemblies. Another possibility is that the aggregation could be a two step process involving a nucleation step at first, where nanoparticles form dimers, trimers and nanoparticle oligomers of various lengths and a second process where oligomers aggregate with each other forming networks suggesting that once all single particles have been included in oligomers (fast process), oligomers start aggregating (slow process). This implies that at high salt, no single particles should be found in solution. This hypothesis is supported by previous observations. [230,239] The aggregates eventually precipitate and washing the pellet with water or adding citrate did not enable resolubilization of the nanoparticles within aggregates. The electrostatic destabilization process is irreversible.

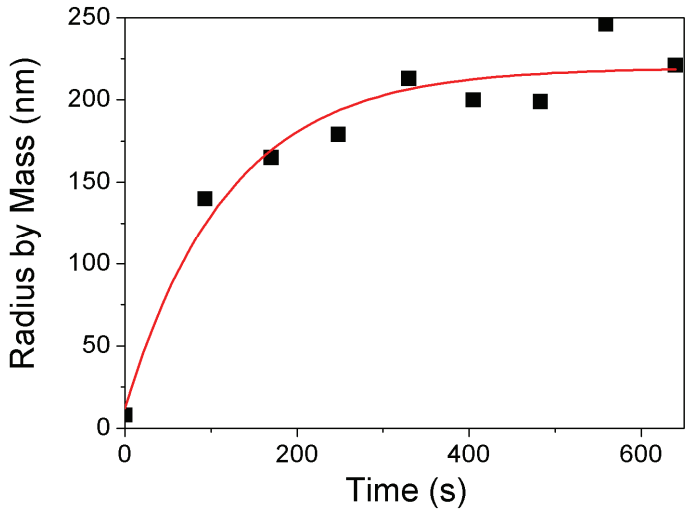

Fig. 5.14 DLS plot of aggregating 20 nm gold nanoparticles measured in radius by mass as a function of time in seconds. The first measurement at time 0 was performed on a sample of colloidal gold solution mixed with an appropriate volume of water. Subsequent measurements were taken over 60 second periods at 25°C.

To summarize, metal nanoparticles possess charged surfaces in order to prevent aggregation. In the case of the gold particles used here, anionic citrate molecules are responsible for maintaining electrostatic stabilization. Aggregation of such nanoparticles occurs when the surface charge are neutralized by decreasing the pH or by the addition of a source of cations, thus lowering the long range electrostatic repulsions and allowing short range attractive forces to (Van der Waals forces) dominate. [192,230] However, ionic neutralization using singly charged cations does not lead to the complete depletion of surface charge. This is believed to be due to cations "polarizing" the gold particles by positioning themselves away from one another at the nanoparticle surface due to their same charge resulting in string like aggregates. [230,239] Adding colloidal gold to a salt solution resulted in the formation of aggregates with intrinsic absorbance in the near-IR range. This process is fast and aggregates grow larger over time. Using NaCl or KCl concentration increases the molar absorptivity of aggregates but this effect has a saturation point above which additional salt does not seem to further improve absorbance. In earlier work, gold nanoparticles were inserted in the shell of polymeric microcapsules and used to convert light to heat, rupturing the microcapsules' wall and

releasing encapsulated material. [233] The formation of aggregates of gold nanoparticles (at high concentrations) on polyelectrolyte microcapsules was previously demonstrated [130] but their response to irradiation, permeability and surface roughness have not been investigated.

5.2.2 PREPARATION OF GOLD AGGREGATES-FUNCTIONALIZED MICROCAPSULES

Polyelectrolyte microshells functionalized with homodispersed and aggregated gold nanoparticles were constructed on 4.62 μm silica particles. The polyion layers were prepared using the LbL assembly protocol with solutions of PDDA, gold and PSS, alternatively, until eight polyelectrolyte layers were obtained. For non-aggregated nanoparticles, 250 μL of colloid gold solution was mixed with 750 μL of water and added to PDDA-coated particles. To obtain aggregates of gold nanoparticles, an aliquot of 250 μL of colloidal gold solution was added to a 750 μL NaCl solution (0.1 M) and left to vortex at low speed for 60 seconds before being used to resuspend the solution of silica particles coated with a PDDA layer. Gold application was repeated before each PSS layer to assure that we obtained samples with consistent gold coverage throughout the wall. At the end of the shell assembly, the coated silica particles were treated with hydrofluoric acid (0.3 M) and thoroughly rinsed with water to remove the acid. Hollow capsules with an average diameter of 4.8 μm and possessing the following shell structure were obtained: $(PDDA/Au/PSS)_4$. To lighten the text, shells containing homodispersed and aggregated nanoparticles are abbreviated as Homo-Au4 and Agg-Au4, respectively. Light microscopy images obtained from the LSCM instrument showed homogeneous microcapsule samples with narrow size distribution.

PDDA proved to be superior to other polycations as it was the polyelectrolyte that could take the most gold per surface area as confirmed by measuring the UV-visible spectra of the supernatant after each gold addition. Figure 5.15 shows representative TEM images of a dried microcapsule treated four times with 250 μL aliquots of colloidal gold solution (4×10^{11} NPs/mL) where nanoparticles were added as such (left) and as aggregates (right). In the homodispersed case, nanoparticles were distributed evenly throughout the shell (Figure 5.15 left). On the other hand, a capsule impregnated with gold nanoparticle aggregates shows that only aggregates (Figure 5.15 right). In previous work, aggregates were introduced in polyelectrolyte shells by admixing nanoparticles with polyelectrolytes but this approach yielded large clusters or bundles of nanoparticles. [233] Aggregates obtained by the approach described here yields what can be described as “nanonetworks”.

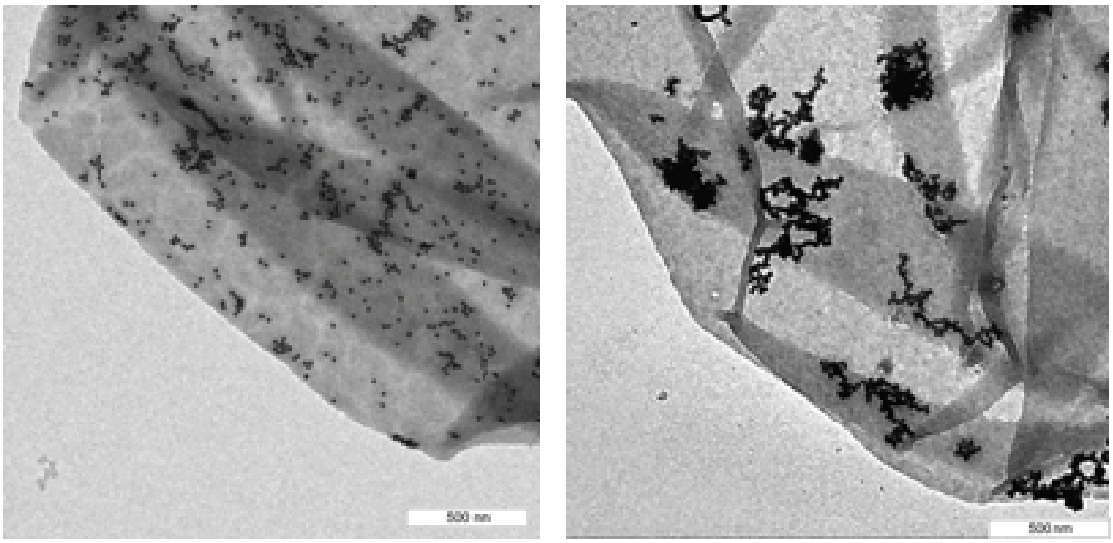

Fig. 5.15 TEM of dried Homo-Au4 and Agg-Au4 microcapsules. On the left nanoparticles were added to the LbL capsule preparation as such. On the right, gold nanoparticles were first added to a solution of NaCl before being added to the capsules preparation.

The capsules from the two samples shown in Figure 5.15 contained the same concentration of nanoparticles. The supernatant taken out after each adsorption step was found to contain less than 1 % of the amount of gold added indicating that most gold nanoparticles added during the polyelectrolyte shell assembly adsorb and remain in the capsule wall. A significant loss of nanoparticles, aggregated or not, was observed in the washing steps following gold addition during attempts to build shells with the structure $(PAH/Au/PSS)_4$. This is attributed to the fact that PAH is a weak polyelectrolyte with a significantly lower charge density than PDDA.

5.2.3 THERMAL SHRINKAGE AS A FUNCTION OF GOLD DISTRIBUTION

The thermal shrinking behaviors of capsules containing aggregated, non-aggregated and no gold nanoparticles were compared. To this end, an aliquot of capsule solution was placed in a thermostated bath for 20 minutes, left to cool and stained was with a 10^{-7} M solution of rhodamine 6G for observation by LSCM. Incubation temperatures were selected between room temperature and 80°C. At least 20 capsules were measured for each temperature using LSCM in order to determine the average diameter of the heated samples.

Figure 5.16 illustrates the heat shrinking behavior of the three shell types. The plotted thermal curves are surprisingly similar in shape. It was found that microshells containing gold nanoparticles needed higher temperatures to shrink to the same diameter than those capsules containing no gold. Within the range of temperature where capsules shrank, Homo-Au4 shells needed about 12 K more than the control while Agg-Au4 capsules needed an additional 7 K. Figure 5.16 illustrates that in the case of capsules with non-aggregated particles, the minimal diameter to which capsules could be shrunk to is higher than the other two types of capsules. This suggests that during heating the decreasing surface area brings neighboring gold nanoparticles in the microcapsule wall closer to one another so that they inhibit further shell shrinkage via percolation. One would then expect a shell containing more particles or homogeneously distributed particles to be more affected by interparticle effects since encounters between particles is expected be more frequent than those in a microshell containing gold nanoparticles with larger interparticle distance.

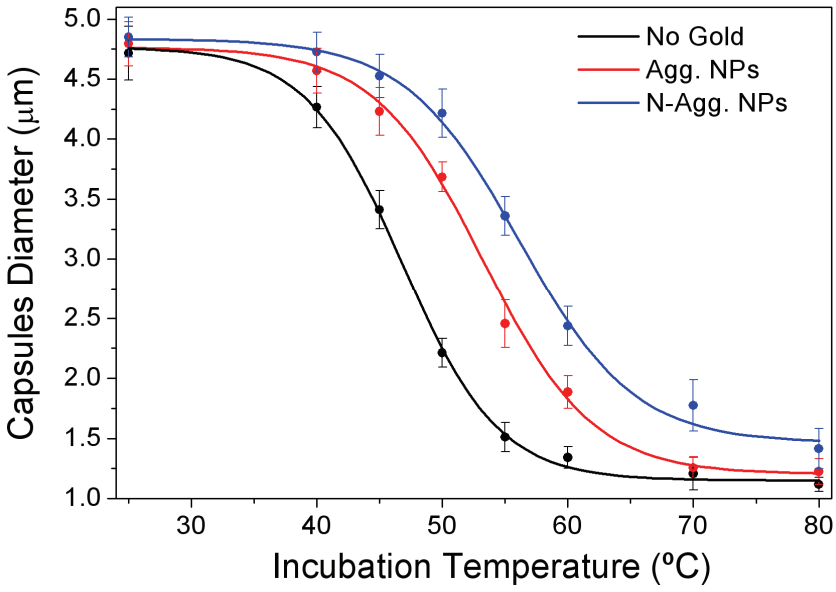

Fig. 5.16 Heat-shrinking behavior of $(PDDA/Au/PSS)_4$ microcapsules with aggregated and non-aggregated nanoparticles as well as shells lacking particles a function of incubation temperature.

5.2.5 PERMEABILITY OF DEXTRAN AS A FUNTION OF MOLECULAR WEIGHT

The influence of gold nanoparticles on the relative permeability of polymeric microcapsules to neutral polymers with different molecular weights was investigated. For all experiments, a 20 μL aliquot of microcapsule solution was transferred to an Eppendorf tube and immersed in a water bath for 20 minutes at a desired temperature according to the data from Fig. 5.15. The aliquot of shrunk microshells was then mixed with a solution of fluorescently labeled dextran of desired molecular weight (*i.e.* 3 kDa or 70 kDa). The permeability of different microshells was determined by monitoring the number of shells permeable to dextran as a function of capsule diameter. The sample mixture was then deposited onto a glass slide and probed by LSCM for "leakiness" as a function of shell diameter. The fluorescence profiles of at least 20 capsules per data point were measured. A given capsule was considered permeable when, after the incubation period, its inner fluorescence was at least 50 % that of the surrounding medium.

Fig. 5.17 summarizes the results obtained. It was found that, at comparable diameters, the effective permeability of thermally shrunk microshells doped with gold nanoparticles is very different than the permeability of a control samples containing no nanoparticles. The hollow capsules were typically found to contain no fluorescence (permeability ratio = 0) or the same fluorescence as the surrounding medium (permeability ratio = 1). At the exception of capsules that were not shrunk, the permeability of capsules was greater for shells containing no gold than capsules containing non-aggregated nanoparticles. As expected, 70 kDa dextran permeated the polymeric wall somewhat less efficiently than 3 kDa dextran for all samples. However, the ability of 3 kDa and 70 kDa dextran to diffuse through the shell to a similar extent could suggest that pores in the capsule wall through which dextran molecules diffuse are larger than either dextran molecules used. Yet, the close relationship between capsule diameter and permeability to polymers of significantly different molecular weight remains difficult to access. The most probable explanation for this discrepancy is that dextran, as most polymers, possesses different conformations in solution and enters the microcapsule cavity in their linear form rather than in a globular or entangled shape. The main chain cross-section of two polymers made from the same units is expected to be identical and, solely based on this fact, dextran molecules of different length should permeate microcapsules equally regardless of their thickness. These results suggest that dextran enters microcapsule predominantly in a linear conformation and that the tendency for the three capsule types to be more permeable to 3 kDa dextran is most likely due to its lower entropy in comparison to 70 kDa dextran.

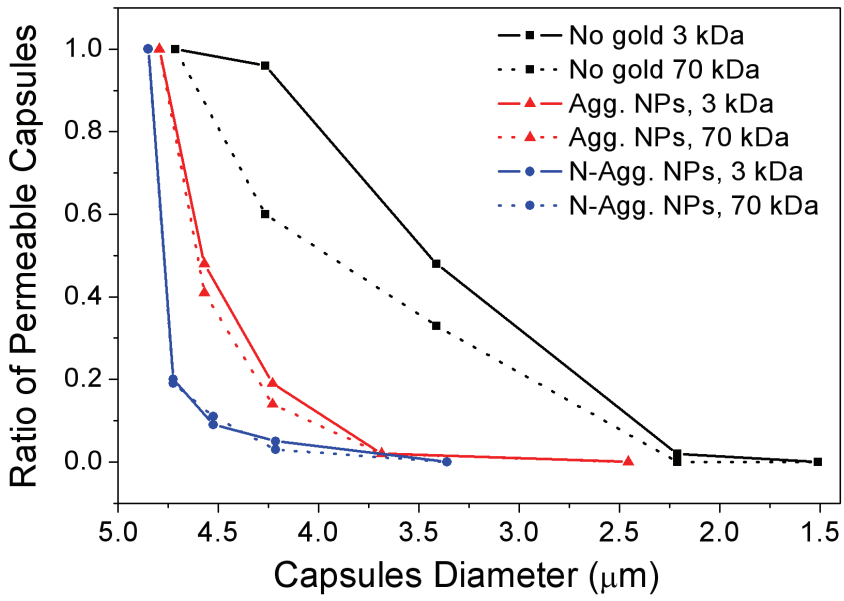

Fig. 5.17 Relative permeability of $(PDDA/Au/PSS)_4$ microcapsules containing no gold (black), aggregated (red) and non-aggregated gold nanoparticles (blue) as a function of diameter. Polymeric shells were thermally shrunk to different sizes in the range of temperatures from 35 to 55°C and at 5°C intervals. The ratios of permeable capsules were determined from LSCM by measuring the fluorescence profiles of 60 capsules per data point.

Shell permeability is not largely different for polymers of significantly different molecular weights at the exception of $(PDDA/PSS)_4$ shells. At the macroscopic scale, the polyelectrolyte mesh of the capsule shell can be imagined as being dotted with channels of various sizes through which molecules can permeate. Since two neutral polymers of different molecular weights do not permeate the microshells to an identical degree, it can be said that the channels' diameter are limited and thus contribute to some sort of size exclusion. To be true, this assumes that the diffusion of the polymer at constant temperature is in equilibrium, that is, polymers are free to flow in or out of the capsule they can permeate. Assuming that diffusion of a neutral polymer only depends on its size, the enthalpy change associated with the polymer's diffusion must be zero. The Gibbs free energy of diffusion is therefore dictated by the entropy of the polymer. The number of possible conformations of a polymer within the limited diameter of channels within the capsule wall decreases with increasing molecular weight explaining why the longer polymer permeates the microcapsule wall more difficultly than a shorter one.

While entropic limitations conveniently explains why there is a difference in shell permeability to dextran of different molecular weights, this argument does not account for the much greater difference between samples of microcapsules with different nanoparticle distribution. The results shown in Figure 5.17 suggest that the incorporation of nanoparticles in the wall has a large effect on the permeability of polymeric thin films. This is counter-intuitive since in the absence of laser excitation, permeability should be a property of the polymeric portion of the shells as permeating molecules cannot pass through dense nanoparticles. Yet, even after shrinking capsules containing a low surface density of nanoparticles by as little as 5 % of their original diameter, between 50 % and 80 % of the capsules became impermeable dextran. This effect at such a low surface coverage and small decrease in diameter cannot be explained by percolation frequency between nanoparticles as in heat shrinking behavior. This information provides a basis for the size requirements necessary for encapsulation using different wall/nanoparticle compositions.

5.2.5 THERMAL ENCAPSULATION AS A FUNCTION OF DEXTRAN CONCENTRATION

It is generally accepted that the concentration of a substance that can permeate the microcapsule shell increases during heat shrinking from the moment the shell turns impermeable to this substance. This is supported by Figure 5.17 from the previous section which illustrates that virtually every capsules containing either distribution of gold nanoparticles and having a diameter of 4.8 μm became impermeable to dextran (3 kDa, 70 kDa) once shrunk to 3.5 μm while preserving the ability to decrease in diameter. Although this change in concentration was not quantified, the fluorescence intensity of encapsulated fluorescent dextran was found to increase as encapsulated molecules are confined to a smaller volume.

The microcapsule wall acts as a semi-permeable membrane with low permeability to large molecules but high permeability to water molecules so that osmotic effects can usually be neglected. As a result of the concentration difference of a particular substance across the capsule wall, a diffusive force arises upon shrinking the capsules to smaller diameters. This diffusive force opposes the capsule shrinking to a certain extent and is expected to increase with higher concentration of encapsulated substance. To verify this hypothesis, a 50 μL of capsule solution containing aggregated or non-aggregated gold nanoparticles was heated in a thermostated bath at 60°C in presence of different concentrations of AF 594-labeled dextran (MW = 10 kDa). After cooling for 5 minutes, samples that had been heated were sedimented by

centrifugation and washed with water twice to remove the non-encapsulated dextran still present in the supernatant. The calculated diameters of thermally shrunk microcapsules were averaged by LSCM. The results are presented in Figure 5.18.

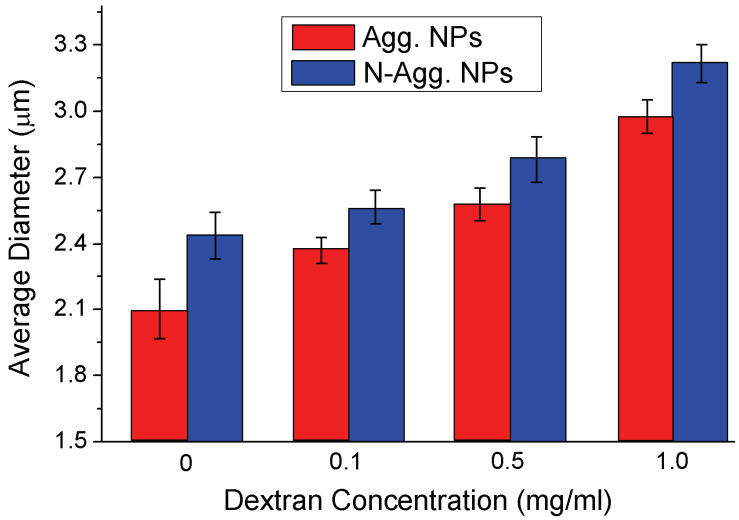

Fig. 5.18 Influence of the concentration of dextran on shell diameter. Microcapsules doped with aggregated and non-aggregated gold nanoparticles were thermally shrunk at 60°C for 20 minutes in the presence of dextran concentration from 0.1 to 1.0 mg/ml. The diameters of twenty shells were measured by laser scanning confocal microscopy for each data point.

It was found that both types of microcapsules shrink to a lesser extent with increasing concentration of dextran from 0.1 mg/mL to 1.0 mg/mL. The data also supports previous observations that despite containing the same mass of nanoparticles, shells functionalized with homodispersed gold are more resistant to heat than shells containing aggregated nanoparticles. The effect appears to be consistent within the range of dextran concentration used and in combination with aforementioned heat shrinking data may serve as a reference to select the correct parameters in order to obtain capsules of a desired diameter and concentration of encapsulated substance. Based on the discussion in *section 5.1.3*, it was expected that attempts at encapsulating dextran concentrations greater than 1.0 mg/mL could limit the shrinking process to a point where encapsulation is expected to be somewhat saturated, limiting the number of shells with encapsulated material after thermal shrinking since a number of them would be unable reach the necessary wall density to remain impermeable. Therefore, the behavior observed in Figure 5.18 is consistent with the

assumption that a diffusive force is generated by the dextran as the volume of the shell is decreased. Furthermore, the capsule shells were found to remain non-fluorescent after being added to a solution of labeled dextran molecules and subsequently washed supporting that albeit diffusing through the capsule's wall; the uncharged dextran does not bind to the polyelectrolytes the shell and therefore is not expected to interfere with the shrinking process.

5.2.6 SHELL THICKNESS BEFORE THERMAL TREATMENT

Based on the variations in thermal shrinkage and permeability discussed so far, it was hypothesized that these changes may be the result of an influence of the gold nanoparticles over shell thickness. If this were true, the shell of samples containing non-aggregated gold nanoparticles would be expected to possess more polyelectrolyte material or a denser structure. A change in overall shell density directly due to the presence of nanoparticles is unlikely due to two facts: first, the permeability of the different capsules would differ before heating, and second the fact that the shells contain a relatively low gold content that should have no consequence over the shell areas containing no nanoparticles. The latter point will be discussed at the end of this section.

The thickness of capsules before and after heat treatment was measured by AFM (from the areas containing no gold nanoparticles), Table 4. Before shrinkage, the average the shell thicknesses of control capsules lacking gold and those with non-aggregated and aggregated gold nanoparticles were 19.4 ± 1.1 nm, 19.2 ± 1.5 nm and 19.5 ± 1.2 nm, respectively. No significant difference in the wall thickness was found between the three capsules types. This is consistent with our observation in Figure 5.18 that the microcapsules were all equally permeable to two different dextran sizes before heating. Samples of each microcapsule solution were then thermally treated to verify our aforementioned hypothesis. For capsules that were shrunk, the average shell thickness of the control and aggregated gold nanoparticles samples were found to increase by 6 % and 17 %, respectively. A surprisingly large change in the wall thickness of ca. 35 % was measured for microshells containing non-aggregated gold nanoparticles. The shrinking temperatures were selected from Figure 5.16 in order to obtain microcapsules of approximately 4.4 μm in diameter (90 % of their original diameter) – the size at which a significant difference in permeability occurs, as illustrated in Figure 5.17.

TABLE 4 SHELL THICKNESS AS A FUNCTION OF CAPSULE DIAMETER

	Control		Aggregated NPs		Non-Aggregated NPs	
	Diam. (μm)	Thick. (nm)	Diam. (μm)	Thick. (nm)	Diam. (μm)	Thick. (nm)
Bef. T	4.9 ± 0.3	19.4 ± 1.1	4.8 ± 0.2	19.2 ± 1.5	4.9 ± 0.3	19.5 ± 1.2
After T	4.5 ± 0.2	20.6 ± 0.8	4.4 ± 0.3	23.2 ± 0.9	4.4 ± 0.3	30.1 ± 0.8

[a] Statistical measurements were calculated from the average thickness of 30 capsules.

5.2.7 SHELL THICKNESS AFTER THERMAL TREATMENT

In the previous section it was shown that the diameter of capsules shells does not significantly differ before thermal treatment whether they contained nanoparticles or not, and that a large difference in shell thickness appears immediately after shells began to shrink. A possible explanation is that polymeric material accumulates around the nanoparticles themselves during LbL assembly. In solution, positively charged PDDA-coated silica particles absorb all of the negatively charged gold nanoparticles added. The latter remain electrostatically attached to the PDDA layer despite centrifugation and several washings in water as confirmed by measuring the UV-visible spectra of the supernatants at various microshells preparation steps. Since 20 nm colloidal gold particles have a diameter comparable to the final shell thickness itself, it can be postulated that significant quantities of polyelectrolyte material absorb around the gold nanoparticles.

The absorption of polyelectrolytes around nanoparticles and their subsequent insertion in polymeric shells was discussed in previous work. [22] The surface filling factor (F_S) was calculated to be 0.05 for the Homo-Au4 microshells used for the permeability studies. The mere presence of nanoparticles cannot be the sole reason for the permeability changes previously observed. [230] Instead, we have to consider that a spherical 20 nm particle has a considerably larger surface area than the planar surface of microcapsule it is in contact with. It is reasonable to assume that some of the material absorbed around the particle can diffuse in its periphery during thermal treatment, making shell regions between gold nanoparticles thicker/denser, leading to a change in wall permeability. To verify the validity of this

argument, we first looked for indications that the roughness of the shells changes during thermal treatment using AFM.

Figure 5.19 illustrates the roughness differences between microcapsules doped with non-aggregated (A-B) and aggregated (C-D) nanoparticles, before (A,C) and after (B, D) thermal treatment. In each image, the position of some gold particles is indicated with an arrow. The surface of heated microcapsules was found to become much smoother and generally, the shape of nanoparticles became better defined (Figure 5.18). This second observation suggest a thinning of the material coating the nanoparticles occurs during heating and that this material was most likely redistributed in shell areas around the nanoparticles. It is found by comparing Figure 5.19 A and C that capsules containing non-aggregated gold nanoparticles are much rougher than shells doped with aggregates. It follows that during LbL assembly of the microcapsules, a rougher surface comes with more surface area available for subsequent layers to adhere. Since the aggregates found in the samples consist of a dozen to hundreds of particles, much of the gold surface is occupied by adjacent particles within the aggregate. The differences in the thickness of microcapsules containing aggregated and non-aggregated nanoparticles that were discussed in Table 4 support this argument. Experiments involving the fusion of capsules at high temperature showed that the lateral polymer diffusion within the microcapsule wall is kinetically very slow. [126] Yet, these experiments did not take surface tension effects into consideration, which in our case is assumed to be the driving force for polymers spreading away from the nanoparticles. It should be noted that the large roughness of the capsules, combined with the presence of folds and the different distribution of nanoparticles of these samples made it impossible to compare sample roughness quantitatively.

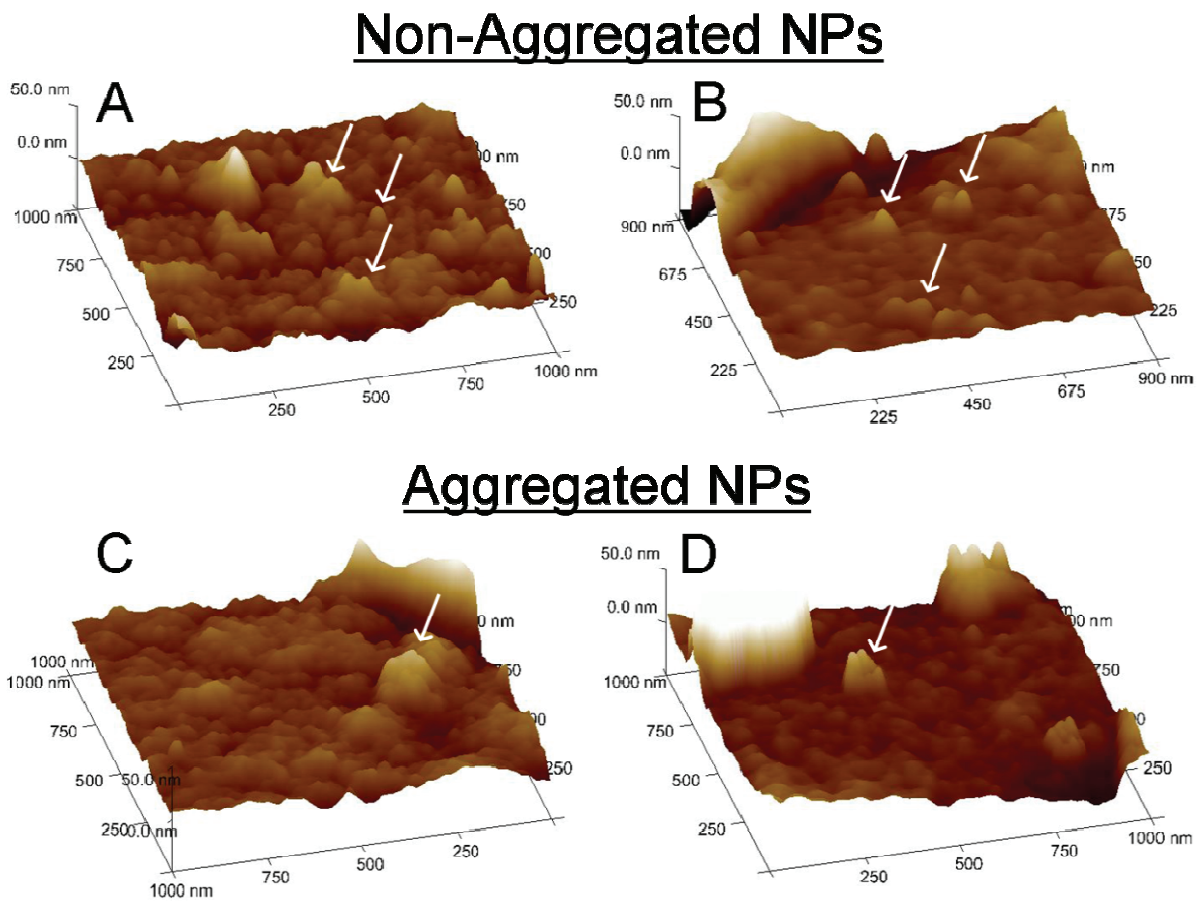

Fig. 5.19 Temperature related changes in capsule surface roughness for Homo-Au4 and Agg-Au4 shells. Top: 3D representation of the surface profiles of capsules doped with non-aggregated gold nanoparticles before (A) and after heating at 40°C for 20 minutes (B). Below: Capsules containing aggregates of gold nanoparticles before (C) and after heating (D). Some single particles (A, B) and aggregates (C, D) are indicated by an arrow in the images. Areas shown corresponds to 0.9 -1 μm^2. The height scale is 50 nm.

Müller and co-workers showed that at high temperatures, the shell components of a PDDA/PSS capsule switch from a glassy to viscoelastic state, a phenomenon accompanied by a reduction in the wall surface tension and corresponding tendency of the capsule wall to reduce its surface area. [21] Surface tension effects account for the tendency of shell material to diffuse around the shell at temperatures above T_g. At elevated temperature (T↑), polymeric material that covers the gold nanoparticles melts and diffuses to lower areas in order to reduce the surface area of the shell that is exposed to water – a surface tension effect. After cooling down,

the now thicker/denser interparticle regions of shell are less permeable to the same molecule. Figure 5.20 summarizes the general hypothesis proposed here by showing an illustration of a cross-section of a shell containing two embedded gold nanoparticles that is permeable to a given molecule.

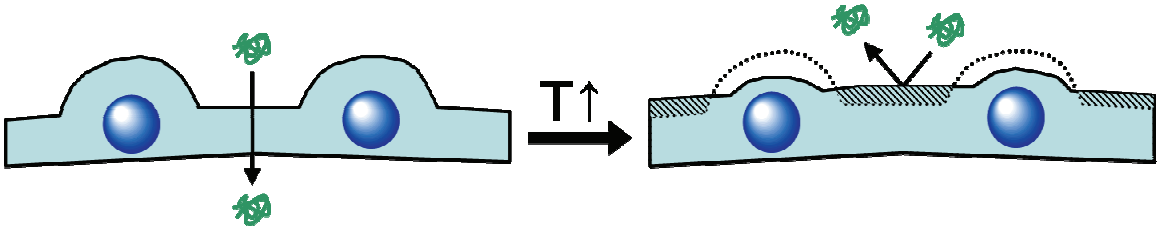

Fig. 5.20 Schematic of the temperature-induced shell thickness variation. A cross-sectional representation of a PDDA/PSS multilayer containing gold nanoparticles before and after thermal treatment. During thermal treatment surface tension effects force the excess polyelectrolyte material surrounding gold particles to move and rise the average interparticle wall thickness, decreasing the shell permeability.

5.2.8 THERMAL SHRINKAGE AS A FUNCTION OF POLYELECTROLYTE MOLECULAR WEIGHT

It is known that the polyelectrolyte complex of PDDA and PSS has a significantly lower T_g than either of its individual components in solution. While different polyelectrolyte complexes are expected to possess different T_g values due to the differences in their structure within the microcapsule's wall (*e.g.* charge density, entanglement, water and ionic content), it was hypothesized that a simple way to preserve the integrity of a certain type of capsule and changing its T_g might be to change the molecular weight of one of its constituents.

The influence of the molecular weight of PDDA on the thermal shrinking of microcapsules was investigated by DSC. DSC was used to determine the T_g of microcapsules constructed from PDDA with four different ranges of molecular weights, namely; very low (VL-PDDA, 100 kDa), low (L-PDDA, 100-200 kDa), medium (PDDA, 200-350 kDa) and high (H-PDDA, 350-500 kDa). A micro-calorimeter and a very high microcapsule concentration were required for these measurements. Since the interest in DSC measurements was not in obtaining perfect samples but rather in measuring the glass transition of the polymer complexes they contained, $CaCO_3$ microparticles instead of the more expensive silica were used as a sacrificial

template. Template removal was done by mixing the coated microparticles with a solution of the chelating agent EDTA. After complete template dissolution, each sample was thoroughly rinsed. Capsules obtained in this fashion appeared aggregated in the light microscope and had an average diameter of 3.0 μm. The samples were degassed for several minutes and DSC measurements were conducted in water in a closed cell at constant pressure and volume. The results are illustrated in Figure 5.21.

The molecular weights indicated correspond to the highest possible molecular weight of the particular PDDA according to the provider. It was found that T_g increase with increasing molecular weight of PDDA from 31°C for capsules built from 100 kDa PDDA to 42°C for capsules built form 350-500 kDa PDDA. As a rule of thumb, each 100 kDa increase in PDDA molecular weight corresponds to a 2°C increase in T_g.

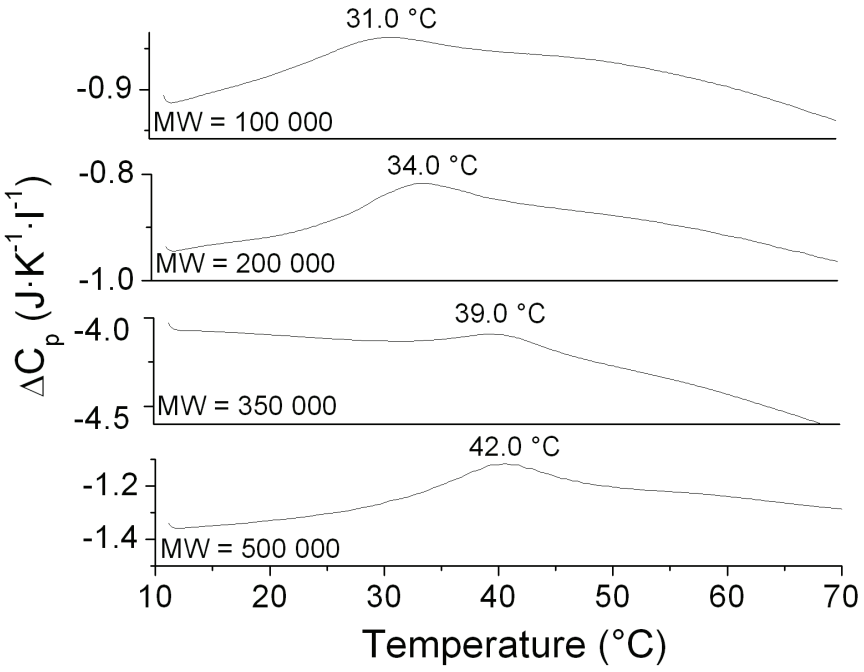

Fig. 5.21 Thermographs of $(PDDA/PSS)_4$ polymeric microcapsules constructed from PDDA of different molecular weights. From top to bottom: VL-PDDA, L-PDDA, PDDA, H-PDDA.

Based on the DSC measurements, heat shrinking experiments were done using microcapsules with the layer structure $(PDDA/PSS)_4$ assembled on silica particles. PDDA of three different ranges of molecular weights were used in LbL assembly, namely; very low (VL-

PDDA, 100 kDa), low (L-PDDA, 100-200 kDa) and medium (PDDA, 200-350 kDa). Removal of the template yielded homodispersed hollow shells with an average diameter of 4.1 μm for shells containing VL-PDDA, 4.4 μm for shells containing L-PDDA and 4.5 μm for shells constructed from PDDA. An aliquot of each sample was transferred to a 0.5 mL tube and immersed in a thermostated bath at various temperatures for 20 minutes and their diameter measured by LSCM. In addition to possess a smaller diameter than other microcapsules, shells constructed from VL-PDDA disappeared during incubation which indicates that the shell structure was not stable probably due to VL-PDDA forming layers that are too thin to preserve the capsule's integrity after core dissolution. This could possibly be remedied by adding more layers to the capsules shells which would also ultimately alter their mechanics. For laser opening experiments, 200-350 kDa PDDA/PSS was chosen as T_g conveniently spans the incubation temperature of living cells which were later to be experimented upon (Section 5.3).

5.2.9 EFFECT OF GOLD DISTRIBUTION ON NEAR-IR RELEASE

Microcapsules with the shell structure $(PDDA/Au/PSS)_4$ and an average diameter of 4.6 μm were used to compare the release efficiency of shells containing non-aggregated and aggregated gold nanoparticles. The gold content was split equally over the 4 PDDA layers during shell assembly for an overall filling factor of 0.01. Encapsulation of AF 555-labeled dextran (MW = 10 kDa) was performed by incubating an aliquot of capsules and dextran (0.1 mg/mL) in a thermostated bath maintained at 54°C and 59°C for Agg-Au4 and Homo-Au4 capsules, respectively. These temperatures were chosen from the data plotted in Figure 5.16 to obtain samples of comparable diameter, and thus of similar wall thicknesses and fluorescence intensities. The capsules were finally sedimented and washed twice in water. In accordance with the data obtained from the permeability studies, the samples retained the encapsulated material and no changes in fluorescence intensity were found even after 12 months of storage (4°C, dark conditions).

$(PDDA/Au/PSS)_4$ microshells with encapsulated dextran were then irradiated using the laser setup equipped with an infrared laser diode (λ = 830 nm) with a maximum operating voltage of 1.4 V. By adjusting the voltage, the incoming beam intensity can be selected anywhere from about 10 to 100 mW. [127] A 100X microscope objective is used to focus the laser beam onto individual capsules and a white light coupled to a camera and a monitor provides visualization.

For irradiation experiments, a sample cell was prepared by transferring 10 µL of capsules solution onto a PDDA coated glass wafer, covering it with a smaller glass cover slip and sealing the edges of the cover with lacquer. Marking were typically made on the cover slide to ease the selection and retrieval of irradiated areas. Thirty capsules were irradiated in each experiment, positioning focused laser beam in line with pre-selected microcapsules in one area of the sample. The sample cell was placed in a holder and the beam was set in focus with the microscope objective before being positioned on the microcapsules. Visualization of the fluorescent content of the microcapsules before and after irradiation was done separately by LSCM.

The release of encapsulated materials from the microcontainers containing non-aggregated and aggregated nanoparticles was remarkably different. In the former case, none of the microcapsules exposed to the laser beam could be opened within the whole range of incident laser powers thus confirming that no photo-bleaching of the AF 555 fluorophore takes place. This is shown in Figure 5.22, where LSCM captions of a set of 8 capsules loaded with fluorescent dextran before (A) and after (B) laser irradiation with incoming intensity set at 90 mW. In addition, the fluorescence of these unopened microcapsules remained unchanged after two weeks of storage at 4°C supporting that the laser session produced no significant damaged to the shell that could have induced the encapsulated dextran to slowly diffuse out. A graph plotted using the percentage of open capsules as a function of laser intensity gives a flat line (C). In sharp contrast, the dextran in microcapsules with aggregated nanoparticles was entirely released at about 70 mW. In 5.22 D, a set of 7 capsules, 6 of which were irradiated with the infrared laser for 5 seconds at 65 mW were subsequently opened (E). The capsule that remains fluorescent after irradiation was deliberately kept away from the laser to demonstrate the fluorescence intensity of the capsules did not change after the irradiation of proximal capsules. The percentage of microcapsules optically opened in this manner decreased at lower intensity (Figure 5.22 F, hard line). The minimum laser power required to remotely open capsules containing aggregated gold nanoparticles was found to be ca. 10 mW. At intensities below 60 mW, a second laser exposure of 10 seconds was performed on microshells that were not open the first experiment. It was found that up to 12 % more capsules could be opened after the second irradiation trial. Repeating the irradiation procedure more than twice or increasing the time of irradiation above 10 seconds did not further improve the ratio of opened/closed capsules, at any given intensity. A derivative plot of the data points was obtained (Figure 5.22

F, dashed line). The peak of this curve, centered at 36 mW, is referred to as the threshold intensity (TI). TI is defined as the intensity necessary to open more than 50 % of capsules.

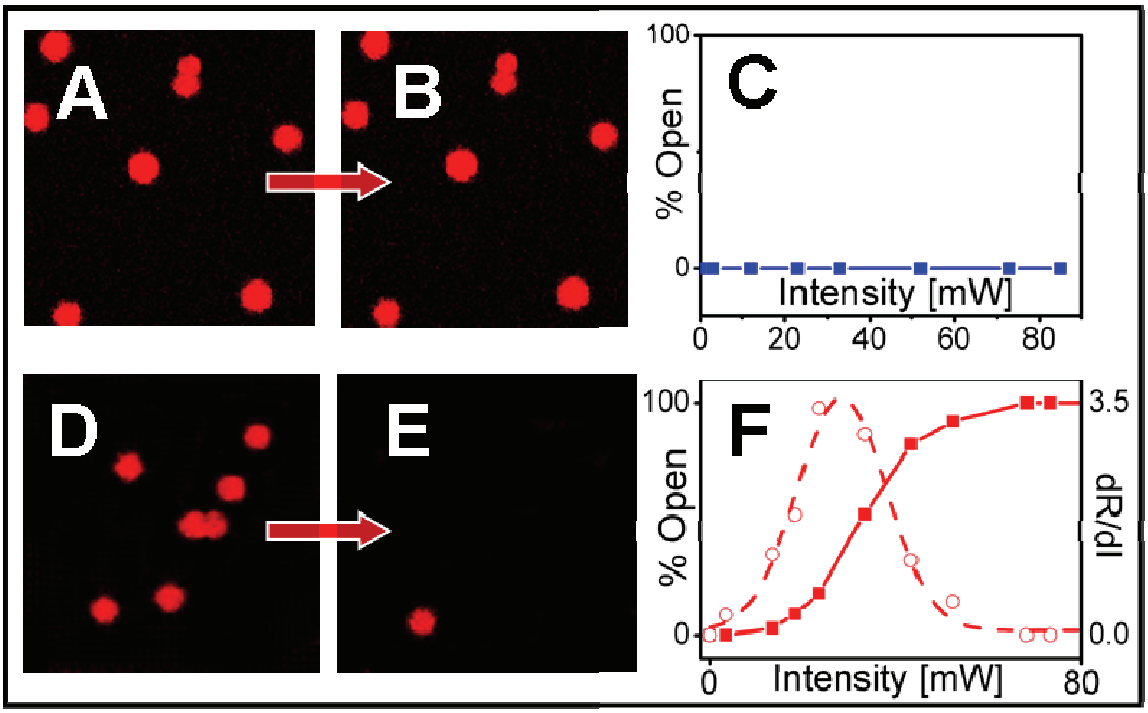

Fig. 5.22 Remote release of encapsulated dextran by near-IR. Upper panel: Representative LSCM caption of Homo-Au4 microcapsules filled with AF 555 dextran before (A) and after (B) exposure to infrared laser. No capsules could be open at any power intensity (C). Lower panel: Agg-Au4 capsules with encapsulated dextran before (D) and after (E) exposure to infrared laser using an incident intensity of 65 mW. A plot correlating the % of capsules opened (30 capsules per measurement) as a function of power (F, hard line) and its derivative (F, dashed line) are shown.

The moderately broad range of laser intensities required to open capsules (ca. 60 mW) can be partially attributed to the size of gold nanoparticles assemblies sandwiched within the shell. The LSCM images D-F in Figure 5.22, demonstrate that upon irradiation the capsules released their fluorescent content entirely. In addition, the laser-induced release of material from microcapsules observed in LSCM was never accompanied by their deformation or "explosion" which was observed in the previous work [240] and which may limit applications due to potential damages to encapsulated materials and surrounding.

In order to explain how different arrangements of gold nanoparticles on laser-induced release behavior we first need to consider the spectroscopic changes found in aggregated nanoparticles. The near-IR absorption of the aggregates of nanoparticles originates from the interaction of dipole moments of two or more gold nanoparticles. The broadness of the aggregation peak presented in Figure 5.2 supports the fact that after adding salt the resulting nanoparticle assemblies have a large size distribution. The number of particles per aggregates in capsules was estimated by TEM and found to vary largely, from roughly 15 to about 100 particles per assembly. DLS was used attempting to monitor the average size of gold nanoparticles assemblies as a function of time (Figure 5.13), but each measurement needed about 60 seconds and much of the aggregation process occurs within this time period. In some instances we observed that incorporating larger aggregates containing more than 300 gold nanoparticles bring about defects to the microshells and renders encapsulation less efficient. The main criterion to partially control the size of the aggregates of citrate stabilized colloidal gold appears is the duration of incubation of gold nanoparticles with salt as shown in Figure 5.12, left. The order and rate of the mixing the electrolyte and gold solutions also have a great influence over the aggregation behavior. [191]

The second point that should be considered to explain the high release efficiency of capsules containing aggregated nanoparticles concerns the localization of the particles over a small area of the microcapsule wall. Microcapsules containing non-aggregated gold nanoparticles require relatively intense laser irradiation, which, in turn, is more likely to induce irreversible damages to the shell, its cargo and host environment (*i.e.* living tissue, cell). It is hypothesized that confining gold nanoparticles as an aggregate to a small volume within a capsule shell, leads to a localization of the heat produced by the nanoparticles upon light absorption. Therefore, aggregating gold nanoparticles potentially increases the surface-to-volume ratio of the near-IR absorbing nanoparticles, inducing the temperature of the shell material surrounding the absorption centers to rise and accumulate in a larger area. In this sense, using non-aggregated particles has the double disadvantage of not absorbing much in the IR range and having to absorb much more light to produce enough heat to melt sufficiently thick regions of polyelectrolyte complex so that a change in wall permeability can occur. A milder temperature increase around an aggregate of gold nanoparticles, just sufficient to exceed the glass transition (T_g) of the surrounding polyelectrolytes within the shell is plausible.

Being less dense above T_g, molten regions of the capsule shell are more permeable, allowing encapsulated material to leak out (or solution components to flow in) its membrane. The individual T_g value of PDDA (70°C) and PSS (200°C) are significantly lower in an aqueous environment. [241] Using DSC, it was shown in Figure 5.21 that $(PDDA/PSS)_4$ shells in water possess an endothermic peak centered at 39°C, with an onset situated at about 35°C. Taking into account that experiments were done at an ambient temperature of 25°C and assuming that T_g for $(PDDA/Au/PSS)_4$ capsules does not vary significantly from that of $(PDDA/PSS)_4$ shells, it is highly probable that an increase of about 10°C necessary to exceed T_g is achievable.

5.2.10 EFFECT OF TEMPERATURE ON NEAR-IR LASER RELEASE

The effect of temperature on the energy requirements to open microshells containing aggregated and non-aggregated nanoparticles was investigated. Samples were prepared by thermally shrinking 4.6 μm $(PDDA/Au/PSS)_4$ capsules to 2.3 μm in presence of 0.1 mg/mL AF 555 dextran (MW = 10 kDa). A sample cell was then prepared for irradiation experiments. To control the sample temperature, sample cells were placed in an aluminum block designed to fit in the laser path and conduct laser irradiation experiments. Once the sample cell was put inside the block and an insulating cover placed on top, the block was connected to a thermostated bath, set at an appropriate temperature and left to equilibrate for 15 minutes before irradiating. 40 capsules were irradiated with the bath set at 4°C and 40°C. The bath temperature of 40°C was selected because while this temperature exceeds T_g for PDDA/PSS, it did not induce further shrinking from the microcapsules after the sample cell was left in the cell at that temperature for 60 minutes. Setting the bath to 55°C led to capsule shrinkage. This suggests that although a highest bulk temperature was obtained for the samples, this one was probably just below the T_g for the PDDA/PSS complex (onset at 35°C).

The results of opening capsules functionalized with aggregates of nanoparticles at the two temperatures using different near-IR laser intensities are shown in Figure 5.23. Microcapsules containing homodispersed gold nanoparticles could not be opened at either temperature. The threshold near-IR laser intensity needed to open microcapsules incubated at approximately 40°C was found to be 25 mW and all the capsules were opened at 42 mW. In sharp contrast, the threshold value of identical capsules incubated at 4°C was found to be 65 mW whereas not all the capsules could be opened at the maximum laser intensity. Extrapolating the curve taken at 4°C to 100 % (y axis) gives 128 mW, which is described as the approximate laser intensity necessary to open all capsules at that temperature. These values are in agreement with the

values found for these capsules at 25°C, which were 36 mW for threshold and 70 mW for complete opening. This suggests that more than three times more energy is necessary to open all the capsules of a sample at 4°C than a sample with the bulk temperature maintained near 40°C.

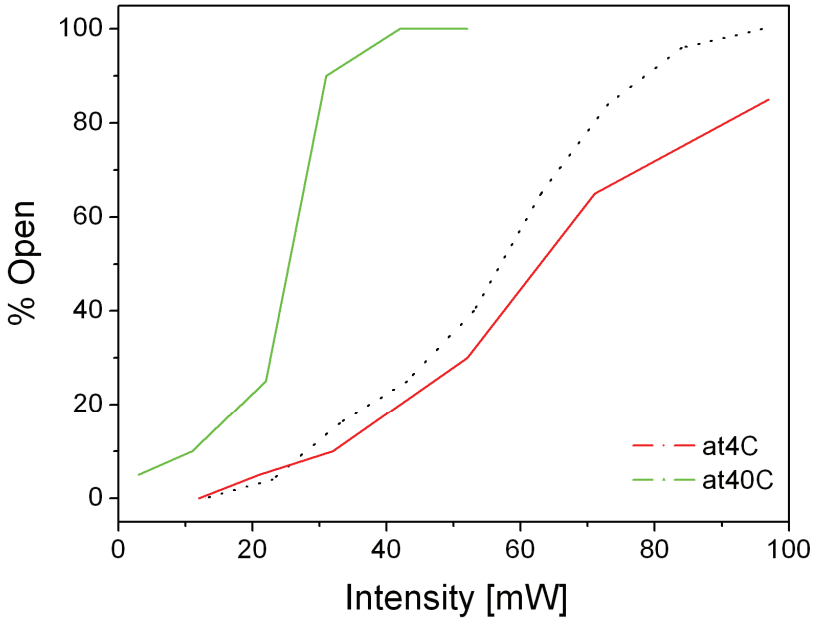

Fig. 5.23 Temperature-dependence on dextran release using Agg-Au4 capsules containing aggregates of gold nanoparticles under near-IR. The dotted line illustrates the position of the curve for Agg-Au4 at room temperature (Figure 5.36 F).

5.2.11 EFFECT OF SALT CONCENTRATION ON NEAR-IR LASER RELEASE

Salts are known to affect polyelectrolyte microcapsules by weakening the electrostatic interactions within the shell. At high enough concentration, salts induce capsules to swell and can even trigger the dissolution the microcapsules. The laser opening experiments and results discussed so far were all done in the absence of salt. The effect of adding salt on the energy requirements to open microshells containing aggregated gold nanoparticles was investigated. Samples were prepared by thermally shrinking 4.9 μm $(PDDA/Au/PSS)_4$ capsules to about 2.5 μm in presence of 0.1 mg/mL AF 555 dextran (MW = 10 kDa). A sample cell was then prepared for irradiation experiments. Before irradiation, the samples were resuspended in a NaCl solution so that the final salt concentration was 0.15 M or 1 M. The samples were kept in salt

for 60 minutes before near-IR laser irradiation experiments were performed to insure that the NaCl concentration was low enough so that the encapsulated material would not be release due to the presence of salt alone. The results are shown in Figure 5.24.

It is obvious that salt in solution as a profound effect on the release of encapsulated material from microcapsules functionalized with aggregates of gold nanoparticles suggesting that the electrostatic interactions within the shell is weakened by the presence of salt. Incubation of the microcapsules with 2 M NaCl led to capsule aggregation. Capsules treated with 1 M NaCl were found to be partially aggregated but no capsules had been found empty after 60 minutes in presence of the salt. Capsules treated with 0.15 M NaCl looked identical to capsules that contained salt. TI for capsules treated with no salt, 0.15 M NaCl and 1 M NaCl were found to be 58 mW, 38 mW and 26 mW, respectively. The difference in threshold observed here with the samples discussed in the previous sections is attributed to the difference in shell diameter since larger silica particles were used. A large difference in the threshold laser intensity of 20 mW was observed between capsules opened by IR in the absence of salt capsules irradiated in the presence of 0.15 M NaCl. A further decrease of 12 mW in laser intensity was required to open capsules in the presence of 1 M NaCl, which corresponds to a salt concentration increase of over 6.5 fold. High salt also led to aggregation of capsules which is undesirable.

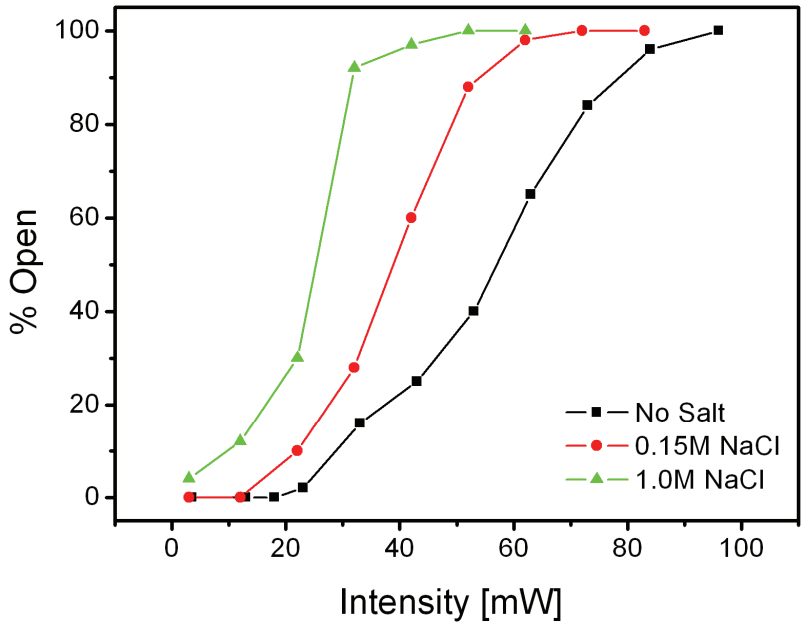

Fig. 5.24 Ionic strength-dependence on dextran release using Agg-Au4 capsules containing aggregates of gold nanoparticles under near-IR.

5.2.12 EFFECT OF CAPSULE DIAMETER ON NEAR-IR LASER RELEASE

In view of the observation made in the previous section that a microcapsule constructed on a larger template size led to a drastic change in the capsule sensitivity to the IR laser, the effect of capsule diameter as a function of laser intensity was investigated. Two aliquots of Agg-Au4 capsule solution were thermally shrunk to average diameters of 2.66 μm and 2.93 μm in presence of 0.1 mg/mL AF 555 dextran (MW = 10 kDa). A sample cell was then prepared for irradiation experiments. The sample shrunk to 2.47 μm presented in the previous section is used as a reference for the samples discussed here. A summary of the effect of a capsule sample shrunk to three different sizes on the percentage of capsules that could be opened as a function of near-IR laser intensity is shown in Figure 5.39. It is clear from this data that smaller capsules require less energy to be opened than larger capsules. TI for capsules shrunk to 2.47 μm, 2.66 μm and 2.93 μm were found to be 58 mW, 63 mW and 78 mW, respectively. Capsules shrunk to 3.8 μm and larger diameters could not be opened under normal conditions despite the presence of aggregates of gold within the shell.

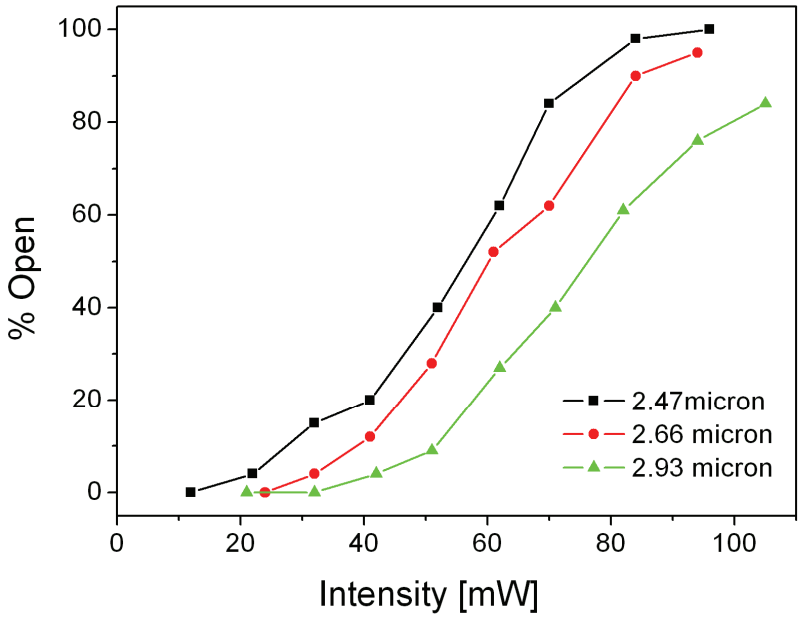

Fig. 5.25 Capsule diameter-dependence on dextran release using Agg-Au4 capsules containing aggregates of gold nanoparticles.

This finding comes with a surprise since it was expected that capsules shrunk to smaller diameters, consequently having thicker walls, would be require more energy to be opened. This could suggest that the nanoparticle aggregates within shells does not create a fully open "pore" as previously thought, but might instead result in a change in wall density around the aggregates. Assuming such a density change to be identical in capsules of any shell thickness, it was suggested that the mechanism of optical release of encapsulated material from microcapsules containing metallic nanoparticles is not solely function of the number of nanoparticle presents, shell thickness or diameter but it is also strongly dependant on the diffusive force of the encapsulated material. The same capsules used in this section were shrunk in presence of 0.4 mg/mL to obtain shells with an average diameter of 2.45 μm. A cell sample was then prepared, irradiated at various near-IR laser intensities and the results were compared to shell incubated shrunk to 2.47 μm in the presence of 0.1 mg/mL of dextran. The resulting curves are presented in Figure 5.26. The results support that encapsulating a higher concentration dextran improves significantly the efficiency of release by laser excitation. This result also supports aforementioned observations where it was shown that the concentration of dextran used creates a diffusive force that opposes the heat shrinking.

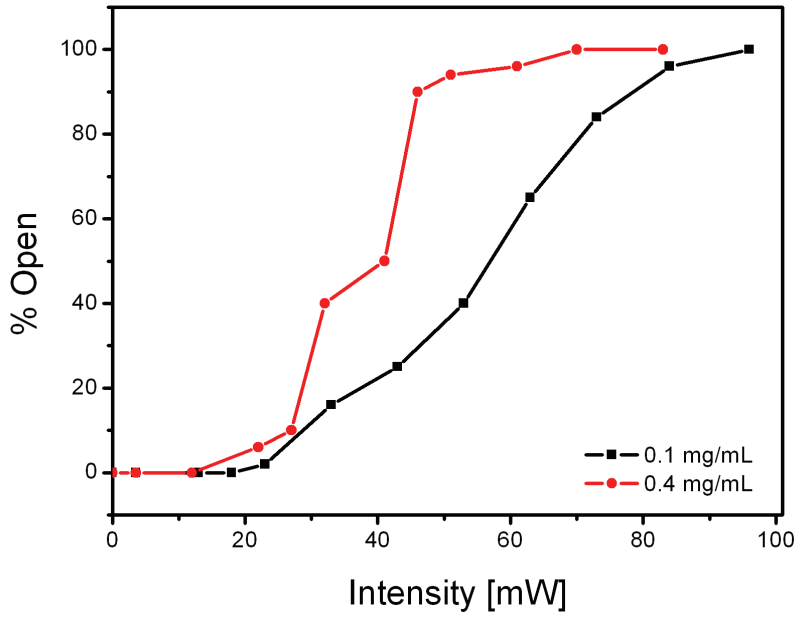

Fig. 5.26 Dextran concentration-dependence on IR release using Agg-Au4 capsules containing aggregates of gold nanoparticles. The samples had comparable average diameters of 2.45 μm and 2.47 μm for the sample used in the red and black curves, respectively.

5.2.13 SIMULATING THE HEAT DISTRIBUTION AROUND NANOPARTICLE ASSEMBLIES

The release of encapsulated polymer upon near-IR laser illumination from microcapsules containing aggregated nanoparticles was assumed to be due in part to their higher absorption of laser light. Just like homodispersed nanoparticles, aggregated gold particles absorb photons to produce heat, yet there is a significant difference in the release efficiency of microcapsules with different nanoparticle distributions. It was hypothesized that the difference in local nanoparticle density between the homodispersed and the aggregated state may play a role in the observed effect. However, the shell temperature distribution around gold nanoparticles cannot be directly measured at such small scales. The temperature rise on non-aggregated and aggregated gold nanoparticles was simulated to verify whether the hypothesis concerning the relative near-IR release efficiencies based on gold nanoparticle distribution is sound. To this end, the program Femlab (Comsol AB, USA) was used. The program operates using Fourier's Law for heat conductivity using the system's heat conductivity (k), area (A), absorption coefficient (Q). With the proper parameters, Femlab solves complex integrations under the assumption that the system exists in boundary free conditions.

In the simulations, the heat capacity of water was taken 4200 J/kg K, heat conductivities of water and gold are 0.54 W/mK and 320 W/mK, respectively, the size of nanoparticles taken was 20 nm, the absorption coefficient of nanoparticles, Q, is ~2 at the surface plasmon resonance (520 nm) and $Q \sim 0.02$ at 830 nm. Using these parameters the temperature rise on a single gold nanoparticle was calculated to be ~ 0.5 K when illuminated at 830 nm with a power of 50 mW. In the simplest aggregation case where a short linear chain of gold nanoparticles is formed, a second absorption peak can be found in the near-IR region of electromagnetic spectrum. The absorption coefficient at 830 nm for an aggregate of nanoparticles is estimated to increase fivefold (Q ~ 0.1) in comparison with stand alone nanoparticles. In addition, another effect that contributes to temperature rise upon aggregation is surface-to-volume ratio upon bringing nanoparticles in close proximity, which was estimated to contribute up to 30 % of the temperature rise. The resulting simulated thermographs are presented in Figure 5.27.

The temperature increase was adjusted due to absorption change of aggregation. It was found that although a single nanoparticle was calculated to increase its immediate environment by less than 1 K, a linear assembly of four nanoparticles was able to produce up to 7 K. If a small aggregate composed of merely four gold nanoparticles already has the potential to produce a significant temperature rise, then the larger and more complex aggregates induce larger

temperature rises. Examples of a non-aggregated and linear assembly type of nanoparticle distribution in microshells are shown in Figure 5.27 *A* and *B*, respectively. The microcapsules used for this work where found to possess aggregates containing between a dozen to over a hundred of gold nanoparticles assembled in linear or mesh-like aggregates. We suspect the larger, more common mesh-like type of nanoparticle assembly to be the result of several linear structures aggregating together. Larger aggregates are expected to produce even higher temperature rises than estimated here since the heat produced by every nanoparticle within the assembly accumulates locally. This is illustrated in the simulation of Figure 5.27 *B* where the heat produced by the centermost linear structure appears to overlap with that of a second nearby assembly (no cooler blue region is visible between the two complexes). On the other hand, the non-aggregated nanoparticles do not induce substantial temperature rise, Figure 5.27 *A*. As noted above, the closely located nanoparticles increase temperature due to higher surface-to-volume ratio and interacting dipole moments induced on each nanoparticle. The results in this work present a clear manifestation of this phenomenon.

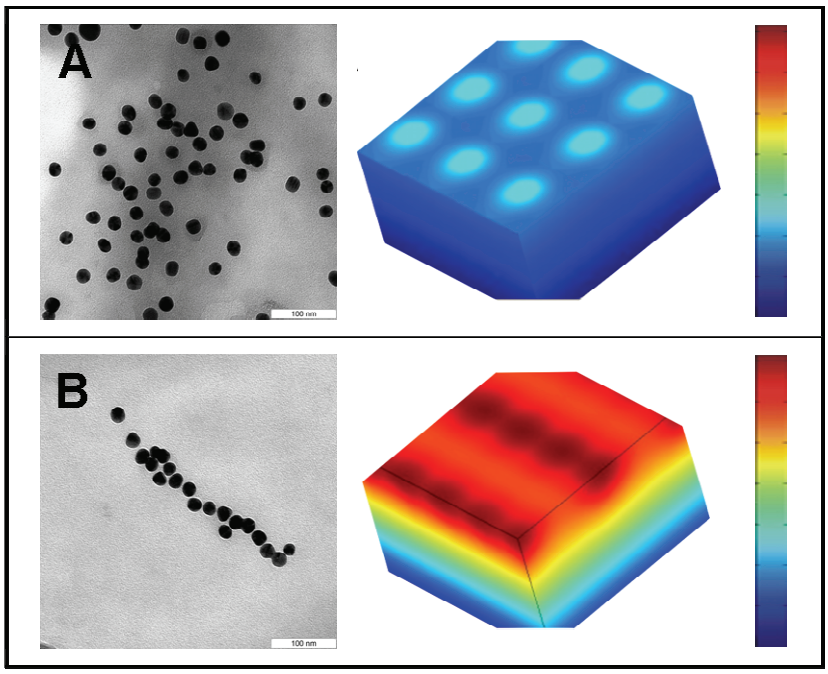

Fig. 5.27 Modeling the temperature distribution for golf nanoparticles. Top panel: Non-aggregated nanoparticles do not possess absorption in the near-IR part of the spectrum. For 20 nm nanoparticles the absorption coefficient is about 0.02, so the temperature rise at 50 mW of incident power is less than 1 degree. Lower panel: For a single line of four aggregated nanoparticles a temperature rise of 7 K can be produced (red color). TEM images of uniform

distribution and aggregates of nanoparticles are shown on the left side of corresponding simulations. The scale bars for the TEM images are 100 nm.

5.2.14 PREPARATION AND IR-INDUCED RELEASE FROM GIANT CAPSULES

To demonstrate that the principles of laser-nanoparticle interaction to sensitize microshells to light can be expanded to other types of microcontainers, giant polyelectrolyte capsules with a diameter 10-100 fold larger than traditional polyelectrolyte capsules were functionalized with gold nanoparticles and tested for release capabilities. As illustrated in Figure 5.28A, microcapsules fabricated in this way exhibit an internal osmotic pressure which puts the membrane under tension. Another difference relative to the capsules discussed in previous sections is that the extensive cross-linking between PSS and DAR within microshells reinforces their mechanical properties. Previously reported 5 μm capsules have approximately the same dimension as the laser beam with a quasi isotropic release of encapsulated material upon laser irradiation. The use of larger capsules allows a site specific positioning of the laser beam to open the capsules at a well defined spot, leading to a directional release of the encapsulated species. Moreover, such capsules allow large amounts of materials to be encapsulated in comparison to 5 μm capsules, making such capsules great candidates as pulse or slow-releasing microcontainers. A clear example of this is the encapsulation of smaller microcapsules with different loads within giant capsules. [67]

Dextran-hydroxyethylmethacrylate [101,242] (dex-HEMA) microgels with an average size of 150 μm were synthesized by aqueous emulsion polymerisation of dex-HEMA and DMAEMA (see Figure 5.28A for chemical structures) in poly(ethylene glycol) (PEG) as continuous phase (note that at high concentration aqueous dextran and PEG solution are immiscible). Initiation of radical polymerisation of the methacrylate moieties of the dex-HEMA and DMAEMA leads to the formation of solid microgels with a positive ζ-potential of 25 ± 2 mV, which is required for the microgel to further serve as template for LbL deposition. PSS and DAR were chosen as polyelectrolytes for LbL coating of the microgels. This polyelectrolyte pair is able to from a covalent cross linked structure and has been reported previously to yield polyelectrolyte membranes with increased mechanical strength and low permeability. [151] Recently we have shown that dex-HEMA/DMAEMA microgels coated with 2 bilayers PSS/DAR resulted in exploding microcapsules upon degradation of the microgel core. [67] Cross-linking between PSS

and DAR was allowed to occur spontaneously under ambient light conditions (Figure 5.28A). Therefore, for the present work the number of bilayers was increased to four to improve the shells' stability upon degradation of the microgel core. Dex-HEMA microgels are degradable by virtue of carbonate esters which connect the polymerized methacrylates with the dextran backbone. To obtain hollow capsules the $(PSS/DAR)_4$ coated microgels were treated in a sodium hydroxide solution. When the microgel core degrades, the degradation products, being the 19 kDa dextrans used to synthesize dex-HEMA, are expected to remain within the capsule membrane in a soluble state, exerting an osmotic pressure on the capsule membrane. The radial effect of this osmotic pressure on the membrane should enhance the opening of the capsule membrane upon laser irradiation. Finally the capsules were washed to remove the alkaline medium and stored as a suspension in water. Hollow capsules were obtained by dissolving the dex-HEMA core in a 1M sodium hydroxide solution for 10 minutes followed by extensive washing with water (Figure 5.28A).

The capsules were treated with a solution of gold nanoparticles aggregates to make them sensitive to IR, as previously described (*Section 5.2.2*). The average size of nanoparticle assemblies is determined by the amount of time the gold nanoparticles spend in salty water and the growths stops when added to the capsule solution. The number of nanoparticles per aggregate as well as their morphology can be roughly determined from the aggregation conditions as previously discussed (*Section 5.2.1*). The aggregates' distribution on the microshell is random and the number of aggregate per capsules can be approximated by adjusting the amount of gold used relative to the number of capsules used.

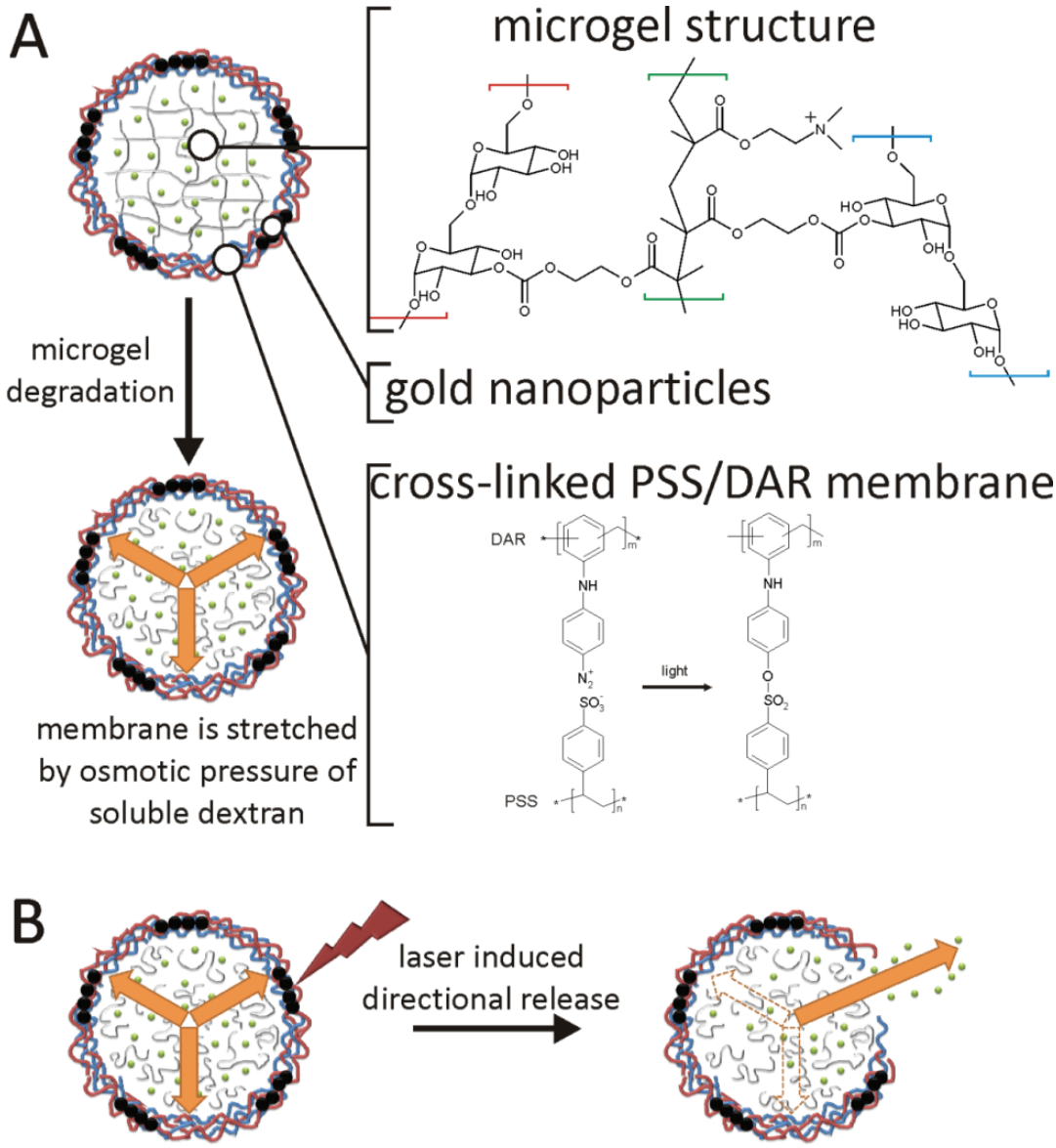

Fig. 5.28 Schemes of giant capsules functionalized with aggregates of gold. A) Molecular structure of the polymerised dex-HEMA/DMAEMA hydrogel network (top) and the covalent cross linked multilayer membrane optained from DAR and PSS (lower). (B) Laser induced opening of a capsules at a desired area and the release of encapsulated material in a preselected direction. The degradation products of the dex-HEMA/DMAEMA hydrogel onto the polyelectrolyte membrane exert an osmotic pressure against the capsule wall (arrows).

Electron microscopy was used to visualize the microcapsules' construction process. Figure 5.29A shows a SEM image of uncoated microgels exhibiting a smooth surface. However, after LbL coating microgels (Figure 5.29B) display a rough vermiculate structure. Such behavior is typical for LbL coated microgels as a differential drying between microgel core and polyelectrolyte membrane takes place upon sample preparation prior to SEM imaging. [243] Similar findings were reported by McAloney *et al.* who studied planar multilayers by AFM. [56,244] After microgel dissolution in alkaline medium and washing to remove residual ions, collapsed structures of hollow capsules are clearly observed on the SEM image in Figure 5.29C. TEM revealed the presence of the gold nanoparticles on the surface of the hollow capsules which appear as nano-networks of dark dots (Figure 5.29D).

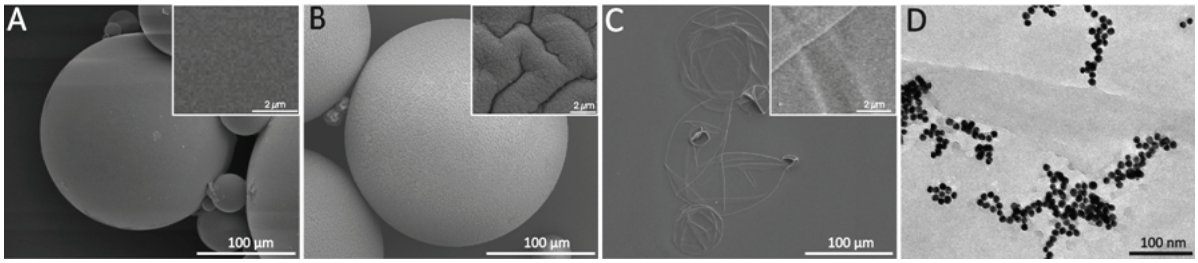

Fig. 5.29 Scanning electron microscopy images of hydrogel-templated shells. (A) uncoated dex-HEMA/DMAEMA microgels, (B) $(PSS/DAR)_4$ coated microgels and (C) hollow $(PSS/DAR)_4$ capsules obtained after dissolution of the microgel core. The insets show magnified images. (D) Transmission electron microscopy image of the hollow $(PSS/DAR)_4$ capsules functionalized with gold nanoparticles.

In order to accelerate the release from the capsules after opening we relied upon the osmotic pressure exerted by the degradation products of the dex-HEMA/DMAEMA microgels. Microgels with a solid concentration of 30 % (w/w) were produced, upon dissolution of the microgel core the diameter of the capsules increases with approximately a factor 1.2 as determined by LSCM measurements. Assuming no diffusional loss of dextran degradation products, the increase in volume results in a decrease in dextran concentration by a factor of approximately 1.82. This leads to a final dextran concentration of approximately 16 % (w/w) within the hollow capsules.

The osmotic pressure of such a dextran solution can be estimated from literature to be 70 kPa. [245] The assumption that no or few leakage of dextran degradation products through the

$(PSS/DAR)_4$ membrane occurs during dissolution of the microgel core was verified by confocal microscopy using fluorescently FITC labeled 20 kDa dextran as probe. Note that the molecular weight of the fluorescent probe was similar to that of the dextran (MW~ 19 kDa) used for the synthesis of 100 the dex-HEMA. Figure 5.30 A shows a confocal microscopy image of uncoated dex-HEMA/DMAEMA microgels incubated in the FITC-dextran solution. Clearly the fluorescent probe can diffuse inwards the microgels. However, after $(PSS/DAR)_4$ coating of the microgels followed by microgel dissolution, the obtained hollow capsules (Figure 5.30 B) became impermeable to the fluorescent probe. As both molecular weight of the fluorescent probe and the dex-HEMA degradation products are similar it is indeed reasonable to assume that no or few leakage of dextran degradation products through the $(PSS/DAR)_4$ membrane occurs upon dissolution of the microgel core.

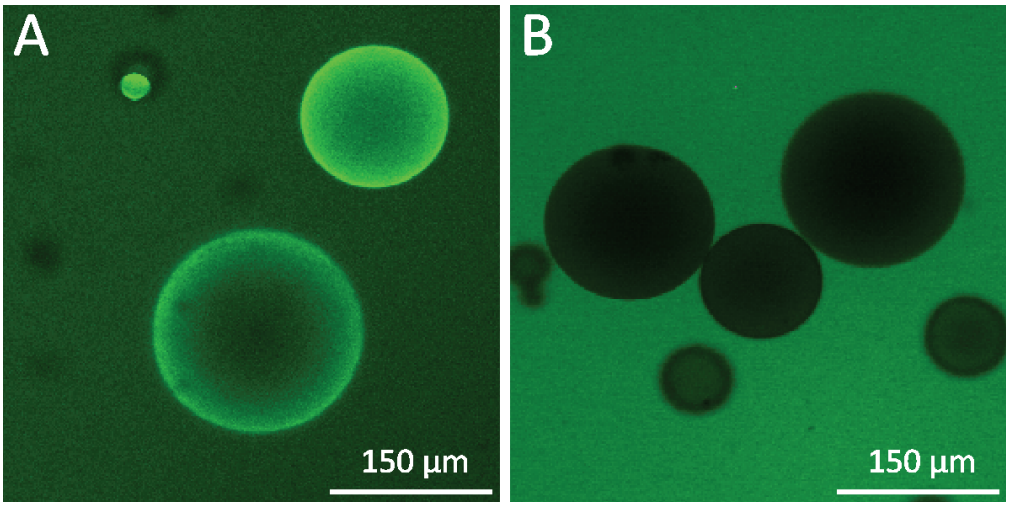

Fig. 5.30 Confocal microscopy images of microgels. (A) Dex-HEMA/DMAEMA microgels and (B) hollow $(PSS/DAR)_4$ capsules incubated in a 0.5 mg/ml 20 kDa FITC-dextran solution.

Finally, it is shown that the hollow capsules can be opened at specific sites on the giant capsules by activating the gold nanoparticles with IR laser light. Dex-HEMA/DMAEMA microgel templated $(PSS/DAR)_4$ shells containing FITC-dextran were used for this purpose. Upon irradiating the capsule shell at 830 nm (10 Hz, 0.3 µJ) an aggregate present on the shell locally produces large quantities of thermal energy, which rapidly accumulate in the surrounding materials (polyelectrolytes, water), overheating them. The result observed within a few seconds of irradiation is the destruction of the area of the capsule wall surrounding the gold aggregate. Such holes can be seen by optical microscopy in transmission mode (Figure 5.31,

insets). Due to the residual osmotic pressure of approximately 70 kPa present within the capsules, the encapsulated FITC-dextran is released. The same experiment was performed using capsules that were treated with homodispersed gold nanoparticles as well as capsules that were not treated with gold nanoparticles and no release could be obtained in either case. This result is in agreement with the data discussed in *Section 5.2.9*. It should be noted that when capsules with aggregates of gold nanoparticles where irradiated at a pulse frequency of 1 Hz, only one case of release in over 20 capsules even after exposure to the laser for periods of 5 minutes was observed. This is probably because, at lower pulse frequency, the thermal energy released by the gold nanoparticles has enough time to dissipate in the surrounding medium between pulses and is unable to accumulate and damage the shell. Determining a precise energy density in order to open the microshells is not possible using this system. The release is the result of heating the nanoparticle aggregates, which vary in size and correspondingly vary in near-IR absorption. The duration of release in turn, depends on the size of the hole created by the absorption centre (*i.e.* nanoparticles) upon irradiation. As a result, increasing pulse frequency or laser power should both increase the probability of forming a hole in the microshell but cannot be used to control its size. Most importantly, it is seen from these results that the overall direction in which the FITC-dextran is released can be determined by irradiating the desired area of the microcontainers. Gold aggregates were easy to locate on the capsules surface using a light microscope and their number could be increased if need were to open several holes in any type of thin membranes.

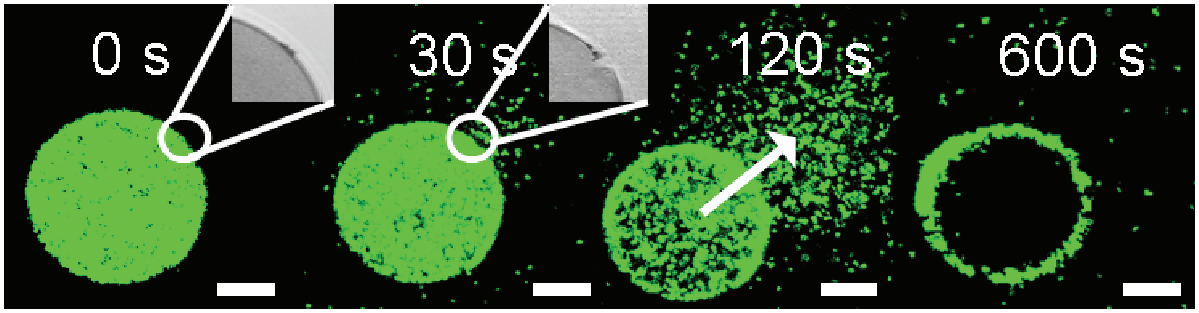

Fig. 5.31 LSCM snapshots of site-specific release from a giant polyelectrolyte capsules by IR laser activation. The inset shows the pore in the polyelectrolyte shell. The arrow indicates the direction of release as osmotic pressure drives encapsulated material out of the capsule. The scale bar represents 50 μm.

5.2.2 CONCLUSIONS

Polyelectrolyte PDDA and PSS hollow shells were constructed and doped with citrate stabilized gold nanoparticles in either uniform (non-aggregated) or aggregated (possessing near-IR peak) state. For encapsulation by thermal shrinking, microcapsules with non-aggregated gold nanoparticles require more thermal energy than those with aggregates, while both types require higher temperatures than the control sample containing no nanoparticles. This behavior is attributed to the limitations in lateral movement of polymers due to the introduction of nanoparticles in the mesh. In the thermally shrunken state, the permeability of the microshells to dextran polymers is the highest for microcapsules possessing no nanoparticles, while it is the lowest for microcapsules with uniform distribution of nanoparticles. This is attributed to the wall of the microshells becoming thicker or denser at elevated temperatures as a result of additional polymeric material that formed multilayers around the gold particles diffusing between neighboring gold particles. Fluorescent dextran molecules were encapsulated into polymeric microshells doped with non-aggregated or aggregated gold nanoparticles and no leakage was observed in either sample for months after the encapsulation. Release of the encapsulated materials from capsules containing aggregates of gold particles can be performed at low power of near-IR laser, while no release takes place for capsules containing non-aggregated gold particles. This difference is explained by more efficient, localized temperature rise around aggregates of gold. IR release efficiency may be improved by various factors: (1) at high bulk temperature (but below T_g), less heat from the laser-nanoparticle interaction is necessary to cross T_g and allow release, (2) upon addition of salt the interaction between polyions are weakened facilitating release, (3) smaller capsule diameter increases the diffusive force connected with the encapsulated material, and (4) encapsulating larger concentration of cargo also appears to be related to diffusive force requirements. Release of encapsulated material was also demonstrated on hydrogel-templated $(PSS/DAR)_4$ giant microshells coated with aggregates of gold nanoparticles. However, in this case a pulsed near-IR laser source was necessary because much of the energy release by the nanoparticles upon illumination is lost in the surrounding medium. Near-IR laser aimed at a specific location on the giant capsule permits for direction-specific release of encapsulated materials. The dynamics of the release was shown to last over minutes making these structures interesting in regard with specific targeted delivery. Further acceleration of capsule disruption could perhabs be achieved by incorporating the nanoparticle within the PSS/DAR matrix, thus maximizing the shell's surface area affected by the laser/nanoparticles interaction. This

approach is envisioned to find applications in drug delivery or lab-on-a-chip applications. The results presented in this work are relevant for intracellular delivery, [40] membranes [246] and other light- and thermo- responsive materials in general.

5.3 LASER INDUCED RELEASE OF MATERIAL IN LIVING CELLS

5.3.1 NOTE

All of the studies discussed so far with regards to shell mechanics and near-IR release were performed with the intention of developing laser-addressable microdelivery systems for cell studies. In section *5.1* parameters that may improve mechanical stability and reduce the risk of losing encapsulated material from damaged capsules during cellular uptake were presented. In section *5.2*, key factors which influence laser-induced release from microcapsules doped with gold nanoparticles were studied. The following sub-sections (*5.3.2* to *5.3.4*) provide the reader with an overview of studies the author was directly involved in which combined the information gathered so far to the use of optically addressable microcapsule technology for experimentation on living cells. The work presented uses microcapsules doped with homodispersed gold nanoparticles. The incorporation of aggregates of gold particles and gold nanorods in microcapsules for *in vitro* studies are still under investigation and will not be presented here. While the author developed the microshells used in these studies and actively participated in the experimental design, sample characterization and data analysis, most of the cell manipulations studies are credited to Dr. Almuneda Munoz-Javier (Marburg University, Germany).

The following investigations were designed to solve open questions in the literature that needed answers: (1) What is the fate of the released cargo after laser-induced release? (2) What is the cell survival chance after laser-induced release? (3) Which parameters can help prevent microcapsule deformation upon capsule internalization?

5.3.2 FATE OF MICROCAPSULES AFTER INTERNALIZATION BY CELLS

Previous studies have demonstrated that micron-size polyelectrolyte capsules can be internalized by living cells, such as human breast cells (MDA-MB-435S, MCF-7 cell lines) as well as cells from the African green monkey and from other human tissues such as kidney (HEK 293T), bone marrow and colon (LIM1215). [19] The internalization process was also shown to result in capsules becoming deformed which can jeopardize the purpose of developing remotely addressable shells as damaged capsules may release their cargo before needed. Here we investigated whether capsule deformation can be avoided during cellular uptake.

Ten capsules samples were prepared on MF, $CaCO_3$ and SiO_2 colloidal particles using the LbL assembly protocol to produce $(PDDA/PSS)_n$ and $(PAH/PSS)_n$ shells as model systems. These capsules and their properties are listed in Table 5 below. Various templates were chosen for this study because just like the polyelectrolyte shell constituents, core material is can also affect the stiffness of capsules. MF for instance was shown to leave short oligomers in the capsule's cavity upon dissolution [76] which can have a significant impact the shells' mechanical properties. Additionally, some capsules were prepared with and without encapsulated material since encapsulated cargo is also known to influence the stiffness of microshells. [104,247] Encapsulation in of SNARF-1 dextran (a pH sensitive fluorophore) or AF 488 dextran was performed by heat treatment. Two samples were left with the template undissolved. The final diameters of all samples were situated between 3.0 and 5.0 µm. Shells impregnated with gold nanoparticles were compared with shells lacking nanoparticles. In all cases, templates were washed several times prior LbL assembly and 2 mg/mL polyelectrolyte solutions were prepared in 0.5 M NaCl. Some samples also contained either AF 488 dextran or TRITC in the shell. To produce hollow capsules, MF particles were decomposed under acidic conditions, $CaCO_3$ particles were treated with EDTA and SiO_2 was dissolved by treatment it HF. The final shell compositions were of the general structure $(PDDA/PSS)_n$ and $(PSS/PAH)_n$ with various diameter, and bilayers number (*n*) depending on the sub-study. Cell studies were conducted by adding aliquots of capsule solution to mouse embryonic fibroblast cells (NIH 3T3) or human breast adenocarcinoma cells (MCF 7). Details of the ten samples investigated are presented in Table 5.

TABLE 5 SUMMARY OF CAPSULES SAMPLES PREPARED FOR CELL RELEASE

Sample	Shell	Template	Diameter	Nanoparticles	Label in Shell	Encapsulate	Note
1	$(PDDA/PSS)_4$	SiO_2	3 µm	Au 20 nm	-	-	-
2	$(PDDA/PSS)_6$	SiO_2	3 µm	Au 20 nm	-	-	-
3	$(PDDA/PSS)_8$	SiO_2	3 µm	Au 20 nm	-	-	-
4	$(PDDA/PSS)_2$	SiO_2	3 µm	Au 20 nm	-	-	Undissolved
5	$(PDDA/PSS)_4$	SiO_2	4.5 µm	-	-	AF 488	-
6	$(PSS/PAH)_4$	MF	5 µm	-	AF 488	-	-
7	$(PSS/PAH)_4$	MF	5 µm	-	AF 488	-	Undissolved
8	$(PSS/PAH)_5$	$CaCO_3$	5 µm	-	SNARF-1	-	-
9	$(PSS/PAH)_2$	$CaCO_3$	5 µm	-	TRITC	-	-
10	$(PDDA/PSS)_4$	SiO_2	4.5 µm	-	TRITC	AF 488	-

Figure 5.32 show LSCM captions of MCF 7 cells that were incubated with $(PSS/PAH)_4$ shells labeled with AF 488 dextran (green fluorescence), with (Table 5, **6**) and without (**7**) the template dissolved. It is clearly showed that both hollow shells and particles were internalized by both cell types. The cells' walls were stained with Di-8 Anepps (red). To confirm that the cells were internalized, LSCM captions were taken from the x-y (from above, middle panel) and from the x-y (from the side, bottom panel) perspectives, thus providing undisputable evidence that the capsules were indeed in the cell interior. No deformation of the shells was observed in the capsules with the undissolved MF core. Hollow shells, however, were deformed during uptake as illustrated from the LSCM captions on the right.

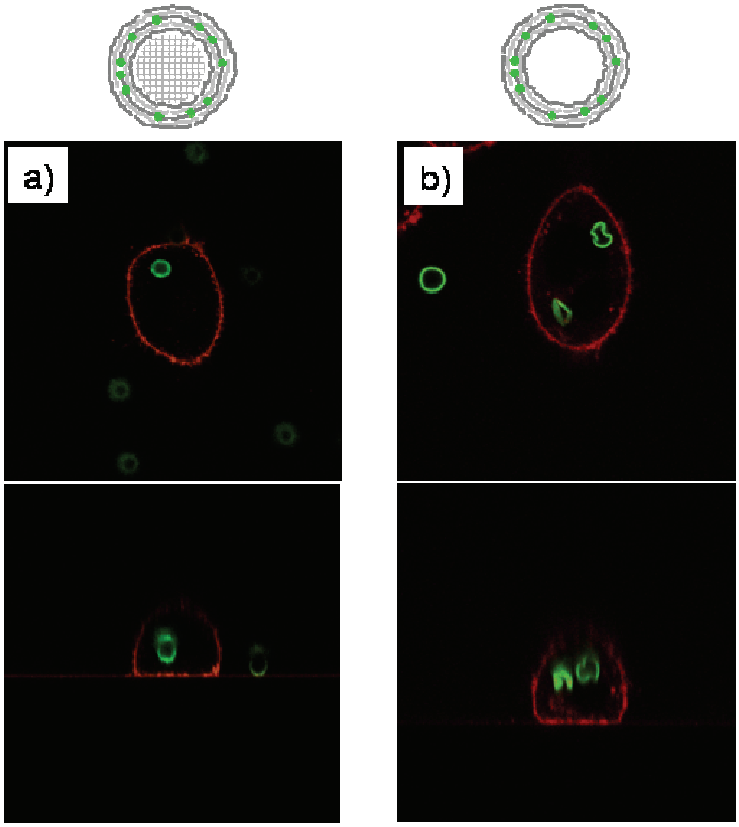

Fig. 5.32 LSCM images of cells with internalized with $(PSS/PAH)_4$ shells labeled with AF 488 dextran. On the left side, the microshells were added to the cell medium before core dissolution as schemed on top. On the right, the same experiment performed with microcapsules of identical shell construction but lacking the template. The middle panel shows LSCM captions of shells (green) and cell walls (red) in the x-y plane. The bottom panel confirms internalization of capsules in cells by looking at the same sample from the x-z direction. The right column illustrates that capsules are deformed upon cellular uptake. From [202].

Unfortunately, internalization studies using different number of polyelectrolyte layers and addition of nanoparticles in the shell construct (**1-4, 10**) in an attempt to thicken and reinforce the microcapsule shell yielded inconclusive results as no correlation was found between microcapsules' deformation upon internalization by cells and the number of bilayers in the capsule wall.

The localization of internalized microcapsules inside cells was elucidated by encapsulating the pH-sensitive SNARF-1-dextran which emits photons in two distinct wavelength ranges depending of the local pH. SNARF therefore acts as a fluorescent pH indicator. [202] The endocytotic process by which cells ingest materials in their environment, typically begins with the formation of a compartment (endosome, lysosome, phagosome) made up of cell wall material that contains extracellular material (*i.e.* a capsule in this case). Depending on the nature of the uptaken material, the compartment tends to adopt a more acidic pH before sorting out its content to the appropriate destination in the cell. Fluorescence microscopy revealed a color change in the fluorescent encapsulated dextran from red (alkaline, cell growth medium) to green (acid) for microcapsules suspected to be internalized by cells (Figure 5.33). This confirms that the capsules (**8**) colocalized with cells are not only internalized but also that they are themselves encapsulated inside an intracellular compartment.

With regards to deformation, it was found that microcapsules having thinner walls (*i.e.* less layers) (**4, 8**) are almost always deformed after cellular uptake and often lost their cargo. Shells with encapsulated dextran (**5, 10**) also got deformed but tended to retain their cargo. This is in agreement with our results in *Section 5.1*, where it was shown that capsules that were thermally shrunk to encapsulate a substance are mechanically more stable than unshrunk capsules with the same construction. Deformation appeared to progress over time and it was found that certain cell lines are more aggressive in the sense that capsules were more extensively damaged upon uptake by breast cancer cells than by fibroblast cells.

In summary, these results offer a definite proof that capsules are indeed internalized by cells. However, deformation is problematic and although loss of the encapsulated substance is not always observed when shells were thermally shrunk it is still significant. In the following sub-section, it will be shown how implementing the knowledge obtained from the mechanical deformation studies presented in *Section 5.1* were used to improve the mechanical stability of capsules upon cellular internalization.

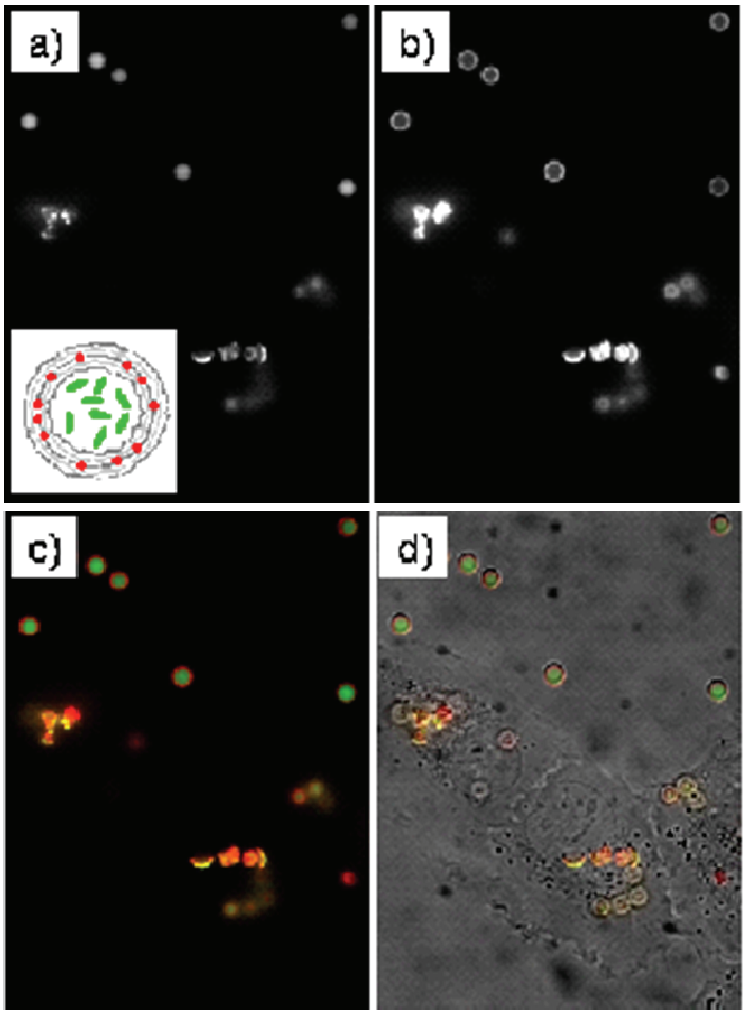

Fig. 5.33 LSCM images of MDA-MB 435s cells which have been incubated for 30 hours with capsules. The walls of the $(PDDA/PSS)_4$ capsules were labeled with rhodamine (red) and AF 488 dextran (green) was thermally encapsulated in the cavity. a) Fluorescence image of the Alexa 488. b) Fluorescence of rhodamine. c) Color overlay of (a) and (b). d) Overlay (c) and the phase contrast image showing the cells and capsules. Clearly the deformation of incorporated capsules can be seen, whereas all capsules in the cell medium have preserved their spherical shape. From [202].

5.3.3 DEFORMATION OF MICROCAPSULES BY LIVING CELLS

In the previous section, it was shown that most microshells investigated had a tendency to become deformed upon cellular uptake, but focused mainly in proving that polyelectrolyte microcapsules can be internalized by cells and to show where in the cells such capsules reside. In the work summarized here, the aim was to use the information on the parameters affecting capsules' stability presented in *Chapter 5.1*, and attempt to apply it in cells.

Microcontainers were incubated in presence of living cells in order to monitor how the incorporation of gold nanoparticles in capsules affects their mechanical stability *in vitro*. Gold nanoparticle-functionalized $(PDDA/Au/PSS)_4$ capsules (F_S = 0.07) and control $(PDDA/PSS)_4$ capsules were prepared. Additionally for this study, 5 nm and 20 nm gold nanoparticles were used during microcapsules assembly yielding two capsule samples each containing a unique nanoparticle size. Three samples were then thermally shrunk in a solution containing 0.1 mg/mL AF 555 dextran to average diameters of 4.0 μm, 2.8 μm and 2.3 μm. The capsules that were internalized by cells were monitored by a camera equipped with fluorescence and phase contrast imaging. The proportion of microshell that deformed in the uptake process was determined as a function of nanoparticles content and capsule diameter. In addition, two different types of cell lines; fibroblast and breast cancer cells referred to as NRK and MDA-MB-435s, respectively, were used in order to determine whether the degree of shell deformation found with a given cell line compares between different cell lines.

Figure 5.34 shows microscopy images of MDA-MDA-435s cells that were incubated with microcapsules. White arrows indicate non-deformed microcontainers outside the cell. A dashed yellow line indicates the position of the cell nucleus. A sketch of the general appearance of capsules after internalization is shown in inset. On the left side of the figure, capsules without gold particles thermally shrunk to 4 μm (a). Beneath, the same capsule sample but thermally shrunk to 2.3 μm (b). On the top right, capsules containing gold nanoparticles shrunk to 4 μm (c) and to 2.3 μm on the bottom right (d). The majority of capsules that were internalized in (a), (b) and (c) were found to be deformed after internalization by the cells although less frequently in the case of the smaller $(PDDA/PSS)_4$ capsules. Most capsules in (d) were found to be unaffected by the cellular uptake. In all captions, it can be seen that capsules situated outside the cell were not deformed.

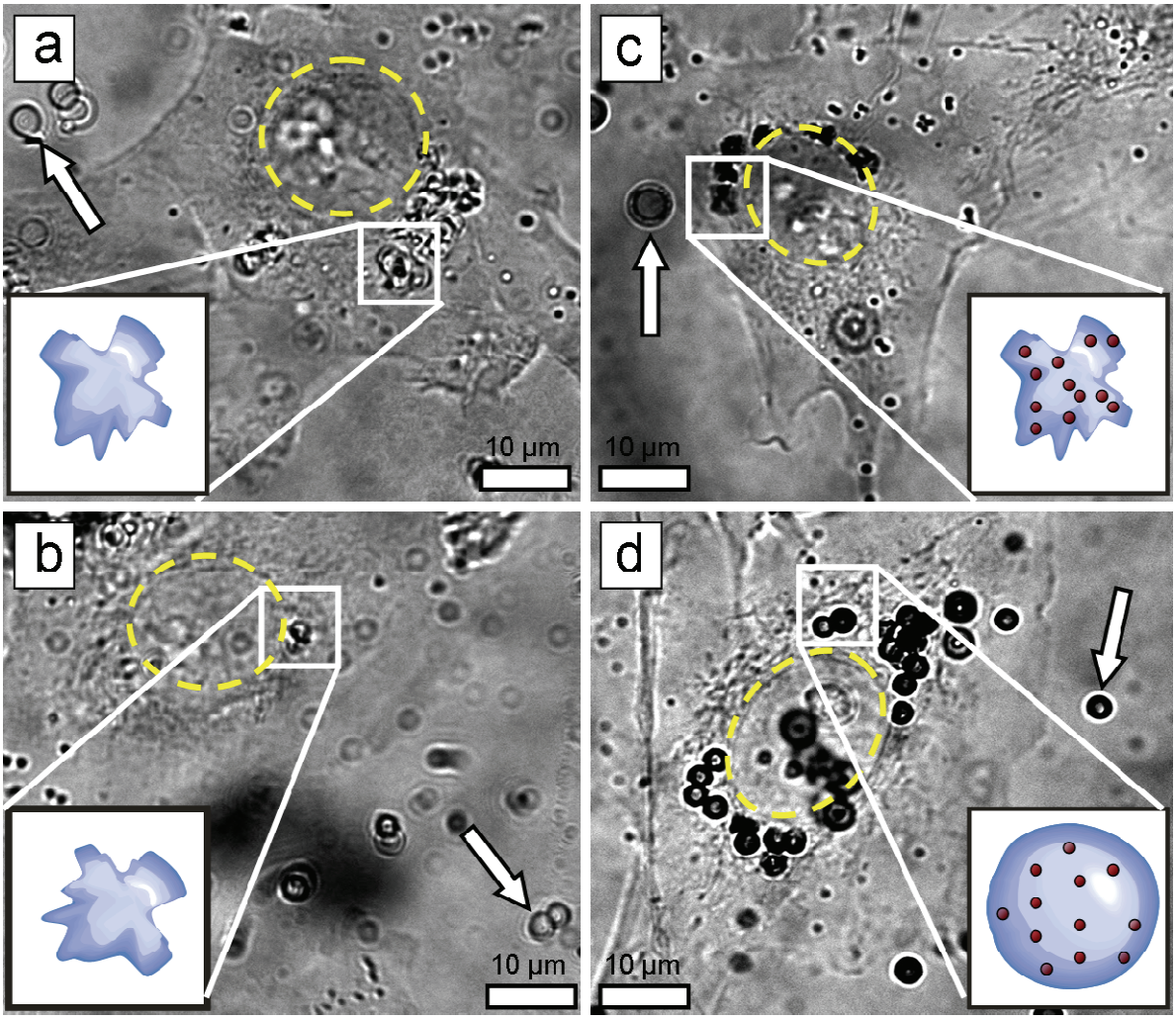

Fig. 5.34 Microscopy images of MDA-MDA-435s cells with internalized capsules. On the left, capsules without gold particles thermally shrunk to 4 µm (a) and to 2.3 µm (b). On the right, capsules containing gold nanoparticles shrunk to 4 µm (c) and to 2.3 µm (d). White arrows indicate non-deformed microcontainers outside the cell. A dashed ovoid line indicates the position of the nucleus of the cell that internalized capsules. The scale bars measure 10 µm.

It was shown in *Section 5.1.4* that a $(PDDA/Au/PSS)_4$ microshell with a nanoparticle surface coverage of 28 % possesses a Young's modulus nearly five times greater than a shell with a 7 % surface coverage. On the other hand, thermally shrinking a $(PDDA/Au/PSS)_4$ microshell with a 7 % gold coverage to about half of its original diameter gained a stiffness similar to shells with a 28 % nanoparticle load. A careful analysis of the proportion of microcapsules that were

deformed after cellular uptake was carried to determine whether the incorporation of gold nanoparticles truly had such a large influence on capsule stability after internalization. A minimum of four hundred capsules per sample were examined to determine the proportion of internalized microcapsules deformed.

Figure 5.35 summarizes the findings compiled for shells internalized by NRK cells. First, after only a very little shrinkage to 4 μm or about 10 % of the capsules' original size, an average of 97 % of all microshells were found to deform, no matter which cell line was used. When shrunk to an average of 2.8 μm, only the shells doped with 20 nm gold particles were found to have a significant improvement in shell stability, with about 11 % of shells that remained intact after being incorporated by the NRK cells. However, still no significant improvement was observed in any of the shells ingested by the cells MDA-MB-435s cells. It is only at a diameter of 2.3 μm, which corresponds to 50 % of their initial diameter that the shells became truly more resistant to deformation. The best results were obtained with NRK cells and capsules containing 20 nm gold particles for which 81 % of the capsules remained intact after being internalized. Using the same type of cells, 38 % of the shells containing no gold and 60 % of shells containing 5 nm gold particles were found intact.

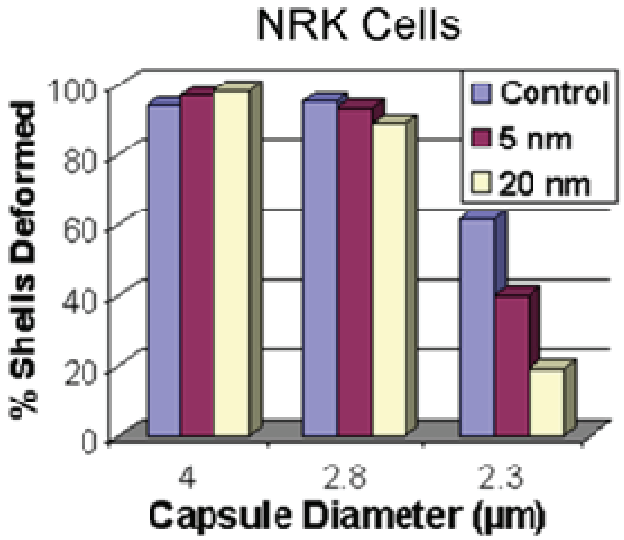

Fig. 5.35 Statistics of the deformation of $(PDDA/Au/PSS)_4$ microshells containing gold nanoparticles or not, as a function of nanoparticle size (5 nm, 20 nm) and capsule diameter in presence of NRK cells. Average capsule diameters were calculated from 30 capsules. At least 400 capsules were monitored for each experiment.

These results illustrate that the presence of gold nanoparticles in the shells can greatly improve the shell stability over mechanical deformation, but this stability becomes significant only for microshells shrunk to smaller diameters. Similarly, the mechanical stability of shells shrunk to 2.3 μm containing no gold, as well as 5 nm and 20 nm gold nanoparticles was found to greatly improve when internalized by MDA-MB-435s cells. However, in this case, while both control capsules and shells doped with 20 nm particles displayed a 79 % of intact shell after cellular uptake, shells doped with 5 nm particles were found to be much less with a 42 % success rate. This discrepancy is not currently understood but could be related to the internalization mechanism of MDA-MB-435s cells.

5.3.4 LASER-INDUCED RELEASE FROM MICROCAPSULES AND CELL VIABILITY

The release of substances from polyelectrolyte microcapsules functionalized with gold nanoparticles inside living cells is not a novelty as such. Gold nanomaterials constitute an ideal vector to induce release by heating the capsule shell. As discussed in *Section 5.2*, careful capsule designing may allow the laser-nanoparticle interaction to produce a temperature increment of just a few Kelvin above ambient temperature, which would be sufficient to change the capsules permeability and release materials in a highly controlled fashion. The following summarize the work presented in ([203]).

Gold nanoparticle-functionalized $(PDDA/Au/PSS)_4$ capsules (F_S = 0.12) were prepared in accordance with the protocol described in *Section 5.1*. The shell was impregnated with gold sulfide/gold (AuS_2) nanoparticles with a mean diameter of 30 nm at layers 3 and 5. AuS_2 nanoparticles were provided by Dr. Sucha (Ludwig-Maximilian University, Germany) and synthesized according to the protocols available in the literature. [248] AF 594 dextran and CB dextran were individually encapsulated by incubation with the capsule sample at 64°C for 20 minutes. The dextran concentration in both cases was 0.5 mg/mL. In recent studies, AuS_2 particles were found to possess a highly efficient laser-nanoparticle heating potential mainly due to their large size but it was also found that less microcapsules functionalized with AuS_2 nanoparticles were able to encapsulate substances due to defect created during the capsule preparation. Consequently, AuS_2 particles were only used in the work described in the present section. The average diameter of the microcapsules after encapsulation was 2.4 μm. The thermally shrunk capsules were rinsed in water and used as such for cell internalization and remote release experiments.

$(PDDA/AuS_2/PSS)_4$ capsules with encapsulated dye were incubated in a culture of MDA-MB-435s breast cancer cells for 24 hours. After this period, the growth medium was replaced with fresh medium to remove capsules that were not ingested by cells. The cell culture plate was then mounted on an x-y-z stage in a laser setup similar to the one previously described (830 nm, 0-100 mW) equipped with a 40 x microscope objective and a fluorescence camera. The release of fluorescent encapsulated substances could therefore be monitored live. A *LIVE/DEAD Viability/Cytotoxicity Assay Kit* was used to monitor whether cells survived the laser release. This assay is based on fluorescent probes that emit green photons when the cell is alive (positive esterase activity) and red photons when the cell is dead (specifically binds certain nucleic acids but can only enter the nucleus when the nuclear membrane integrity is compromised, *i.e.* dying cell). Laser intensities of 0 to 31 mW were used to illuminate microcapsules.

The principal findings of this work consist in that at high laser power (31 mW) the irradiated capsules released their content but at the expense of cell death. Using a low laser intensity of 1 mW or less was not sufficient to open capsules. At 2.3 mW, however, capsules were opened and cells were found to survive and even divide after the encapsulated dextran was released. Figure 5.36 shows two internalized capsules loaded with fluorescent AF 594 dextran before (left) and after (right) remote opening of the microcontainer on the right of the cell nucleus using a laser intensity of 2.3 mW. It can be seen that the dextran spreads throughout the cytosol, but is unable to spread through the nuclear membrane, a very selective biological barrier. Diffusion of the dye inside the nucleus over time would have supported that the cell was “injured” by the laser-induced capsule opening. Based on the assay used, it was determined that at 2.3 mW of laser intensity, 70 % of the cells in which a capsule was irradiated survived. At 31 mW, a 0 % survival rate was found.

Another important outcome of this work, lays in the laser intensity needed to open the capsules which are significantly lower than the intensities used in for the experiments performed in water. The irradiation threshold intensity was lowest for capsules subjected to high temperature (25 mW) and high salt (26 mW). While quantitative studies were conducted for each of these effects independently in Agg-Au4 shells, the results shown where show that the combination of these can also allow for Homo-Au4 shell types to be open at relatively low laser intensity. The conditions inside the cytosolic space at incubation temperature (37°C) combine both of these parameters to an extent, which could explain the surprisingly low

intensity needed. However, the AuS_2 nanoparticles used in these microcapsules might also have contributed to the high release efficiency.

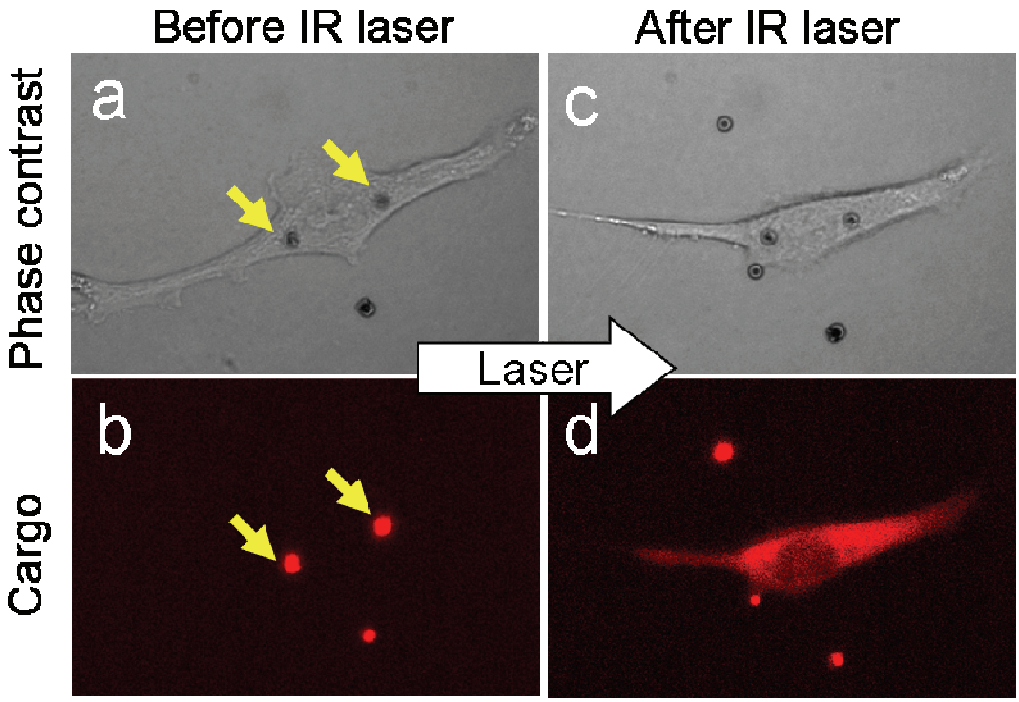

Fig. 5.36 Remote release of encapsulated dextran inside living cells from gold functionalized microcapsules using a near-IR laser at 830 nm. Before release, the microcapsules (indicated by two arrows) are found to be undamaged and internalized in the cell. After irradiation with the laser, the dextran was released and spread throughout the cytosol of the cell without penetrating the nuclear membrane. From [203].

5.3.5 CONCLUSIONS

In this section, it was demonstrated how polyelectrolyte microcapsules containing gold nanoparticles represent a unique tool to study living systems. Such microcapsules were internalized by various cell types and used to deliver encapsulated material to the intracellular compartments upon laser irradiation. The capsules, which have a tendency to deform upon cellular uptake, were found to become more resistant to deformation by the incorporation of metal nanoparticles and more importantly, by thermal shrinkage, which is also a convenient way to encapsulate materials after microcapsule preparation. While the all microcapsules

displayed a poor resistance to deformation when thermally shrunk to larger volumes, shells shrunk to about 50% of their original size showed significant improvements with around 80% of intact capsules found in some cases. Shells doped with larger particles and shrunk to smaller diameter were found to be generally more stable, less inclined to deformation. Rendering the microshells resistant to the endocytotic mechanical deformation forces is important in order to prevent the free release of encapsulated substances before at an unwanted time.

The internalization of microcapsules was demonstrated by imaging cells that were incubated with microcapsules with LSCM in different planes. Similarly, the remote release of encapsulated dextran was found to occur upon near-IR laser irradiation. Cell viability after release of material was also investigated. At a laser intensity of 31 mW, release would occur but the cells did not survive. At a laser intensity of 2.3 mW it was found that cells could survive the release with a 70 % success rate whereas 1 mW was too low to induce release and a corresponding 100 % cell survival rate.

6 OPTICALLY ADDRESSABLE CAPSULE SHELLS CONTAINING PDT AGENTS

The assembly of polyelectrolyte microshells containing porphyrin and phthalocyanine dyes and their response to light irradiation are discussed. These porphyrinoid dyes are known for their high fastness and to catalyze the formation of radicals and/or singlet oxygen upon exposure to light (Section 2.7.2.1). The motivation behind the work presented in this section was to demonstrate the possibility of incorporating functional dyes in polymeric microshells without resorting to chemical modifications and to damage the latter by triggering the catalytic properties of these dyes. Should this approach be successful, it may then be possible to remotely release encapsulated materials from microcapsules at low irradiation intensity over relatively long exposure time, sharply contrasting with the effects observed when using metal nanoparticles which induce release from microcapsules in the order of seconds (Section 5.2). Incorporation of functional dyes in polyelectrolyte microcapsules had to be done without chemically altering the functional reagent so as to prevent changing their catalytic properties as well as the mechanical properties of the shells.

The porphyrin TPPS as well as the phthalocyanines Fe(I) phthalocyanine tetrasulfonic acid (FePcS), Cu(I) phthalocyanine tetrasulfonic acid (CuPcS), Al(III) phthalocyanine chloride tetrasulfonic acid (AlPcS) and phthalocyanine tetrasulfonic acid (PcS) (see structure examples in Section 3.1.3) were selected as photo-active compounds, each differing in their photocatalytic and aggregation behaviour with respect to one another. Additionally, each is substituted with four sulfonic acid groups (pKa ~ 0), strong Lewis acids expected to facilitate the dyes' incorporation in the polyelectrolyte multilayer.

6.1 SPECTROSCOPIC PROPERTIES OF TPPS IN SOLUTION

In order maximize the concentration of dye molecules per microcapsules, various LbL designs were assembled on flat substrates and studied by UV-visible spectroscopy. The visible spectroscopy and aggregation behavior of porphyrinoid dyes is strongly dependant on their environment concentration making it possible to monitor the relative content and organization of the dye in solution. Figure 6.1 (Left) shows that the UV-visible spectra of TPPS changes drastically in the pH value range between 9.5 and 2.4. The large change in the absorbance

profile at below pH 4 is due to the aggregation state of TPPS, which exists as a monomer in water above this pH and as a dianion that forms J-aggregates at lower pH values (Figure 6.1, right). Therefore, at basic pH, TPPS exists as a negatively charged monomer and is expected to form a favorable binding interaction with polycations.

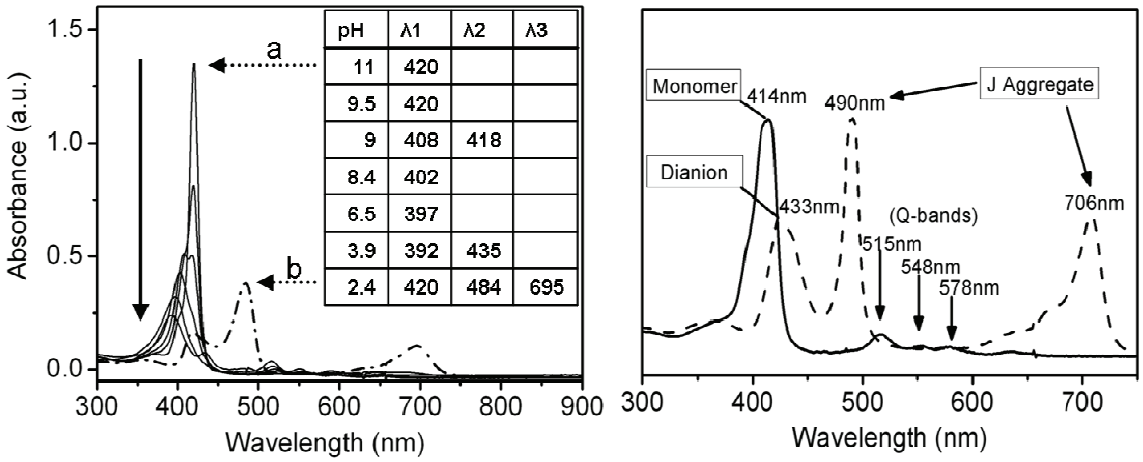

Fig. 6.1 UV-visible spectra of TPPS as a function of pH and aggregation state, left and right, respectively. The major absorption peaks at different pH values can be seen in the table. Right: UV-visible absorption spectra showing the spectroscopic attributes of TPPS in its monomeric and dianionic forms.

Experiments involving mixtures of polyelectrolytes and dyes were conducted using an excess of amine groups corresponding to approximately 400 times the amount of dye used (calculations can be found in Sub-section 6.5). This was done in order to avoid the strong tendency of such dyes to form aggregates at high concentration and two prevent partitioning the dye molecules between the polymer and the solution which could also lead to aggregation between polymer/dye complexes. [175,186,249] The saturation point for porphyrinoid dyes in solution can be anywhere from a few molars to completely insoluble depending on the chemistry of the dyes and the solution conditions. [176]

The UV-visible spectra of TPPS mixtures with several polyelectrolytes were monitored to test whether complexation between the species is possible in solution. However, PAH was the only polycation that appear to affect the spectroscopic properties of TPPS. Figure 6.2 shows that mixing PSS and TPPS has no effect on the TPPS absorption spectrum, while the PAH+TPPS mixture displays a blue shift of the main absorption band of TPPS (Soret band) from 413 nm to

387 nm. Prior mixing, the PAH solution had a pH of 5, addition of an equal volume of TPPS solution (10^{-7} M) at pH 11 brought the overall solution pH at 6.5. The pH of a PAH solution, however, should be adjusted to less than 7 at which most of its amino moieties are positively charged to favor the multilayer assembly process. [16,17,116,250,251] The λ_{max} of the PAH+TPPS solution at pH 6.5 was situated at 387 nm. This corresponds to a blue-shift of approximately 10 nm when compared to the the TPPS solution at pH 6.5 shown in Figure 6.1, suggesting that the PAH has an influence on the dye's electronic properties by interacting with it. A blue shift of the main Soret band of TPPS was previously attributed to self-assembling of TPPS to form H aggregates. [176] A parallel stacking of TPPS monomers leads to such aggregates with blue shift of the Soret band. [252,253] Similar aggregation phenomenon and blue shift was observed for TPPS in association with the polyelectrolyte polybrene at neutral pH. [254] The hypsochromic shift of the Soret band of TPPS on interaction with PAH, suggests that the porphyrin displays a strong tendency to form extended self-aggregates on oppositely charged free polyelectrolyte. In addition, the 500-600 nm spectral region containing Q-bands, which is visible for TPPS in solution above pH 4 completely vanished at pH 6.5 in presence of PAH. The mixture of TPPS monomers with the negatively charged polyelectrolyte PSS (final pH 9) resulted in no color change of the porphyrin solution. The corresponding UV-visible spectrum (Figure 6.2) showed no major shift in the Soret band indicating that there is no interaction between the two negatively charged species.

The spectroscopic data suggests that a complexation between PAH and TPPS occurs in solution. The zeta potential of the PAH+TPPS solution was measured in 50mM NaCl and showed to be about 21 mV. Hence a method involving adding PAH and TPPS together was adopted for microcapsules assembly. The coiled nature of PAH in the shell of polyelectrolyte capsules is thought to prevent the formation of long range aggregates of TPPS on the capsule surface. Also, the formation of J-aggregates can be excluded due to the absence of the characteristic peak at 490 nm. Instead, the peak at 425 nm can be attributed to the formation of dianionic species $[H_4TPPS]^{2-}$, which is blue shifted from 433 nm upon adsorption to the polyelectrolyte capsule shell. [253]

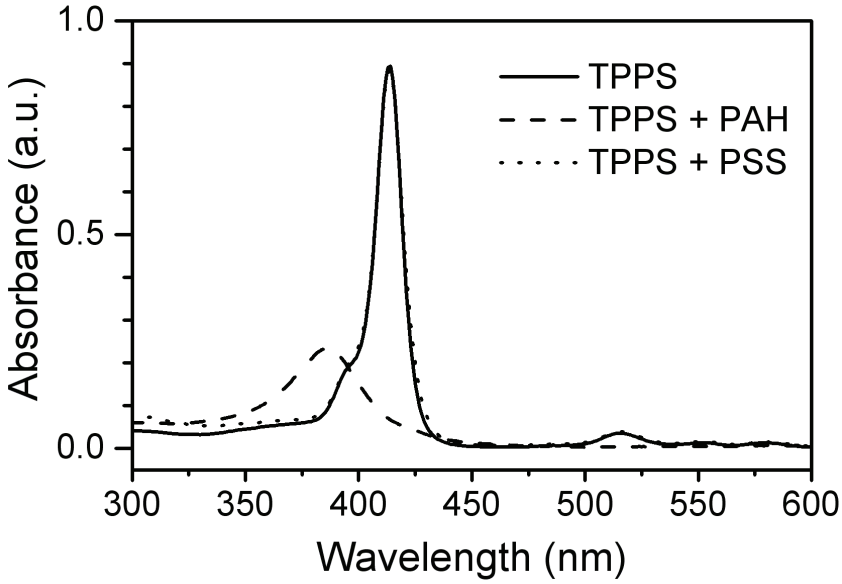

Fig. 6.2 UV-visible spectra of TPPS admixed with PAH and PSS. TPPS (hard line) on interaction with PAH (dashed line) show a hypsochromic shift of the main absorption band but does not change upon mixing with PSS (dotted line).

6.2 SPECTROSCOPIC PROPERTIES OF PHTHALOCYANINE DYES IN SOLUTION

Phthalocyanines (Pc) readily dissolve in concentrated sulfuric acid but in water to a much lower degree while sulfonated Pc (PcS) are soluble in water (Section 3.1.3). Metal complex formations can influence the visible light absorption of Pc but has little impact on the UV absorption region. In metallo-Pc compounds, the four benzene rings hardly have any influence on the spectroscopic properties but substituent on these rings can alter the absorption. [147,255] Normalized absorbance spectra of PcS, FePcS and AlPcS are presented in Figure 6.3.

The spectra of phthalocyanine dyes typically shows a Soret band in the 320-350 region and intense Q bands between 600 and 750 nm. Unlike TPPS, the Q bands are quite intense in PcS. The bathochromic shift of these bands for FePcS and AlPcS (relative to PcS) is most likely due to the metal destabilizing the highest occupied molecular orbital (HOMO) rather than to a stabilization of the lowest unoccupied molecular orbital (LUMO). [256] The main UV band was found to be 328 nm, 352 nm, 326 nm and 328 nm for PcS, AlPcS, FePcS and CuPcS (not shown), respectively. PcS and FePcS were found to contain one primary peak each with a shoulder at 605 nm and 632 nm. AlPcS and CuPcS both displayed two strong visible bands at 614 nm and

693 nm for CuPcS; 607 nm and 677 nm for AlPcS. The spectra support that PcS compounds offers a good range of absorption in the orange-red portion of the spectrum. Unlike the porphyrin TPPS, polyelectrolytes did not alter the absorption properties of PcS.

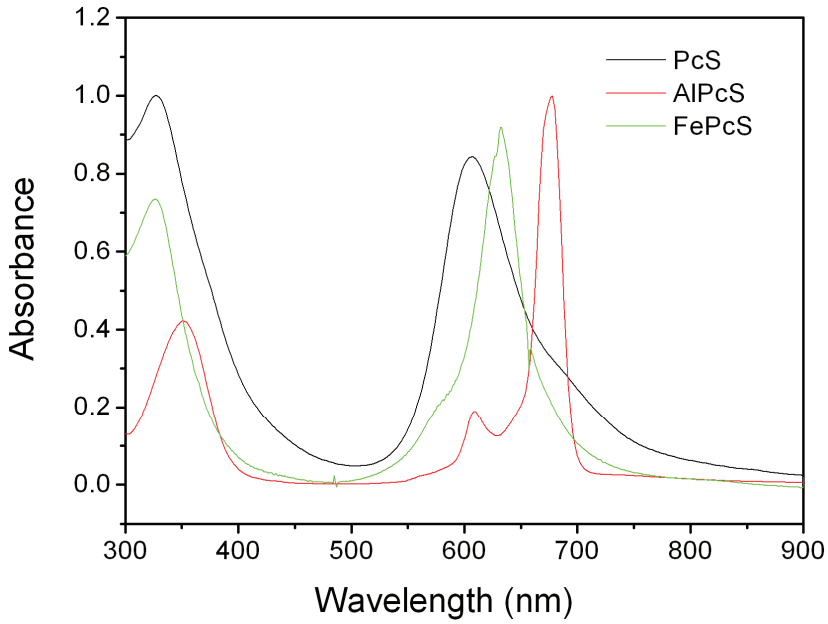

Fig. 6.3 UV-Visible spectra of PcS, AlPcS and FePcS.

6.3 SPECTROSCOPIC PROPERTIES OF TPPS IN LBL POLYELECTROLYTE FILMS

To investigate which of various strategies was most efficient to incorporate TPPS in PAH/PSS films, various LbL film constructs were assembled onto clean, PEI-treated quartz wafers. The progression of assembly was monitored by UV-visible spectroscopy and searched for the approach permitting the most TPPS to be incorporated in the polyelectrolyte multilayers. Polyelectrolyte and TPPS used had respective solution concentrations of 2 mg/mL (0.5 M NaCl) and 10^{-7} M. Figure 6.4 shows the UV-visible spectra taken after each layer addition when PAH and TPPS were mixed prior addition to the substrate to produce the following film structure $(PSS/PAH+TPPS)_5PSS$. The gradual increase in absorption throughout the spectrum suggests that the PAH+TPPS layer is sufficiently homogeneous to allow charge overcompensation so that the next oppositely charged layer can adhere. The consistent increase in the TPPS absorption region at 425 nm supports that the TPPS content increases with the number of layers. Also, the addition of PSS visible at 225 nm does not seem to lead to TPPS desorption as the absorbance of the latter at 425 nm appears to remain unaffected.

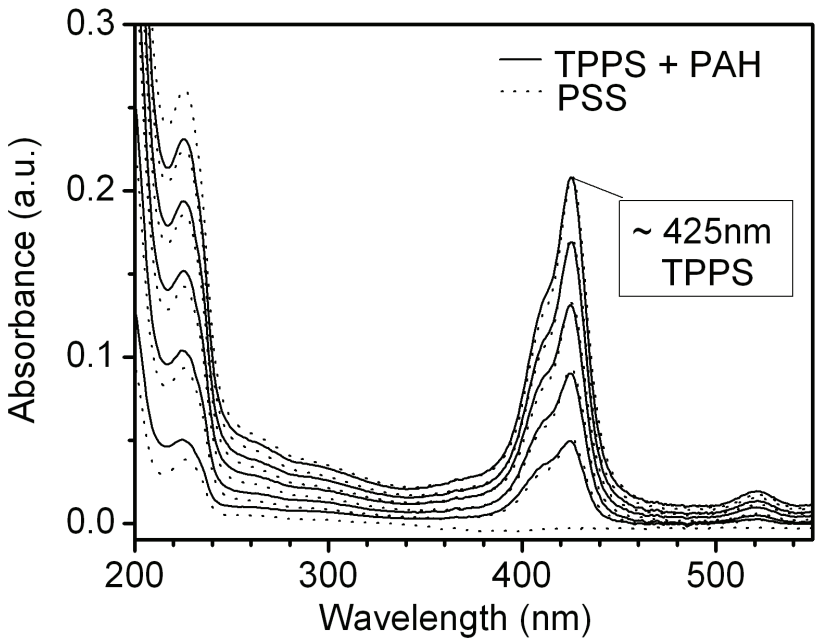

Fig. 6.4 UV-visible spectra of the LbL assembly of $(PSS/PAH+TPPS)_5PSS$. The spectra were taken after each layer addition on a polyethylenimine-coated quartz slide.

In another approach, the system $(PSS/PAH/TPPS)_4PSS$ where the PAH and TPPS were added separately on a polyethylenimine coated quartz substrate was investigated (Figure 6.5). The substrate was carefully rinsed between each addition step. The resulting spectra taken after each layer addition shows that small amounts of TPPS are incorporated in the film when TPPS is added as a separate step between PAH and PSS layers. Figure 6.5A shows the enlarged portion of the 200-250 nm spectral window from the main spectrum illustrating that PSS absorbs consistently to the TPPS-coated PAH layer. Figure 6.5B also shows a gradual increase in the main TPPS absorption region. Another interesting piece of information is provided from 6.5B; the main absorption peak at 420 nm is red-shifted to 425 nm immediately after PSS is added suggesting a change in the optical properties of the dye when sandwiched between PAH and PSS polyelectrolytes. This contrasts with the lack of influence PSS had on the spectrum of TPPS when in solution (Figure 6.2). The red shift could be an indication that PcS forms J-aggregates upon PSS absorption. These measurements were performed at constant pH and ionic strength so that they cannot be attributed to solvent properties. This effect is absent when TPPS and PAH are added as a single layer (Figure 6.4).

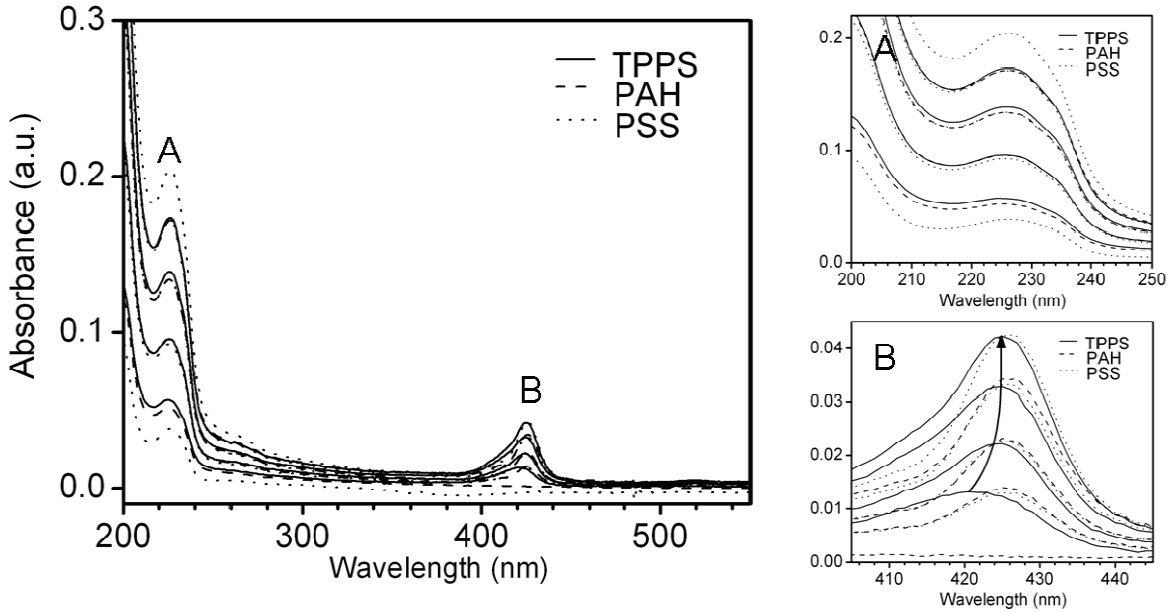

Fig. 6.5 UV-visible spectra of the LbL assembly of $(PSS/PAH/TPPS)_4PSS$. Inset A shows consistent PSS absorption on the substrate at each addition, confirming that the TPPS absorbed (inset B) does not significantly affect the surface charge of the PAH coating. Inset B also shows that the main absorption band of TPPS is red-shifted as subsequent layers are added atop of it.

When TPPS is added along with PSS in a single step to construct microcapsules with the following composition; $(PAH/PSS)_2(PAH/PSS+TPPS)_4PAH$, or sequentially following PSS to yield $(PAH/PSS/TPPS)_5PAH/PSS$, the polyelectrolyte PSS was preferentially adsorbed and the PS particles did not change in color confirming that TPPS does not compete nor complex with PSS for the positively charged PAH layer. This was confirmed spectroscopically monitoring the assembly of $(PSS/TPPS/PAH)_4PSS$ on a flat substrate, which showed that virtually no TPPS was incorporated in the structure using this approach (Figure 6.6). Comparing the spectroscopic data of adding PAH and TPPS together as opposed to sequentially, reveals that the former strategy leads to a seven fold increase in TPPS content relative to the sequential approach.

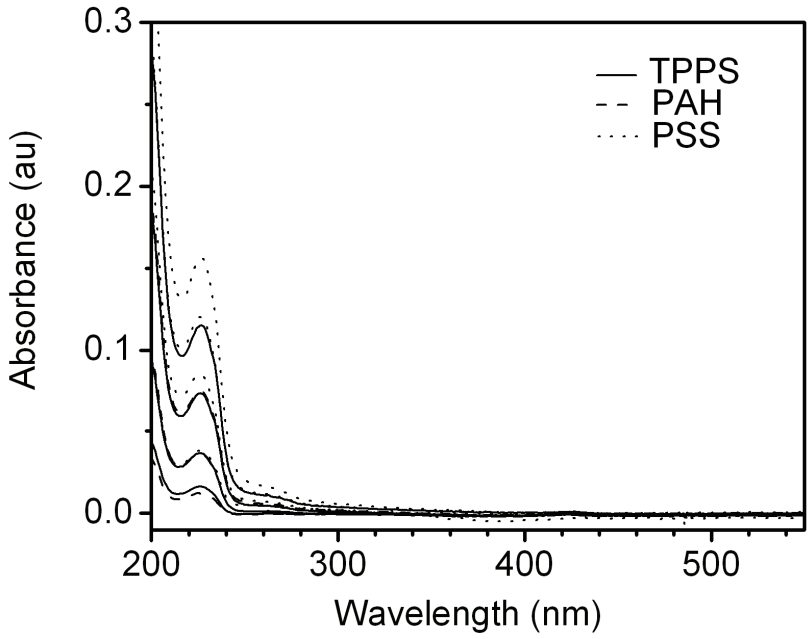

Fig. 6.6 UV-visible spectra of the LbL assembly of $(PSS/TPPS/PAH)_4PSS$. TPPS is not absorbed within the multilayer structure using this approach on a planar substrate.

6.4 QCM OF POLYELECTROLYTE/PHTHALOCYANINE COMPOSITE FILMS

Quartz crystal microbalance (QCM) was used to monitor the assembly of multilayer films as a function of frequency change in the quartz crystal rather than spectroscopy. In order to get a general understanding of the favorable assembly procedure for phthalocyanine-doped multilayer films, CuPcS and FePcS were chosen for this study. As in section 6.1, we looked at adding the dyes sequentially and by premixing them with polyions. While the spectroscopic properties of PcS in solution were indifferent to the presence of polyions, the polyelectrolytes PDDA and PSS were chosen as a model system since a stronger color change of the LbL films was observed for these polymers in preliminary tests. The deposition was done using a robotic dipper and the quartz crystal frequency measured after each layer addition after drying. A PEI/PSS base was used for each assembly. Besides the control $PEI(PSS/PDDA)_4PSS$, four samples were made: $(PDDA/FePcS)_7PDDA$, $(PDDA/CuPcS)_7PDDA$, $(PDDA/FePcS/PSS)_5$, and $(PDDA/CuPcS/PSS)_5$. Figure 6.7 illustrates the results obtained for multilayers of PDDA/PSS with and without PcS. Each point is the average value of three measurements.

A notable decrease in deposited mass was observed after each CuPcS treatment (layers 2, 5, 8, 11, 14). The FePcS-containing film had a frequency difference (Sum dF) of 1575 Hz after

5 layers of PDDA/FePcS/PSS compared to 789 Hz for PDDA/CuPcS/PSS and 1210 Hz for PDDA/PSS films with the same number of layers. It is known from Eq. 3.8 that the frequency difference (Sum dF) and absorbed mass (m) vary linearly. Therefore films containing FePcS contain twice as much material on average than CuPcS treated films and 25 % more material than PDDA/PSS films. In addition, it can be seen from the graphs in Figure 6.7 that the mass of absorbed materials merely changes after each PSS additions in the case of CuPcS films unlike FePcS whose frequency sum varies consistently. This suggest that CuPcS slows the absorption of PSS, thus interfering with the LbL procedure, which could be due to the extra valency available at the central copper atom which may allow stronger interactions to form between the dye and PDDA. On the other hand, the iron atom of FePcS has two additional coordination points bound to two oxygen atoms extending perpendicularly to the plane of the molecule, perhaps lowering their affinity to the PDDA layer.

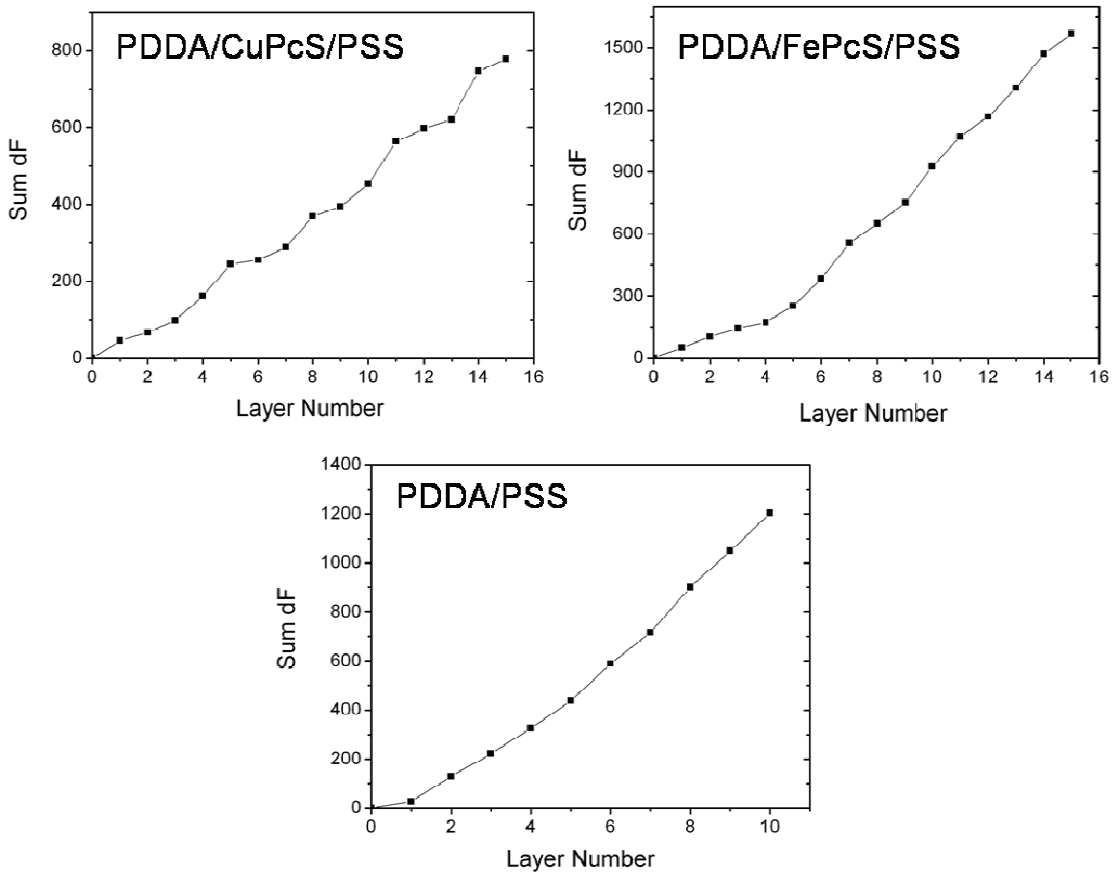

Fig. 6.7 QCM data of PcS dyes sandwiched between PDDA/PSS multilayers.

Figure 6.8 illustrates the QCM data of multilayers assembled in the absence of PSS. It is clear from this that while films of PDDA and tetrasulfonated phthalocyanines are possible, the layers are quite thin. In both cases, a mass is absorbed upon each PcS layer but a significant portion of it desorbs upon addition of PDDA. In addition, because the mass increases rather linearly on average, it can be said that the mass loss at each PDDA layer is primarily the result of a large proportion of PcS desorbing but that enough PDDA is still allowed to bind to allow full layers to be deposited. In view of these results and the admixing procedure discussed in the previous section, admixing the PcS complex prior layer additions and sequential addition of the dye (sandwiched between oppositely charged polyelectrolyte layers) were considered the best approaches to construct microcapsules by LbL.

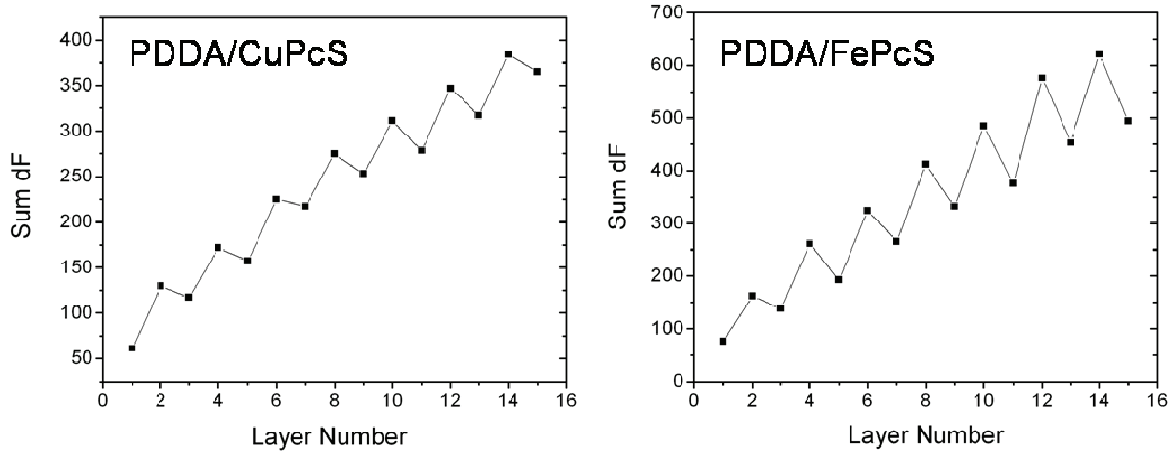

Fig. 6.8 QCM data of PDDA/PcS multilayers.

6.5 PREPARATION OF TPPS-(PAH/PSS)$_4$ COMPOSITE SHELLS

Capsules containing TPPS in the shell were prepared on 10.25 µm and 4.62 µm PS particles. The template was coated with two bilayers of PAH and PSS, starting with PAH and then by 4 bilayers of (PAH+PP/PSS) followed by an additional layer of PAH to obtain a final composition of (PAH/PSS)$_2$(PAH+TPPS/PSS)$_4$PAH. The PAH/TPPS layer was made by re-suspending the PSS-coated latex particles in PAH solution followed by rapid addition of equal volume of TPPS solution. After each layer addition, the particles were washed thrice in MilliQ water. After deposition of required number of layers, the supernatant was removed from the TPPS-PE coated polystyrene precipitate and the latter resuspended in THF. Core dissolution was conducted in HF for shells coated on silica particles.

6.6 ZETA POTENTIAL OF TPPS-POLYELECTROLYTE CAPSULES

The adsorption of the polyelectrolyte on the PS core was monitored by zeta-potential analysis, which revealed a reversal of charge at each stage of polyelectrolyte adsorption (Figure 6.9). An initial value of -26 mV corresponds to surfactant stabilized PS latex particles and subsequent alternating zeta potentials indicate multilayer film growth on the PS particles.

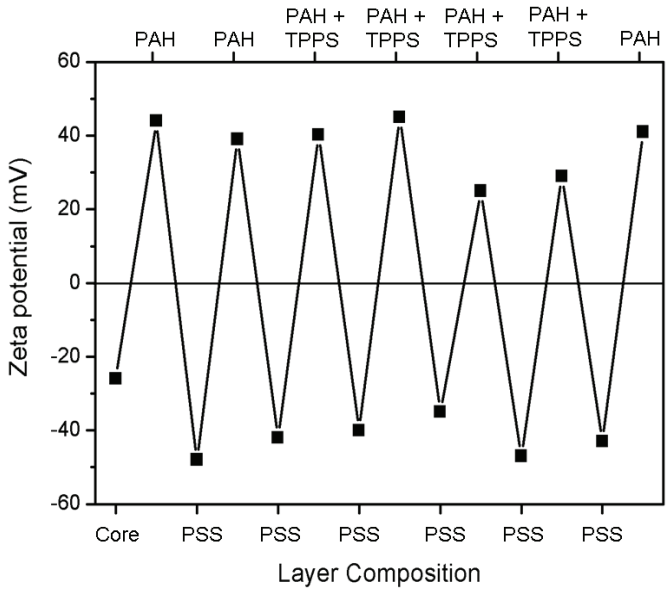

Fig. 6.9 Zeta-potential analysis at each stage of polyelectrolyte/TPPS adsorption.

6.7 ESTIMATION OF PERCENT INCORPORATION OF TPPS IN CAPSULE'S SHELL

During capsule assembly, the UV-visible spectra of the supernatants after each layer additions were measured, which showed that while 100 % of TPPS is adsorbed at each addition, between 2 and 10 % of TPPS is lost during subsequent layer addition, primarily during the next PSS additions. Based on these results, we estimated the approximate TPPS content adsorbed onto 50 mg of PS template (500 ml solution, 10% w/v) to be 9.7 x 10^{-8} mol (96.9%) and the corresponding loss to be 3.2 x 10^{-9} mol (3%). The amount of TPPS lost upon addition of the next PSS layer lessened as the number of layers increased, presumably due to the increase in available surface area as more layers are added to the PS particles.

The molecular weight of the amine monomer of PAH being 93.6 g/mol (C_3H_8NCl) means that a 2 mL aliquot of a 2 mg/mL polymer solution corresponds to 4.3 x 10^{-5} mole of

amine. The mole ratio of amine divided by TPPS equals 430. Using such an excess of amine PAH insures that the functional dye preferably interacts with the polyelectrolyte rather than to form aggregates with itself in ionic solution, which are optically inactive.

6.8 SPECTROSCOPIC PROPERTIES OF TPPS IN LBL POLYELECTROLYTE CAPSULES

The spectroscopic properties of $(PAH/PSS)_2(PAH+TPPS/PSS)_4PAH$ hollow capsules were investigated using UV-visible spectroscopy. For UV analysis, capsules were constructed using 4.62 µm PS particles to improve the signal-to-noise ratio of the measurements. It was previously shown that the UV-visible spectrum of TPPS in aqueous solution (in its monomeric tetraanionic state $[H_2TPPS]^{4-}$) exhibits a main Soret band in the visible range at 413 nm along with weak Q bands at 515 nm, 548 nm and 578 nm (Figure 6.1). The corresponding UV-visible spectrum of TPPS-PE capsules showed slightly red shifted Soret and Q bands at 425 nm and 520 nm, 555 nm, 595 nm, respectively (Figure 6.10). A similar red shift was observed when measuring the UV-Visible spectra of the same multilayer system on a polyethylenimine coated quartz substrate (Figure 6.5B). Sarasivan *et al.* previously detected the dianion state of TPPS at the surface of polymeric microcapsules, which resulted in a red shift of the Soret band from 415 nm to 435 nm. [186] Our results are in agreement with those observations suggesting that TPPS forms dianoic complexes to some extent in the microshells.

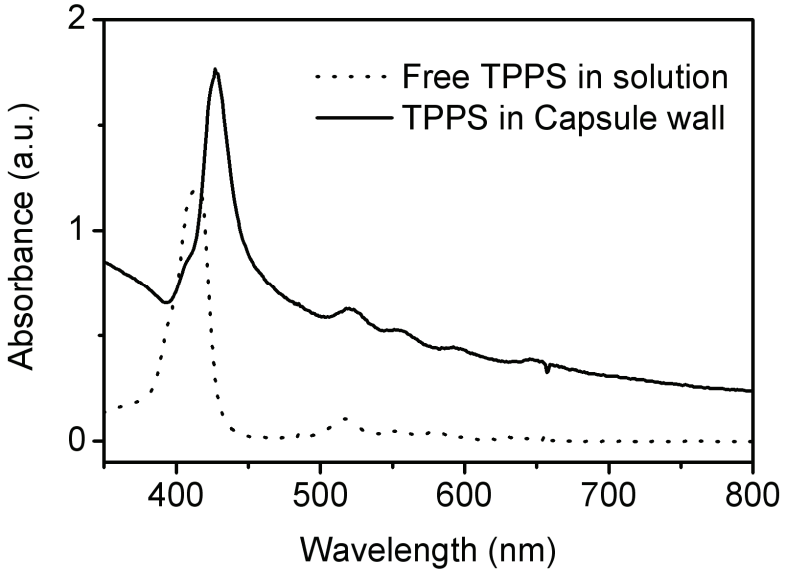

Fig. 6.10 UV-visible spectra of TPPS-PE capsule solution (solid line) showing a red shift of the main absorption band from that of a solution of free TPPS (dotted line).

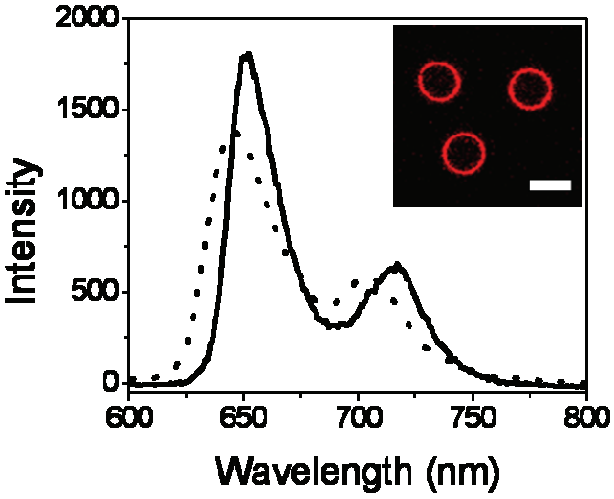

Fig. 6.11 Fluorescence spectra of a solution of TPPS monomers (dotted line) and that of a solution containing TPPS-PE capsules (solid line). Inset: LSCM image showing the fluorescent nature of capsule wall. (Scale bar measures 20 μm).

Removal of the PS core with THF gave red sediment containing hollow TPPS-PE capsules, which was then thoroughly washed to eliminate residual THF. The fluorescence spectra of TPPS monomers in aqueous solution exhibits two broad emission bands at 644 nm and 704 nm corresponding to the (0-0) and vibronic (0-1) transition of the free base $[H_2TPPS]^{4-}$ (Figure 6.11, dotted line). Similarly, TPPS-PE capsules showed two emission bands at 650 nm and 715 nm, confirming the formation of fluorescent capsules (Figure 6.11, hard line). The fluorescence intensity remained unchanged even after three months of storage in darkness at 4°C suggesting that the dye is well anchored within the multilayer. LSCM showed intact, hollow capsules with fluorescence emerging only from the shell wall (Figure 6.11, inset).

6.9 WALL MORPHOLOGY AND THICKNESS

Scanning electron microscopy (SEM) was used to image the shell morphology. Figure 6.12 shows a representative SEM image of a dried $(PAH/PSS)_2(PAH/TPPS)_4PAH$ capsule (diameter 10.2 μm. The structure appeared as if covered with particulate matter, which is atypical for PAH/PSS based microcapsules. At higher magnification, the rough surface becomes obvious.

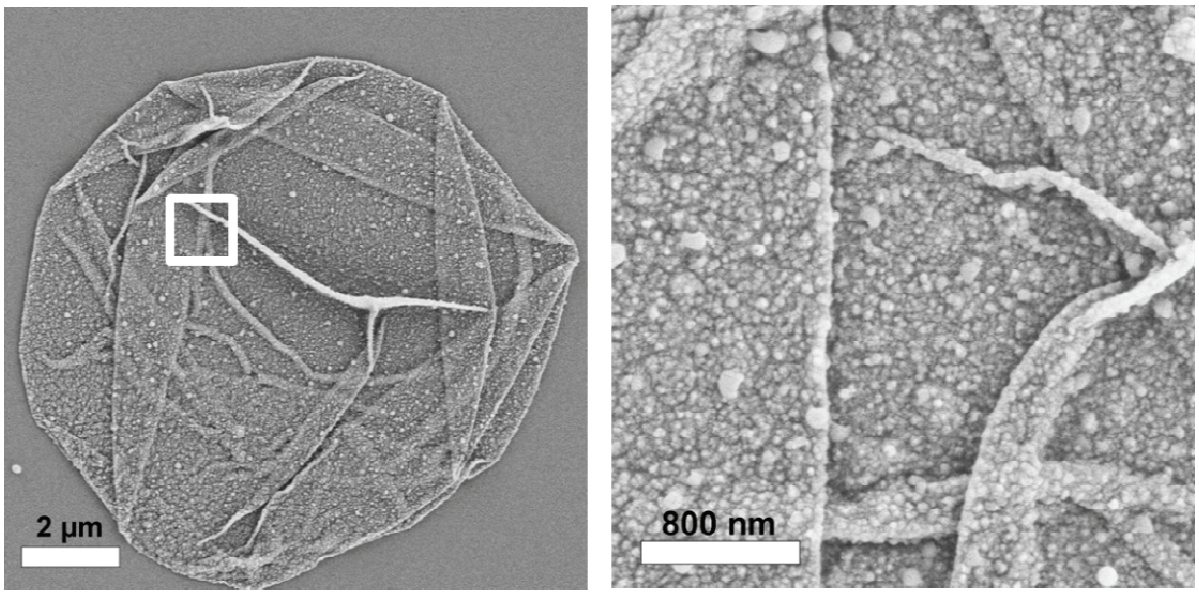

Fig. 6.12 SEM micrograph of dried TPPS-PE capsule. Inset illustrates a magnified area from a different shell but to the scale illustrated on the left.

Shell morphology was also investigated by AFM which allows qualitative and quantitative information to be gathered from the capsules. Figure 6.13 shows an AFM image reconstruction of a typical capsule (diameter 4.7 µm). The thickness of the capsule wall was determined by averaging the thicknesses of 15 capsules. Capsules were found to possess a relatively homogeneous surface with folds and creases resulting from the solvent evaporation during sample preparation. AFM imaging confirmed a rough shell surface, which may be due to the presence of small TPPS aggregates within the microshell. The average wall thickness of TPPS-doped capsules was found to be 28.8 nm ± 1.4 corresponding to a layer thickness of 3.6 nm ± 0.1. Capsules prepared in the absence of porphyrin under the same conditions have nearly layer thicknesses.[16,250] However, when the same assembly was done on flat substrates and monitored by UV-visible spectroscopy (Figure 6.4), it appeared that the layers should be thicker as more material absorbed at each layer then in the case where only PAH and PSS absorbed (Figure 6.6). A likely explanation for this discrepancy between the measurements is that the conditions (*e.g.* relative humidity) under which UV-visible spectroscopy and AFM measurement were done differed. [197]

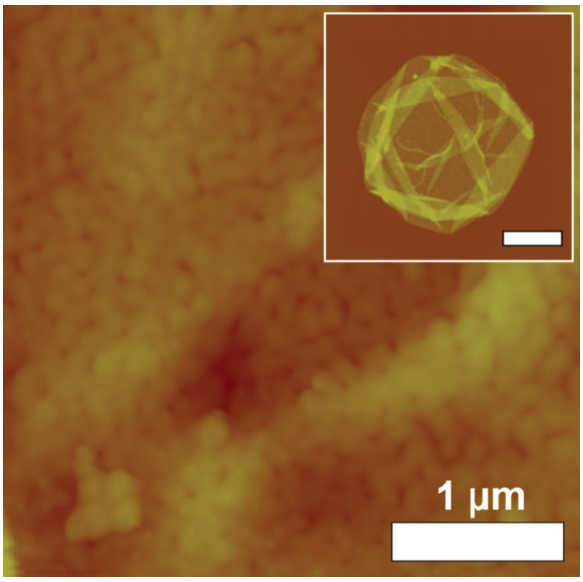

Fig. 6.13 High resolution AFM image of a TPPS-PE capsule wall section. The inset shows the whole capsule (scale bar 2 µm).

6.10 PHTHALOCYANINE/POLYELECTROLYTE COMPOSITE SHELLS

Capsules containing PcS, FePcS or AlPcS in the shell were prepared on 4.62 µm PS particles as well as 4.78 µm SiO_2 particles. 4 bilayers of (PAH+Pc/PSS), (PDDA+Pc/PSS) and (PDDA/Pc/PSS) were assembled for each template, where Pc denotes any of the four phthalocyanine. The polycation+PcS layer was made by premixing equal volumes of dye (10^{-7} M, 0.5 M NaCl) and polymer (2 mg/mL, 0.5 M NaCl) solutions. The dye solutions were prepared with in ionic solution to preserve the final salt concentration in the polyelectrolyte/Pc mixture. The adsorption steps were carried out at room temperature for 20 minutes. After each layer addition, the particles were washed thrice. Once the required layer number was obtained, the supernatant was removed and the templates dissolved according to the general polystyrene and silica dissolution procedures available in the methods section. The samples prepared are summarized in Table 6.

The coloration parameter in Table 6 corresponds to the relative intensity of blue hue of the sample pellet following each centrifugation step. This color is the first indication of the dyes adhering strongly or not to the capsule shell and it generally became more intense as more layers were added. The samples constructed on silica using PAH as a polycation (Table 6, **4-6**) appeared to have the strongest coloration before core dissolution but could not keep their integrity upon dissolution with an ammonium fluoride buffer solution (pH 4). PAH/PSS shells

are sensitive to strong acids due to the weak nature of the polyion PAH which causes the electrostatic interactions between PAH and PSS to weaken. Therefore, a mild pH ammonium fluoride buffer is usually suitable to dissolve silica coated with a weak polyelectrolyte but not in this case, suggesting that Pc dyes weaken Coulombic interactions between layers. Shells of PDDA+Pc/PSS and PDDA/Pc/PSS assembled on silica (**1-3**) however, remained intact during HF core dissolution but lost much of the dye presumably because their sulfonate groups became fully protonated at the low pH conditions of dissolution. In the case of shells constructed on PS particles, PDDA based constructs (**7-9**) yielded aggregated capsules with low dye content. Capsules of PAH on PS (**10-12**) had a much stronger color than PDDA containing ones, in agreement with the spectroscopy data obtained for TPPS in the previous section but were also quite aggregated. Capsules constructed by adding Pc as a separate layer (**13, 15**) to obtain the structure PDDA/Pc/PSS produced good quality samples but appeared completely white, at the exception of AlPcS sample (**14**).

TABLE 6 SUMMARY OF CAPSULES SAMPLES CONTAINING PHTHALOCYANINE DYES

Sample	Shell	Template	Sample?	Colour intensity	Note
1	$(PDDA+PcS/PSS)_4$	SiO_2	yes	Low	-
2	$(PDDA+AlPcS/PSS)_4$	SiO_2	yes	Medium	Fluorescence in cavity.
3	$(PDDA+FePcS/PSS)_4$	SiO_2	yes	None	-
4	$(PAH+PcS/PSS)_4$	SiO_2	no	-	-
5	$(PAH+AlPcS/PSS)_4$	SiO_2	no	-	-
6	$(PAH+FePcS/PSS)_4$	SiO_2	no	-	-
7	$(PDDA+PcS/PSS)_4$	PS	yes	Low	Aggregation.
8	$(PDDA+AlPcS/PSS)_4$	PS	yes	Medium	Fluorescence in shell, aggregation.
9	$(PDDA+FePcS/PSS)_4$	PS	yes	None	Aggregation.
10	$(PAH+PcS/PSS)_4$	PS	yes	Medium	Aggregation.
11	$(PAH+AlPcS/PSS)_4$	PS	yes	Medium	Aggregation.
12	$(PAH+FePcS/PSS)_4$	PS	yes	Medium	Aggregation.
13	$(PDDA/PcS/PSS)_4$	SiO_2	yes	None	-
14	$(PDDA/AlPcS/PSS)_4$	SiO_2	yes	Low	-
15	$(PDDA/FePcS/PSS)_4$	SiO_2	yes	None	-

Overall, Table 6 shows that much effort was invested in building shells functionalized with Pc, a more potent PDT agent than TPPS, but yielded few positive results. It can be said that unlike the system PAH+TPPS/PSS, PS templates appear to are not suitable for the strategies used with Pc, which were in turn based on QCM data and the spectroscopic data obtained from TPPS complexes, as microcapsule aggregation results. In turn silica cores are not preferred for the assembly of PAH+Pc/PSS systems as they lost their integrity upon core dissolution. Finally, while PAH appeared to favor the incorporation of Pc in the shell, the use of PDDA does not.

These samples were then further investigated by LSCM. Samples built from FePcS and PcS displayed no noticeable fluorescence. $(PDDA+AlPcS/PSS)_4$ capsules assembled on PS particles (2, **8** Figure 6.14) were fluorescent when excited at 633 nm (Figure 6.14B) but not at excitation wavelengths lesser than 594 nm. This was expected as AlPcS displayed intense Q-bands in the region 600-700 nm (see Figure 6.3). For identical shells constructed on silica (**2**), the fluorescence came from the capsule's interior and appeared to have little affinity for its wall (Figure 6.14A). This is most unusual since a portion of the dye not only appears to have diffused from the shell to the hollow cavity but remained there. Usually, small molecules tend to diffuse in and out of thin polyelectrolyte films with ease and are only limited by their interactions with the film constituents and not by size exclusion factors. One possible explanation for this is that AlPcS molecules form higher order aggregates becoming trapped in the shells. [174,176,184] The best quality samples from Table 6 were the three samples obtained using PDDA as a polycation on silica with the layer structure PDDA+Pc/PSS (**1-3**).

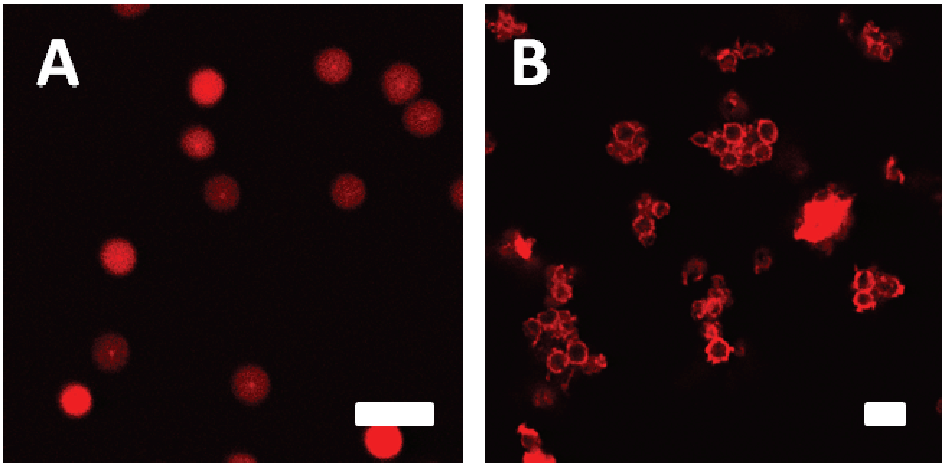

Fig. 6.14 LSCM images of $(PDDA+AlPcS/PSS)_4$ capsules assemble on silica and PS, A and B, respectively. Scale bars measure 10 µm.

6.11 IRRADIATION OF PORPHYRINOID DYE-FUNTIONALIZED POLYELECTROLYTE MICROCAPSULES

The fluorescent $(PAH/PSS)_2(PAH/TPPS)_4PAH$ capsules were further investigated to understand their response to light irradiation using a xenon light source (white light with strong UV emission) and a laser set-up. The capsules were first exposed to UV light using a 150 W xenon lamp (using a light filter to cut off wavelength greater than 400 nm) for 30 minutes to address the Soret band absorption region of the dye, which is centered at 385 nm in the PAH+TPPS complex. Monitoring of the capsules by LSCM before and after light exposure showed no change in morphology of the capsules. Also, no spectral changes in UV-visible and fluorescence measurements were observed prior to and after irradiation. Capsules were then irradiated in presence of the oxidising agent hydrogen peroxide (H_2O_2, 30% w/v), which enhances the photocatalytic effects of porphyrin, but no change in morphology was observed suggesting that the light intensity used is insufficient to induce the oxidizing potential of TPPS. In a previous study, it was shown that under similar conditions, azobenzene-containing capsules shrink considerably under UV light irradiation, a feat that is attributed to specific physical properties of azobenzene molecules in response to light exposure. [158] Also, it has been shown that capsules formed from polyelectrolytes like PSS which contain UV absorbing aromatic groups shrunk on UV irradiation. [157,160]

The Q bands region of the spectrum of TPPS (500-600 nm) was then investigated to test the stability of $(PAH/PSS)_2(PAH/TPPS)_4PAH$ capsules on exposure to laser light was tested using a 70 mW laser set-up. A drop of the capsule solution was mounted on a microscope slide and irradiated with a wavelength of 532 nm. The laser irradiation caused no changed in capsule morphology indicating the capsules were stable to the intense radiation (Figure 6.15, top panel). The capsule solution was then mixed with H_2O_2 and irradiated in an identical way. Interestingly, a distinct deformation of the capsule wall was noticed within few seconds of irradiation (Figure 6.15, bottom panel). It should be noted that the oxidizing agent by itself did not cause the deformation of the capsule (Figure 6.15, bottom panel, (a)). Thus, in presence of an oxidizing agent laser irradiation of porphyrin-polyelectrolyte capsules results in disruption of the capsule wall. This effect, however, was observed for about 40 % of the irradiated capsules, suggesting that variations in capsule geometry make some shells more resistant to the effects of the dye. Increasing the volume content of peroxide to 50 % did not appear to further improve the damages caused from laser irradiation. The fluorescence intensity of TPPS

remained after several laser exposures indicating that no photodegragation occurred. This offers a new strategy to remote opening of capsules wherein a functional dye can be used to trigger a major photochemical response in the microcapsules' wall. The incorporation of an IR dye into capsules was previously reported, [21] which upon irradiation also damaged the capsules but at the expense of photobleaching the dye. Samples **1-3** from Table 6 were exposed to UV and visible light from a xenon source but their morphology was not found to be altered even in the presence of hydrogen peroxide. This lack of response especially from $(PDDA+AlPcS/PSS)_4$ capsules, which appeared promising candidates as one could conclude from their ability to maintain AlPcS within the shell cavity, could be due to several factors including to the dye molecules adopting a conformation that does not favor their oxidative properties or quenching effects arising from being sequestered between polyelectrolytes.

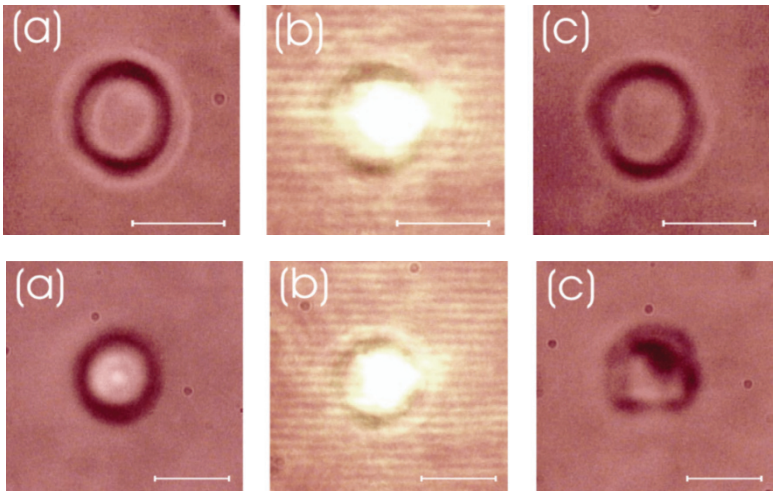

Fig. 6.15 Effect of laser light irradiation on TPPS-functionalized capsules: (top panel) without and (bottom panel) with H_2O_2. Images of the capsule (a) before, (b) during and (c) after laser irradiation (scale bar = 10 μm).

6.12 CONCLUSIONS

A new approach to remotely affect polyelectrolyte capsules with laser light was demonstrated. The functional porphyrin dye TPPS was introduced into PAH/PSS shells as a light harvesting center to mediate damages to the microcapsules. Spectroscopic and QCM studies on flat films revealed that the most favorable approaches to incorporate the small tetrasulfonated porphyrinoid dyes are to insert it between polyelectrolyte layers or to form a dye/polymer complex before treating the substrate with the desired layer. For samples prepared with TPPS, stable capsules were obtained following the template dissolution and the shells possessed a

wall thickness similar to that of TPPS-free capsules. On laser irradiation (532 nm) in presence of an oxidizing agent, the capsules became rapidly deformed. The shell disruption mechanism is believed to be chemical in origin – mediated by the dye - since no ionizing light sources were used and capsule containing no TPPS did not react to laser irradiation, even in the presence of an oxidizing agent. This mechanism relies on the excited triplet state of TPPS molecules, which transfer their energy to the nearby oxidizing agent to produce highly reactive hydroxyl radicals. [183,257]

Light induced effects were not observed in PcS incorporated capsules. The explanation for this lack of response can be explained in terms photophysical properties for PcS, and FePcS which both possess relatively short triplet state half time in the order of nano-seconds. As a result, despite having high quantum which should favor the production of singlet oxygen and radicals, the excited complex returns to ground state presumably too fast for chemical reactions to occur. [180,258] Thus, CuPcS was put aside due to its reportedly low triplet state quantum yield. [258] On the other hand, AlPcS was reported to possess a triplet state with both long lifetime and quantum yield. [178] Yet, the incorporation of Pc dyes in shells came with much aggregation issues. In one silica-based sample, AlPcS was found to diffuse inside the capsules hollow interior during dissolution and remain there. This interesting self-encapsulation property is unusual and deserves further studies as it is beyond the scope of the work discussed here. Another factor to take into account for all of the dyes used in this work is that immobilization inevitably reduces their photoreactivity due to the time required for the reactant to diffuse through the polymer mesh. [259] In addition, it cannot be excluded that the interaction of the dye molecule with polyelectrolytes might have some quenching effect although one study showed that the reactivity of polymer-bound AlPcS retained a good catalytic activity and improved stability over the unbound monomer. [260]

It is expected that further investigation with porphyrinoid-functionalized shells could reveal new ways to adjust light response in photoresponsive shells according to one's needs. The photodynamic process which appears to disrupt or weaken the polyelectrolyte multilayers is a much milder approach than the heating process triggered by metal nanoparticle, where the observed effect is extremely fast. Thereby incorporation of suitable functional dyes like porphyrins/metalloporphyrins could contribute to the development of photoactive capsules system, which can be opened at lower irradiation intensity.

7 GENERAL CONCLUSIONS

The present work illustrates well the complexity and diversity of potential applications for light addressable polyelectrolyte microcapsules. For most part, the studies presented were conducted in water but specific examples of investigations involving living cells were also conducted. While the aim remained focused towards biologically integrative microcapsules, the true range of applications for remotely addressable microcontainers extends far beyond biology and could be integrated in other industries such as food, textile and coatings.

Pulsed, 355 nm near-UV laser irradiation was found to be destructive for microcapsules at above fluencies of 40 mW/cm^2, even for microshells containing no specific chromophores for this wavelength region. On the other hand, no change in capsule morphology was observed upon irradiation at lesser power density. Similar results were obtained after the synthesis and incorporation of an azobenzene-modified PAH polyion in the microcapsule shell, yielding microshells that specifically absorbed in the near-UV wavelengths used. Based on these observations and the literature, it was concluded that ablation effects are responsible for damaging the shells at high laser power density. However, the high energy requirements to damage capsules with this approach necessitated the development of microshells with enhanced specific absorption hopefully preventing ablation effects to occur. CW near-UV irradiation was then used in order to obtain response with a less energetic light source.

Three types of azobenzene-substituted PAH were synthesized, characterized and incorporated in polyelectrolyte microcapsules. The polymer Azo1-PAH showed reversible *trans-cis* isomerization in UV-visible spectroscopy while the synthesis of Azo3-PAH resulted in a low solubility product that could not be used in capsule construction. Shells constructed using the new modified polymers showed no response to near-UV irradiation. This was attributed to the very limited azobenzene grafting ratios obtained using the grafting approach used, between 1 % and 5 %, because the viscosity of the reaction mixture increased with the mass of azobenzene monomers used. PAzo, a fully azobenzene-substituted polyanion was found to form stable microcapsules in combination with PAH. LSCM studies revealed that $(PAH/PAzo)_3PAH/PVS$ capsules have the ability to encapsulate materials upon exposure to UV. This was attributed to the shrinking and restructuration of the microshells to a denser, less permeable structure as a result of continuously summoning *trans-cis* isomerization of the azobenzene moieties in the microcapsules.

The incorporation and distribution of gold nanoparticles in microshells proved to be useful to optically release encapsulated materials. All studies involving microcapsules doped with gold nanoparticles were conducted using PDDA/PSS shells as model systems. The main reason for this choice was the well characterized ability of such microshells to become denser and less permeable upon heating. The temperature at which such encapsulation takes place is directly related to the glass transition of the polymers used in capsules' construction. Impregnating PDDA/PSS microshells with a nanoparticles surface coverage greater than 15 % can significantly improve the latters' mechanical stability, as demonstrated by thermal shrinking, permeability studies and colloidal probe AFM. However, a surface coverage of 28 % also limited the shell's response to thermal encapsulation due to the increase in percolation effects between nanoparticles as the capsules shrink. The concentration of dextran encapsulated by thermal treatment of the capsules was found to render the shells stiffer but also to limit their ability to shrink as a result of the pressure arising from the encapsulated dye. However, the most important parameter affecting shell stiffness was found to be its thickness which can be adjusted by thermal shrinking. This was also demonstrated in living cells, which otherwise tend to crush the microcapsules upon internalization.

The distribution of gold nanoparticle is affected in ionic solution resulting in aggregates with near-IR absorption capabilities. Microcontainers functionalized with aggregates of gold nanoparticles could be remotely opened in water upon near-IR laser irradiation using as little as 10 mW, approximately one order of magnitude less intensity than previously reported. Capsules doped with homodispersed nanoparticles could not be opened under the same conditions. Near-IR release efficiency was significantly improved by adjusting some proximal solution factors, such as: increasing temperature, adding salt, increasing the concentration of encapsulated substance and using capsules with smaller diameter. Some simulations demonstrated that this improvement in light addressability when using gold aggregates results from the improved heating capability of aggregated nanoparticles, which locally melts the microshell wall material decreasing the permeability of this one.

In accordance with our aims for this work, it was found that capsules that are thermally shrunk and doped with nanoparticles can be internalized by living cells in culture without deforming. LSCM allowed to locate the internalized capsules in the endo/lysosomal compartment for some time after cellular uptake and could be remotely opened using near-IR to release their cargo in the cytosolic space. Using a laser intensity of 30 mW for capsule

activation was found to be detrimental for cells, which tend to die. However, at a laser intensity of 2.3 mW the cells survived laser-induced release and could even divide afterward. Aggregates of gold nanoparticle were also used to sensitize giant, Dex-HEMA hydrogel templated microcapsules to near-IR. Due to their large volume and surface area, holes could be formed in the shell of such capsules by selectively targeting a region of the shell and thus inducing direction specific release.

Porphyrinoid dyes typically used for photodynamic therapy were incorporated in PAH/PSS and PDDA/PSS constructs to sensitize the shells to light but exploring an alternate light activated release approach. Functional dyes such as these trigger chemical reactions, an interesting prospect to remotely address capsules not explored before. To minimize dye losses from the capsule construct alternative LbL strategies were investigated by UV-visible spectroscopy and QCM and forming a complex of tetrasulfonated dye with the polycation was particularly effective in the case of the porphyrin dye TPPS. TPPS was thus incorporated in PAH/PSS shells, which were broken when irradiated with light in presence of an oxidizing substance probably due to the dye catalyzing the conversion of the oxidizing substance to radicals and/or singlet oxygen. Shells containing phthalocyanines, a group of dyes which absorb predominantly at around 670 nm, could not be damaged in the same fashion and proved to be more difficult to handle as aggregation and poor incorporation of dye was commonplace in most the capsule assembly methods tested. However, the aluminum phthalocyanine was found to accumulate in silica-templated PDDA/PSS capsules, which constitutes an intriguing phenomenon that surely deserves further investigation.

In summary, this work introduces novel light sensitive microcapsules with the ability of encapsulate or release materials in the near-UV, visible and near-IR spectral regions. Apart from the new insights proposed towards capsules assembly and mechanical stability, it reveals specific microcapsule responses, such as encapsulation and remote release of material under low intensity irradiation conditions are possible using an external trigger such as light by carefully selecting the materials and solution conditions appropriate for the experiments. Even more significant is the knowledge that light responsive microshells could be used in living cells. And yet, only one capsule design was investigated. The applications of optically addressable microcapsules are not limited to drug delivery but are of interest for other field such as microfluidics and surface coating technologies.

BIBLIOGRAPHY

1 G. Decher, *Science* **277** (5330), 1232 (1997).

2 E. Donath, G. B. Sukhorukov, F. Caruso et al., *Angew. Chem., Int. Ed.* **37** (16), 2202 (1998).

3 G. B. Sukhorukov, E. Donath, S. Davis et al., *Polymers for Advanced Technologies* **9** (10-11), 759 (1998).

4 G. B. Sukhorukov, E. Donath, H. Lichtenfeld et al., *Colloids and Surfaces a-Physicochemical and Engineering Aspects* **137** (1-3), 253 (1998).

5 G. Sukhorukov, A. Fery, and H. Mohwald, *Progress in Polymer Science* **30** (8-9), 885 (2005).

6 A. A. Antipov, G. B. Sukhorukov, S. Leporatti et al., *Colloids Surf., A* **198**, 535 (2002).

7 A. G. Skirtach, P. Karageorgiev, M. F. Bedard et al., *Journal of the American Chemical Society* **130** (35), 11572 (2008).

8 A. A. Antipov and G. B. Sukhorukov, *Advances in Colloid and Interface Science* **111** (1-2), 49 (2004).

9 G. B. Sukhorukov, M. Brumen, E. Donath et al., *Journal of Physical Chemistry B* **103** (31), 6434 (1999).

10 W. F. Dong, S. Q. Liu, L. Wan et al., *Chemistry of Materials* **17** (20), 4992 (2005).

11 B. S. Kim, O. V. Lebedeva, K. Koynov et al., *Macromolecules* **38** (12), 5214 (2005).

12 W. F. Dong, G. B. Sukhorukov, and H. Mohwald, *Physical Chemistry Chemical Physics* **5** (14), 3003 (2003).

13 K. Kohler and G. B. Sukhorukov, *Advanced Functional Materials* **17** (13), 2053 (2007).

14 C. Y. Gao, S. Leporatti, S. Moya et al., *Chem.--Eur. J.* **9** (4), 915 (2003).

15 R. Mueller, K. Kohler, R. Weinkamer et al., *Macromolecules* **38** (23), 9766 (2005).

16 C. Dejugnat and G. B. Sukhorukov, *Langmuir* **20** (17), 7265 (2004).

17 T. Mauser, C. Dejugnat, and G. B. Sukhorukov, *Macromol Rapid Comm* **25** (20), 1781 (2004).

18 G. B. Sukhorukov, A. A. Antipov, A. Voigt et al., *Macromol Rapid Comm* **22** (1), 44 (2001); T. Shutava, M. Prouty, D. Kommireddy et al., *Macromolecules* **38** (7), 2850 (2005).

19 B. G. De Geest, S. De Koker, G. B. Sukhorukov et al., *Soft Matter* **5** (2), 282 (2009).

20 B. Radt, T. A. Smith, and F. Caruso, *Advanced Materials* **16** (23-24), 2184 (2004).

21 A. G. Skirtach, A. A. Antipov, D. G. Shchukin et al., *Langmuir* **20** (17), 6988 (2004).

22 A. G. Skirtach, C. Dejugnat, D. Braun et al., *Nano Lett.* **5** (7), 1371 (2005).

23 G. B. Sukhorukov, A. L. Rogach, B. Zebli et al., *Small* **1** (2), 194 (2005).

24 L. Hartmann, M. Bedard, H. G. Borner et al., *Soft Matter* **4** (3), 534 (2008).

25 A. Katchalsky and P. Spitnik, *Journal of polymer science* **2**, 432 (1947).

26 S. E. Burke and C. J. Barrett, *Pure and Applied Chemistry* **76** (7-8), 1387 (2004).

27 H. Dautzernberg, W. Jaeger, J. Kötz et al., *Polyelectrolytes: Formation, Characterization and Application*. (Hanser Publishers, Munich, 1994).

28 G. J. Fleer, M. A. Cohen Stuart, J. M. H. M. Scheutjens et al., *Polymers and Interfaces* (Chapman & Hall, London, 1993).

29 K. N. Bakeev, V. A. Izumrudov, S. I. Kuchanov et al., *Macromolecules* **25** (17), 4249 (1992).

30 A. F. Thunemann, M. Muller, H. Dautzenberg et al., *Polyelectrolytes with Defined Molecular Architecture Ii* **166**, 113 (2004); H. Dautzenberg and N. Karibyants, *Macromolecular Chemistry and Physics* **200** (1), 118 (1999).

31 G. Decher, *Photonic and Optoelectronic Polymers* **672**, 445 (1997).

32 K. M. Lenahan, Y. X. Wang, Y. J. Liu et al., *Advanced Materials* **10** (11), 853 (1998).

33 A. Izquierdo, S. S. Ono, J. C. Voegel et al., *Langmuir* **21** (16), 7558 (2005); J. B. Schlenoff, S. T. Dubas, and T. Farhat, *Langmuir* **16** (26), 9968 (2000).

34 P. A. Chiarelli, M. S. Johal, J. L. Casson et al., *Advanced Materials* **13** (15), 1167 (2001).

35 P. A. Chiarelli, M. S. Johal, D. J. Holmes et al., *Langmuir* **18** (1), 168 (2002).

36 Y. Lvov, G. Decher, and G. Sukhorukov, *Macromolecules* **26** (20), 5396 (1993); O. E. Selina, S. Y. Belov, N. N. Vlasova et al., *Russian Journal of Bioorganic Chemistry* **35** (1), 103 (2009); L. I. Shabarchina, M. M. Montrel, G. B. Sukhorukov et al., *Russian Journal of Physical Chemistry* **74** (11), 1908 (2000); G. B. Sukhorukov, H. Mohwald, G. Decher et al., *Thin Solid Films* **285**, 220 (1996); A. P. R. Johnston, H. Mitomo, E. S. Read et al., *Langmuir* **22** (7), 3251 (2006).

37 T. Borodina, E. Markvicheva, S. Kunizhev et al., *Macromol Rapid Comm* **28** (18-19), 1894 (2007).

38 M. Y. Gao, C. Lesser, S. Kirstein et al., *Journal of Applied Physics* **87** (5), 2297 (2000); G. B. Sukhorukov, A. L. Rogach, M. Garstka et al., *Small* **3** (6), 944 (2007).

39 L. H. Han, T. J. Tang, and S. Chen, *Nanotechnology* **17** (18), 4600 (2006); D. Radziuk, A. Skirtach, G. Sukhorukov et al., *Macromol Rapid Comm* **28** (7), 848 (2007); X. Tao and J. M. Su, *Current Nanoscience* **4** (3), 308 (2008).

40 A. G. Skirtach, A. M. Javier, O. Kreft et al., *Angew. Chem., Int. Ed.* **45** (28), 4612 (2006).

41 B. G. De Geest, A. G. Skirtach, T. R. M. De Beer et al., *Macromol Rapid Comm* **28** (1), 88 (2007).

42 D. G. Shchukin, I. L. Radtchenko, and G. B. Sukhorukov, *Chemphyschem* **4** (10), 1101 (2003).

43 X. Tao, J. B. Li, and H. Mohwald, *Chem.--Eur. J.* **10** (14), 3397 (2004).

44 M. F. Bedard, S. Sadasivan, G. B. Sukhorukov et al., *J. Mater. Chem.*, DOI: 10.1039/b818774f (2009).

45 A. A. Mamedov, N. A. Kotov, M. Prato et al., *Nature Materials* **1** (3), 190 (2002).

46 K. Glinel, A. Moussa, A. M. Jonas et al., *Langmuir* **18** (4), 1408 (2002); R. Steitz, W. Jaeger, and R. von Klitzing, *Langmuir* **17** (15), 4471 (2001); U. Voigt, W. Jaeger, G. H. Findenegg et al., *Journal of Physical Chemistry B* **107** (22), 5273 (2003); B. Schoeler, G. Kumaraswamy, and F. Caruso, *Macromolecules* **35** (3), 889 (2002).

47 B. Schoeler, E. Poptoschev, and F. Caruso, *Macromolecules* **36** (14), 5258 (2003).

48 G. B. Sukhorukov, J. Schmitt, and G. Decher, *Berichte Der Bunsen-Gesellschaft-Physical Chemistry Chemical Physics* **100** (6), 948 (1996).

49 S. T. Dubas and J. B. Schlenoff, *Macromolecules* **34** (11), 3736 (2001).

50 N. A. Kotov, *Nanostructured Materials* **12** (5-8), 789 (1999).

51 S. T. Dubas and J. B. Schlenoff, *Macromolecules* **32** (24), 8153 (1999).

52 W. B. Stockton and M. F. Rubner, *Macromolecules* **30** (9), 2717 (1997).

53 R. S. Pontes, M. Raposo, C. S. Camilo et al., *Phys Status Solidi A* **173** (1), 41 (1999); L. Y. Wang, Z. Q. Wang, X. Zhang et al., *Macromol Rapid Comm* **18** (6), 509 (1997).

54 S. A. Sukhishvili and S. Granick, *Macromolecules* **35** (1), 301 (2002).

55 J. Ruths, F. Essler, G. Decher et al., *Langmuir* **16** (23), 8871 (2000).

56 R. A. McAloney, M. Sinyor, V. Dudnik et al., *Langmuir* **17** (21), 6655 (2001).

57 P. Lavalle, C. Picart, J. Mutterer et al., *Journal of Physical Chemistry B* **108** (2), 635 (2004); C. Picart, P. Lavalle, P. Hubert et al., *Langmuir* **17** (23), 7414 (2001).

58 G. Ladam, P. Schaad, J. C. Voegel et al., *Langmuir* **16** (3), 1249 (2000).

59 M. Salomaki, I. A. Vinokurov, and J. Kankare, *Langmuir* **21** (24), 11232 (2005).

60 C. Porcel, P. Lavalle, V. Ball et al., *Langmuir* **22** (9), 4376 (2006).

[61] G. Decher and J. B. Schlenoff eds., *Multilayer Thin Films*. (Wiley-VCH verlag, Weinheim, 2003).

[62] R. K. Iler, *J. Colloid Interface Sci.* **21**, 569 (1966).

[63] T. M. S. Chang, *Science* **146**, 524 (1964).

[64] A. Voigt, H. Lichtenfeld, G. B. Sukhorukov et al., *Industrial & Engineering Chemistry Research* **38** (10), 4037 (1999).

[65] C. S. Peyratout and L. Dahne, *Angew Chem Int Edit* **43** (29), 3762 (2004); H. Möhwald, E. Donath, and G. Sukhorukov, *Multilayer thin films*. (Wiley-VCH Verlag, Weinheim, 2003).

[66] B. G. De Geest, S. De Koker, K. Immesoete et al., *Advanced Materials* **20** (19), 3687 (2008); A. N. Zelikin, Q. Li, and F. Caruso, *Chemistry of Materials* **20** (8), 2655 (2008); W. J. Tong, C. Y. Gao, and H. Mohwald, *Chemistry of Materials* **17** (18), 4610 (2005).

[67] B. G. De Geest, M. J. McShane, J. Demeester et al., *Journal of the American Chemical Society* **130** (44), 14480 (2008).

[68] Y. J. Wang, V. Bansal, A. N. Zelikin et al., *Nano Lett* **8** (6), 1741 (2008).

[69] B. G. De Geest, W. Van Camp, F. E. Du Prez et al., *Chem Commun* (2), 190 (2008); B. G. De Geest, W. Van Camp, F. E. Du Prez et al., *Macromol Rapid Comm* **29** (12-13), 1111 (2008).

[70] L. A. Connal, C. R. Kinnane, A. N. Zelikin et al., *Chemistry of Materials* **21** (4), 576 (2009); C. J. Ochs, G. K. Such, B. Stadler et al., *Biomacromolecules* **9** (12), 3389 (2008).

[71] B. M. Discher, Y. Y. Won, D. S. Ege et al., *Science* **284** (5417), 1143 (1999).

[72] A. S. Angelatos, Y. J. Wang, and F. Caruso, *Langmuir* **24** (8), 4224 (2008); G. Buchel, K. K. Unger, A. Matsumoto et al., *Advanced Materials* **10** (13), 1036 (1998).

[73] P. A. L. Fernandes, G. Tzvetkov, R. H. Fink et al., *Langmuir* **24** (23), 13677 (2008).

[74] G. Tzvetkov, B. Graf, P. Fernandes et al., *Soft Matter* **4** (3), 510 (2008); D. G. Shchukin, K. Kohler, H. Mohvald et al., *Angew Chem Int Edit* **44** (21), 3310 (2005).

[75] A. Gedanken, *Chemistry-a European Journal* **14** (13), 3840 (2008).

[76] G. B. Sukhorukov, D. G. Shchukin, W. F. Dong et al., *Macromolecular Chemistry and Physics* **205** (4), 530 (2004).

[77] B. G. De Geest, C. Dejugnat, M. Prevot et al., *Advanced Functional Materials* **17** (4), 531 (2007); B. G. De Geest, C. Dejugnat, E. Verhoeven et al., *Journal of Controlled Release* **116** (2), 159 (2006).

[78] B. G. De Geest, J. P. Urbanski, T. Thorsen et al., *Langmuir* **21** (23), 10275 (2005); D. B. Shenoy and G. B. Sukhorukov, *Macromolecular Bioscience* **5** (5), 451 (2005).

[79] M. Prouty, Z. H. Lu, C. Leuschner et al., *J. Biomed. Nanotechnol.* **3** (2), 184 (2007).

[80] V. Bosio, F. Dubreuil, G. Bogdanovic et al., *Colloids and Surfaces a-Physicochemical and Engineering Aspects* **243** (1-3), 147 (2004); A. Badia, L. Cuccia, L. Demers et al., *Journal of the American Chemical Society* **119** (11), 2682 (1997); K. Kohler, P. M. Biesheuvel, R. Weinkamer et al., *Physical Review Letters* **97** (18) (2006).

[81] A. M. Yu, Y. J. Wang, E. Barlow et al., *Advanced Materials* **17** (14), 1737 (2005).

[82] K. W. Wang, Q. He, X. H. Yan et al., *Journal of Materials Chemistry* **17** (38), 4018 (2007).

[83] M. F. Bedard, D. Braun, G. B. Sukhorukov et al., *Acs Nano* **2** (9), 1807 (2008).

[84] M. F. Bedard, A. Munoz-Javier, R. Mueller et al., *Soft Matter* **5** (1), 148 (2009).

[85] S. De Koker, B. G. De Geest, C. Cuvelier et al., *Advanced Functional Materials* **17** (18), 3754 (2007).

[86] A. I. Petrov, D. V. Volodkin, and G. B. Sukhorukov, *Biotechnology Progress* **21** (3), 918 (2005).

[87] D. V. Volodkin, N. I. Larionova, and G. B. Sukhorukov, *Biomacromolecules* **5** (5), 1962 (2004).

[88] G. B. Sukhorukov, D. V. Volodkin, A. M. Gunther et al., *Journal of Materials Chemistry* **14** (14), 2073 (2004).

89 D. V. Volodkin, A. I. Petrov, M. Prevot et al., *Langmuir* **20** (8), 3398 (2004).

90 O. Kreft, R. Georgieva, H. Baumler et al., *Macromol Rapid Comm* **27** (6), 435 (2006); B. Neu, A. Voigt, R. Mitlohner et al., *Journal of Microencapsulation* **18** (3), 385 (2001); E. Donath, S. Moya, B. Neu et al., *Chemistry-a European Journal* **8** (23), 5481 (2002).

91 S. Moya, L. Dahne, A. Voigt et al., *Colloids and Surfaces a-Physicochemical and Engineering Aspects* **183**, 27 (2001).

92 G. Schneider and G. Decher, *Nano Lett* **4** (10), 1833 (2004).

93 C. Y. Gao, S. Moya, H. Lichtenfeld et al., *Macromolecular Materials and Engineering* **286** (6), 355 (2001).

94 C. Y. Gao, S. Moya, E. Donath et al., *Macromolecular Chemistry and Physics* **203** (7), 953 (2002).

95 A. A. Antipov, D. Shchukin, Y. Fedutik et al., *Colloids and Surfaces a-Physicochemical and Engineering Aspects* **224** (1-3), 175 (2003).

96 T. Adalsteinsson, W. F. Dong, and M. Schonhoff, *Journal of Physical Chemistry B* **108** (52), 20056 (2004); Y. Itoh, M. Matsusaki, T. Kida et al., *Chem Lett* **33** (12), 1552 (2004).

97 F. Hua, Y. Lvov, and T. H. Cui, *Thin Solid Films* **449** (1-2), 222 (2004); C. Lu, H. Mohwald, and A. Fery, *Journal of Physical Chemistry C* **111** (27), 10082 (2007); D. I. Gittins and F. Caruso, *Journal of Physical Chemistry B* **105** (29), 6846 (2001); Z. F. Dai, A. Voigt, E. Donath et al., *Macromol Rapid Comm* **22** (10), 756 (2001); F. Caruso, D. Trau, H. Mohwald et al., *Langmuir* **16** (4), 1485 (2000).

98 O. Kreft, A. M. Javier, G. B. Sukhorukov et al., *Journal of Materials Chemistry* **17** (42), 4471 (2007).

99 O. Kreft, M. Prevot, H. Mohwald et al., *Angew Chem Int Edit* **46** (29), 5605 (2007).

100 O. Kreft, A. G. Skirtach, G. B. Sukhorukov et al., *Advanced Materials* **19** (20), 3142 (2007).

101 W. N. E. vanDijkWolthuis, J. A. M. Hoogeboom, M. J. vanSteenbergen et al., *Macromolecules* **30** (16), 4639 (1997).

102 A. L. Cordeiro, M. Coelho, G. B. Sukhorukov et al., *Journal of Colloid and Interface Science* **280** (1), 68 (2004).

103 A. Fery and R. Weinkamer, *Polymer* **48** (25), 7221 (2007).

104 V. V. Lulevich, I. L. Radtchenko, G. B. Sukhorukov et al., *Journal of Physical Chemistry B* **107** (12), 2735 (2003); V. V. Lulevich, I. L. Radtchenko, G. B. Sukhorukov et al., *Macromolecules* **36** (8), 2832 (2003).

105 O. I. Vinogradova, D. Andrienko, V. V. Lulevich et al., *Macromolecules* **37** (3), 1113 (2004).

106 C. Y. Gao, E. Donath, H. Mohwald et al., *Angew Chem Int Edit* **41** (20), 3789 (2002).

107 R. Vonklitzing and H. Mohwald, *Langmuir* **11** (9), 3554 (1995); D. Halozan, C. Dejugnat, M. Brumen et al., *J. Chem. Inf. Model.* **45** (6), 1589 (2005).

108 W. F. Dong, J. K. Ferri, T. Adalsteinsson et al., *Chemistry of Materials* **17** (10), 2603 (2005).

109 B. G. De Geest, N. N. Sanders, G. B. Sukhorukov et al., *Chemical Society Reviews* **36** (4), 636 (2007).

110 R. Georgieva, R. Dimova, G. Sukhorukov et al., *Journal of Materials Chemistry* **15** (40), 4301 (2005).

111 J. Heuvingh, M. Zappa, and A. Fery, *Langmuir* **21** (7), 3165 (2005).

112 C. Dejugnat, M. Prevot, and G. B. Sukhorukov, *Abstracts of Papers of the American Chemical Society* **227**, U549 (2004).

113 C. Dejugnat, D. Halozan, and G. B. Sukhorukov, *Macromolecular Rapid Communications* **26** (12), 961 (2005).

114 L. Dahne, I. Stapf, and H. Moehwald, *Abstr Pap Am Chem S* **223**, U380 (2002); K. Itano, J. Y. Choi, and M. F. Rubner, *Macromolecules* **38** (8), 3450 (2005); P. M. Biesheuvel, T. Mauser, G. B. Sukhorukov et al., *Macromolecules* **39** (24), 8480 (2006).

115 T. Mauser, C. Dejugnat, H. Mohwald et al., *Langmuir* **22** (13), 5888 (2006).

116 T. Mauser, C. Dejugnat, and G. B. Sukhorukov, *J. Phys. Chem. B* **110** (41), 20246 (2006).

117 G. Ibarz, L. Dahne, E. Donath et al., *Advanced Materials* **13** (17), 1324 (2001).

118 C. Y. Gao, H. Mohwald, and J. C. C. Shen, *Chemphyschem* **5** (1), 116 (2004).

119 Y. Lvov, A. A. Antipov, A. Mamedov et al., *Nano Lett* **1** (3), 125 (2001).

120 S. Leporatti, C. Gao, A. Voigt et al., *European Physical Journal E* **5** (1), 13 (2001).

121 C. Y. Gao, B. Chen, and H. Mohwald, *Colloids and Surfaces a-Physicochemical and Engineering Aspects* **272** (3), 203 (2006); K. Glinel, G. B. Sukhorukov, H. Mohwald et al., *Macromolecular Chemistry and Physics* **204** (14), 1784 (2003).

122 J. M. Garza, P. Schaaf, S. Muller et al., *Langmuir* **20** (17), 7298 (2004).

123 K. Buscher, K. Graf, H. Ahrens et al., *Langmuir* **18** (9), 3585 (2002).

124 H. L. Tan, M. J. McMurdo, G. Q. Pan et al., *Langmuir* **19** (22), 9311 (2003).

125 P. V. Kamat, *J. Phys. Chem. C* **111** (7), 2834 (2007).

126 Karen Köhler, Universität Potsdam, 2006.

127 K. Kohler, H. Mohwald, and G. B. Sukhorukov, *Journal of Physical Chemistry B* **110** (47), 24002 (2006).

128 K. Kohler, D. G. Shchukin, H. Mohwald et al., *Journal of Physical Chemistry B* **109** (39), 18250 (2005).

129 K. Kohler, D. G. Shchukin, G. B. Sukhorukov et al., *Macromolecules* **37** (25), 9546 (2004).

130 C. Dejugnat, K. Kohler, M. Dubois et al., *Advanced Materials* **19** (10), 1331 (2007).

131 K. Kohler, C. Dejugnat, M. Dubois et al., *Journal of Physical Chemistry B* **111** (29), 8388 (2007); G. Ibarz, L. Dahne, E. Donath et al., *Chemistry of Materials* **14** (10), 4059 (2002).

132 R. Mueller, L. Daehne, and A. Fery, *Journal of Physical Chemistry B* **111** (29), 8547 (2007).

133 M. Prevot, C. Dejugnat, H. Mohwald et al., *Chemphyschem* **7** (12), 2497 (2006).

134 D. A. Gorin, S. A. Portnov, O. A. Inozemtseva et al., *Physical Chemistry Chemical Physics* **10** (45), 6899 (2008).

135 Z. H. Lu, M. D. Prouty, Z. H. Guo et al., *Langmuir* **21** (5), 2042 (2005).

136 S. H. Hu, C. H. Tsai, C. F. Liao et al., *Langmuir* **24** (20), 11811 (2008).

137 P. Rivera Gil, L. L. del Mercato, P. del-Pino et al., *Nano Today* **3** (3-4), 12 (2008).

138 K. S. Suslick, D. A. Hammerton, and R. E. Cline, *Journal of the American Chemical Society* **108** (18), 5641 (1986); D. G. Shchukin and H. Mohwald, *Physical Chemistry Chemical Physics* **8** (30), 3496 (2006).

139 W. B. Cai and X. Y. Chen, *Small* **3** (11), 1840 (2007); F. H. Meng, Z. Y. Zhong, and J. Feijen, *Biomacromolecules* **10** (2), 197 (2009); T. H. Yu, Z. B. Wang, and T. J. Mason, *Ultrasonics Sonochemistry* **11** (2), 95 (2004); M. R. Prausnitz and R. Langer, *Nature Biotechnology* **26** (11), 1261 (2008).

140 D. Dalecki, *Annual Review of Biomedical Engineering* **6**, 229 (2004).

141 B. G. De Geest, A. G. Skirtach, A. A. Mamedov et al., *Small* **3** (5), 804 (2007); A. G. Skirtach, B. G. De Geest, A. Mamedov et al., *Journal of Materials Chemistry* **17** (11), 1050 (2007); D. G. Shchukin, D. A. Gorin, and H. Moehwald, *Langmuir* **22** (17), 7400 (2006); G. B. Sukhorukov and H. Mohwald, *Trends in Biotechnology* **25** (3), 93 (2007).

142 E. Araya, I. Olmedo, N. G. Bastus et al., *Nanoscale Research Letters* **3** (11), 435 (2008); M. J. Kogan, N. G. Bastus, R. Amigo et al., *Nano Lett* **6** (1), 110 (2006).

143 D. A. Gorin, D. G. Shchukin, A. I. Mikhailov et al., *Technical Physics Letters* **32** (1), 70 (2006).

144 A. Vogel and V. Venugopalan, *Chemical Reviews* **103** (2), 577 (2003).

145 L. V. Zhigilei, P. B. S. Kodali, and B. J. Garrison, *Journal of Physical Chemistry B* **102** (16), 2845 (1998).

146 P. E. Dyer and R. Srinivasan, *Applied Physics Letters* **48** (6), 445 (1986).

147 Heinrich Zollinger, *Color Chemistry. Syntheses, Properties, and Applications of Organic Dyes and Pigments.*, 3rd ed. (VHCA, Switzerland, 2006).

148 H. Rau, in *Photochemistry and Photophysics*, edited by J. F. Rabek (CRC Press, Inc., Florida, 1990), Vol. 2.

149 K. Ishii, T. Hamada, M. Hatakeyama et al., *Chembiochem* **10** (2), 251 (2009).

150 W. X. Cao, S. J. Ye, S. G. Cao et al., *Macromol Rapid Comm* **18** (11), 983 (1997); J. S. Chen, R. Kohler, T. Gutberlet et al., *Soft Matter* **5** (1), 228 (2009); J. Y. Chen, L. Huang, L. M. Ying et al., *Langmuir* **15** (21), 7208 (1999); J. Q. Sun, T. Wu, Y. P. Sun et al., *Chem Commun* (17), 1853 (1998).

151 H. G. Zhu and M. J. McShane, *Langmuir* **21** (1), 424 (2005).

152 I. Pastoriza-Santos, B. Scholer, and F. Caruso, *Advanced Functional Materials* **11** (2), 122 (2001).

153 V. Zucolotto, N. M. B. Neto, J. J. Rodrigues et al., *Journal of Nanoscience and Nanotechnology* **4** (7), 855 (2004).

154 I. Suzuki, T. Ishizaki, T. Hoshi et al., *Macromolecules* **35** (2), 577 (2002); O. M. Tanchak and C. J. Barrett, *Macromolecules* **38** (25), 10566 (2005).

155 R. H. El Halabieh, O. Mermut, and C. J. Barrett, *Pure and Applied Chemistry* **76** (7-8), 1445 (2004).

156 J. L. Casson, D. W. McBranch, J. M. Robinson et al., *J. Phys. Chem. B* **104** (50), 11996 (2000); S. Dante, R. Advincula, C. W. Frank et al., *Langmuir* **15** (1), 193 (1999).

157 K. Katagiri, A. Matsuda, and F. Caruso, *Macromolecules* **39** (23), 8067 (2006).

158 M. Bedard, A. G. Skirtach, and G. B. Sukhorukov, *Macromol Rapid Comm* **28** (15), 1517 (2007).

159 H. N. Guan, D. F. Chi, J. C. Yu et al., *Pesticide Biochemistry and Physiology* **92** (2), 83 (2008); Y. X. Hu, J. P. Ge, Y. G. Sun et al., *Nano Lett* **7** (6), 1832 (2007); L. M. Bronshtein, P. M. Valetskii, and M. Antonietti, *Vysokomol. Soedin., Ser. A Ser. B* **39** (11), 1847 (1997).

160 K. Katagiri, K. Koumoto, S. Iseya et al., *Chemistry of Materials* **21** (2), 195 (2009).

161 D. G. Shchukin, E. Ustinovich, D. V. Sviridov et al., *Photochemical & Photobiological Sciences* **2** (10), 975 (2003).

162 E. V. Skorb, D. G. Shchukin, and D. V. Sviridov, *Molecular and Nanoscale Systems for Energy Conversion*, 75 (2008).

163 H. C. Leventis, I. Streeter, G. G. Wildgoose et al., *Talanta* **63** (4), 1039 (2004).

164 K. S. Kim, J. Y. Lee, B. J. Park et al., *Colloid and Polymer Science* **284** (7), 813 (2006).

165 Sung-Hoon Kim, *Functional Dyes*. (Elsevier, Amsterdam, 2006).

166 F. Caruso, H. Lichtenfeld, E. Donath et al., *Macromolecules* **32** (7), 2317 (1999); Z. F. Dai, A. Voigt, S. Leporatti et al., *Advanced Materials* **13** (17), 1339 (2001).

167 C. Kirchner, A. M. Javier, A. S. Susha et al., *Talanta* **67** (3), 486 (2005).

168 N. Gaponik, I. L. Radtchenko, M. R. Gerstenberger et al., *Nano Lett* **3** (3), 369 (2003); T. Jamieson, R. Bakhshi, D. Petrova et al., *Biomaterials* **28** (31), 4717 (2007); P. Sharrna, S. Brown, G. Walter et al., *Advances in Colloid and Interface Science* **123**, 471 (2006).

169 A. G. Skirtach, P. Karageorgiev, B. G. De Geest et al., *Advanced Materials* **20** (3), 506 (2008).

170 M. C. DeRosa and R. J. Crutchley, *Coord. Chem. Rev.* **233**, 351 (2002).

171 M. R. Detty, S. L. Gibson, and S. J. Wagner, *J. Med. Chem.* **47** (16), 3897 (2004); M. Lapes, J. Petera, and M. Jirsa, *Journal of Photochemistry and Photobiology B-Biology* **36** (2), 205 (1996).

172 D. Phillips, *Pure Appl. Chem.* **67** (1), 117 (1995).

[173] Z. Gasyna, N. Kobayashi, and M. J. Stillman, *Journal of the Chemical Society-Dalton Transactions* (12), 2397 (1989).

[174] A. D. Schwab, D. E. Smith, C. S. Rich et al., *Journal of Physical Chemistry B* **107** (41), 11339 (2003).

[175] Z. C. Wang, C. J. Medforth, and J. A. Shelnutt, *Journal of the American Chemical Society* **126** (51), 16720 (2004).

[176] Y. Egawa, R. Hayashida, and J. I. Anzai, *Langmuir* **23** (26), 13146 (2007).

[177] R. R. Carballo, V. C. Orto, J. A. Hurst et al., *Electrochimica Acta* **53** (16), 5215 (2008); G. de la Torre, P. Vazquez, F. Agullo-Lopez et al., *Journal of Materials Chemistry* **8** (8), 1671 (1998); P. Peumans, A. Yakimov, and S. R. Forrest, *Journal of Applied Physics* **93** (7), 3693 (2003); L. Valli, *Advances in Colloid and Interface Science* **116** (1-3), 13 (2005).

[178] K. Palewska, M. Sujka, B. Urasinska-Wojcik et al., *Journal of Photochemistry and Photobiology a-Chemistry* **197** (1), 1 (2008).

[179] W. S. Chan, J. F. Marshall, R. Svensen et al., *Photochem. Photobiol.* **45** (6), 757 (1987).

[180] J. R. Darwent, P. Douglas, A. Harriman et al., *Coord. Chem. Rev.* **44** (1), 83 (1982).

[181] H. R. Rawls and Vansante.Pj, *J. Am. Oil Chem. Soc.* **47** (4), 121 (1970).

[182] P. S. Vincett, E. M. Voigt, and Rieckhof.Ke, *J. Chem. Phys.* **55** (8), 4131 (1971).

[183] H. Kolarova, R. Bajgar, K. Tomankova et al., *Toxicology in Vitro* **21** (7), 1287 (2007).

[184] R. Augulis, V. Snitka, and R. Rotomskis, *Self Formation Theory and Applications* **97-98**, 191 (2004).

[185] J. Crusats, J. Claret, I. Diez-Perez et al., *Chem. Commun.* (13), 1588 (2003); R. Rotomskis, R. Augulis, V. Snitka et al., *J. Phys. Chem. B* **108** (9), 2833 (2004).

[186] S. Sadasivan, K. Kohler, and G. B. Sukhorukov, *Advanced Functional Materials* **16** (16), 2083 (2006).

[187] X. Tao, J. B. Li, J. Hartmann et al., *New Journal of Chemistry* **28** (12), 1579 (2004).

[188] D. G. Shchukin and D. V. Sviridov, *Journal of Photochemistry and Photobiology C-Photochemistry Reviews* **7** (1), 23 (2006).

[189] F. Caruso, *Advanced Materials* **13** (1), 11 (2001).

[190] M. A. El-Sayed, *Acc. Chem. Res.* **37** (5), 326 (2004); J. Perez-Juste, I. Pastoriza-Santos, L. M. Liz-Marzan et al., *Coord. Chem. Rev.* **249** (17-18), 1870 (2005); A. G. Skirtach, P. Karageorgiev, B. G. De Geest et al., *Adv. Mater.* (2008).

[191] U. Kreibig and L. Genzel, *Surf. Sci.* **156** (Jun), 678 (1985).

[192] T. J. Norman, C. D. Grant, D. Magana et al., *J. Phys. Chem. B* **106** (28), 7005 (2002).

[193] A. S. Angelatos, B. Radt, and F. Caruso, *Journal of Physical Chemistry B* **109** (7), 3071 (2005).

[194] G. H. Wu, A. Milkhailovsky, H. A. Khant et al., *Journal of the American Chemical Society* **130** (26), 8175 (2008).

[195] V. Pardo-Yissar, R. Gabai, A. N. Shipway et al., *Advanced Materials* **13** (17), 1320 (2001); A. N. Shipway and I. Willner, *Chem Commun* (20), 2035 (2001); C. Mangeney, F. Ferrage, I. Aujard et al., *Journal of the American Chemical Society* **124** (20), 5811 (2002).

[196] J. Blazevska-Gilev, Z. Bastl, J. Subrt et al., *Polymer Degradation and Stability* **94** (2), 196 (2009); J. Blazevska-Gilev, J. Kupcik, J. Subrt et al., *Polymer Degradation and Stability* **91** (2), 213 (2006); J. Kupcik, J. Blazevska-Gilev, J. Subrt et al., *Polymer Degradation and Stability* **91** (11), 2560 (2006); J. Pola, J. Kupcik, V. Blechta et al., *Chemistry of Materials* **14** (3), 1242 (2002); J. Pola, J. Kupcik, S. M. A. Durani et al., *Chemistry of Materials* **15** (20), 3887 (2003).

[197] R. Kugler, J. Schmitt, and W. Knoll, *Macromolecular Chemistry and Physics* **203** (2), 413 (2002).

[198] A. N. Volkov, C. Sevilla, and L. V. Zhigilei, *Applied Surface Science* **253** (15), 6394 (2007).

[199] W. J. Tong and C. Y. Gao, *Journal of Materials Chemistry* **18** (32), 3799 (2008).

200 H. C. Fischer and W. C. W. Chan, *Current Opinion in Biotechnology* **18** (6), 565 (2007).
201 A. M. Javier, O. Kreft, A. P. Alberola et al., *Small* **2** (3), 394 (2006).
202 A. M. Javier, O. Kreft, M. Semmling et al., *Advanced Materials* **20** (22), 4281 (2008).
203 A. M. Javier, P. del Pino, M. F. Bedard et al., *Langmuir* **24** (21), 12517 (2008).
204 R. Bhattacharya, P. Mukherjee, Z. Xiong et al., *Nano Lett* **4** (12), 2479 (2004); R. Bhattacharya, C. R. Patra, R. Verma et al., *Advanced Materials* **19** (5), 711 (2007).
205 S. G. Wang, W. T. Lu, O. Tovmachenko et al., *Chemical Physics Letters* **463** (1-3), 145 (2008).
206 T. S. Hauck, A. A. Ghazani, and W. C. W. Chan, *Small* **4** (1), 153 (2008).
207 B. G. De Geest, R. E. Vandenbroucke, A. M. Guenther et al., *Advanced Materials* **18** (8), 1005 (2006).
208 B. Cappella and G. Dietler, *Surf Sci Rep* **34** (1-3), 1 (1999).
209 F. Dubreuil, N. Elsner, and A. Fery, *European Physical Journal E* **12** (2), 215 (2003); A. Fery, F. Dubreuil, and H. Mohwald, *New Journal of Physics* **6** (2004).
210 J.L. Hutter and J. Bechhoefer, *Rev. Sci. Instrum.* **64** (7), 1868 (1993).
211 J. E. Sader, *Journal of Applied Physics* **84** (1), 64 (1998).
212 F. Dubreuil, N. Elsner, and A. Fery, *Europhys. J. E* **12** (2), 215 (2003).
213 A. Fery, F. Dubreuil, and H. Möhwald, *New Journal of Physics* **6**, 18 (2004).
214 D. Myers, *Surfaces, Interfaces and Colloids: Principles and Applications*, 2nd ed. (Wiley-VCH, New York, 1999).
215 G. Sauerbrey, *Zeitschrift f. Physik* **155**, 206 (1959).
216 M. Rodahl, F. Hook, and B. Kasemo, *Anal Chem* **68** (13), 2219 (1996); M. Rodahl and B. Kasemo, *Sensor Actuat a-Phys* **54** (1-3), 448 (1996).
217 S. A. Portnov, A. M. Yashchenok, A. S. Gubskii et al., *Instruments and Experimental Techniques* **49** (6), 849 (2006).
218 E. Poptoshev, B. Schoeler, and F. Caruso, *Langmuir* **20** (3), 829 (2004); H. Abramczyk and I. Szymczyk, *Journal of Molecular Liquids* **110** (1-3), 51 (2004).
219 A. Ashkin, *Biophysical Journal* **61** (2), 569 (1992); R. C. Gauthier, *Applied Physics Letters* **67** (16), 2269 (1995); S. C. Grover, R. C. Gauthier, and A. G. Skirtach, *Optics Express* **7** (13), 533 (2000).
220 A. M. Raichur, J. Voros, M. Textor et al., *Biomacromolecules* **7** (8), 2331 (2006).
221 A. G. Skirtach, A. M. Javier, O. Kreft et al., *Angewandte Chemie-International Edition* **45** (28), 4612 (2006).
222 B. Radt, T. A. Smith, and F. Caruso, *Advanced Materials* **16** (23-24), 2184 (2004).
223 R.J. Young and P.A. Lovell, *Introduction to Polymers*, Second ed. (Stanley Thornes Ltd, Cheltenham, UK, 1991).
224 A. S. Angelatos, K. Katagiri, and F. Caruso, *Soft Matter* **2** (1), 18 (2006).
225 G. Moller, M. Harke, H. Motschmann et al., *Langmuir* **14** (18), 4955 (1998).
226 M. Castelnovo and J. F. Joanny, *Langmuir* **16** (19), 7524 (2000); J. F. Joanny and M. Castelnovo, *Abstracts of Papers of the American Chemical Society* **219**, U510 (2000); D. Kovacevic, S. van der Burgh, A. de Keizer et al., *Langmuir* **18** (14), 5607 (2002).
227 M. Auch, PhD Thesis, University of Potsdam, 1999.
228 F. Dubreuil, D. G. Shchukin, G. B. Sukhorukov et al., *Macromol. Rapid Commun.* **25** (11), 1078 (2004).
229 N. Elsner, F. Dubreuil, R. Weinkamer et al., *Progress in Colloid and Polymer Science* **132**, 117 (2006).
230 A. N. Shipway, M. Lahav, R. Gabai et al., *Langmuir* **16** (23), 8789 (2000).
231 N. Felidj, G. Levi, J. Pantigny et al., *New Journal of Chemistry* **22** (7), 725 (1998); K. C. Grabar, R. G. Freeman, M. B. Hommer et al., *Anal Chem* **67** (4), 735 (1995); B. J. Olivier and C. M. Sorensen, *Journal of Colloid and Interface Science* **134** (1), 139 (1990).

232 K. S. Mayya, V. Patil, and M. Sastry, *Langmuir* **13** (15), 3944 (1997); M. Sastry, V. Patil, and K. S. Mayya, *Journal of Physical Chemistry B* **101** (7), 1167 (1997).

233 A. G. Skirtach, C. Dejugnat, D. Braun et al., *J. Phys. Chem. C* **111** (2), 555 (2007).

234 A. N. Shipway, E. Katz, and I. Willner, *Chemphyschem* **1** (1), 18 (2000).

235 S. D. Puckett, J. A. Heuser, J. D. Keith et al., *Talanta* **66** (5), 1242 (2005).

236 X. Huang, W. Qian, I. H. El-Sayed et al., *Lasers in Surgery and Medicine* **39** (9), 747 (2007).

237 G.A. Ozin and A. Arsenault, *Nanochemistry: a chemical approach to nanomaterials*. (Royal Chemistry Society, London, 2005).

238 C. Burns, W. U. Spendel, S. Puckett et al., *Talanta* **69** (4), 873 (2006); A. N. Shipway, M. Lahav, R. Blonder et al., *Chemistry of Materials* **11** (1), 13 (1999).

239 T. Kim, C. H. Lee, S. W. Joo et al., *Journal of Colloid and Interface Science* **318** (2), 238 (2008).

240 A. O. Govorov, W. Zhang, T. Skeini et al., *Nanoscale Research Letters* **1** (1), 84 (2006).

241 C. O. M'Bareck, Q. T. Nguyen, A. Metayer et al., *Polymer* **45** (12), 4181 (2004); S. C. Yeo and A. Eisenberg, *Journal of Macromolecular Science-Physics* **B13** (3), 441 (1977).

242 R. J. H. Stenekes, S. C. De Smedt, J. Demeester et al., *Biomacromolecules* **1** (4), 696 (2000).

243 D. G. De Geest, S. De Koker, J. Demeester et al., *J. Control. Release* (doi: 10.1016/j.jconrel.2009.01.017).

244 R. A. McAloney, V. Dudnik, and M. C. Goh, *Langmuir* **19** (9), 3947 (2003).

245 B. G. Stubbe, K. Braeckmans, F. Horkay et al., *Macromolecules* **35** (7), 2501 (2002); B. G. Stubbe, F. Horkay, B. Amsden et al., *Biomacromolecules* **4** (3), 691 (2003).

246 C. Y. Jiang, S. Markutsya, Y. Pikus et al., *Nat. Mater.* **3** (10), 721 (2004).

247 G. Ladam, C. Gergely, B. Senger et al., *Biomacromolecules* **1** (4), 674 (2000).

248 H. S. Zhou, I. Honma, H. Komiyama et al., *Phys Rev B* **50** (16), 12052 (1994).

249 Z. C. Wang, C. J. Medforth, and J. A. Shelnutt, *Journal of the American Chemical Society* **126** (49), 15954 (2004).

250 A. I. Petrov, A. A. Antipov, and G. B. Sukhorukov, *Macromolecules* **36** (26), 10079 (2003).

251 A. I. Petrov, A. V. Gavryushkin, and G. B. Sukhorukov, *Journal of Physical Chemistry B* **107** (3), 868 (2003).

252 N. C. Maiti, S. Mazumdar, and N. Periasamy, *J. Phys. Chem. B* **102** (9), 1528 (1998).

253 N. C. Maiti, S. Mazumdar, and N. Periasamy, *J. Porphyrins Phthalocyanines* **2** (4-5), 369 (1998).

254 M. Ioki, S. Igarashi, and T. Yotsuyanagi, *Anal. Sci.* **11** (1), 123 (1995).

255 B. F. Hoskin, S. A. Mason, and J. C. B. White, *J. Chem. Soc., Chem. Commun.*, 554 (1969).

256 N. Kobayashi, H. Konami, C. C. Leznoff et al., (VCH, Weinheim, 1996), Vol. 4, pp. 343.

257 S. G. Afonso, R. E. de Salamanca, and A. M. D. Batlle, *Brazilian Journal of Medical and Biological Research* **32** (3), 255 (1999).

258 R. W. Redmond and J. N. Gamlin, *Photochem. Photobiol.* **70** (4), 391 (1999).

259 A. P. Schaap, A. L. Thayer, E. C. Blossey et al., *J. Am. Chem. Soc.* **97** (13), 3741 (1975); M. Nowakowska, M. Kepczynski, and K. Szczubialka, *Macromol. Chem. Phys.* **196** (6), 2073 (1995).

260 R. Gerdes, O. Bartels, G. Schneider et al., *Polym. Adv. Technol.* **12** (3-4), 152 (2001).

PUBLICATIONS

1. Optically Driven Encapsulation Using Novel Polymeric Hollow Shells Containing an Azobenzene Polymer*, Bédard M, Skirtach AG, Sukhorukov GB*. Macromol. Rapid Comm., **2007**, *28*, 1517-1521.

2. Polyelectrolytes and porphyrin hollow capsules possessing laser-responsive oxidative properties*, Bédard MF, Sadasivan S, Skirtach AG, Sukhorukov GB*. J. Mat. Chem.*,* **2009**, *19*, 2226-2233.

3. On the Mechanical Stability of Polymeric Microcontainers Functionalized with Nanoparticles, *Bédard MF, Javier A, Mueller R, Skirtach AG, del Pino P, Fery A, Parak WJ, Sukhorukov GB.* Soft Matt., **2009**, *5*, 148-156.

4. Towards Self-Assembly of Nanoparticles on Polymeric Microshells: Near-IR Release and Permeability, *Bédard MF, Braun D, Sukhorukov GB, Skirtach AG.* ACS Nano, **2008.** *2*, 1807-1816*.*

5. Reversibly Permeable Nanomembranes of Polymeric Microcapsules, *Skirtach AG, Karageorgiev P, Bédard MF, Sukhorukov GB, Möhwald H*. J. Am. Chem. Soc. **2008***. 130*, 11572-11573.

6. Uptake of Colloidal Polyelectrolyte Coated Particles and Polyelectrolyte Multilayer Capsules by Living Cells*. Muñoz-Javier A, Kreft O, Semmling M, Kmpter S, Skirtach AG, Bruns O, del Pino P, Bédard MF, Rädler J, Käs J, Plank C, Sukhorukov GB, Parak WJ*. Adv. Mat., **2008**, *20*, 4281-4287.

7. Remotely controlled release of cargo from inside the cavity of polyelectrolyte capsules to the cytosol of cells. *Muñoz-Javier A, del Pino P, Bédard MF, Skirtach AG, Ho D, Sukhorukov GB, Plank C, Parak WJ*. Langmuir. **2008**, *24*, 12517-12520.

8. CO_2-Switchable Oligoamine Patches Based on Amino Acids and their Use to Build Polyelectrolyte Containers with Intelligent Gating*, Hartmann L, Bédard M, Börner HG, Möhwald H, Sukhorukov GB, Antonietti M*. Soft Matt., **2008**, *4*, 534-539.

9. Polymeric microcapsules with light responsive properties for encapsulation and release, *Bédard MF, De Geest B, Skirtach AG, Möhwald H, Sukhorukov GB*, Review, Adv.Coll.Interf.Sc., **Accepted.**

10. Relaxation times of colloidal iron platinum in polymer matrixes, *Puerto Morales M, Bédard MF, Zhang F, Zanella M, Sukhorukov GB, del Mercato L, Parak WJ*, J. Mat. Chem., **Accepted**.

11. Controlled intracellular release of peptides from microcapsules to follow antigen presentation on MHC class I molecules, *Palankar R, Skirtach AG, Kreft O, Bédard MF, Garstka M, Gould K, Möhwald H, Sukhorukov GB, Winterhalter M, Springer S,* Small, **Accepted**.

12. Synthesis and site-specific release for giant polyelectrolyte capsules, *Bédard MF, De Geest BG, Sukhorukov GB*, *Skirtach AG*, Soft Matter, **Accepted**.

13. Nanoparticle Mediated Optoporation for Switchable Membranes and Intracellular Drug Release, *Skirtach AG, Bédard MF, Karageorgiev P, Braun D, Sukhorukov GB Möhwald H*, **Submitted**.

14. Nanoparticles Distribution Control: Low Concentration Limit, *Parakhonsky BV, Bédard MF, Bukreeva TV, Sukhorukov GB, Möhwald H, Skirtach AG*, **Submitted**.

15. The Impact of Temperature, Ionic Strength and Sample Properties on Controlling Optoporation in Thin Polyelectrolyte Membranes, *Bédard MF, Skirtach AG, Sukhorukov GB,* **In Preparation**.

16. Synthesis of water soluble polyelectrolyte coated $NaYF_4$:Yb,Er by sonochemistry, *Bédard MF, Radzuik D, Sukhorukov GB Möhwald H, Shchukin D, Skirtach AG*, **In Preparation**.